Characterisation of the MICE Experiment

Sophie Charlotte Middleton

High Energy Physics

Blackett Laboratory

Imperial College London

A Thesis submitted in partial fulfilment of the requirements
of the degree of Doctor of Philosophy
in the Department of Physics at Imperial College London

August 8, 2018

Abstract

Muon beams of low emittance would deliver intense, well-characterised neutrino beams necessary to explicate the physics of flavour at a Neutrino Factory and for high-luminosity lepton-antilepton collisions at a multi-TeV muon collider. The International Muon Ionisation Cooling Experiment (MICE), based at the Rutherford Appleton Laboratory, aims to demonstrate ionisation cooling, the technique proposed to reduce the emittance of muon beams at such facilities.

An ionisation cooling channel has been constructed. The muon beam traverses a low-Z absorber material, losing energy via ionisation. The phase space volume occupied by the beam is reduced, resulting in transverse cooling. This thesis presents two independent analyses accomplished through exploiting data obtained during the "Step IV" commissioning of MICE.

Muons can decay within the cooling channel. The presence of electron contaminants within MICE will generate systematic uncertainties on the cooling measurement. The angular distribution of decay electrons is dependent upon the muon polarisation. It is, therefore, imperative to characterise the impact of depolarization in the channel. Chapter 4 presents a unique measurement of the polarisation of the MICE muon beam at the downstream calorimeter. For an initially unpolarised muon beam a polarisation of: -0.021 $\pm$ 0.243 (stat.) $\pm$ 0.185 (sys.) $\pm$ 0.007 (depol.) $\pm$ 0.001 (det.) is obtained, appropriately identifying the polarisation of the beam at the point of decay, within acknowledged errors.

MICE is devised to possess an on-axis magnetic field. It is paramount that misalignment in the cooling channel is characterised. Chapter 5 ascertains a measurement of the central Focus Coil's transverse position using single particle transfer matrices. No misalignment of the Focus Coil's magnetic axis, relative to the beam axis, is observed, within the limits of the analysis. This innovative technique can be employed by any multi-element accelerator system where particle co-ordinates are quantified upon entering and exiting a constituent magnet.

Declaration of Originality

The work presented in this thesis is my own unless explicitly stated otherwise. Chapters 1 and 2 introduce and expatiate upon accepted and verified concepts of contemporary particle and accelerator physics respectively. Discussion of such is necessary to present a comprehensive overview of the motivations for construction of the Muon Ionisation Cooling Experiment. All major results are referenced where appropriate.

Chapter 3 gives a synopsis of the design goals of the Muon Ionisation Cooling Experiment together with a detailed discussion of the various hardware and software techniques employed by the experiment in order to accomplish its aims.

Chapter 4 and 5 detail two independent analyses. The analysis techniques outlined in these chapters are entirely my own work, from conception to implementation, unless explicitly stated. The analysis procedures outlined in both chapters were novel and unique. The method exhibited in Chapter 5 provides an innovative approach to calculating magnet misalignment using the transfer matrices of single particles. A measurement of this kind has never been done before.

Both analyses exploit existing libraries and data structures inherent within the MICE Analysis User Software (MAUS). However, in order to complete the polarisation study, presented in Chapter 4, substantial upgrades to MAUS were carried out by myself. These gave MAUS the functionality which permitted the monitoring of particle spin and utilised the GEANT4's spin tracking algorithms. The data used in both Chapters 4 and 5 belongs to the MICE experiment the data is structured according to the standardised MAUS libraries.

It is noted in Chapter 2 that MICE must gain a better understanding of Multiple Coloumb Scattering which acts to counter ionisation cooling. Throughout the first year of my PhD I carried out a preliminary study which compared numerous models of multiple scattering and energy loss to data from the MuScat experiment, a predecessor to MICE. Chapter 2 presents some of the results of that study and utilises data obtained by MuScat. A primitive version of the MAUS simulation is compared to the data along with ICOOL and various versions of GEANT4. As part of this study I made some upgrades to MAUS which aimed to characterise the processes of multiple scattering and energy loss with the intention being to acquire data and build improved, data-based, models of both physical processes for the MICE absorber materials. However, due to insufficient MICE data at the time this work was discontinued at the beginning of 2014 and will now be completed by other members of the collaboration. There was no data from MICE available to compare with simulation at the point this thesis was originally written and therefore this discussion is only included to help illustrate the need for further study.

-Sophie Charlotte Middleton

Copyright Declaration

Acknowledgments

This thesis is dedicated to my Mum, Bernadette, for her unwavering support throughout my academic life and for providing me with the confidence that made my dream a reality. Everything I have achieved is due to your encouragement, Thank You.

I'd like to express my gratitude to David Colling for allowing me the opportunity to pursue a PhD in the High Energy Physics group. It is an one I am very grateful to have had.

Additional thanks must be granted to my colleagues, both at Imperial and on the MICE experiment, for making this rollercoaster such an enjoyable ride. It has been a pleasure to work amongst such intelligent and friendly people. In particular I'd like to show my appreciation to both Melissa and Celeste for all the time we spent drinking, chatting and even singing into the early morning after long days of collaboration meetings and additionally for your support over the final year.

My final acknowledgement goes to my sister, Phoebe, and to all the friends I've made during my time in London for always being there at the end of a hard day for a good night out - thanks for the memories and for making my time in this absurd city the best time of my life.

"We look for stranger things, because that's just who we are."

—Kyrre Gørvell-Dahll

Contents

List of Figures

List of Tables

Chapter 1

Introduction & Motivations

Before beginning to characterise the Muon Ionisation Cooling Experiment, it is essential to examine the numerous motivations for pursuing muon beam cooling. This chapter will introduce contemporary understanding of the Standard Model of particle physics, first qualitatively, and then phenomenologically, prior to considering the possibility of Beyond Standard Model physics. It is the desire to gain a more complete comprehension of particle physics which stimulates the effort to construct both a multi-TeV Muon Collider or Neutrino Factory. This chapter presents a synopsis of the physics goals of both facilities and outlines the importance of demonstrating muon ionisation cooling in order to make either a reality.

1.1 The Standard Model

1.1.1 Overview: Fundamental Particles

The Standard Model[1] of particle physics describes a universe populated with subatomic particles, each classified as either a fermion, (spin = 1/2), or a boson, (spin = 1, 0). These are summarised in Figure 1.1. The Standard Model interprets the electromagnetic, weak and strong forces as the consequences of an exchange of vector gauge bosons:

1. Electromagnetic interactions, which occur between electrically charged particles, are mediated by the massless photon (γ), first described by the theory of Quantum Electro-Dynamics (QED) [2] [3] [4].

2. The strong force acts between "colour charged" particles, such as quarks, and is mediated by the massless gluon (g). The Standard Model incorporates eight gluons and, as gluons themselves have "colour charge," self-interactions also occur. Strong interactions are characterised by the theory of Quantum Chromo-Dynamics (QCD) [5].

3. Weak interactions are a result of the exchange of either a charged, $W^{\pm}$, boson or a neutral, Z^0, boson; all three weak gauge bosons are massive. The $W^{\pm}$ bosons are electromagnetically charged and,

[1] many good synopses of the Standard Model can be found, much of this summary is derived from [1]

consequently, interactions involving the $W^{\pm}$ bosons are coupled to the electromagnetic interactions. Electroweak theory was developed as a combined description of the electromagnetic and weak forces and proposes that these forces are manifestations of the same fundamental process [6] [7] [8].

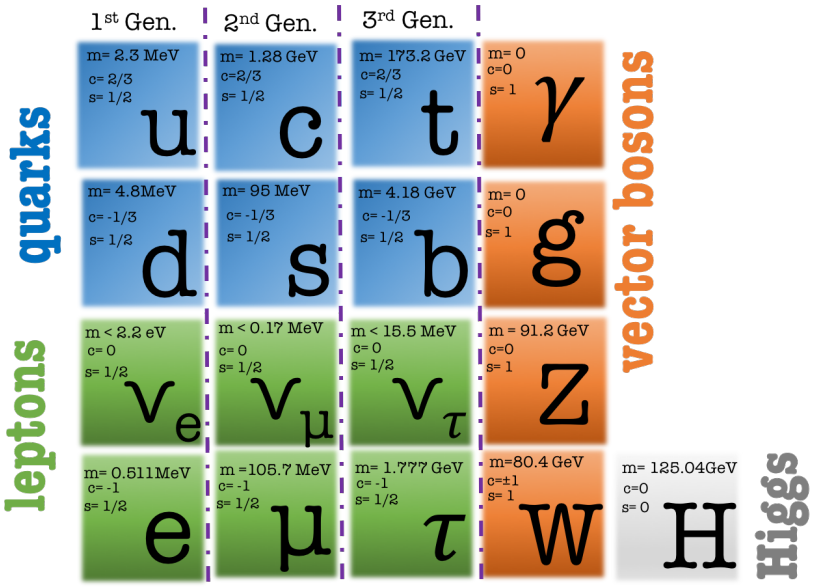

Figure 1.1: Summary of the various quark, leptons and gauge bosons presented in the Standard Model alongside measurements of, or limits on, the mass, charge and spin of each particle. These values were taken from [9]. In addition to the four vector gauge bosons in the Standard Model (coloured orange) the Standard Model predicts a scalar Higgs boson particle, with a spin of 0. The CMS and ATLAS detectors, based at the Large Hadron Collider (LHC), began seeing indications of a Higgs-like particle in 2012. The latest measurements of that particle's mass is 125.04 ± 0.21(stat) ± 0.11 (sys) GeV/c^2 [10].

Fermions are further subcategorised as either leptons or quarks. Within the Standard Model there exists six leptons: the electron (e), muon (μ), tau (τ) and their corresponding neutrinos, ν_e, ν_μ, ν_τ. Leptons are related in pairs, or "generations," based upon their respective flavours (e, μ, τ). The electron, muon and tau leptons all possess an electric charge with their associated neutrinos being electrically neutral and having comparatively small mass. It was assumed, at the time of the Standard Model's formulation, that the neutrinos were massless; this was later proven not to be the case. Discussion of the experimental evidence for neutrino mass is provided in Section 1.2 and the repercussions for the neutrino sector examined in Section 1.4.

The six flavours of quark, *up* (u), *down* (d), *strange* (s), *charm* (c), *bottom* (b) and *top* (t), which inhere in the Standard Model are again divided into three "generations" of quark pairs, the first, and lightest, generation being the *up* and *down*, the second being the *charm* and *strange* and the final, and heaviest, pair being the *top* and *bottom*. The quarks are themselves "colour-charged," hence, they too experience the strong force. In reality quarks form bound, colourless states either as quark-antiquark doublets ($q\bar{q}$) in mesons or quark/antiquark triplets ($qqq/\bar{q}\bar{q}\bar{q}$) in baryons.

The Standard Model combines two major extant theories: Electroweak Theory and Quantum Chromo-Dynamics (QCD); its theoretical underpinnings are considered in Section 1.1.2. Spontaneous symmetry breaking [11] accounts for the mass of the $W^{\pm}$ and Z^0 bosons. All massive particles acquire their mass via

the Higgs Mechanism - a detailed discussion of which is given in Section 1.1.3. A consequence of the Higgs Mechanism is the existence of a Higgs boson. The Standard Model Higgs boson is a scalar, spin-0 particle originally suggested, in 1964, by Robert Brout, Francois Englert, Peter Higgs, Gerald Guralnik, C.R Hagen and Tom Kibble [12] - [17]. In 2012 the first indications of a Higgs particle were observed at the Large Hadron Collider [18] [19]. Subsequent results from both the ATLAS and CMS detector have confirmed the observed particle has a spin of 0, even parity [20] [21] and a mass of 125.04 $\pm$ 0.21(stat) $\pm$ 0.11 (sys) GeV/c^2 [10].

1.1.2 Phenomenology of the Standard Model

The Standard Model relies on quantum field theories [22], constructed upon locally invariant Lagrangian. Particles correspond to quantised excitations in these fields. Imposing gauge symmetries leads to interactions between particles and gauge fields are introduced as mediators of these interactions. Noether's theorem [23] is fundamental to the Standard Model and states that every continuously differentiable symmetry of the Lagrangian of a theory corresponds to a conserved quantity.

The Standard Model is locally invariant under transformation by the $SU(3)_C \otimes SU(2)_L \otimes U(1)_Y$ gauge group. $SU(3)_C$ is the group governing the strong force interactions which couple to colour charge, C. $SU(2)_L$ and $U(1)_Y$ are groups governing the electroweak interactions. The sub-script L refers to the fact that the weak force is maximally parity violating [24] and only interacts with left handed fermions. Y defines electro-weak hyper-charge and is related to the particle's charge, Q, and the third component of the iso-spin, I_3, by the expression:

$$Q = I_3 + \frac{Y}{2}, \tag{1.1}$$

I_3 is $\pm\frac{1}{2}$ for left-handed fermions and 0 for all other particles.

Within the Standard Model fermions can be represented by spin-half spinors which can be split into left-handed (L) and right-handed (R) components using the projection operators $P_L = \frac{1}{2}(1-\gamma^5)$ and $P_R = \frac{1}{2}(1+\gamma^5)$ respectively. Left-handed spinors transform as a doublet, written as

$$\psi_L = \begin{pmatrix} u_i \\ d_i \end{pmatrix}_L \quad , \quad \begin{pmatrix} \nu_i \\ l_i \end{pmatrix}_L , \tag{1.2}$$

where i represents the fermion generation ($i = 1, 2, 3$). u_i are the "up-type" quarks (u, c, t) and d_i are the "down-type" quarks (d, s, b). l_i are the leptons e, μ, τ and ν_i are the corresponding neutrinos. The right-handed ψ_R are represented as singlet states, invariant under $SU(2)_L$.

Gauge symmetries in theories with fermions require the addition of an interacting vector boson per symmetry generator to preserve gauge invariance. $SU(3)_C$ has eight generators, thus, the eight vector bosons of the strong force arise which correspond directly to the eight physical gluons. $SU(2)_L$, has three generators whose three vector bosons: $\mathbf{W}_\mu = (W^1_\mu, W^2_\mu, W^3_\mu)$ mix with the one vector boson from $U(1)_Y$:

B_μ to form the electroweak force. The physical electroweak force gauge bosons, γ, Z^0 and $W^\pm$, are a result of mixing between these gauge fields such that

$$W^\pm = \sqrt{\frac{1}{2}}(W_\mu^1 \mp iW_\mu^2), \tag{1.3}$$

$$Z_\mu = B_\mu sin\theta_w - W_\mu^3 cos\theta_w, \tag{1.4}$$

$$A_\mu = B_\mu cos\theta_w + W_\mu^3 sin\theta_w, \tag{1.5}$$

where θ_w defines the Weinberg angle, A_μ is the photon field, Z_μ is the Z^0 field and the fields $W_\mu^\pm$ correspond to the $W^\pm$ bosons.

The intention of the Standard Model is to amalgamate all three forces into one Lagrangian, $\mathcal{L}$, expressed as

$$\mathcal{L} = i\bar{\psi}_i\gamma^\mu D_\mu\psi_i - \frac{1}{4}F_{\mu\nu j}F_j^{\mu\nu}, \tag{1.6}$$

assuming all particles are massless, where $i = 1, 2, 3$ indicates the 3 particle generations and $F_{\mu\nu j}F_j^{\mu\nu}$ is a sum of the free terms of all the Standard Model gauge bosons. D_μ is the covariant derivative which makes the Lagrangian invariant under a $SU(2)_c \otimes U(1)_Y$ gauge transformation and is written as

$$D_\mu = \partial_\mu + ig_1\frac{\tau_i}{2}W_\mu^i + i\frac{1}{2}g_2 Y B_\mu + ig_3\frac{\lambda_a}{2}G_\mu^a. \tag{1.7}$$

Local gauge invariance is achieved when τ_i are the generators of $SU(2)_C$, Y is the constant of $U(1)$, λ_a are the generators of $SU(3)_C$ and g_i are the coupling constants of the fields.

To account for fermion masses Equation 1.6 should include a term of the form

$$\mathcal{L}_f = -m\bar{\psi}\psi = -m(\bar{\psi}_R\psi_L - \bar{\psi}_L\psi_R), \tag{1.8}$$

where $\bar{\psi}$ is the adjoint of ψ. However, as the left and right handed components transform differently under $SU(2)_L$ and $U(1)_Y$, using this expression would break the gauge symmetry of the Lagrangian. Likewise, to account for the observed $W^\pm$ and Z^0 masses an additional Lagrangian term,

$$\mathcal{L}_V = \frac{1}{2}m_v^2 W_\mu W^\mu, \tag{1.9}$$

needs to be introduced, this will, once again, break the gauge invariance. In order to preserve the underlying symmetries and allow the weak gauge bosons to possess mass the electroweak symmetry must be spontaneously broken. The mechanism by which this takes place is the Higgs Mechanism.

1.1.3 Spontaneous Symmetry Breaking and The Higgs Mechanism

In the previous formulation all gauge bosons appear massless as introducing a mass term of the form of an integer-spin field of the form of Equation 1.9 is not invariant under the $SU(2)_L \otimes U(1)_Y$ gauge transformation.

The Higgs Mechanism introduces spontaneous symmetry breaking without destroying the gauge invariance of the electroweak theory. It provides a way for the gauge bosons and fermions to acquire mass by requiring that the symmetry of a system be spontaneously broken when the vacuum state of the system is not invariant under local gauge transformation but the Lagrangian density is.

This may be accomplished by introducing a scalar field, "The Higgs field", defined as a $SU(2)$ doublet with two complex scalar terms, represented as

$$\Phi = \begin{pmatrix} \phi^+ \\ \phi^0 \end{pmatrix} = \begin{pmatrix} \phi_1 + i\phi_2 \\ \phi_3 + i\phi_4 \end{pmatrix}. \tag{1.10}$$

The Lagrangian density for this field is

$$\mathcal{L}_{Higgs} = (D_\mu \Phi)^\dagger (D^\mu \Phi) - V_{Higgs}(\Phi^\dagger \Phi), \tag{1.11}$$

where D_μ is the electroweak covariant derivative described in Equation 1.7. V is the vacuum potential given by

$$V_{Higgs} = \mu^2 \Phi^\dagger \Phi + \lambda (\Phi^\dagger \Phi)^2, \tag{1.12}$$

where λ and μ are constants parameterising the self-interactions and masses of the scalar fields. When $\mu^2 < 0$ the symmetry is no longer unique, it takes the form of a continuous ring in the complex plane. The vacuum expectation value (VEV) for Φ will occur at a potential minimum i.e. when $\frac{\partial V}{\partial \Phi^\dagger \Phi} = 0$. By convention this is:

$$\Phi_{vacuum} = \frac{1}{\sqrt{2}} \begin{pmatrix} 0 \\ v + h(x) \end{pmatrix} \quad , \quad v = \sqrt{\frac{-\mu^2}{\lambda}}, \tag{1.13}$$

where v is the VEV and $h(x)$ is the Higgs field expressed as a quantum fluctuation about this value. The VEV is zero for the charged component and, therefore, preserves the electromagnetic symmetry but non-zero for the neutral component thus breaking electroweak gauge invariance. This is spontaneous symmetry breaking.

Substituting the expression in Equation 1.13 into Equation 1.11, the Higgs Lagrangian density after symmetry breaking can be written as

$$\mathcal{L}_{Higgs} = \frac{1}{2} \partial_\mu h \partial^\mu h - \frac{1}{2} \mu^2 h^2 + \frac{v^2}{8} [g_2^2 W_\mu^+ W^{+\mu} + g_2^2 W_\mu^- W^{-\mu} + (g_1^2 + g_2^2) Z_\mu Z^\mu]. \tag{1.14}$$

at leading order (higher order terms are present and result in addition of triple and quartic Higgs self-

interaction terms). This results in $W^{\pm}$ and Z^0 boson masses of $\frac{g_2^2 v^2}{2}$ and $\frac{v}{2}\sqrt{g_1^2+g_2^2}$ respectively. In addition the Higgs Mechanism has introduced a massive scalar Higgs boson, h, with mass $\sqrt{2}\mu$.

Fermion mass terms are introduced via Yukawa interactions between the fermions and Higgs field of the form

$$\mathcal{L}_{Yukawa} = -\lambda_f(\bar{\psi}_L\phi\psi_R + \bar{\psi}_R\phi\psi_L) = -\frac{\lambda_f}{\sqrt{2}}(\bar{\psi}_L\psi_R + \bar{\psi}_R\psi_L)v - \frac{\lambda_f}{\sqrt{2}}(\bar{\psi}_L\psi_R + \bar{\psi}_R\psi_L)h. \tag{1.15}$$

where $\lambda_f = \frac{\sqrt{2}m_f}{v}$ is the fermion coupling and is proportional to the fermion mass. The first term in this expression represents the fermion mass term, the second describes its interaction with the Higgs boson. Equation 1.15 implies heavier fermions have stronger coupling to the Higgs boson. The Standard Model gives no prediction of these Yukawa couplings, however, they can be determined from the observed masses of the fermions.

1.1.4 Understanding The Higgs Boson

The discovery of a particle with a mass of $\approx$ 125 GeV and ($J^p = 0^+$) at the LHC is widely interpreted as a Higgs boson as anticipated by the Standard Model. New physics can potentially be revealed in detailed studies of the Higgs boson parameters. In order to do so it is necessary to gain precision measurements of [25]:

1. The mass of the Higgs boson and its width,
2. The Higgs branching fractions and related coupling,
3. The Higgs coupling to top quark,
4. The Higgs self-couplings,
5. The total Higgs decay width,
6. Any exotic Higgs Decays.

To reach the desired precision on these quantities, higher intensity Higgs production than is achievable at LHC is essential. A muon collider, in which Higgs production occurs via $\mu^+\mu^-$ annihilation, would be the ideal machine for a"Higgs Factory" [26]. The additional physics advantages will be explored in Section 1.3.

1.2 Beyond the Standard Model

Since its formulation the Standard Model has successfully explained many experimental results. The particles and the 18 free parameters have been tested with extraordinary precision, in some cases up to 1 part in a trillion [27]. However, there remains a number of unresolved matters which have engendered some controversy:

1. **The Hierarchy Problem:**

The Hierarchy Problem arises from the issue of naturalness within the Standard Model resulting from the light Higgs boson. At tree level the Higgs mass is $\sqrt{2}\mu$, radiative corrections adjust the mass, such that

$$m_h^2 = 2\mu + \Delta m_h^2. \tag{1.16}$$

Figure 1.2 gives a representation of the radiative corrections to the Higgs mass resulting from a fermion and a scalar boson loop. The coupling of a fermion to the Higgs boson in the form $\lambda_f \bar{\psi}\phi\psi$, outlined in Section 1.1.3, yields a correction of

$$\Delta m_h^2 = -\frac{|\lambda_f|^2}{8\pi^2}[\Lambda^2 \ldots], \tag{1.17}$$

where Λ is the momentum cut off. Although the true value of Λ remains unknown it can be as high as the Planck scale, $\Lambda_{planck} \approx 10^{19}$GeV, where gravitational interactions become significant. Given that there are so many quantum corrections to the square of the Higgs mass it would be anticipated that the Higgs mass be large, and comparable to the Planck mass; however, this is not concordant with observation.

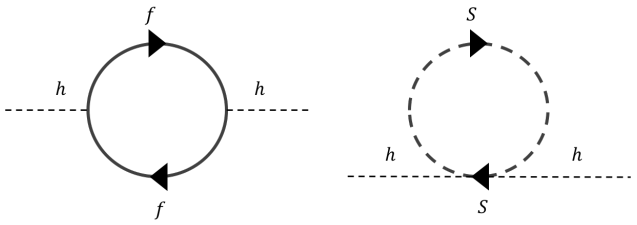

Figure 1.2: First-order correction to the mass of the Higgs boson from fermion, f, (left) and scalar, S, (right) loop.

In order to maintain the light Higgs mass observed experimentally with a Planck scale cutoff, $\Lambda \approx \Lambda_{planck}$, there must be a fine tuning which produces a perfect cancellation of the Higgs bare and corrected masses to a precision of 36 orders of magnitude [1]. A more theoretical overview of this Hierarchy Problem may be found in [22].

One way of accounting for this Hierarchy Problem is through Supersymmetry (SUSY), in which new, heavier supersymmetric partners of each Standard Model particle are introduced with spin differing by a half-an-integer. The theoretical underpinnings of SUSY are considered in detail in [28] [29] [30] [31]. Consequently, within SUSY every Standard Model fermionic particle, described in Figure 1.1, has a bosonic superpartner and vice versa. The bosonic and fermionic loop contributions, illustrated in Figure 1.2, contribute with opposite signs. As a result, the loop contributions of one particle to the Higgs mass are cancelled by the loop contributions of its superpartner, permitting a mass at the scale

measured by experiment.

The search for supersymmetric particles continues at the Large Hadron Collider. Currently, no conclusive proof of the existence of supersymmetric particles has been established. A summary of the Run-1 CMS and ATLAS supersymmetry searches can be found in [32][2].

Other theoretical solutions intending to resolve this Hierarchy Problem invoke extra dimensions in addition to the $3+1$ dimensions perceived. With these additional dimensions taken into account the fundamental Planck mass could in fact be small, meaning that gravity is actually strong, but this must be compensated by the number of the extra dimensions and their size. This would explain the physical weakness of gravity as being a result of a loss of flux to these extra dimensions. Further theoretical examination of this concept is presented in [33]. Again there is no experimentally verified proof to support the existence of additional dimensions with the latest results from ATLAS summarised in [34] and CMS in [35]. The search to explain the Hierarchy Problem continues.

2. **Dark Matter and Dark Energy:**

Cosmological observations have established that 70% of the density of the universe can be mathematically described by a cosmological constant attributed to a dark energy scalar field which is responsible for the acceleration of the universe [36]. Of the remaining 30%, only 17% are Standard Model particles implying 83 % are some additional, "dark" matter not detailed within the Standard Model [37].

The existence of dark matter would explain the rotational motions of galaxies [38] and gravitational lensing [39] as well as elucidating anisotropies in the cosmic microwave background [40]. There are several observations that are consistent with the dark matter theory, however, there is yet to be an observation of a particle that might constitute dark matter. Many theories of dark matter composition suggest it consists of weakly interacting massive particles (WIMP) which interact only via the weak and gravitational forces [41]; supersymmetric particles have been hypothesised as potential candidates.

3. **Antimatter-Matter Asymmetry:**

The Standard Model predicts that the Big Bang created equal quantities of matter and antimatter. In such a scenario matter-antimatter pairs would have annihilated in the early universe, leaving nothing except pure energy. This is contrary to what is observed physically and almost all of what remains in nature comprises of matter; antimatter is only observed in high energy processes such as cosmic ray interactions or within accelerators. It seems, therefore, that following the Big Bang, the majority of the matter and antimatter did annihilate, nonetheless, a small fraction of baryonic matter endured as a consequence of some inherent asymmetry. There are numerous theories concerning the origin of this

[2]More recent results have been published. As there are many different working groups looking into various different SUSY signatures only a summary is cited here

asymmetry, all beyond the Standard Model. The majority of these theories propose the asymmetry is a manifestation of CP violation.

CP violation in the weak sector has been established at LHCb [42] and Belle and Babar [43] and could contribute to the matter-antimatter asymmetry. Nevertheless, CP violation in the quark sector cannot completely explain the level of asymmetry which existed in the early universe [44]. In order to resolve the antimatter-matter asymmetry via CP violation alone it must additionally be present in the lepton sector - this will be considered in Section 1.4.

4. **Gravity:**

The Standard Model offers no approach to unify gravity with the three other fundamental forces. There have been numerous endeavours to add a "graviton" into the Standard Model, nevertheless, its existence is yet to be experimentally verified [45]. Furthermore, the Standard Model would require modification if it were to be consistent with both observation and General Relativity, the most successful theory of gravity thus far [46] [47].

5. **Understanding Neutrino Mass and Mixing:**

The Standard Model envisages massless neutrinos. Neutrino oscillations were predicted by Pontecorvo in 1957 [48] and throughout the succeeding decade Ray Davis's Homestake experiment [49] corroborated the theory, presenting evidence for a deficit in the observed solar neutrino flux relative to Standard Model solar predictions. This became acknowledged as "the solar neutrino problem."

In 1998 neutrino oscillations were confirmed experimentally when the Super-Kamikande experiment observed variations in flavour of atmospheric neutrinos [50]. This was conclusively confirmed for solar neutrinos by SNO in 2002 [51]. Both found that at a given time after production a neutrino with initial flavour α has some calculable probability of being flavour β. This can only occur if, contrary to the predictions of the Standard Model, the neutrinos possess mass. Section 1.4 presents a detailed discussion on the implication of neutrino mass and the experimental effort now underway to provide a complete model of the universe incorporating massive neutrinos.

1.3 Multi-TeV Muon Colliders

In order to address many of the issues outlined in Sections 1.1.4 and 1.2 it is necessary to produce very high energy particle collisions. This section explores the various proposed future particle colliders which could provide the required energies.

1.3.1 The Large Hadron Collider and HL-LHC

The Large Hadron Collider (LHC) [52] program is expected to extend until 2022. CMS is anticipated to collect $300fb^{-1}$, with similar performance predicted at ATLAS [53]. LHC Run-II is presently underway with a 13 TeV centre-of-mass energy facilitating searches for new gauge bosons and fundamental scalar particles. The future findings of the LHC program may help probe some of the phenomena discussed; nevertheless, it is probable that not all the issues outlined in Section 1.2 will be fully elucidated in its lifetime. It will be necessary to construct higher energy multi-TeV machines in order to gain a complete understanding of the universe.

An ambitious High-Luminosity upgrade program to the LHC (HL-LHC) has been proposed [54]. The HL-LHC is aiming for an order-of-magnitude increase in luminosity on the LHC through the use of Nb_3Sn superconducting magnets, superconducting compact "crab" cavities and luminosity levelling as key ingredients.

1.3.2 Electron-Positron Linear Colliders

There are two chief international efforts to build high energy e^+e^- linear colliders: the International Linear Collider (ILC) [55], which would operate at centre-of-mass energy of 500 GeV with the possibility of this increasing to 1TeV, and the Compact Linear Collider (CLIC) [56] with centre-of-mass energy 3TeV. Despite having lower energies than the LHC, $e^+ - e^-$ collisions are much simpler to analyse than those involving hadrons. A linear collider could help make precise measurements of the various Higgs properties outlined in Section 1.1.4.

1.3.3 Muon Colliders

A Muon Collider would be the perfect candidate for a multi-TeV collider or Higgs factory due to the muons relatively large mass. The Higgs Mechanism couples to the square of a leptons's mass, so coupling in $\mu^+\mu^-$ collisions would be $\approx 4 \times 10^4$ stronger than the coupling in e^-e^+ collisions. This means that, unlike in the case of the electron collider, the direct s-channel Higgs production, displayed in Figure 1.3, has a significant cross-section ($\mu^+\mu^- \rightarrow h(126GeV) \approx 40pb$) presented in Figure 1.4. At a luminosity of $L = 10^{31}cm^{-2}/s$ a muon facility with $E_{beam} \approx m_h/2GeV$ could provide $\approx 4000h/10^7s$ operational "year" [57].

Furthermore, the spin precession of the muons will permit energy measurements at extremely high accuracy ($dE/E \geq 10^{-6}$ [57]). $\mu^+\mu^-$ colliders, consequently, would have improved energy resolution compared to similar electron machines [58]. Muon colliders would enable precise measurements of narrow resonances, high precision measurements of the Higgs mass ($\delta M = 0.1MeV$) and direct measurements of it's width ($\delta\Gamma = 0.24MeV$ for an integrated luminosity of $100pb^{-1}$). More exact determination of branching fractions of various production and decay channels may additionally be conceivable [59].

In addition to direct s-channel Higgs production, a multi-TeV muon collider would allow:

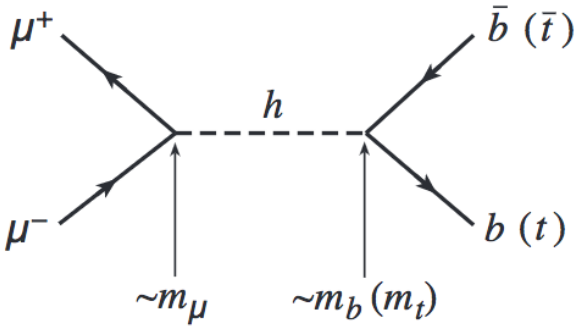

Figure 1.3: Feynman diagram for the direct production of a Standard Model Higgs boson via the combination of a muon-anti-muon pair. The larger coupling of the muon to the Higgs boson means that this s-channel has an enhanced cross-section in comparison to the similar production channel for electrons [58]. Here there is a subsequent $h \to b\bar{b}$ decay.

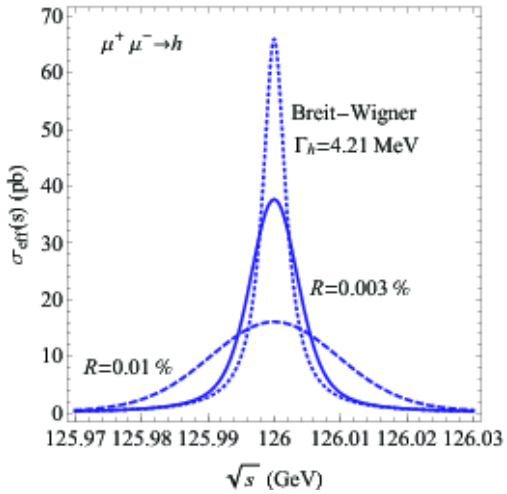

Figure 1.4: Effective cross section for $\mu^+\mu^- \to h$ versus the collider energy for the Standard Model Higgs boson production ($m_h = 126GeV$). A Breit-Wigner line shape with $\Gamma = 4.21MeV$ is shown (dotted curve). The solid and dashed curves compare beam energy resolutions,R, for two proposed beams [60].

1. Studies of the Higgstrahlung production channel, shown in Figure 1.5.

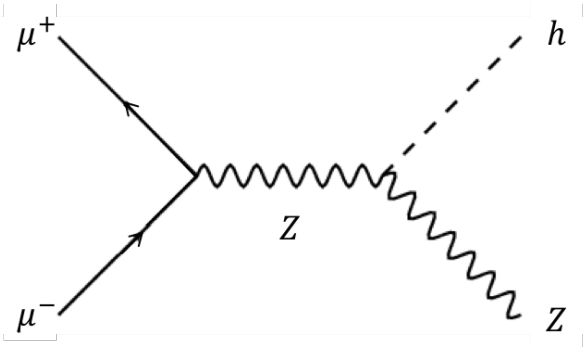

Figure 1.5: Feynman diagram for the Higgstrahlung process: $\mu^+\mu^- \to Zh$, mediated by a Z, as displayed here.

2. Examination of the triple-Higgs self-coupling terms via the WW fusion channel. A Feynman diagram is exhibited in Figure 1.6. These couplings are predicted in the Standard Model in terms of the known Higgs mass; probing these couplings allows tests for beyond Standard Model physics. It is expected that

the LHC could achieve measurement of these trilinear couplings with an uncertainty of $\approx +30\%$ and $\approx -20\%$, a muon collider could reduce this as low as $\pm 11\%$ [61]. Double Higgs production at a muon collider can proceed via the s-channel but the cross section for this non-resonant process is very small, of order 1.5 ab, providing less than one signal event in $500 fb^{-1}$before branching ratios and selection efficiencies are folded in [62]. The LHC is sensitive to the Higgs coupling through Higgs pair production via gluon fusion but its ability to measure the coupling is impeded by large backgrounds [63].

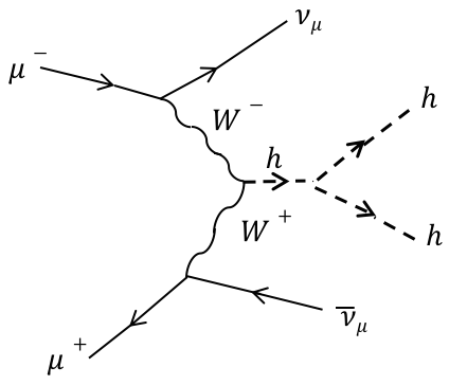

Figure 1.6: Feynman diagram for the production of a Higgs via $\mu^+\mu^- \to \nu_\mu\bar{\nu}_\mu W^+W^- \to \nu_\mu\bar{\nu}_\mu hh$. Analysis of this decay allows measurement of Higgs boson third order self coupling, $\lambda_{hhh} = \lambda$.

3. Analysis of the channel: $\mu^+\mu^- \to t\bar{t}h$ would provide direct access to the top-quark-Higgs Yukawa coupling. This would, however, necessitate at least 5 ab^{-1} of integrated luminosity.

4. Study of the b-quark-Higgs Yukawa coupling and the search for invisible decay modes of the Higgs boson. Although searches for $h \to b\bar{b}$ are being conducted at the LHC, the absence of QCD background noise in the muon collider means the properties of this decay can be more accurately determined at a muon facility.

5. Access to $h \to c\bar{c}$ which could be reachable at a level of $\approx 8\sigma$ [64].

6. Production of $\approx 10^9$ Z-bosons at an upgraded luminosity of $\approx 10^{33} cm^{-2}s^{-1}$. This would permit a "Giga-Z program" at the facility.

7. Continuation of searches for supersymmetric particles and extra dimensions.

Circular muon colliders would be at the fore-front of the energy frontier producing highly tuned, high centre of mass energy lepton colliders which would not suffer from radiative losses, unlike similar e^+e^- circular colliders. Also, unlike hadron colliders, such as the HL-LHC, the interactions in muon colliders would not be convoluted by parton distribution functions meaning reduced QCD backgrounds. The s-channel production process permits determination of the mass, total width, and the cross-sections of many Higgs decay final states to very high precision. The Higgs mass, total width and the cross-sections can additionally be exploited to constrain the parameters of the Higgs and supersymmetrtic sector.

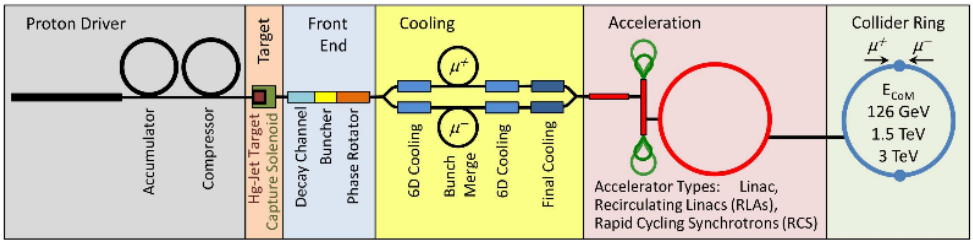

Figure 1.7: Schematic diagram of a typical design for a multi-TeV muon collider [59]: Protons are accelerated toward a liquid mercury target producing pions. These pions are confined using a solenoidal field before entering a decay channel where muons are produced. The resulting muons are bunched prior to being cooled and accelerated via both a linac and fixed-field alternating gradient (FFAG) accelerators. The muons then traverse the downstream collider ring. The "front end" is similar to that for the Neutrino Factory (Figure 1.12); however, the cooling is now more problematical as 6-D cooling, instead of 4-D, is required prior to the muons entering the downstream accelerator systems. This means reducing the phase-space volume of the muon beam in both the longitudinal and transverse directions, as opposed to the transverse-only, 4D, cooling. The emittance, a measure of the spread of the beam, would have to be reduced by a factor of 10^6 [65] in 6D to produce a feasible muon collider. This is the main technical challenge in the construction of such a machine.

Figure 1.7 displays the functional elements of a proposed Muon Collider. A multi-Gev bunched proton beam is delivered to a liquid mercury target yielding pions. A solenoidal field surrounds the target, confining the charged pions and guiding them into a decay channel where they decay to produce the necessary muons (or anti-muons) and anti-neutrinos (or neutrinos) via:

$$\pi^-(\pi^+) \rightarrow \mu^-(\mu^+) + \bar{\nu}_\mu(\nu_\mu). \tag{1.18}$$

The subsequent muons are captured longitudinally by RF cavities prior to entering a "cooling channel." A muon beam deriving from pion decays will exhibit a large momentum spread which it is imperative to reduce by a factor of 10^6 [65] in order to accomplish the necessitated luminosity at the downstream collider. "Cooling" in this sense simply means diminishing the momentum spread of the beam. A muon collider demands the muon beam be cooled in both the transverse and longitudinal phase-space directions. To realise the desired luminosity a beam measuring ≈ 0.025 mm in the transverse plane and ≈ 70 mm in the longitudinal direction is required [66]. This corresponds to a reduction of 10^4 in the transverse phase space and 10^2 in the longitudinal phase space. This must be performed promptly ($\approx$ msec) to avoid muon decay. Section 2.4 will examine the various traditional beam cooling techniques and their unsuitability for use with a muon beam. **Ionisation cooling is the only viable means of attaining the required muon cooling but is yet to be physically observed.**

Once "cooled," the muon beam would be accelerated and injected into a collider ring; the inclusion of the various accelerator sub-systems would depend on the desired final muon beam energy. In the case of a Higgs Factory a compact collider ring with a circumference of ≈ 300 m (assuming a centre of mass energy $\approx 125GeV$) would be used whereas for a multi-TeV scale muon collider the circumference would be of order of several kilometres.

1.3.4 Choosing Between a Muon Collider and e^+e^- Linear Collider

In addition to the physics benefits outlined in Section 1.3.3, the muon collider also has the advantage of being relatively low cost and smaller in size [67] in comparison to competitor machines such as the HL-LHC or the $e^+ - e^-$ linear colliders. The muon ionisation cooling section remains the principle technical risk in the construction and operation of a muon collider. **The Muon Ionisation Cooling Experiment (MICE) [68] aims to make the first measurements of sustainable ionisation cooling of a muon beam. It is, therefore, the first stage in making a muon collider of the design portrayed in Figure 1.7 a reality and forms the focus of this thesis.**

1.4 The Impact of Neutrino Mass

The observation of neutrino oscillations and the subsequent conclusion that neutrinos possess mass is the only experimentally verified result that is incompatible with the Standard Model. This section aims to give a theoretical overview of neutrino oscillations followed by an exploration of the implications of neutrino mass and experimental efforts underway to assimilate it.

1.4.1 Phenomenology of Neutrino Oscillations

Neutrino oscillations is the phenomenon whereby neutrinos created with a specific lepton flavour $\alpha = \{e, \mu, \tau\}$ are measured at a later point in time, t, to have a different flavour $\beta = \{e, \mu, \tau\}$. A detailed derivation of the phenomenology governing neutrino oscillations is given in [69]. The following discussion is based on this review.

Neutrino oscillations arise due to the fact that the three neutrino flavour eigenstates ν_l, where $l = \{e, \mu, \tau\}$, are not identical to the mass eigenstates ν_i, where $i = \{1, 2, 3\}$. The two states can be considered to be a coherent superposition of one another. Within the Standard Model (SM) neutrinos are described by a chiral left-handed (L) flavour field denoted as $\nu_{lL}(x)$, where $l = \{e, \mu, \tau\}$. In the formalism of local quantum field theory these left-handed flavour neutrino fields for the lepton current in the charged current (CC) weak interaction Lagrangian are linear combinations of the fields of three (or possibly more) neutrinos $\nu_{iL}(x)$ with non-zero masses for at least one i:

$$\nu_{lL}(x) = \sum_i U_{li}\nu_{iL}(x); \tag{1.19}$$

where $\nu_{iL}(x)$, is the LH component of the field of ν_i, possessing a mass m_i. $U_{li}$is the Pontecorvo-Maki-Nakagawa-Skata (PMNS)[3] [48] [70] matrix. In the case where n neutrino flavours and n massive neutrinos exist, U is an $n \times n$ matrix with $\frac{n(n-1)}{2}$ Euler angles and $\frac{n(n+1)}{2}$ phases. All existing data on neutrino oscillations can be explained assuming 3 neutrino flavours ($n = 3$) mixing in vacuum. This is the minimal

[3]in natural units such that $\hbar = c = 1$

neutrino mixing scheme and can account for the currently available data on the oscillations of the solar (ν_e), atmospheric (ν_μ and $\bar{\nu}_\mu$), reactor ($\bar{\nu}_e$) and accelerator (ν_μ and $\bar{\nu}_\mu$) neutrinos. Thus,

$$\nu_{lL}(x) = \sum_{i=1}^{3} U_{li}\nu_{iL}(x). \tag{1.20}$$

In the case of 3 neutrino flavours and 3 massive neutrinos U is an 3×3 unitary neutrino mixing matrix parametrised by 3 Euler angles, and, depending on whether the massive neutrinos, ν_i, are Dirac or Majorana particles (the effort to determine their nature is discussed in Section 1.4.5), by 1 or 3 CP violation phases [71] [72]. In this case the PMNS matrix is defined as

$$U = \begin{pmatrix} U_{e1} & U_{e2} & U_{e3} \\ U_{\mu 1} & U_{\mu 2} & U_{\mu 3} \\ U_{\tau 1} & U_{\tau 2} & U_{\tau 3} \end{pmatrix}. \tag{1.21}$$

This may be expanded, such that

$$U = \begin{pmatrix} 1 & 0 & 0 \\ 0 & c_{23} & s_{23} \\ 0 & -s_{23} & c_2 3 \end{pmatrix} \begin{pmatrix} c_{13} & 0 & s_{13}e^{-i\delta} \\ 0 & 1 & 0 \\ -s_{13}e^{-\delta} & 0 & c_{!3} \end{pmatrix} \begin{pmatrix} c_{12} & s_{12} & 0 \\ -s_{12} & c_{12} & 0 \\ 0 & 0 & 1 \end{pmatrix} \begin{pmatrix} 1 & 0 & 0 \\ 0 & e^{i\alpha_{21}/2} & 0 \\ 0 & 0 & e^{i\alpha_{31}/2} \end{pmatrix}, \tag{1.22}$$

where $s_{ij} = sin(\theta_{ij})$, $c_{ij} = cos(\theta_{ij})$ with $\theta_{ij} = [0, \pi/2]$, $\delta = [0, 2\pi]$ is the Dirac CP violation phase. α_{21} and α_{31} are two Majorana CP violation phases.

Splitting the U matrix into these 4 sub-matrices in Equation 1.22 makes further discussions of experimental data easier. The first of these matrices corresponds to parameters reached via "atmospheric" and "accelerator" data, the second to parameters measured via "reactor " and "accelerator" based experiments and the third to parameters obtained via "reactor" and "solar" neutrino data. The 4th and final matrix contains the α phase terms which are physically meaningful only if neutrinos are Majorana particles. If Neutrinoless Double Beta Decay ($0\nu\beta\beta$) occurs, these factors influence its rate -this will be discussed in Section 1.4.5.

From the matrix in Equation 1.22 it is apparent that the fundamental parameters characterising the 3-neutrino mixing are:

1. The 3 angles, θ_{12}, θ_{23} and θ_{13};
2. Depending on the nature of massive neutrinos, either 1 Dirac (δ) or 1 Dirac + 2 Majorana (δ, α_{21} and α_{31}) CP violation phases; and,
3. The masses of the 3 neutrinos denoted by m_1, m_2 and m_3.

If a neutrino ν_α is emitted from a neutrino source and observed, via a CC weak interaction process, by a

detector, located a distance L from the source and at time T the amplitude A of the probability that neutrino ν_β will be observed can be written as

$$A(\nu_\alpha \to \nu_\beta) = \sum_i U_{\beta i} D_i U^\dagger_{i\alpha}. \tag{1.23}$$

The neutrino here is assumed to be travelling through a vacuum. $D_i = D_i(p_i; L, T)$ describes the propagation of ν_i between the source and the detector, while $U^\dagger_{i\alpha}$ and $U_{\beta i}$ are the amplitudes to find ν_i in the initial and in the final flavour neutrino state respectively. It follows, from quantum mechanics considerations [73], that

$$D_i = D_i(\bar{p}_i; L, T) = e^{-i\bar{p}_i(x_f - x_0)} = e^{-i(E_i T - p_i L)} \quad \text{with} \quad p_i = |\vec{p}_i|, \tag{1.24}$$

where x_0 and x_f are the space-time co-ordinates of the points of neutrino emission and detection, $T = (t_f - t_0)$ and L is the z component of $\vec{x}_f - \vec{x}_0$. The interference factor $D_i D^*_j$ depends on the phase

$$\delta\psi_{ij} \cong \frac{m_i^2 - m_j^2}{2p} L = 2\pi \frac{L}{L^\nu_{ij}} \cdot sgn(m_i^2 - m_j^2), \tag{1.25}$$

assuming $p = (p_j + p_k)/2$, and,

$$L^\nu_{ij} = 4\pi \frac{p}{|\Delta m^2_{ij}|} \cong 2.48m \frac{p[MeV]}{\Delta m^2_{ij}[eV^2]} \tag{1.26}$$

is the neutrino oscillation length associated with Δm^2_{ij}. p is considered to be the zero neutrino mass momentum, $p = E$. The phase difference in Equation 1.26 is Lorentz-invariant.

Combining Equations 1.23, 1.24 and 1.25 gives the oscillation probabilities for $\nu_\alpha \to \nu_\beta$ and $\bar{\nu}_\alpha \to \bar{\nu}_\beta$:

$$P(\nu_\alpha \to \nu_\beta) = \sum_j |U_{\beta i}|^2 |U_{\alpha i}|^2 + 2 \sum_{i>j} |U_{\beta i} U^*_{\alpha i} U_{\alpha j} U^*_{\beta j}| \cdot cos\Big(\frac{\Delta m^2_{ij}}{2p} L - \psi_{\alpha\beta;ij}\Big), \tag{1.27}$$

and

$$P(\bar{\nu}_\alpha \to \bar{\nu}_\beta) = \sum_j |U_{\beta i}|^2 |U_{\alpha i}|^2 + 2 \sum_{i>j} |U_{\beta i} U^*_{\alpha i} U_{\alpha j} U^*_{\beta j}| \cdot cos\Big(\frac{\Delta m^2_{ij}}{2p} L + \psi_{\alpha\beta;ij}\Big), \tag{1.28}$$

respectively, where $\alpha, \beta = e, \mu, \tau$ and $\psi_{\alpha\beta;ij} = arg(U_{\beta i} U^*_{\alpha i} U_{\alpha j} U^*_{\beta j})$. From Equation 1.25 it becomes evident that there must be at least two non-degenerate neutrino masses and lepton mixing, $U \neq 1$, in order for neutrino oscillations to occur. This oscillation effect will be large when

$$\frac{|\Delta m_{ij}|^2}{2p} L = 2\pi \frac{L}{L_{ij}} > 1, \quad i \neq j. \tag{1.29}$$

The physical interpretation of this condition is that the neutrino oscillation length should be of the order of, or smaller than, the source-detector distance L. If this were not the case the oscillations would not have

time to develop before the neutrinos reach the detector.

A CP asymmetry, A_{CP}, can be measured as the difference between Equations 1.27 and 1.28 such that

$$A_{CP}^{\alpha\beta} = P(\nu_\alpha \to \nu_\beta) - P(\bar{\nu}_\alpha \to \bar{\nu}_\beta) = 4\sum_{i>j} Im\big[U_{\beta i}U_{\alpha i}^{*}U_{\alpha j}U_{\beta j}^{*}\big] sin\Big(\frac{\Delta m_{ij}^2 L}{2p}\Big). \tag{1.30}$$

In the case of 3-neutrino mixing all different $Im(U_{\beta i}U_{\alpha i}^{*}U_{\alpha j}U_{\beta j}^{*}) \neq 0$, $\alpha \neq \beta = e, \mu, \tau$ and $i \neq j = 1, 2, 3$ coincide up to a sign as a consequence of the unitarity of U. Consequently, [69]

$$A_{CP}^{e\mu} = -A_{CP}^{\tau e} = A_{CP}^{\tau\mu} = 4Im\big[U_{\mu 3}U_{e3}^{*}U_{e2}U_{\mu 2}^{*}\big]\Big(sin\frac{\Delta m_{32}^2}{2p}L + sin\frac{\Delta m_{21}^2}{2p}L + sin\frac{\Delta m_{13}^2}{2p}L\Big). \tag{1.31}$$

The $Im(U_{\mu 3}U_{e3}^{*}U_{e2}U_{\mu 2}^{*})$ term controls the magnitude of CP violation effects in neutrino oscillations in the 3 neutrino mixing scenario. If $sin(\Delta m_{ij}^2/2p)L \approx 0$ for $(ij) = (32)$ or (21) or (13) then $A_{CP}^{\alpha\beta} = 0$ unless three $\Delta m_{ij}^2 \neq 0$ for $(ij) = (32), (21), (13)$. The requirement that $Im(U_{\mu 3}U_{e3}^{*}U_{e2}U_{\mu 2}^{*}) = 0$ is a necessary, and sufficient, condition for having Dirac-type leptonic CP violation, independent of whether neutrinos are Majorana or Dirac particles. However, in the case of Majorana neutrinos there is the additional possibility of Majorana-type CP violation.

1.4.2 Matter Effects on Neutrino Oscillations

The theoretical argument posed in Section 1.4.1 assumes that neutrinos are travelling in a vacuum. When neutrinos traverse matter the pattern of neutrino oscillations is altered. This is known as the Mikheyev, Smirnov, Wolfenstein (MSW) effect [74] [75]. The presence of matter leads to an enhancement of the oscillation probabilities $P(\nu_e \to \nu_\mu)$ and $P(\bar{\nu}_e \to \bar{\nu}_\mu)$. This effect is utilised by many experimental searches to determine the sign of Δm_{31}^2 and Δm_{32}^2 [76].

1.4.3 The Neutrino Mass Hierarchy

It was demonstrated in Section 1.4.1 that the probability of two flavours mixing is proportional to the squared mass difference of the two eigenstates. For three neutrino mass states, three mass differences, Δm_{21}^2, $|\Delta m_{32}^2|$ and $|\Delta m_{31}^2|$, can be expressed. Δm_{21}^2 and $|\Delta m_{32}^2|$ have been measured via observation of solar and atmospheric neutrino oscillations respectively (Table 1.1).

Neutrino oscillation experiments can only probe the squared difference of the masses, consequently, the absolute values of m_1, m_2 and m_3 remain undetermined, as does the sign of Δm_{32}^2. This is acknowledged as the "neutrino mass hierarchy problem." If m_3 is heavier than m_2, the hierarchy is said to be "normal," otherwise it is "inverted," as depicted in Figure 1.8.

Ascertaining the mass ordering of the neutrinos is an imperative step in constructing a unified theory of the universe in addition to having an influence on the quest to determine whether neutrinos are Dirac or Majorana particles. Once an understanding of the ordering of the neutrino mass states is gained, the

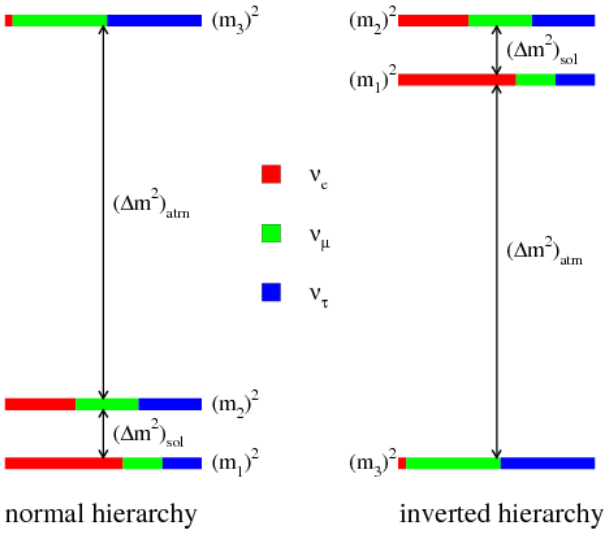

Figure 1.8: Summary of the two conceivable mass orderings of the three neutrinos [77]. The "normal" mass hierarchy designates a situation analogous to what is observed amongst other Standard Model leptons i.e. where m_3 is heaviest. Also depicted is the "inverted" scenario showing the possibility that the neutrino mass ordering is reversed from the "normal" situation.

uncertainty on a measurement of the CP-violating phase, δ, is significantly reduced. In addition, knowledge of the mass hierarchy would delineate the scope for future Neutrinoless Double Beta Decay experiments, seeking to resolve the mass nature of the neutrino, by limiting the domain for observation of a signal. The ultimate goal of all neutrino experiments is to formulate a model that explains the observed neutrino masses and mixing patterns, and relates this to the well-known charged lepton masses - explaining the mass hierarchy is, therefore, essential.

Most of the knowledge regarding Δm^2_{13} originates from atmospheric neutrino experiments which generally measure the probability

$$P_{\mu\mu} = 1 - sin^2 2\theta_{23} sin^2\Big(\frac{\Delta m^2_{13} L}{4E}\Big) + \text{“}sub - leading,\text{”} \tag{1.32}$$

in which the leading term is not sensitive to the sign of Δm^2_{13}.

One way of determining the nature of the neutrino mass hierarchy is by measuring neutrino oscillations for neutrinos travelling through matter. The MSW effect (Section 1.4.2) changes $\nu_\mu \rightarrow \nu_e$ probability of oscillation from

$$P_{\mu e} = sin^2\theta_{23} sin^2\theta_{13} sin^2\Big[\frac{\Delta m^2_{13} L}{4E}\Big] + \text{“}sub - leading\text{”} \tag{1.33}$$

to

$$P_{\mu e} \approx sin^2\theta_{23} sin^2\theta^{eff}_{13} sin^2\Big(\frac{\Delta^{eff}_{13} L}{4E}\Big), \tag{1.34}$$

where

$$sin^2\theta_{13}^{eff} = \frac{\Delta_{13}^2 sin^2 2\theta_{13}}{\left(\Delta_{13}^{eff}\right)^2}, \quad \Delta_{13}^{eff} = \sqrt{(\Delta_{13} cos 2\theta_{13} - A)^2 + \Delta_{13}^2 sin^2 2\theta_{13}}, \quad \Delta_{13} = \frac{\Delta m_{13}^2}{2E}, \quad A = \pm\sqrt{2} G_F N_e. \tag{1.35}$$

A is the matter potential which is + for neutrinos and − for anti-neutrinos , N_e is the electron density in matter and G_F is the Fermi coupling constant [69]. With high enough statistics the mass hierarchy can be established from comparisons of the rate of $\nu_\mu \rightarrow \nu_e$ with $\bar{\nu}_\mu \rightarrow \bar{\nu}_e$ oscillations at a long baseline neutrino facility. If the neutrino masses are ordered normally then $\nu_\mu \rightarrow \nu_e$ will be enhanced and if inverted the opposite is true. Hyper-K [78] (Section 1.4.8) and the Neutrino Factory (Section 1.5) could help determine the mass hierarchy in this way.

1.4.4 CP Violation and Measuring δ

CP Violation in the lepton sector may assist in explaining how leptogenesis could lead to the baryonic asymmetry in the universe. Consequently, it is crucial that the CP violating phase, denoted as δ, is accurately determined. Measuring this phase will, however, require new neutrino machines or extensive upgrades to current ones and improved understanding of the relevant systematic uncertainties.

In 2016 the $NO\nu A$ experiment published two results from their search for $\nu_\mu \rightarrow \nu_e$ transitions [79] [80] reporting an excess with 3.3σ significance. This disfavours $0.1\pi < \delta < 0.5\pi$ in the inverted mass hierarchy scenario and $0.25\pi < \delta < 0.95\pi$ in the normal mass hierarchy scenario both at the 90% confidence level [80]. In 2017 the T2K experiment published results [81] exhibiting a discrepancy in the appearance of ν_e and $\bar{\nu_e}$. For the normal hierarchy the CP conservation hypothesis ($\delta = 0, \pi$) is excluded at 90% confidence level. The experiment continues to analyse data and there is support to extend the experiments running into a second run, T2K-II.

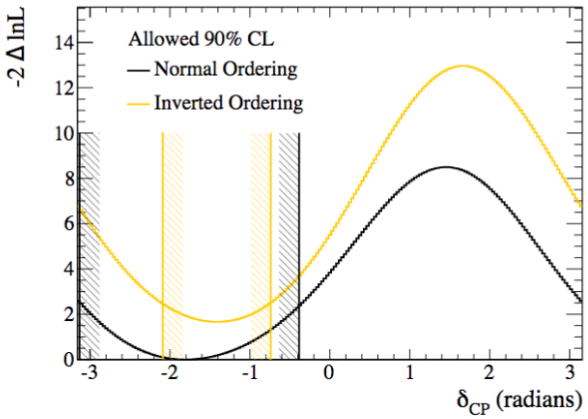

Figure 1.9: The T2K $2\Delta lnL$ as a function of δ, the CP phase, for the normal (black) and inverted (red) mass ordering. The vertical lines show the corresponding allowed 90% confidence intervals, calculated using the Feldman-Cousins method. $sin^2\theta_{13}$ is marginalised using the reactor measurement as prior probability [81].

1.4.5 Nature of Neutrinos - Dirac or Majorana?

All other known Standard Model fermions are Dirac particles [82], meaning they have distinct anti-particles as opposed to Majorana particles which are their own anti-particle [83] [84]. It is still not known whether neutrinos are Dirac or Majorana particles.

The neutrinos with definite mass ν_i will be Dirac fermions if the particle interactions conserve some additive lepton number, e.g. the total lepton charge $L = L_e + L_\mu + L_\tau$. If no lepton charge is conserved ν_i will be Majorana fermions. It follows that one way to establish the nature of neutrinos is to investigate Neutrinoless Double Beta Decay ($0\nu\beta\beta$); the process in which two electrons are released from the weak decay of a nucleus without neutrinos. If this process were observed it would violate lepton number conservation, confirming neutrinos to be Majorana in nature. The measurement of the corresponding half-life with sufficient accuracy, would not only be verification that the total lepton charge is not conserved, but would provide information on the type of neutrino mass spectrum [85], Majorana phases in U [86] and the absolute scale of neutrino masses [87]. There are several experiments currently searching for $0\nu\beta\beta$ via different detection methods: COBRA [88], CUORE(CUORE-0 [89] , DCBA [90], EXO [91], GERDA [92], KamLAND-Zen [93], Majorana [94] and XMASS [95]. There are many other experiments such as SuperNEMO which are currently under construction to continue the search [96]. As of 2016, GERDA has obtained a half-life limit of 2.1×10^{25} [97] years with 21.6 kg.yr exposure with searches with 136Xe. Kamland-Zen and EXO-200, yielded a limit of 2.6×10^{25} yr [98].

1.4.6 Neutrino Helicity - The Existence of Sterile Neutrinos?

"Sterile" neutrinos are a hypothetical type of neutrino which interact only via gravity and can be broadly defined as a neutral lepton with no ordinary weak interactions except those induced by mixing. One possible candidate for such particles are right-handed neutrinos, however, not the only possibility. Right-handed neutrinos would be weak isospin singlets with no weak interactions except through mixing with the left-handed neutrinos. A theoretical overview of the implication of additional neutrino states can be found in [99]. All experimentally observed active neutrinos have so far had left-handed helicity.

A few anomalies in the very short baseline oscillation measurements and cosmological data analyses have emerged which may allude to additional, sterile, neutrino states. The first hint came from the GALLEX and SAGE experiments which measured the rate of neutrinos coming from the sun in the 1980s and 1990s. A recent reanalysis has exposed an unexplained 14±5% deficit in the recorded ν_e this is referred to as the "Gallium anomaly" [100]. In addition, numerous analyses of the flux of $\bar{\nu}_e$ from reactors have suggested a deficit of $\bar{\nu}_e$ at the 98.6% C.L [101]. This is denoted as the "reactor antineutrino anomaly." When combined both anomalies disfavour the no-oscillation hypothesis at 99.97% (3.6 σ). A third - "accelerator"- anomaly stems from measurements at the LSND [102] accelerator experiment which evaluated the oscillation $\nu_e \rightarrow \nu_\mu$ at a baseline of L= 30m. LSND measured an excess of neutrinos which would be consistent with the existence of a sterile neutrino with $\Delta m^2_{41} \approx 1eV^2$. Further support for this excess was presented by the

MiniBooNE [103] experiment based at Fermilab at the 2.8 σ level [104]. Confirmation of the existence of sterile neutrinos may require the construction of high intensity neutrino sources such as NUSTORM [105] or a Neutrino Factory (see Section 1.5).

1.4.7 Current Experimental Limits

Table 1.1 summarises the latest experimental results [9]. Here θ_{12} was measured by solar neutrino experiments combined with KamLAND results [106], θ_{23} was obtained from atmospheric neutrinos [107] and θ_{13} was recently measured by both T2K [108] and Daya Bay Collaborations [109]. The δ CP violation phase quoted in the table is a combination of limits set in [110] , [111], [112] with the consideration of more recent results from Noνa [79], [80] and T2K [81]. It must be noted that these PMNS measured values are therefore quite different from those of the CKM matrix, which is unity on diagonal and small elsewhere.

Parameter	Best Fit	3σ
$\Delta m^2_{21}[10^{-5}eV^2]$	7.37	6.93 - 7.97
$\lvert\Delta m^2\rvert[10^{-3}eV^2]$	2.50 (2.46)	2.37-2.63 (2.33 - 2.60)
$sin^2\theta_{12}$	0.297	0.250 - 0.354
$sin^2\theta_{23}$, $\Delta m^2 > 0$	0.437	0.379 - 0.616
$sin^2\theta_{23}$, $\Delta m^2 < 0$	0.569	0.383 - 0.637
$sin^2\theta_{13}$, $\Delta m^2 > 0$	0.0214	0.0185-0.0256
$sin^2\theta_{13}$, $\Delta m^2 < 0$	0.0218	0.0186 - 0.0248
δ/π	1.35(1.32)	(0.92-1.99) ((0.83-1.99))

Table 1.1: Table showing the latest Measurements of Neutrino Parameters, taken from [9]. The Dirac phase δ has the 2σ limits here as no value is disfavoured at 3σ currently. The values (values in brackets) correspond to $m_1 < m_2 < m_3 (m_3 < m_1 < m_2)$). The definition of Δm^2 used is $= m_2^2 - (m_2^2 + m_1^2)/2$. Therefore, $\Delta m^2 = \Delta^2_{31} - \Delta^2_{21}/2 > 0$, if $m_1 < m_2 < m_3$, and $\Delta m^2 = \Delta m^2_{32} + \Delta^2_{21}/2 < 0$ for $m_3 < m_1 < m_2$.

It follows from all previous neutrino oscillation experiments that in the case of 3-neutrino mixing, one of the two independent neutrino mass squared differences, $\Delta m^2_{21} > 0$ is much smaller than the absolute value of the second one, $|\Delta m^2_{31}|$, $\Delta m^2_{21} \ll |\Delta m^2_{31}|$. From Table1.1: $\Delta m^2_{21}/|\Delta m^2_{32}| \approx 0.03$. In this case, by keeping only the oscillating terms involving Δm^2_{n1}, from Equations 1.27 and 1.28:

$$P(\nu_{\alpha(\beta)} \to \nu_{\beta(\alpha)}) \approx (\bar{\nu}_{\alpha(\beta)} \to \bar{\nu}_{\beta(\alpha)}) \approx \delta_{\alpha\beta} - 2|U_{\alpha n}|^2[\delta_{\alpha\beta} - |U_{\beta n}|^2](1 - cos\frac{\Delta m^2_{n1}}{2p}L). \tag{1.36}$$

Setting $\alpha = \beta = e$ and $n = 3$ gives

$$P(\nu_e \to \nu_e) = P(\bar{\nu}_e \to \bar{\nu}_e) \approx 1 - 2|U_{e3}|^2(1 - |U_{e3}|^2)(1 - cos\frac{\Delta m^2_{31}}{2p}L). \tag{1.37}$$

Similarly, setting $\alpha = e(\mu)$, $\beta = \mu(e)$ and $n = 3$ gives

$$P(\nu_{\mu(e)} \to \nu_{e(\mu)}) \approx 2|U_{\mu 3}|^2|U_{e3}|^2\Big(1 - cos\frac{\Delta m^2_{31}}{2p}L\Big); \tag{1.38}$$

where

$$sin^2\theta_{13} = |U_{e3}|^2, \quad sin^2\theta_{23}cos^2\theta_{13} = |U_{\mu 3}| \quad \text{and} \quad cos^2\theta_{23} = \frac{|U_{\tau 3}|^2}{1 - |U_{e3}|^2}. \tag{1.39}$$

θ_{13} and θ_{23} are the angles of the standard parametrisation of the neutrino mixing matrix. Equation 1.37 describes with a relatively high precision the oscillations of reactor $\bar{\nu}_e$ with $L \approx 1$ km and $n = 3$. It was used in the analysis of the data of the Chooz [113], Double Chooz [114], Daya Bay [109] and RENO [115] experiments. Equation 1.36 with $n = 3$ and $\alpha = \beta = \mu$ describes, with good precision, the effect of "disappearance" due to oscillations of the accelerator ν_μ seen in MINOS [116] and T2K.

1.4.8 Future Experiments

Two major projects aiming to enhance the physics reach in the neutrino sector are currently under construction: Hyper-K [78] and DUNE [117]. These involve upgrading the existing accelerator sources at JPARC and Fermilab respectively and developing novel and more sensitive detectors at these sites.

The proposed "Hyper-K" will succeed the current Super-Kamiokande 50 kt water Cherenkov detector with two 260 kton water Cherenkov detectors. The design and operation of such a system is well understood through many years of operating Super-Kamiokande, however, the increased fiducial volume of the detector will give significantly greater sensitivity to δ and therefore help search for CP violation in the lepton sector. Figure 1.10 shows the expected physics reach of Hyper-K in terms of mass hierarchy as a function of $sin\theta_{23}$ over the first 10 years of its operation for both conceivable mass orderings.

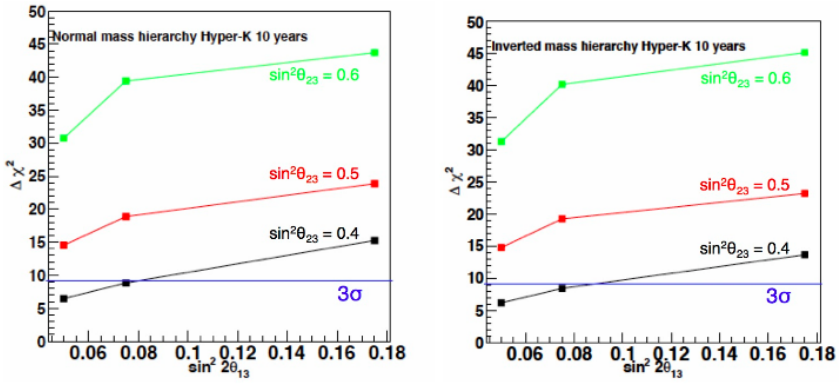

Figure 1.10: Significance of discriminating the mass hierarchy when the true hierarchy is (Left) normal and (Right) inverted, as a function of $sin^2\theta_{13}$ and $sin^2\theta_{23}$, after 10 years of operation of HyperK [78].

Construction of The Deep Underground Neutrino Experiment (DUNE) will involve building a 40 kt liquid argon TPC detector with the neutrino source at Fermilab. This novel detector technology has never been demonstrated at this scale and would provide significant insight into CP violation in the lepton sector. DUNE will have a 1300 km baseline which establishes its key strengths: sensitivity to the matter effect which, as discussed in Section 1.4.2, leads to a large asymmetry in the $\nu_\mu \rightarrow \nu_e$ .v. $\bar{\nu}_\mu \rightarrow \bar{\nu}_e$ oscillation probabilities, the sign of which depends on the mass hierarchy (MH). At 1300 km this asymmetry is approximately $\pm$ 40 % in the region of the peak flux. This is larger than the maximal possible CP-violating asymmetry associated

with δ, meaning that both the mass hierarchy and δ can be determined unambiguously with high confidence within the same experiment. Figure 1.11 shows the significance with which the hierarchy can be determined by DUNE. Further discussions of the physics reach of future neutrino facilities are presented in [118] [119] and [120].

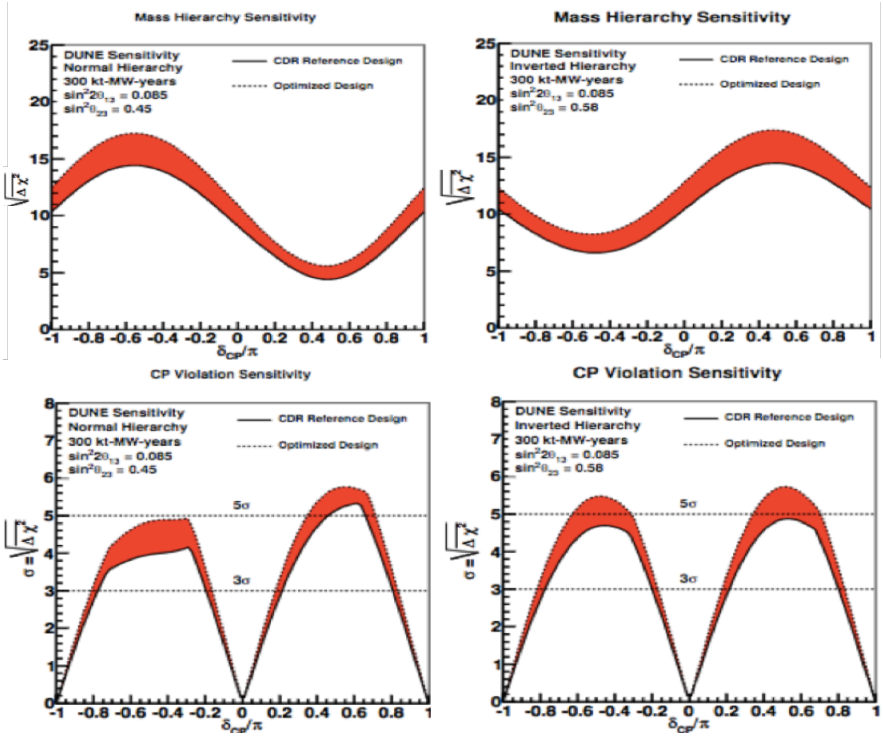

Figure 1.11: The significance with which the mass hierarchy (top) and δ (bottom) can be determined as a function of the value of δ in DUNE for an exposure of 300 kt MW year assuming normal mass hierarchy (MH) (left) or inverted MH (right). The shaded region represents the range in sensitivity due to potential variations in the beam design [117].

DUNE aims to explicitly observe the asymmetry A_{CP} in $\nu_\mu \rightarrow \nu_e$ and $\bar{\nu}_\mu \rightarrow \bar{\nu}_e$ oscillations. This will directly demonstrate the leptonic CP-violation effect. A measurement of δ that is inconsistent with the measurement of A_{CP} could be evidence of of physics beyond the standard three-flavour mode.

1.5 The Neutrino Factory

In order to further probe the neutrino sector it is necessary to make even more precise measurements of neutrino and anti-neutrino oscillation parameters, especially in the channels were the flavours of the final and initial neutrinos differ. The proposed future Neutrino Factory facility would allow the measurement of δ with 5° accuracy and the neutrino mixing angles with a precision to match the quark sector [121]. Figure 1.12 shows the functional elements of the Neutrino Factory.

The Neutrino Factory front end is comparable to that of the muon collider (Figure 1.7). Protons strike a mercury target resulting in pion release. Charged pions decay to produce muons (or anti-muons) and anti-neutrinos (or neutrinos) via Equation 1.18. Given the large momentum spread of the muons which result from pion decay, it is again essential to reduce size of the muon beam allowing it to "fit" into the downstream

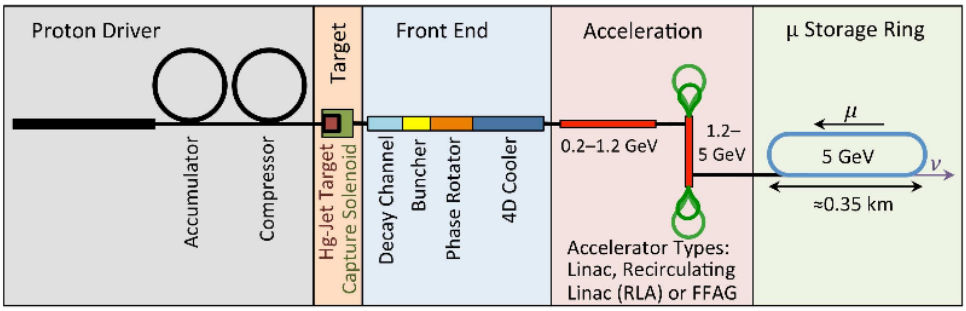

Figure 1.12: Schematic diagram of the typical design for a Neutrino Factory with a 5 GeV muon beam. Pions are produced through placing a liquid mercury target in a proton beam. These pions are confined using a solenoidal field prior to entering into a decay channel where they decay muons and a corresponding neutrino. The resulting muons are guided through the Front-End of the Neutrino Factory before being cooled and accelerated. Eventually the muons will decay, producing the desired neutrino beam of known flavour composition [122].

accelerator systems. In contrast to the muon collider, a Neutrino Factory requires emittance reduction in only the two transverse directions. Once "cooled" the muons are accelerated to 5 GeV and the subsequent muons are accumulated in a racetrack-shaped storage ring. Neutrinos are produced from the muons upon leaving the storage ring. $\mu^-(\mu^+)$ decay via the channel:

$$\mu^-(\mu^+) \rightarrow e^-(e^+) + \bar{\nu}_e(\nu_e) + \nu_\mu(\bar{\nu}_\mu), \tag{1.40}$$

with a branching ratio approaching 100 %. Exploiting muons from a storage ring to produce the neutrino beam has the advantage that the neutrino flux is well understood, and the number of muons produced would be proportional to the power of the proton beam. The current of a monochromatic muon beam can be precisely measured, and the physics of muon decay is well comprehended. The Neutrino Factory offers considerable benefits in terms of higher luminosity, higher purity of the flavour content and better precision in the energy spectrum of the neutrinos generated when compared to a conventional neutrino beam generated directly from pion decay. The straight sections of the muon storage ring are pointed towards remote detectors, so that the flavour of neutrinos arising from the decays can be measured. The "golden channel" of ν_μ appearance i.e. $\nu_e(\bar{\nu}_e) \rightarrow \nu_\mu(\bar{\nu}_\mu)$ is of particular interest. Oscillation analyses search for the "wrong" signed muon being detected at the far detector. A discrepancy in the rate $P(\nu_e \leftrightarrow \nu_\mu)$ and $P(\bar{\nu}_e \leftrightarrow \bar{\nu}_\mu)$ would be evidence of CP violation. The Neutrino Factory would also allow searches for sterile neutrinos.

Muon beam cooling is critical if the Neutrino Factory is to reach its design luminosity offering $\approx 10^{21}$ muon decays per year. A Neutrino Factory requires the transverse width to be reduced from 15-20 mm to 2-5 mm [121]. This, once again, reiterates the importance of the MICE experiment in providing experimental verification that muon ionisation cooling is feasible.

1.6 Summary

This chapter has summarised the remaining outstanding issues within the current understanding of particle physics and explored the possibility of the construction of either a multi-TeV Muon Collider or Neutrino Factory in order to resolve them. Figures 1.7 and 1.12 show schematic designs for both machines respectively. **Muon ionisation cooling would be vital for the operation of either and is yet to be experimentally realised. The Muon Ionisation Cooling Experiment (MICE) [68] aims to make the first measurements of this technique and will, therefore, pave the way for the construction of Neutrino Factory and Muon Collider. This thesis presents analyse which formed part of the commissioning stage of MICE with publication of the first measurement of ionisation cooling expected in 2018.**

Chapter 2

Ionisation Cooling

The motivations for construction of both a Neutrino Factory or Muon Collider were outlined in Chapter 1. To actualise either it is necessary to experimentally demonstrate the process of muon ionisation cooling.

MICE, the Muon Ionisation Cooling Experiment [68], is a proof-of-principle machine developed at the Rutherford Appleton Laboratory, UK. MICE aims to ascertain the first measurement of sustainable ionisation cooling of a muon beam and is, consequently, the first step towards both a Neutrino Factory or Muon Collider. The following chapter will define concepts of accelerator physics required to enable a complete theoretical understanding of the process of ionisation cooling. A formal definition of beam emittance is given in Section 2.3 and derivation of the "cooling equation" is provided in Section 2.4.3. This is the fundamental equation governing the process of emittance reduction in matter. Section 2.5 discusses the two main physical processes, energy loss and multiple scattering, which must be parameterised in order to characterise "cooling" within MICE.

2.1 Co-ordinate Systems

2.1.1 Phase Space

Every particle within a beam may be described by a phase space, a set of six co-ordinates consisting of two transverse spatial co-ordinates (x, y), and the corresponding transverse momenta (p_x, p_y), and two longitudinal co-ordinates: the time in the laboratory frame (t) and particle energy (E). t is often replaced with the longitudinal distance, z. It is possible to describe an entire beam as an ensemble of particles using their probability density function in phase-space.

2.1.2 Trace Space

The trace space can be obtained from the phase space defined in Section 2.1.1 by transforming the momenta according to:

$$x' = \frac{p_x}{p_z} = \frac{dx}{dz}, \tag{2.1}$$

and

$$y' = \frac{p_y}{p_z} = \frac{dy}{dz}. \tag{2.2}$$

In trace space, the transverse momenta p_x and p_y, are replaced by x' and y' which now define the divergence of the particle trajectory away from the longitudinal axis in the respective directions.

2.2 Single Particle Motion: Transfer Maps

Transfer maps are operators which describe a particle's motion as it traverses a magnetic field. This section derives the first order transfer maps for a single particle traversing a solenoidal field. Single particle transfer maps will be used in Chapter 5 as a way of quantifying magnet misalignment in the MICE cooling channel. The approach taken in this chapter is based on [123]. Section 2.2.1 derives the Hamiltonian for a single, charged particle. Transfer maps are found by expanding this Hamiltonian as a power series via Taylor expansion.

2.2.1 The Hamiltonian for Particle Motion in Accelerators

The motion of a particle, of momentum $\vec{p}$ and charge q, in an electromagnetic field is governed by the Lorentz force, denoted as [124]

$$\frac{d\vec{p}}{dt} = q[\vec{E} + \vec{v} \times \vec{B}], \tag{2.3}$$

where the electric field ($\vec{E}$) and magnetic field ($\vec{B}$) can be expressed in terms of 3-vector potential ($\vec{A} = (A_X, A_Y, A_Z)$) and scalar potential ($\Phi$), such that

$$\vec{E} = - \bigtriangledown \Phi - \frac{\partial \vec{A}}{\partial t}, \tag{2.4}$$

and,

$$\vec{B} = \bigtriangledown \times \vec{A}. \tag{2.5}$$

Using 4-vector notation a 4-vector potential $\vec{A}$ can be defined as $\vec{A} = (\Phi, A_X, A_Y, A_Z)$. The Hamiltonian for the particle moving in a general electromagnetic field, with canonical phase space vector $\vec{u_T^c} =$

$(T, P_T^c, X, P_X^c, Y, P_Y^c)$, is then

$$H_z = qA_Z - [(P_T^c - q\Phi)^2 - m^2 - (P_X^c - qA_X)^2 - (P_Y^c - qA_Y)^2]^{1/2}, \tag{2.6}$$

where m is the particle's mass, taking z as the independent variable and using natural units. Upper case letters are used here to denote a spatial co-ordinate in the lab frame. Later lower case will be associated with the deviation from the reference trajectory corresponding to each co-ordinate. $\vec{P^c}$ is the canonical momentum, which is related to the kinetic momentum by $P_i^c = P_i^k + qA_i$; P_T^k is the particle's energy and T is time in the lab frame.

Along the axis of a solenoid the field exists only in the longitudinal direction, z, hence $\vec{B_z} = (0, 0, B_z)$. Near to the axis, the potential 4-vector is [123]:

$$\vec{A} = (0, -YU(Z, \rho^2), XU(z, \rho^2), 0), \tag{2.7}$$

where $\rho^2 = X^2 + Y^2$ and

$$U = \sum_{n=0}^{\infty} \frac{(-1)^n (\rho^2) b_{2n}}{2^{2n+1} n!(n+1)!}, \tag{2.8}$$

with

$$b_{2n} = \frac{\partial^{2n} B_z(0, 0, z)}{\partial z^{2n}}. \tag{2.9}$$

As both A_z and ϕ are 0, the Hamiltonian may be expressed as

$$H_z = -[(P_T^c)^2 - m^2 - (P_X^c - qA_X)^2 - (P_Y^c - qA_Y)^2]^{1/2}. \tag{2.10}$$

In MICE, supposing perfect optical alignment, it is conceivable to define a reference trajectory parallel to the z axis. Transverse deviations from this reference trajectory are denoted as lower case letters x and y. In order to perform a perturbation expansion of the system it is necessary to transform the Hamiltonian to deviation variables relative to a reference particle at time $T_0 = \frac{z}{v_z^0}$ and with momentum p_0^c.

A complete set of deviation variables $(t, p_t^c, x, p_x^c, y, p_y^c,)$ can be defined by introducing the transformation function:

$$F_2 = Xp_x^c + Yp_y^c + [T - T_0](p_t^c + p_0^c). \tag{2.11}$$

A generating function of the second kind, labelled F_2 here, transforms lab (upper case) phase space co-ordinates to deviation (lower case) co-ordinates following rules outlined in [125]. The deviation variables can be related back to the lab co-ordinates such that

$$x = X, \tag{2.12}$$

$$y = Y, \tag{2.13}$$

$$t = T - T_0, \tag{2.14}$$

$$p_x^c = P_X^c, \tag{2.15}$$

$$p_y^c = P_Y^c, \tag{2.16}$$

$$p_t^c = P_T^c + p_0^c. \tag{2.17}$$

A new Hamiltonian, (H_z^{new}) with phase space co-ordinates $\vec{u}^c = (t, p_t^c, x, p_x^c, y, p_y^c)$ can be associated with the deviation variables and related back to the old Hamiltonian, (H_z^{old}), using Equation 2.10, meaning

$$H_z^{new} = H_z^{old} + \frac{\partial F_2}{\partial z} = H_z^{old} - \frac{p_t^c + p_t^0}{v_z^0} = -[(p_t^c + p_t^0)^2 - m^2 - (p_x^c - qA_x)^2 - (p_y^c - qA_y)^2]^{1/2} - \frac{p_t^c + p_t^0}{v_z^0}. \tag{2.18}$$

The Hamiltonian can be generalised (as Hamiltonian K) and expanded in terms of a power series,

$$K = K_0 + K_1 + K_2 + \ldots K_n, \tag{2.19}$$

where K_i is a homogeneous polynomial of degree i. Using a Binomial expansion and the expression for the vector potential in the axial symmetric field, outlined in Equation 2.7, it can be shown [123] that

$$K_0 = \frac{p_0}{v_0}(1 + v_0^2), \tag{2.20}$$

$$K_1 = 0, \tag{2.21}$$

and

$$K_2 = \frac{p_x^c + p_y^c}{2p} - \frac{B_0}{2p}(xp_y^2 - yp_x^2) + \frac{B_0^2}{8p}(x^2 + y^2) + \frac{p_z^2}{2p\beta_{rel}\gamma_{rel}}. \tag{2.22}$$

p, β_{rel} and γ_{rel} are the relativistic parameters of the reference particle and $B_0 = qB_z$. K_0, K_1 and K_2 can now be used to obtain the transport maps for the particle, this will be accomplished in Section 2.2.2.

2.2.2 First Order Transfer Maps

A map, $\underline{\underline{M}}$, transforms a single particle vector at some point z^{in} to a point further along the beamline, denoted by z^{fin}:

$$\underline{\underline{M}} u^c(z^{in}) = u^c(z^{fin}). \tag{2.23}$$

From Hamilton's equations [125], it can be shown that vector $\vec{u}$ evolves via the equation,

$$\frac{d\vec{u}}{dz} = [\vec{u}, K]. \tag{2.24}$$

where the transfer map between z and $z + dz$ can, therefore, be defined as

$$\underline{\underline{M}}(dz) = 1 - [K, dz] = 1 - : K : dz = 1 - (: K_0 : + : K_1 : + : K_2 : + \quad \ldots)dz, \tag{2.25}$$

the Lie (::) operator and Poisson brackets are defined by

$$: f : g = [f, g] = -[g, f] = \frac{\partial f}{\partial q_i}\frac{\partial g}{\partial p_i} - \frac{\partial f}{\partial p_i}\frac{\partial g}{\partial q_i}. \tag{2.26}$$

Discussion of Lie Algebra and its importance in accelerator physics can be found in [126]. $\underline{\underline{M}}$ can be truncated to the i-th order transfer map, denoted as $\underline{\underline{M}}_i$. Given the derived K_i coefficients, defined by Equations 2.20 to 2.22, it becomes apparent that M_2 is the first non-unitary transfer map and is subsequently referred to as the first order transfer map. Using Equation 2.25 and the expression for K_2, given in Equation 2.22, M_2 may be computed as

$$M_2 = 1 - [K_2, dz] = 1 - \left(\frac{\partial K_2}{\partial q_i}\frac{\partial}{\partial p_i} - \frac{\partial K_2}{\partial p_i}\frac{\partial}{\partial q_i}\right)dz \tag{2.27}$$

$$= 1 + \begin{pmatrix} 0 & \frac{-1}{p\beta_{rel}\gamma_{rel}} & 0 & 0 & 0 & 0 \\ 0 & 0 & 0 & 0 & 0 & 0 \\ 0 & 0 & 0 & \frac{1}{p} & \frac{B_0}{2p} & 0 \\ 0 & 0 & \frac{-B_0^2}{4p} & 0 & 0 & \frac{B_0}{2p} \\ 0 & 0 & -\frac{B_0}{2p} & 0 & 0 & \frac{1}{p} \\ 0 & 0 & 0 & \frac{-B_0}{2p} & \frac{-B_0^2}{4p} & 0 \end{pmatrix} dz.$$

In the case where the transverse and longitudinal components of the transfer matrix are decoupled $\underline{\underline{M_2}}$ can be decomposed into two matrices:

$$\underline{\underline{M_{2\perp}}} = 1 + \begin{pmatrix} 0 & \frac{1}{p} & \frac{B_0}{2p} & 0 \\ -\frac{B_0^2}{4p} & 0 & 0 & \frac{B_0}{2p} \\ -\frac{B_0}{2p} & 0 & 0 & \frac{1}{p} \\ 0 & \frac{-B_0}{2p} & \frac{-B_0^2}{4p} & 0 \end{pmatrix} dz, \tag{2.28}$$

and

$$\underline{\underline{M_{2||}}} = 1 + \begin{pmatrix} 0 & -\frac{1}{p\beta_{rel}\gamma_{rel}} \\ 0 & 0 \end{pmatrix} dz,$$

representing the transverse and longitudinal components respectively. When $B_0 = 0$, many of the elements within $\underline{\underline{M}}_{\perp}$ become "0. These matrices then depict a particle travelling with a "straight track" meaning the particle continues along its momentum trajectory unimpeded. In this scenario the x and y co-ordinates are decoupled and each transverse position, x or y, evolves as a linear function with a gradient of x' or y' respectively. In such a scenario the magnet is said to resemble a "drift space" with transfer map $\underline{\underline{M}}_{drift}$ between the upstream and downstream trace space given by

$$\underline{\underline{M}}_{drift} = \begin{pmatrix} 1 & L & 0 & 0 \\ 0 & 1 & 0 & 0 \\ 0 & 0 & 1 & L \\ 0 & 0 & 0 & 1 \end{pmatrix}. \tag{2.29}$$

When the particle is travelling within solenoidal field then x and y can no longer be considered as independent co-ordinates. There exists an inherent coupling in the transverse plane which results from the Larmor precession of charged particles in the magnetic field and the particle adheres to a "helical track." In Chapter 5 the transfer matrix of the MICE solenoidal Focusing Coil is derived using least squares mapping between 2 sets of particle 4D co-ordinates upon entrance and exit of the Coil. It is essential that all 4 trace space components are considered in this case.

2.2.3 Higher Order Transfer Maps

In Section 2.2.1 a Taylor expansion was used to demonstrate that the Hamiltonian, K_z, can be expanded into a power series. The first three coefficients K_0, K_1 and K_2 were derived assuming a solenoidal field with axial symmetric potential, from Equation 2.7. Second order terms may be acquired using Equation 2.18 [127] such that

$$K_3 = \frac{p_t^0 p_t^c}{2p^2} K_2, \tag{2.30}$$

and,

$$\underline{\underline{M_3}} = \underline{\underline{M_2}} + : K_3 := \underline{\underline{M_2}} + \frac{p_t^0}{2p^2}(p_t^c : K_2 : + : p_t^c : K_2). \tag{2.31}$$

These are purely chromatic. Higher order terms may also be obtained but are more complicated, having varying B_z dependencies, thus they are disregarded here. For simplicity, in the ensuing discussion only the first order transfer map is considered.

2.2.4 Properties of the First Order Transfer Map

By integrating Equation 2.25 it follows that the transfer map, for an infinitesimal slice of the magnetic field, may be expressed as

$$M(z \to z + dz) = e^{-:H_z:dz} = e^{:G_z:} = 1 + :G: + \frac{:G:}{2!} + \ldots, \tag{2.32}$$

where G is referred to as the Lie Group Map operator [128].

In the preceding sections the first order transfer map for transporting a single particle through a single magnet element was derived. The transfer map of a beam line composed of a series of n magnet elements can be obtained by joining the transfer maps of the individual magnets in sequence [129] such that

$$M = e^{:f_1:} e^{:f_2:} \ldots e^{:f_n:}, \tag{2.33}$$

where f_i is the Lie transfer map of $i-$th magnet element. Lie algebra can be exploited to turn these multiple maps into a single Lie map known as the one-turn-map in accelerator physics if the beam line is a closed loop [128].

The canonical coordinates of a charged particle leaving an element, u^{fin}, can be expressed as an expanded multivariate Taylor power series of its coordinates on entering the element, u^{in}, meaning

$$u^{fin}_{i,1} = \sum_{j=1}^{6} M_{ij} u^{in}_{j,0} + \ldots, \tag{2.34}$$

where M_{ij} are the components of the first order transfer map of the element. $u_{j,0}$ and $u_{j,1}$ are the j-th canonical coordinate at the entrance and the exit of the element. Consequently, the co-ordinates of u^{fin} are a linear combination of u^{in}. These linear combinations, geometrically, correspond to rotations, stretches, and skews. Under a linear transformation straight lines stay straight, and ellipses stay elliptical.

Transfer maps of large periodical structures are symplectic meaning that they obey Poincarre Integral Invariance [130]. A consequence is that the volume of phase space occupied by a closed surface of trajectories is conserved. This is Liouville's Theorem [131] and will be discussed in detail in Section 2.3.1.

The condition for a matrix to be symplectic is

$$\underline{\underline{M}}^T \underline{\underline{J}} \underline{\underline{M}} = \underline{\underline{J}} \tag{2.35}$$

where $\underline{\underline{J}}$ is

$$\begin{pmatrix} 0 & 1 & 0 & 0 & 0 & 0 \\ -1 & 0 & 0 & 0 & 0 & 0 \\ 0 & 0 & 0 & 1 & 0 & 0 \\ 0 & 0 & -1 & 0 & 0 & 0 \\ 0 & 0 & 0 & 0 & 0 & 1 \\ 0 & 0 & 0 & 0 & -1 & 0 \end{pmatrix}. \tag{2.36}$$

It can be shown that the first order solenoidal linear transfer map $\underline{\underline{M_2}}$ obeys this condition for canonical momenta. A consequence of the symplectic condition is that the transfer matrix must have a determinant of 1 [128].

2.3 Collective Motion and Beam Emittance

The principal parameter used to quantify muon cooling is the beam emittance, ϵ. In order to formally define beam emittance the collective motion of the particle ensemble must be considered. This section begins by outlining the founding principle of beam optics - Liouville's theorem. This concept is then related back to the single particle transfer maps outlined in Section 2.2 via consideration of a beam "covariance matrix." It is advantageous to consider the geometrical interpretation of single particle emittance before continuing to interpret emittance for an ensemble beam in terms of this covariance matrix.

2.3.1 Liouville's Theorem

Liouville's Theorem [131] states that the overall volume occupied by a beam of particles in phase space is invariant, assuming only conservative forces are acting i.e. magnetic focusing or bending. It is axiomatic that the shape of the ellipse may alter but the overall volume in phase space will remain constant.

This concept derives from consideration of a beam of non-interacting particles with continuous density function $h = h(t, x, y, E, p_x, p_y, p_z)$ in a closed system, assuming no external forces. h must obey the continuity equation, [130], such that

$$\bigtriangledown.(h\vec{v}) + \frac{\partial h}{\partial t} = 0 \tag{2.37}$$

$$\implies h \bigtriangledown .\vec{v} + \vec{v}.\bigtriangledown h + \frac{\partial h}{\partial t} = 0, \tag{2.38}$$

where $\vec{v}$ is the velocity vector of the particles in the beam constructed from the canonical position and momentum of each particle in the phase space. Using Hamilton's equations it follows that $\frac{dh}{dt} = 0$ so the phase space density is constant in time.

The first order transfer map outlined in Section 2.2 is both linear and symplectic, ensuring that the area of the beam in phase space under such a transportation is conserved and, consequently, Liouville's theorem is satisfied. In reality, within the MICE cooling channel the very large momentum spread of the beam cause significant chromatic aberrations. Second and higher order transfer maps must be studied in which beam transport is no longer a linear transformation (Section 2.2.3). The difficulty in MICE comes from the fact that to cool the beam non-conservative forces must be applied.

2.3.2 The Covariance Matrix

In Section 2.2 the first order transfer map for a single particle in a solenoid was obtained. In a multi-particle system, such as MICE, it is essential to consider the transport of the entire beam through the solenoid.

The density of particles in a volume element at longitudinal point z^{in} can be related to that at subsequent point along the channel, z^{fin} assuming a bunch of particles have a continuous density function denoted by $h(\vec{u})$. Under Liouville's theorem (Section 2.3.1), the density in a volume element is constant under a canonical transformation, thus,

$$h^{fin}(\vec{u}^{fin}) = h^{in}(\vec{u}^{in}). \tag{2.39}$$

From the definition of the transfer matrix ($\underline{\underline{M}}$) it follows that

$$h^{fin}(\vec{u}^{in}) = h^{in}(\underline{\underline{M}}^{-1}\vec{u}^{fin}). \tag{2.40}$$

The properties of a beam, or bunch, of particles can be expressed in terms of moments of the phase space co-ordinates of the particles within the beam such that the N-th order moment is

$$\langle u_{i_1} u_{i_2} \dots u_{i_N} \rangle = \int d^6\vec{u} h(\vec{u}) u_{i_1} u_{i_2} \dots u_{i_N}, \tag{2.41}$$

taken about $\vec{0}$ rather than the centre of the probability distribution. Using Equation 2.39 the N-th order moments at z^{fin} may be written as

$$\langle u_{i_1} u_{i_2} \dots u_{i_N} \rangle^{fin} = \int d^6\vec{u}^{fin} h^{fin}(\vec{u}^{fin}) u_{i_1}^{fin} u_{i_2}^{fin} \dots u_{i_N}^{fin}. \tag{2.42}$$

From 2.40 it follows that

$$\langle u_{i_1} u_{i_2} \dots u_{i_N} \rangle^{fin} = \int d^6\vec{u}^{fin} h^{in}(\underline{\underline{M}}^{-1}\vec{u}^{in}) u_{i_1}^{fin} u_{i_2}^{fin} \dots u_{i_N}^{fin}, \tag{2.43}$$

$$= \int d^6\vec{u}^{in} h^{in}(\vec{u}^{in}) (\underline{\underline{M}}\vec{u}^{in})_{i_1} (\underline{\underline{M}}\vec{u}^{in})_{i_2} \dots (\underline{\underline{M}}\vec{u}^{in})_{i_N}, \tag{2.44}$$

$$= \langle (\underline{\underline{M}}\vec{u}^{in})_{i_1} (\underline{\underline{M}}\vec{u}^{in})_{i_2} \dots (\underline{\underline{M}}\vec{u}^{in})_{i_N} \rangle. \tag{2.45}$$

Considering the simplest case of $N = 2$ and assuming the linear transport result, the following expression can be written:

$$\langle u_{i_1}^{fin} u_{i_2}^{fin} \rangle = \langle \sum_{j_1} (m_{i_1 j_1} u_{j_1}^{in}) \sum_{j_2} (m_{i_2 j_2} u_{j_2}^{in}) \rangle. \tag{2.46}$$

Defining an input covariance matrix as $\underline{\underline{V}}^{in}$ with elements $v_{ab}^{in} = \langle u_a^{in} u_b^{in} \rangle$ and using matrix multiplication means that Equation 2.46 can be rewritten and conveniently expressed as a matrix product where

$$(\underline{\underline{M}}_2 \underline{\underline{V}}^{in} (\underline{\underline{M}}_2)^T)_{i_1 i_2} = \sum_{j1} (m_{i_1 j_1} \sum_{j_2} (v_{j_1 j_2} m_{i_2 j_2})) \tag{2.47}$$

$$= \langle \sum_{j_1} m_{i_1 j_1} u_{j_1}^{in} \sum_{j_2} m_{i_2 j_2} u_{j_2}^{in} \rangle = \underline{\underline{V}}^{fin}. \tag{2.48}$$

Exploiting the fact that the transfer matrix must be symplectic it follows that

$$|\underline{\underline{V}}^{in}| = |\underline{\underline{V}}^{fin}|. \tag{2.49}$$

In Section 2.3.4 it will be shown that this corresponds to a conservation of beam emittance and that the symplectic nature of the transfer maps thus guarantees the phase space volume occupied by the beam is conserved meaning it observes Liouville's theorem.

2.3.3 Geometric Interpretation of Single Particle Emittance

Betatron oscillations arise as particles traverse the accelerator beam line. A particle beam will be comprised of particles with finite divergence angles, described by the trace space parameters x' and y', and positions, x and y, relative to the reference trajectory. In a periodic focusing magnetic lattice, the particles oscillate horizontally and vertically. In the transverse (x, x') plane the motion of each particle forms an elliptical trajectory. A representation of which is exhibited in Figure 2.50.

In 2D the Courant and Snyder invariant [132] describes the particle ellipse in the $x - x'$ transverse plane at point z along the beam line,

$$\epsilon = \gamma(z)x^2 + 2\alpha(z)xx' + \beta(z)x'^2, \tag{2.50}$$

where α, β and γ are parameters which define the geometry of the particle elliptical trajectory in trace space as displayed in Figure 2.1. The area of this ellipse in the transverse (x, x') plane is equal to $\pi\epsilon$ where ϵ is the transverse emittance of a single particle in units of length $\times$ angle (usually $mm \cdot rad$).

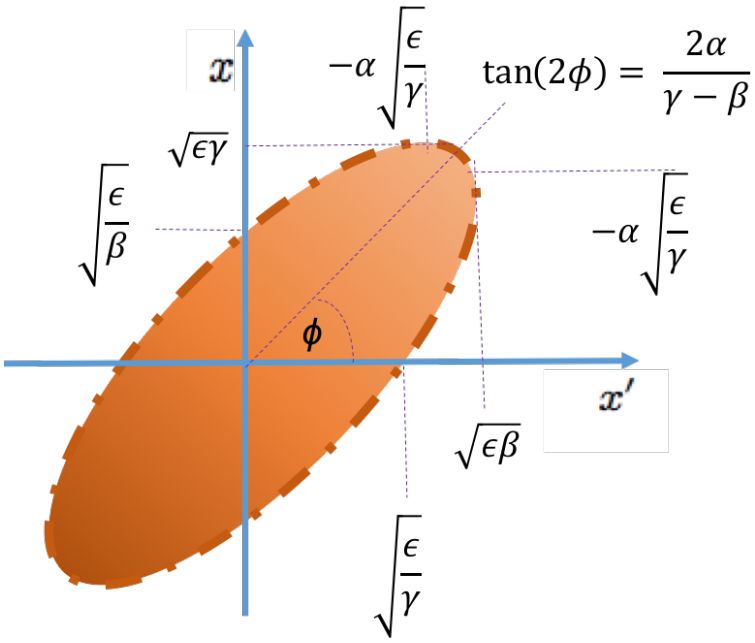

Figure 2.1: Representation of the elliptical contour of single particle in the transverse (x, x') plane. The emittance is proportional to the area of the ellipse with α, β and γ referred to as the "Twiss parameters." These parameters relate to the single particle ellipse dimensions in trace space, as displayed, and may be combined and associated with the emittance via Equation 2.50. ϕ characterises the phase advance.

2.3.4 Defining Beam Emittance

Section 2.3.2 explained how covariance matrices may be utilised to characterise the collective motion of a particle beam. The distribution of particle co-ordinates of a multi-particle beam in 2D can be approximated as a Gaussian probability density function, with mean, μ, and RMS, σ. The ensemble can be modelled by a single covariance matrix, $\underline{\underline{V}}$, expressed as

$$\underline{\underline{V}} = \begin{pmatrix} \sigma_{xx} & -\sigma_{xx'} \\ -\sigma_{x'x} & \sigma_{x'x'} \end{pmatrix}, \tag{2.51}$$

where σ_{ii} is the variance of co-ordinate i and σ_{ij} is the covariance between co-ordinates i and j.

An ellipse can be defined in trace space such that

$$\underline{\underline{V}} = \epsilon \begin{pmatrix} \beta & -\alpha \\ -\alpha & \gamma \end{pmatrix}. \tag{2.52}$$

ϵ is now the "RMS emittance" of the beam. The locus of points forming an elliptical contour in trace space is given by $u^T \underline{\underline{V}}^{-1} u = 1$. Thus, the RMS beam ellipse is interpreted as the contour where $\underline{\underline{V}}$ is the beam covariance matrix outlined in Equation 2.51.

For the Gaussian distribution of particles RMS values of x, x' and xx' are specified by [124]

$$\langle x_n^2 \rangle = \epsilon\beta \quad , \quad \langle x_n'^2 \rangle = \epsilon\gamma \quad \text{and} \quad \langle x_n x_n' \rangle = -\epsilon\alpha, \tag{2.53}$$

where n labels each particle in the beam. The area of the trace space ellipse which describes the RMS particle is then expressed as

$$A = \pi\epsilon = \pi\sqrt{(\epsilon\beta)(\epsilon\gamma) - (\epsilon^2\alpha^2)} = \langle x_n^2\rangle\langle x_n^{'2}\rangle - \langle x_n x_n'\rangle = \pi\sqrt{\sigma_{xx}\sigma_{yy} - \sigma_{x'y'}^2} = \pi\sqrt{|\underline{\underline{V}}|}. \tag{2.54}$$

where the relation $\beta\gamma - \alpha^2 = 1$, a consequence of the geometry of ellipses [132], has been exploited. The RMS beam emittance is intrinsically linked to volume of the RMS particle ellipse in trace space, for the 2D case this is the area in the $x - x'$ plane. Conservation of the phase (or trace) space volume, as implied by the Liouville's theorem (Equation 2.49), results in conservation of beam emittance.

This is generalised to n-dimensions and the volume of the hyper-ellipse (Vol_n) in n-D trace space is related to the $n \times n$ covariance matrix, $\underline{\underline{V}}$ by the expression

$$Vol_n = \frac{\pi^{\frac{n}{2}}}{\Gamma(1 + \frac{n}{2})}|\underline{\underline{V}}|^{\frac{n}{2}}; \tag{2.55}$$

where Γ is the gamma function.

2.3.5 Normalised Beam Emittance

The area, in trace-space, of the ellipse illustrated in Figure 2.1 will not be invariant when the energy of the particle changes i.e. if the particle beam is accelerated. Consequently, beam emittance is often expressed in terms of a "normalised emittance," ϵ_n, where

$$\epsilon_n = \beta_{rel}\gamma_{rel}\epsilon. \tag{2.56}$$

Here γ_{rel} is the Lorentz factor and β_{rel} is the relative velocity. ϵ_n is conserved in acceleration - preserving Liouville's theorem.

2.3.6 Normalised Beam Emittance in MICE

Equation 2.54 provided the emittance for a 2D case when the two transverse directions are not coupled to one-another nor the longitudinal direction. If correlations exist between the transverse x and y components, 4D space must studied. Additionally, if the longitudinal phase space is coupled with the transverse co-ordinates then the full 6D space and emittance must be taken into consideration. Within the MICE cooling channel 4D transverse emittance is measured with the 2D longitudinal emittance being decoupled.

The 4D transverse normalised emittance is specified by

$$\epsilon_n^{\perp} = \frac{1}{m}(|V_{4D}(x, x', y, y')|)^{\frac{1}{4}}; \tag{2.57}$$

and the 2D longitudinal emittance by

$$\epsilon_n^{||} = \frac{1}{m}(|V_{2D}(t,E)|)^{\frac{1}{2}}. \tag{2.58}$$

in natural units with m being the muon mass. It is this $\epsilon_n^{\perp}$ which MICE must reduce in order to demonstrate ionisation cooling. It is important to note that these expressions follow from Equations 2.55 and Equation 2.56. The factor of π/Γ is conventionally disregarded.

2.3.7 Angular Momentum in Solenoidal Optics

Within a solenoid the x and y co-ordinates are coupled. Therefore, a canonical angular momentum L^c can be defined

$$L^c = xp_x - yp_y. \tag{2.59}$$

For an ensemble of particles the mean angular momentum can be defined as

$$\langle L^c \rangle = \langle xp_y \rangle - \langle yp_x \rangle + \frac{B_0}{2}(\langle x^2 \rangle + \langle y^2 \rangle), \tag{2.60}$$

within MICE the build up of canonical angular momentum can be cancelled at the absorber by setting the Focus Coil to operate in "flip" mode. By flipping the fields at the absorber any angular momentum which has built up in the first half of the channel is cancelled out by an opposite sign field in the second half. The MICE magnets, including the Focus Coil, will be discussed in detail in Chapter 3.

2.3.8 Covariance Matrix in 4D Solenoid Optics

In Section 2.2 it was noted that there is an inherent $x-y$ coupling in the transverse plane for a beam in a solenoidal field, resulting in helical tracks. The transverse 4D covariance matrix, $\underline{\underline{V}}_{4D}^{\perp}$, of a particle beam traversing a solenoidal field, assuming the beam is cylindrically symmetric, is [133]:

$$\underline{\underline{V}}_{4D}^{\perp} = mc\epsilon_n \begin{pmatrix} \beta_\perp/p_0 & -\alpha_\perp & 0 & -(\beta_\perp B_0 - \mathcal{L}) \\ -\alpha_\perp & \gamma_\perp p_0 & (\beta_\perp B_0 - \mathcal{L}) & 0 \\ 0 & (\beta_\perp B_0 - \mathcal{L}) & \beta_\perp/p_0 & -\alpha_\perp \\ -(\beta_\perp B_0 - \mathcal{L}) & 0 & -\alpha_\perp & \gamma_\perp p_0 \end{pmatrix}, \tag{2.61}$$

where $p_0 = \langle p_z \rangle$, $\mathcal{L} = mc\epsilon_n/L^c$, $L^c = \langle xp_y - yp_x \rangle$ is the canonical angular momentum. The matrix resembles that of the 2D case, with off-diagonal terms being a result of the particles possessing angular momentum. $\alpha_\perp, \beta_\perp$ and $\gamma_\perp$ are referred to as the 4D transverse Twiss parameters in analogy to the Courant and Snyder formalism.

The determinant of Equation 2.61 is given by the expression:

$$\sqrt{|\underline{\underline{V}}_{4D}^{\perp}|} = p_z^2(\langle x^2\rangle\langle x'^2\rangle - \langle xx'\rangle^2 - \langle xy'\rangle^2). \tag{2.62}$$

Combining this with the definition for beam emittance, the beam envelope Twiss parameters may be related by the expression [133]:

$$\gamma_\perp = \frac{1+\alpha_\perp^2 + (\beta_\perp B_0/2 - \mathcal{L})^2}{\beta_\perp}. \tag{2.63}$$

.

In a vacuum with only magnetic fields, the beam parameters evolve according to $d\beta_\perp/dz = -2\alpha_\perp$ and

$$2\beta_\perp\beta_\perp'' - (\beta_\perp)^2 + 4\beta_\perp^2(B_0/2)^2 - 4(1+\mathcal{L}^2) = 0. \tag{2.64}$$

where $\mathcal{L}$ and ϵ_N are constant. If $\beta_\perp = \beta_i\sqrt{1+\mathcal{L}}$ then the beam envelope beta function $\beta_\perp$ matches the single particle β of particle i.

2.3.9 Acceptance

The acceptance is defined as the maximum emittance that a beam transport line is able to transmit. Acceptance is, consequently, the size of the cross-section of the apparatus in units of phase space. The reason that the muons in a Neutrino Factory must be cooled is that the emittance of the muons which result from pion decay is larger than the acceptance of the downstream accelerator systems.

2.4 Beam Cooling

2.4.1 Traditional Cooling Techniques

Both a Neutrino Factory and a Muon Collider will require high intensity, monochromatic and highly collimated muon beams, of the order GeV and TeV respectively, to achieve their physics goals. Hence, the high emittance muon beam, produced from pion decay, must be cooled to make either a reality. "Cooling" a beam implies reducing the beam's emittance and will allow both to attain the high flux of muons required within the limited acceptance of their sub-structures.

There are presently three prevailing cooling techniques used in electron, hadron and ion machines:

1. **Synchrotron Radiation Cooling:**

   Highly accelerated electron beams emit synchrotron radiation along the direction of their trajectory when accelerated around a circular machine. This produces a damping effect resulting in the beam losing energy and subsequently being "cooled". [134]

2. **Stochastic Cooling:**

   An active feedback loop is exploited to cool the particle beam. Electrical signals that the individual charged particles generate are used to drive an electrostatic kicker, which kicks individual particles back towards the bunch centre, reducing the total beam emittance. [135]

3. **Electron Cooling:**

   An electron beam, with mean velocity equivalent to that of the circulating particles and with small momentum spread, is injected along the straight section of a storage ring containing heavy particles, such as protons. Coulomb scatters act to cool the heavy particle beam. The momentum of the proton beam relative to the bunch centre is transferred to the electrons, resulting in a reduction of the beam emittance. The cooling process continues until the temperature of the protons equals that of the electrons in the centre-of-mass frame. [136]

Due to the muon's finite lifetime of just 2.2 μs these existing techniques are not viable for use within a muon machine. In addition, given that the muon is $\approx$ 200 times heavier than the electron, cooling via synchrotron radiation is implausible. Consequently, the only feasible cooling method applicable to muon beams is "ionisation cooling" which was initially proposed in 1981, [137], but is yet to be experimentally verified.

2.4.2 Ionisation Cooling

The fundamental principle of ionisation cooling is simple: charged particles, i.e. muons, traverse an absorber, losing momentum isotropically as they ionise the absorber material. This leads to a reduction in the normalised emittance of the beam. In MICE the momentum lost in the longitudinal direction is restored using RF cavities ensuring only the transverse momentum is diminished and only 4D cooling is observed.

2.4.3 The Cooling Equation

A "cooling equation" can be obtained illustrating the approximate change in normalised emittance as a beam traverses an absorber material of length z.

Assuming cylindrical symmetry and utilising solenoid optics the deviation in beam size (σ_x) and divergence angle, relative to the beam axis, ($\sigma_{x'}$), can be written as:

$$\sigma_x = \sqrt{\beta_\perp \epsilon}, \tag{2.65}$$

and

$$\sigma_{x'} = \sqrt{\frac{\epsilon}{\beta_\perp}}; \tag{2.66}$$

where $\beta_\perp$ is the optical beta function, expressed in Section 2.3.8. Here the emittance reduction is assumed to occur at a focus meaning $\sigma_{xx'} = 0$.

From Equation 2.56 normalised emittance (ϵ_n) can be defined as $= \frac{p}{m}\sigma_x\sigma_{x'}$. Taking the derivative to get the change in normalised emittance of the beam per unit distance, z, travelled through the material gives

$$\frac{d\epsilon_n}{dz} = \frac{1}{m}\frac{dp}{dz}\sigma_x\sigma_{x'} + \frac{p}{m}\sigma_x\frac{d\sigma_{x'}}{dz}. \tag{2.67}$$

Through taking the derivative of the mass shell condition, $E^2 = p^2 + m^2$, the expression $dp = \frac{E}{p}dE$ can be obtained, such that

$$\frac{dp}{dz} = \frac{E}{p}\frac{dE}{dz} = \frac{1}{\beta_{rel}}\left\langle\frac{dE}{dz}\right\rangle, \tag{2.68}$$

where β_{rel} is particle velocity. Putting this back into Equation 2.67 gives

$$\frac{d\epsilon_n}{dz} = -\frac{\epsilon_n}{p\beta_{rel}}\left\langle\frac{dE}{dz}\right\rangle + \frac{p}{m}\sigma_x\frac{d\sigma_{x'}}{dz}. \tag{2.69}$$

Given that

$$\frac{d\sigma_{x'}^2}{dz} = 2\sigma_{x'}\frac{d\sigma_{x'}}{dz}, \tag{2.70}$$

Equation 2.69 can be re-written as

$$\frac{d\epsilon_n}{dz} = \frac{-\epsilon_n}{p\beta_{rel}}\left\langle\frac{dE}{dz}\right\rangle + \frac{p}{m}\sigma_x\frac{1}{2\sigma_{x'}}\frac{d\sigma_{x'}^2}{dz}. \tag{2.71}$$

Substituting back in the expressions in Equations 2.65 and 2.66 for σ_x and $\sigma_{x'}$ gives

$$\frac{d\epsilon_n}{dz} = \frac{-\epsilon_n}{p\beta_{rel}}\left\langle\frac{dE}{dz}\right\rangle + \frac{p}{m}\frac{\beta_\perp}{2}\frac{d\sigma_{x'}^2}{dz}; \tag{2.72}$$

where the first term represents multiple coulomb scattering and can be approximated to [9]:

$$\frac{d\sigma_{x'}^2}{dz} \approx \left(\frac{13.6MeV}{p\beta_{rel}}\right)^2\frac{1}{X_0}. \tag{2.73}$$

X_0 is the absorber radiation length. Section 2.5 discusses better ways to parametrise multiple scattering to higher orders but for this derivation this basic approximation is sufficient. Substituting Equation 2.73 into Equation 2.72 and remembering that $p = \gamma_{rel}\beta_{rel}m$ and $E = \gamma_{rel}mc^2$ gives the overall equation for change in normalised transverse emittance of a muon beam per unit length:

$$\frac{d\epsilon_n}{dz} = \frac{-\epsilon_n}{\beta_{rel}^2 E}\left\langle\frac{dE}{dz}\right\rangle + \frac{\beta_\perp(13.6MeV)^2}{2\beta_{rel}^3 EmX_0}; \tag{2.74}$$

where E is energy, $\beta_\perp$ is the optical beta function, which describes how focussed the beam is and $\langle\frac{dE}{dz}\rangle$ is

the mean energy loss rate. Equation 2.74 is the "cooling equation."

The first term in Equation 2.74 represents the beam "cooling" and is proportional to the ease with which the absorber is ionised. The second term represents the "heating" effects caused by multiple scattering which opposes the desired cooling and causes the emittance to increase.

The extent to which the beam is cooled is related to the atomic number of the absorber material (Section 2.5.4), therefore, cooling dominates for low-Z materials such as hydrogen. The dependence of the heating term on $\beta_\perp$ shows the importance of focusing the beam. A more focussed beam will experience less heating as the scattering is small relative to the angular spread of the beam. The process of ionisation cooling is summarised graphically in Figure 2.2.

Figure 2.2: A visual representation of Equation 2.74. The black arrow characterises the muon's momentum as it enters the absorber. As the muon traverse the absorber material it loses energy in all directions, shrinking in momentum space. The resulting muon momentum is now represented by green arrow in plot (1). Multiple scattering within the material may then cause heating effects and must be limited as this could increase the formerly reduced (green arrow) transverse momentum (2). The third plot signifies the desired case within MICE when the muon beam subsequently reaccelerated longitudinally such that 4D transverse beam cooling is observed. The blue arrow then represents the end results in 2D [138].

By equating the "cooling" and "heating" terms in Equation 2.74 an equilibrium emittance can be calculated:

$$\epsilon_{eq} \approx \frac{\beta_\perp (13.6MeV)^2}{2\beta m_\mu X_0} \frac{1}{\langle \frac{dE}{dz} \rangle}. \tag{2.75}$$

The smaller this equilibrium emittance is for a particular absorber, the more efficient the reduction in emittance, as less multiple scattering results in less undesirable "heating" needing to be overcome.

In order to demonstrate sustainable ionisation cooling, any factor which acts to increase the transverse emittance must be understood and limited. For the most efficient cooling it is necessary to minimise $\beta_\perp$ while maximising $X_0 \langle \frac{dE}{dz} \rangle$. MICE uses superconducting solenoid focusing, which can give a $\beta_\perp$ as low as $\approx 10cm$, giving large beam divergence at the absorbers so that scattering in the absorbers gives a relatively small contribution to emittance. Liquid Hydrogen and Lithium Hydride absorbers will be used by MICE as both are low-Z materials; therefore maximising cooling.

2.5 Multiple Scattering & Energy Loss

Multiple Coulomb Scattering (MCS) and energy loss are the two fundamental physics processes involved in characterising ionisation cooling. They are traditionally treated separately, the former being the result of nuclear scatters and the latter a result of collisions with electrons. However, there are small correlations induced through inelastic, hard scattering off electrons which result in large angular deflections and large energy transfers [139]. Equation 2.73 gave the PDG approximation for MCS used in the original cooling equation, it includes only muon-nuclear scatters. There is a disagreement between the cooling equation and previous experimental results; this section explores the various attempts to find a better parametrisation of scattering and energy loss in low-Z materials.

2.5.1 The Physical Process

When a muon passes through the absorber material it will interact with the material's constituent atoms, scattering off the atomic potential of the atom and losing energy, a representation of this is exhibited in Figure 2.3.

Equation 2.73 originates from work by Rossi and Greisen [140] which gives the change in mean square scattering angle per unit of material thickness, $\frac{d\langle\theta^2\rangle}{dz}$, as:

$$\frac{d\sigma^2_{x'}}{dz} = \frac{d\langle\theta^2\rangle}{dz} = 8\pi N_A \frac{Z^2}{A} r_e^2 \Big(\frac{m_e c}{p\beta_{rel}}\Big)^2 ln\Big[196 Z^{-1/3}\Big(\frac{Z}{A}\Big)^{1/6}\Big] \tag{2.76}$$

and is derived from the Rutherford's original cross-section [141] through consideration of the probability of a charged particle being scattered by a small angles. In this approximation only interactions with the atomic nucleus are included. The distribution is proportional to Z^2, with the log_n term often ignored, and the scattering potential of the nucleus is represented as a point charge Ze. Both screening by atomic electrons and inelastic scattering from electrons are neglected in this parameterisation. Section 2.5.2 will discuss attempts to incorporate these and involves replacing Z^2 with $Z(Z+1)$, assuming equal contributions from nuclear and electron scattering. As a result, the probability of nuclear scatter scales as Z^2 whereas that off an electron scales as Z.

Consequently, scatters off electrons become more important for the lightest absorber materials such as hydrogen, where Z= 1, and the nuclear and electron potentials have equal magnitude. Energy loss is inversely proportional to mass of the target nucleus so nuclear scatters account for only a small quantity of energy loss and electron scatters dominate. Collisions with electrons can be "soft" which result in atomic energy level excitation or "hard" meaning the electron is ejected from the atom. In the latter case the material is "ionised." Muon energy losses in MICE are predominantly via ionisation as Bremsstrahlung and e^+e^- pair production are negligible at $\mathcal{O}(p_z \approx 200 MeV/c)$ [9].

The kinematics of the interaction are considered in Figure 2.3. A muon, of energy E, mass m_μ and momentum $\vec{p}$, collides with a constituent atomic electron of mass m_e, in the rest frame of the electron.

The muon scatters elastically from the electron at an angle θ, transferring kinetic energy v. The muon has remaining energy $E - v$ and new momentum $\vec{q}$. Exploiting conservation laws along with the expression $E^2 = m^2 + \vec{p}^2$, it can be shown that

$$(m_e + v)^2 - (\vec{p} - \vec{q})^2 = m_e^2, \tag{2.77}$$

and

$$(E - v)^2 - (\vec{q}^2) = m_\mu^2. \tag{2.78}$$

.

The scattering angle θ can be found from the scalar product ($\vec{p}.\vec{q} = |\vec{p}||\vec{q}|cos\theta$) of the two outgoing momentum vectors such that

$$cos(\theta) = \frac{p^2 - (E + m_e)v}{|\vec{p}||\vec{q}|}. \tag{2.79}$$

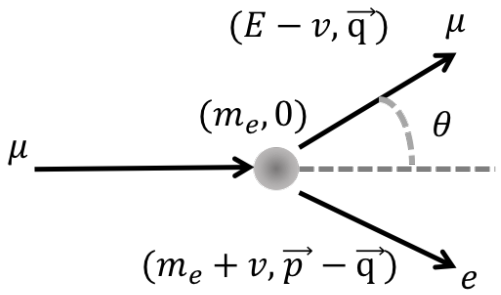

Figure 2.3: Representation of the kinematics of the process of a single scatter off an electron. A muon of energy E and momentum $\vec{p}$ collides with a stationary electron of mass m_e within an absorber atom. The muon is then deflected by an angle θ from its original trajectory and leaves with momentum equivalent to $\vec{q}$. An electron of momentum equivalent to $\vec{p} - \vec{q}$ could also be scattered out of the atoms shell.

When the energy transferred to the atom is equal to the binding energy of a constituent electron to its atomic shell then the electron can be considered free. The kinematic process of a muon scattering off a nucleus is analogous to that illustrated in Figure 2.3, however, elastic collisions from nuclei cause very little energy loss, they simply result in scattering of the muon. Scatters from electrons becomes unimportant as Z increases, as the nuclear charge rapidly dwarfs the scattering potential of the orbiting electrons.

2.5.2 Modelling of Multiple Scattering

There have been many theories regarding the multiple scattering of charged particles by atoms, most notably that of Moliere [142] [143]. Others include: Snyder and Scott [144] [145], Goudsmit and Saunderson [146], and Lewis [147]. All are mathematically closely related, and give exact results if carefully evaluated [9]. More

recent theories, specifically for low Z material such as hydrogen predict lower rates at larger angles. These include that of A. Tollestrup and J. Monroe [148] and W. Allison's ELMS program [149].

The most generalised theory, Moliere theory, states that the distribution of scattering angles is roughly Gaussian for small angles but for larger angles will behave like Rutherford scattering, having larger tails. Highland [150] used Moliere's theory to evaluate Equation 2.76 for different Z targets, with thickness $\Delta z = 0.1X_0$. The projected angular distribution based on the work of Highland, and quoted in the PDG documentation [9], is

$$\theta_0 = \theta_{plane}^{RMS} = \frac{1}{\sqrt{2}}\theta_{space}^{RMS} = \frac{13.6MeV}{\beta_{rel}cp}\sqrt{\frac{\Delta z}{X_0}}[1 + 0.038ln(\frac{\Delta z}{X_0})], \tag{2.80}$$

where θ_{space} is defined as the difference in angle of a particle entering and exiting the material and θ_{plane} is the projection of this onto the plane. θ_0 is defined as the RMS of the angle between the directions projected on a plane of a particle before and after traversing the material, p is momentum in MeV/c. $\frac{\Delta z}{X0}$ is the thickness of the material in radiation lengths. Equation 2.80 is accurate to 11 % or better for $10^{-3} < \frac{\Delta z}{X_0} < 100$. Lynch and Dahl [151] have extended this phenomenological approach by fitting Gaussian distributions to a variable fraction of the Moliere distribution for arbitrary scatterers, and achieve accuracies of 2 % or better. Equation 2.73 uses this expression, minus Highland's log term, and contains no explicit dependence on Z.

Several attempts have been made to account for both electron scatters and the nuclear screening which results from the orbital electrons. Figure 2.4 shows the mean square scattering angle per radiation length predicted by a number of models. With the exception of the closely related PDG and Rossi models all exhibit a clear Z dependence. The Rutherford [141] and Wentzel [152] models have been split into their nuclei, electron and total atomic scattering contributions. It is evident that electron scattering contribution is largest at low Z and minimal at higher Z. The full Wentzel approximation, which accounts for nuclear screening, results in angle predictions approximately 6% lower than the total Rutherford (atomic) prediction for all Z. This is to be expected given the screening reduces the scattering potential seen by the incident particle. The Rutherford and Wentzel formulae both predict less scattering at low Z; this is most significant for hydrogen. The Lynch and Dahl prediction is less than the cooling formula value.

Figure 2.5 shows the predicted θ^{RMS} for a number of simulations and models, including two versions of GEANT4 [153], a generic toolkit developed by the high energy physics community for tracking particles in electric and magnetic fields, and three versions of the muon cooling simulation software, ICOOL [154]. Here GEANT4.9.5 uses a combination of Wentzel's model and the Urban Model [155], based on Lewis Theory, in which scattering at small and large angles are parameterised separately. GEANT4.9.2 uses only the Wentzel model. The material thickness used in these simulations were chosen such that they gave the same PDG θ_{RMS} prediction as for the MICE standard 63 mm LiH absorber. It is evident that there are large variations in the predicted scattering angles. More accurate, data driven modelling of scattering within low-Z materials is necessary for MICE to perform an accurate measurement of ionisation cooling.

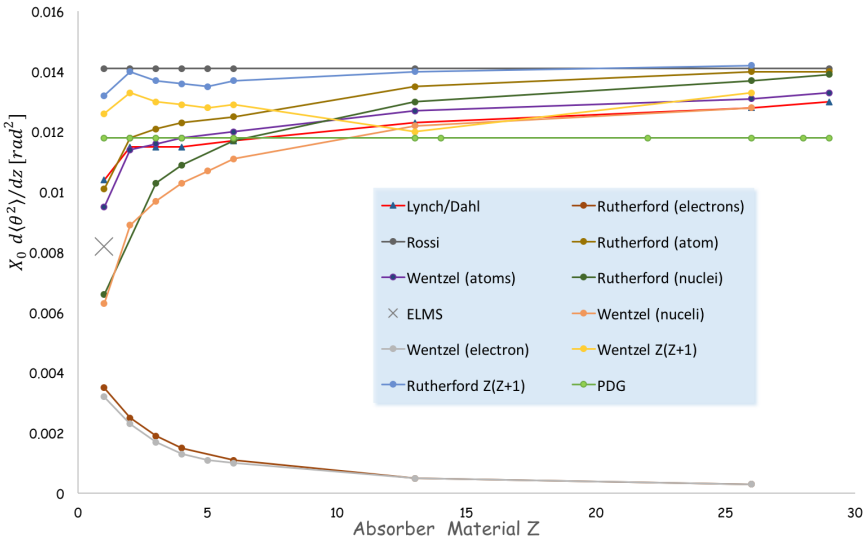

Figure 2.4: Comparisons of mean square scattering angles per X_0 predictions from a number of multiple scattering models for muons of $p_z = 207MeV/c$ traversing various materials of varying atomic number. There is a clear Z dependence for most models. The ELMS prediction was obtained from [139].

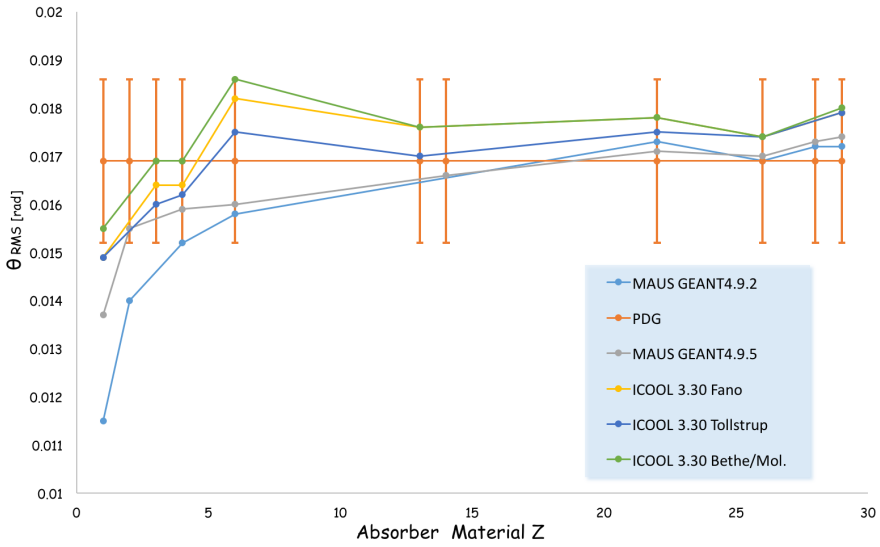

Figure 2.5: Simulations from early versions of MAUS (the MICE analysis and simulation software) are presented utilising two versions of GEANT4 [153] along with simulations using the ICOOL simulation tool [154]. Three models are selected within ICOOL: Bethe [156], Tollestrup [148] and Fano [157]. The absorber thicknesses were scaled to give the same $\Delta z/X_0$ as for 63 mm of LiH. This plot was produced in 2013 to aid the case for an upgrade in MAUS from GEANT4.9.2 to GEANT4.9.5. 10000 muons in an on-axis beam of $p_z = 207MeV/c$ and a step-size of 1 mm were used throughout. The error bars represent the described 11 % error on the PDG equation. The RMS is calculated for central 99 % to improve statistical stability by removing outliers.

2.5.3 Measuring Multiple Scattering: MuScat & MICE

The MuScat experiment [158] [159], based at TRIUMF, took place in the early 2000s with the intention to measure multiple scattering of minimum ionising muons ($\approx 200MeV$) in numerous materials. Figures 2.6a and 2.6b present data from MuScat for both a Liquid Hydrogen and Lithium target respectively, along with various simulations which attempt to model the data. These simulations include two versions of GEANT4, ICOOL and ELMS, based on Allison's work on scattering in liquid hydrogen. Two variations of Moliere's

theory are also presented, one which parametrises the scattering as a function of Z^2 and an alternative approach using $Z(Z+1)$ instead. The Z^2 version excludes scattering from constituent electrons. The $Z(Z+1)$ model rectifies this using Rossi's formulation [140]. While GEANT4 version 9.5 and 9.6 generate similar scattering probabilities at smaller θ values, it is evident neither version nor ICOOL agree well with data for larger scattering angles. This is most apparent for hydrogen.

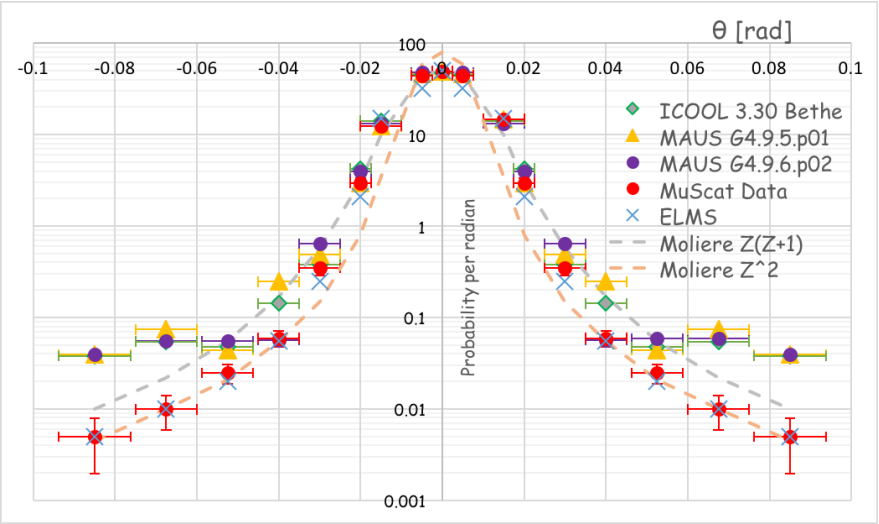

(a)

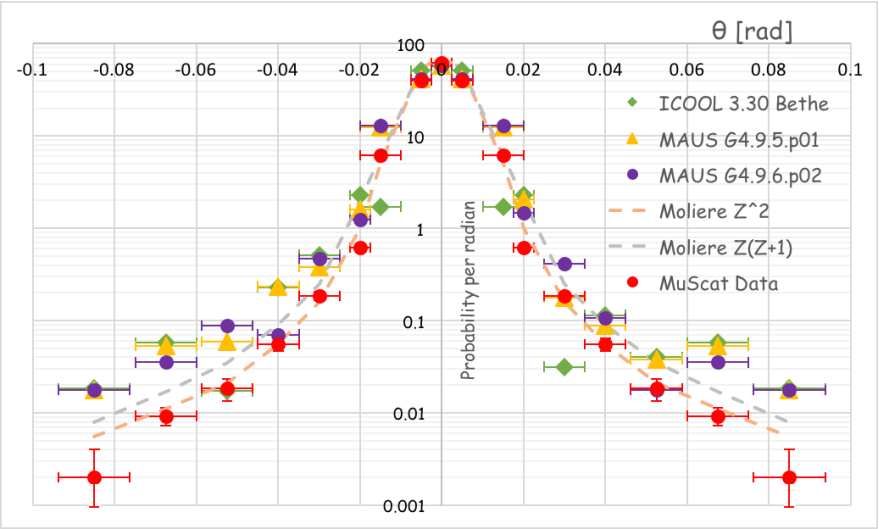

(b)

Figure 2.6: Probability per radian distribution for the MuScat [159] experiment data for (a) liquid hydrogen absorber of thickness 109 mm and (b) lithium absorber of thickness 12.78 mm presented along with numerous simulations which use an on axis beam of 10000 muons with $p_z = 172 MeV/c$ and step size = 1 mm. Two versions of Moliere's theory are also compared: $Z(Z+1)$ and Z^2 ICOOL and MAUS simulations. MAUS currently uses GEANT4.9.6. During the commissioning of MICE a large effort is necessary to gain understanding of the tails of this distribution. This plot was produced in 2013, prior to multiple scattering data taking in MICE.

The MuScat data is only available in a rigid, ready-binned format. The simulations are chosen to have the same number of bins, N, over the same angular range. Both the simulation, s, and data, d, are assigned probability density functions, $p(s)$ and $p(d)$ respectively. For a given sample size, $N_{s,d}$, the number of scatters expected in a given angular bin is $S_i = N_s \times p(s_i)$ and $D_i = N_d \times p(d_i)$. The hypothesis of homogeneity

is that the two histograms represent random values with identical distributions. A χ^2 test statistic can be defined to quantify this. "Weights" are defined: $W_{d,s} = \sum_j^N D_j$ (or S_j) which denote the total projected number of scatter events in each sample. The χ^2 test statistic is then:

$$\chi^2 = \frac{1}{W_s W_d} \sum_{i=1}^{N} \Big(\frac{(W_d S_i - W_s D_i)^2}{(S_i + D_i)} \Big). \tag{2.81}$$

This allows deviations between any model and the data to be quantified. Table 2.1 shows the derived χ^2/ndf values for the two GEANT4 versions and ICOOL. None of the three simulations identify well with the data and the P-Values for all are $<< 1$. It is clear that improved modelling is required to fully comprehend multiple scattering in low Z materials.

Model	χ^2/ndf LH_2	LiH
GEANT4.9.5.p01	18.53	17.88
GEANT4.9.6.p02	28.21	17.94
ICOOL 3.30 Bethe	36.7	40.67

Table 2.1: Table summarising the total χ^2/ndf for GEANT4.9.5, GEANT4.9.6 and ICOOL 3.30 which uses Bethe's parameterisation in this configuration. These are taken relative to the MuScat data presented in [159]. The χ^2/ndf were calculated according to Equation 2.81. All values are relatively large, showing the necessity for further study and re-modelling of multiple scattering in the MICE absorbers. The P-Values associated with these values are $<< 1$.

Prior to making any conclusive cooling measurements MICE must put extensive effort into gaining a better understanding of multiple scattering. A discussion of attempts to use Monte Carlo simulations of MICE to develop additional models of multiple scattering is presented in [160]. Development of simulations of scattering based on real MICE data will form part of the commissioning/calibration stages of the experiment during 2017.

2.5.4 Energy Loss: The Bethe-Bloch Equation and Energy Straggling

At muon energies of the order used by MICE ($\mathcal{O}(200MeV)$) energy losses via ionisation dominate. The mean rate of ionisation energy loss, $\langle \frac{dE}{dz} \rangle$, of the moderately relativistic muons as they traverse the absorber is described by the Bethe-Bloch formula [9],

$$-\Big\langle \frac{dE}{dz} \Big\rangle = K z^2 \frac{Z}{A} \frac{1}{\beta^2} \left[\frac{1}{2} ln(\frac{2 m_e c^2 \beta_{rel} \gamma_{rel} T_{max}}{I^2}) - \beta_{rel}^2 - \frac{\delta^2(\beta_{rel}\gamma_{rel})}{2}) \right]; \tag{2.82}$$

where m_e is the electron mass, K $= 4\pi N_A r_e^2 m_e c^2$, r_e is the classical electron radius and N_A is the Avogadro's number. Z and A are the atomic and mass numbers of the absorber material and T_{max} is the maximum kinetic energy which can be imparted to a free electron in a single collision. I is defined as the mean excitation energy in eV of the atoms in the material and $\delta(\beta_{rel}\gamma_{rel})$ is the density effect correction. According to the Particle Data Group (PDG), [9], the Bethe-Bloch equation is accurate within a few % for

particles in the range $1 < \beta_{rel}\gamma_{rel} < 1000$; in MICE $\beta_{rel}\gamma_{rel} \approx 1$. Figure 2.7 shows the mean energy loss rate in liquid hydrogen (as well as gaseous helium, carbon, aluminium, iron, tin, and lead) [9]. Lithium hydride is not presented in this plot and the amount of energy loss within lithium hydride absorber is dependent on the isotope composition of the lithium used. Energy loss distributions using both the PDG formula (Equation 2.70) and GEANT4 simulations for both ^{6}LiH and ^{7}LiH are presented in [161] for a range of muon momenta.

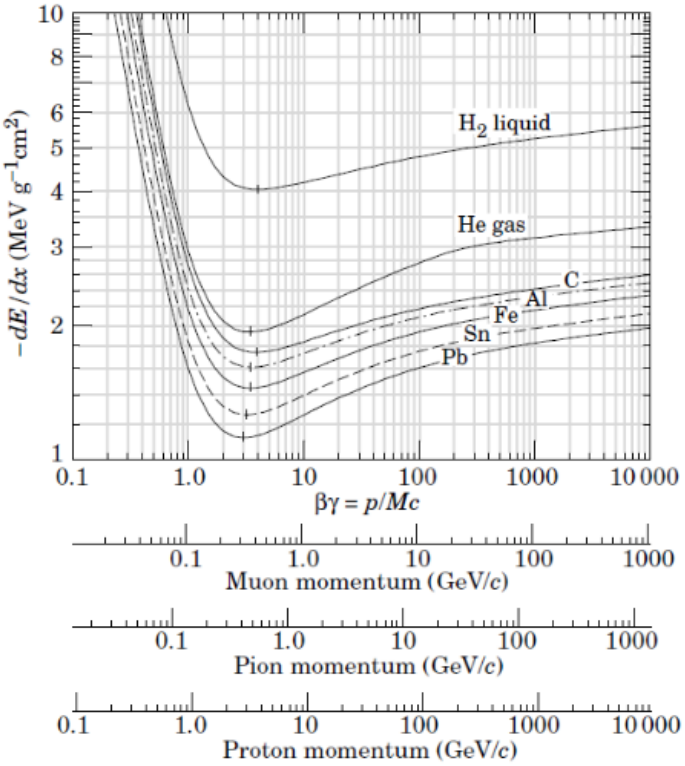

Figure 2.7: Mean energy loss rate in liquid hydrogen, gaseous helium, carbon, aluminium, iron, tin, and lead. Radiative effects, relevant for muons and pions, are not included. These become significant for muons in iron for $\beta_{rel}\gamma_{rel} > 1000$ [9]. Additional distributions for LiH produced in varying relative compositions of ^{6}LiH and ^{7}LiH are presented in [161].

Significant fluctuations (straggling) of the energy loss occur for each step through the material. For a material of moderate thickness (z) the energy loss probability distribution of these fluctuations is described by the Landau-Vavilov distribution [162] [163]. The Landau-Vavilov function uses a Rutherford cross section without atomic binding corrections but with a kinetic energy transfer limit of T_{max}. The most probable energy loss is given by

$$\Delta_p = \zeta\left[ln(\frac{2mc^2\beta_{rel}^2\gamma_{rel}^2}{I}) + ln\frac{\zeta}{I} + j - \beta_{rel}^2 - \delta(\beta_{rel}\gamma_{rel})\right]; \tag{2.83}$$

where $\zeta = (K/2)\langle Z/A\rangle(z/\beta_{rel}^2)MeV$ and $j = 0.2$. The fluctuations in energy loss are determined by the ratio (κ) of the characteristic energy (ζ) and the maximum kinetic energy of the muon: $\kappa = \frac{\zeta}{T_{max}}$.

Figure 2.8 shows the predicted mean energy loss in a range of materials for 4 simulation models. Two versions of GEANT4 are compared to the Bethe prediction and an adjusted ICOOL simulation which incorporates straggling. The most recent version of GEANT4 deviates by $\approx 1-4\%$ from the Bethe predictions in

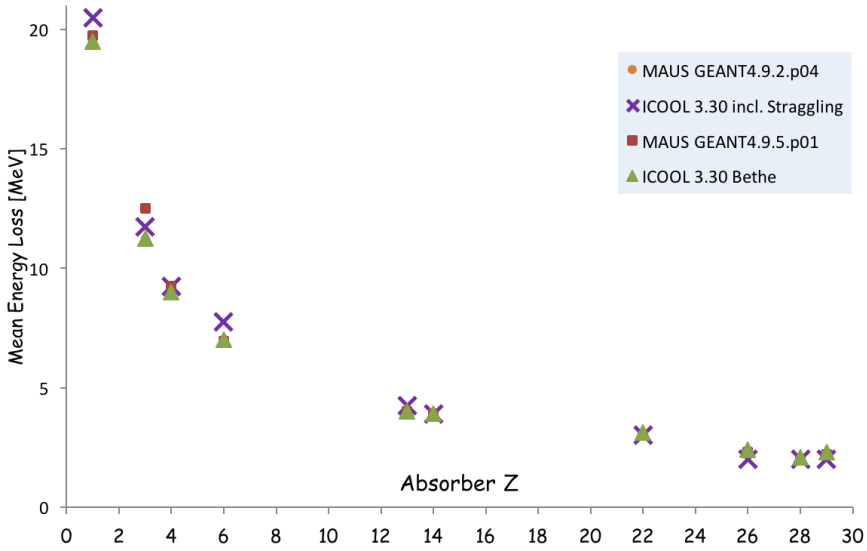

Figure 2.8: Mean energy loss, ΔE, as predicted by simulation software ICOOL v3.30, modelled on the Bethe equation both with and without straggling considerations and GEANT4. The simulations are based on an an on-axis pencil beam of 10000 muons with $p_z = 207 MeV/c$ and step size 1 mm. The thickness of the absorber materials is chosen so $\Delta z/X_0 = 6.49\%$, the expected rate it will be in the MICE LiH absorber.

most materials, with larger deviations of $\approx 7\%$ in Li. The characterisation of energy loss within MICE will form part of the Step IV physics program.

2.5.5 Correlations between Scattering and Energy Loss

Collisions with constituent electrons give rise to correlated energy loss and scattering transfers. The relative contribution of electrons to energy loss and scattering cross-sections for muons traversing liquid hydrogen is studied in detail in [139]. It is concluded that hard electron scatters result in a large energy loss combined with significant scattering. Thus, correlations in the energy loss and scattering exist even in very thin materials. Additionally, in a thick absorber, a muon that loses greater than average energy near the entrance to a material necessarily has a larger cross section for increased scattering, and a highly scattered muon will traverse a longer path length and may lose more energy. Hence second order correlations result. It is from this conclusion that ELMS was developed which generates, by Monte Carlo, a database of energy-loss and momentum transfer pairs in thin absorbers for a range of incident momenta. This method uses double differential cross sections and splits muon collisions into Coulomb collisions with nuclei and electrons and collisions with the atom as a whole. ELMS then samples from these distributions to track particles through an absorber of a given thickness. Figure 2.4 also displays the ELMS prediction which is $\approx 20\%$ below those of the Rutherford and Wentzel atomic expressions. The Lynch and Dahl prediction was significantly larger than the ELMS value. In Figure 2.6a it is evident that ELMS has a much closer agreement with MuScat data than any other model. So far ELMS has only been built for Hydrogen so no comparisons for LiH are available.

Such correlations suggest that muons that scatter more than the average muon will have also lost more

energy and will find themselves towards the back of the bunch. As a result in MICE highly scattered muons will receive more re-acceleration in the RF fields, negating the effect of the high scattering. In other words, the first order correlations could make it easier to cool muons. Further study of both processes is necessary in order to support this. During 2017/18 MICE will measure scattering distributions, simultaneously with cooling (using helical tracks) and with no magnetic fields (using straight tracks).

2.6 Summary

Ionisation cooling is necessary if a future Neutrino Factory or Muon Collider is to reach its design goals. Ionisation cooling describes a reduction in normalised transverse emittance of a particle beam as it passes through a material. In order to efficiently cool a muon beam the experiment will have to overcome heating effects from multiple scattering and stochastic fluctuations in energy loss. The Muon Ionisation Cooling Experiment aims to make the first measurements of sustainable ionisation cooling of a muon beam. Using a low z material such as liquid hydrogen is the best way to do this; however, better understanding and mathematical modelling of both processes is required and will form part of the pre-cooling demonstration phase of the MICE experiment known as “Step IV” .

Chapter 3

The MICE Experiment

The International Muon Ionisation Cooling Experiment (MICE) [68] is a proof of principle machine located at the Rutherford Appleton Laboratory in Oxfordshire, UK, aiming to ascertain the first measurement of ionisation cooling. The pursuit to prove the feasibility of ionisation cooling, defined in Chapter 2, is galvanised by its importance to the successful construction of both a Muon Collider or Neutrino Factory, two of the goals of the particle physics community, outlined in Chapter 1. This Chapter details the design goals of MICE and gives a comprehensive overview of the hardware and software employed by the experiment to attain them.

3.1 MICE Design Goals

The fundamental goals of the Muon Ionisation Cooling Experiment are:

1. To demonstrate the underlying physics processes that contribute to ionisation cooling.
2. To gain an understanding of the practicality of cooling by investigating various modes of operation, incoming beam emittance and beam conditions.
3. To construct and operate a section of a cooling channel long enough to allow for a measurable transverse emittance reduction of 10%.

These will be accomplished by:

1. Exploiting a combination of particle identification techniques and detectors incorporating: 3 time-of-flight detectors [164], 2 scintillating fibre trackers [165], and a downstream calorimetry system consisting of a KLOE [166] light detector and an Electron Muon Ranger [167] to achieve an accuracy of 0.1% on the emittance measurement or better. This corresponds to a 1 % resolution on 10 % emittance reduction.
2. Using a low-Z material, such as liquid hydrogen or lithium hydride, to implement the desired cooling while limiting heating effects due to multiple scattering as outlined in Chapter 2.

3. Utilising RF cavities [168] to re-accelerate the "cooled" muons in the longitudinal direction. This allows the demonstration of sustainable 4D ionisation cooling.

4. Performing the cooling for muon momenta in the range of 140 - 240 MeV/c.

5. Minimising the pion, proton and electron contamination by use of several upstream and downstream particle identification detectors, allowing a very high muon purity to be attained.

3.2 The Beam line

The MICE muon beam line is optimised to allow the production and transportation of muons of momenta ranging from 140 MeV to 240 MeV and with variable emittance, ϵ_n, between $3 - 10 \cdot \pi \cdot$ mm $\cdot$ rad while ensuring a low pion contamination in the MICE cooling channel.

The MICE muon beam is produced by immersing a titanium target in the ISIS 800 MeV proton beam halo. Figure 3.1 shows the MICE beam line relative to the ISIS synchrotron. The subsequent charged pions decay to muons. Positively or negatively charged muons can be selected through choosing an appropriate dipole polarity.

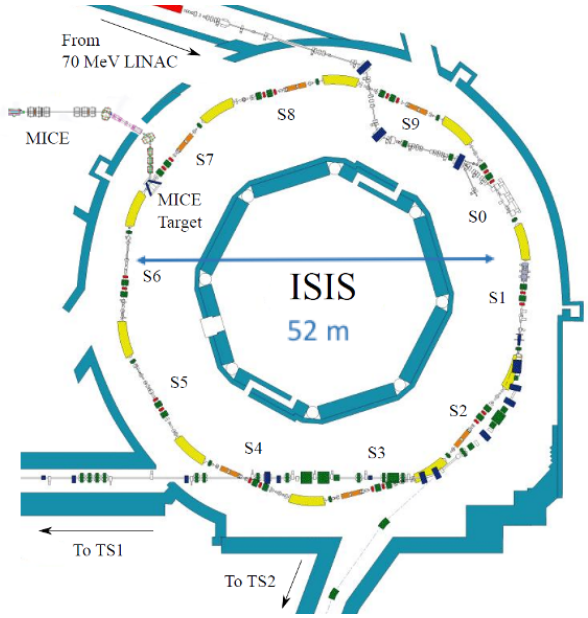

Figure 3.1: The ISIS synchrotron, situated at RAL. MICE dips a titanium target into the 800 MeV proton beam. The resulting pions are then directed into the MICE beam line which is exhibited in Figure 3.2 [138]. ISIS is 52 m in diameter.

A succession of quadrupole triplets, labelled on Figure 3.2 as Q1, Q2 and Q3, are positioned close to the production point in order to capture the pions and direct them towards a dipole magnet, identified as D1 on Figure 3.2. D1 performs the first momentum selection and veers the particle beam through the ISIS wall.

The superconducting decay solenoid, labelled as DS on Figure 3.2, with a maximum field of 5T, length of 5m and bore diameter of 12 cm, is enclosed within the radiation-interlocked Decay Solenoid Area, denoted as DSA on Figure 3.2. It is inside the DS that most of the pions decay to muons. The 5T field induces helical

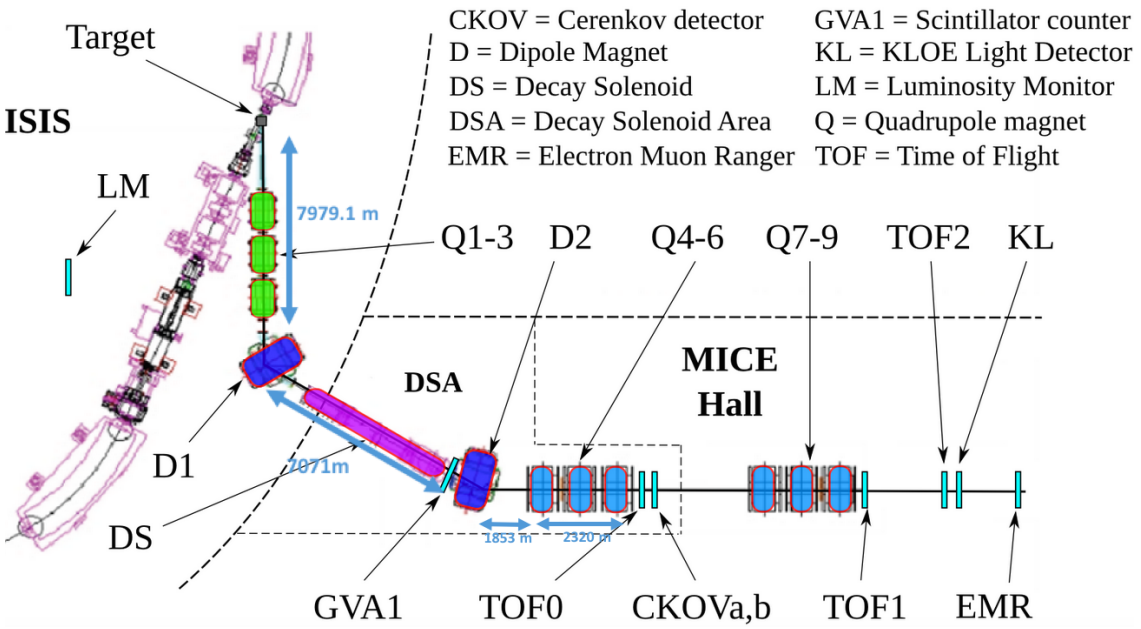

Figure 3.2: Labelled representation of the MICE beam line. Titanium target is immersed into the 800 MeV ISIS proton beam. Resulting pions travel through 3 quadrupoles (Q1-3) and a dipole (D1) before passing through the decay solenoid (DS), a further dipole (D2) and three additional quadrupoles (Q4-6) then deliver the beam to the cooling channel. Supplementary acceleration is subsequently carried out by a final triplet, labelled Q7-9. The MICE cooling channel is in the "Step 1" configuration here [138].

Magnet	Distance from Target [mm]	Max Field [T] / Gradient [T/m]	Radius [mm]
Q1	3000	1.6	101.5
Q2	4400	1.6	101.5
Q3	5800	1.6	101.5
D1	7979.1	1.6	-
DS	12210.7	5.7	57.5
D2	15808.1	0.85	-
Q4	17661.6	2.3	176
Q5	18821.6	2.3	176
Q6	19981.6	2.3	176

Table 3.1: Table summarising the distance of each beam line magnet (along beam line) from the MICE target [169]. Only magnets outside the hall are listed.

trajectories, increasing the path length of the particles in the beam.

A second dipole (D2) bends the particle trajectory further and permits momentum selection in addition to assisting in reducing proton and pion contamination at the downstream end of the beam line. D2 is followed by a second and third quadruple triplet (Q 4,5,6) and (Q 7,8,9) which allow the muon beam to be transported into the MICE cooling channel.

3.2.1 Beam Composition

MICE aims to demonstrate ionisation cooling for several muon beams at various momenta and the dipole magnets (D1 and D2) act to select the momentum distribution of the incoming beam. The first dipole selects pions with a range of momenta proportional to the magnet current. From knowledge of the kinematics of pion decay the decay muons must have momenta in the range: $p_{\mu,min} < p_{\mu} < p_{\mu,max}$. Figure 3.3 illustrates how

by selecting the muons momentum at D1 and D2 the incoming muon beam momentum can be chosen. The red line represents the maximum pion momentum that can be selected at D1 and the blue line represents the minimum momentum at D2. If a momentum of $p_{D1} \geq 200$MeV/c is selected at D1 (A) then $p_{D1} \approx p_{\mu,min}$. By setting $p_{D2} \approx p_{D1}/2$ a backwards going muon beam can be selected. The pion contamination is reduced in this configuration [170].

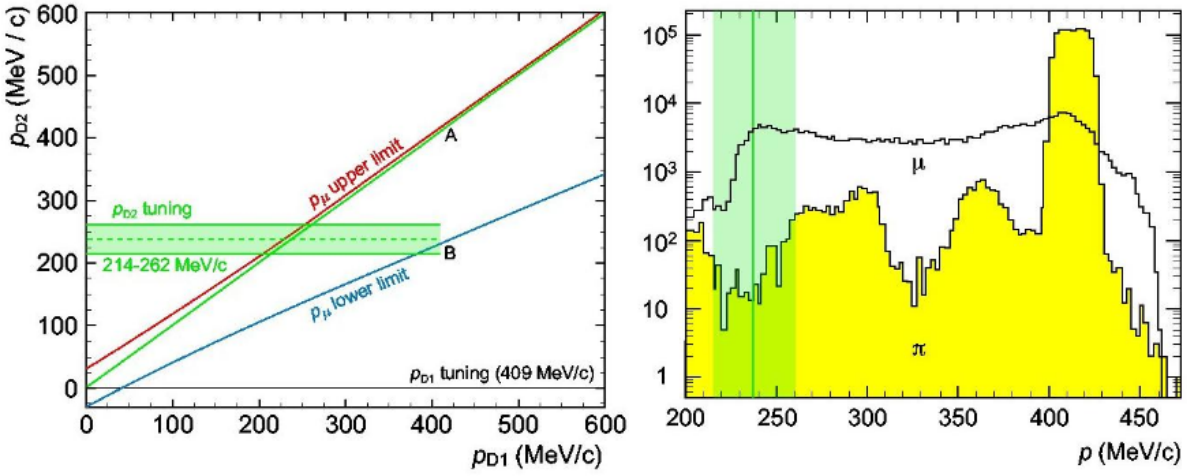

Figure 3.3: (left) Red and blue lines represent the kinematic limits of the spectrum for muons produced in pion decays. D2 can be tuned to produce an almost pion-free beam. (Right) Simulation showing pion and muon spectra at the end of the decay solenoid. Only high momentum pions survive. The green band shows the acceptance of D2, when tuned to the backward-going muon peak [169].

3.3 Cooling Channel Design

3.3.1 Staged Implementation and Timeline

The implementation of the cooling channel in the MICE hall has been executed in a series of stages. The first stage, identified as "Step 1," involved only the particle detectors being present in the cooling channel. This stage was completed in late 2013 and permitted detector and beam line commissioning [169], [171]. Furthermore, "Step 1" allowed measurements of pion contamination [170] to be conducted and the performance of the Electron-Muon Ranger [172], which forms the main part of the downstream calorimeter, to be evaluated.

Presently, and until 2018, the second stage, "Step IV," is underway; a representation of the channel in this configuration is presented in Figure 3.4. In "Step IV" both upstream and downstream scintillator fibre trackers are installed, along with one absorber focusing coil module. No RF cavities are present, and, consequently, "Step IV" acts only as a commissioning stage, where, although ionisation cooling will occur, it will not be sustainable as the longitudinal momentum is not restored.

"Step IV" permits tests of beam propagation in the magnet system and some cooling properties of the absorbers only. The final "Demonstration of Ionisation Cooling" stage [173], in which the channel is in the configuration presented in Figure 3.5, would involve the addition of the RF cavities and would take place

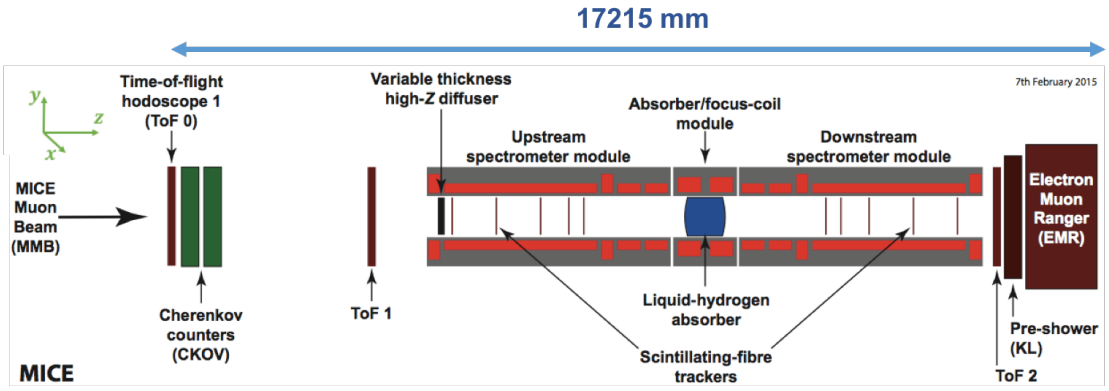

	TOF0 (start)	TOF1	US Start	US End	DS Start	DS End	EMR (End)
Global Position/[mm]	5263	12922	13572	16469	17432	20342	22478

Figure 3.4: Diagram showing the MICE cooling channel in its "Step IV" configuration in which the trackers and 1 Absorber Focus Coil (AFC) are present but no re-acceleration occurs as no RF cavities are in the channel. This stage has taken place from 2015 and continues until 2018. The muon beam will enter the channel from the left, first passing through an initial time-of-flight detector (TOF0), a Cherenkov counter and then a second time-of-flight detector (TOF1). A hit in TOF1 will act as a trigger for the start of a particle "event." A particle's phase space co-ordinates $(x, y, z, p_x, p_y, p_z, t)$ are then measured both upstream and downstream through use of two identical scintillator fibre trackers. Spectrometer solenoids surround each scintillator fibre tracker in order to guide the particle through the channel. Between the two trackers lies the absorber material encased in the Focus Coil Module. MICE may use liquid hydrogen or lithium hydride as part of the "Step IV" stage. A series of particle identification detectors, including a third time-of-flight counter, form the downstream calorimeter [138].

following completion of the "Step IV" program. The addition of the RF cavities and additional absorber material allows for the measurement of sustainable ionisation cooling.

3.3.2 Co-ordinate System

MICE employs cartesian co-ordinates to define the positioning of each detector element and the particle positions within the channel. The MICE cooling channel is designed such that the central axis is the z axis and the x, y co-ordinates describe the transverse plane in which the desired cooling will occur. The MICE co-ordinate system is right-handed, with z parallel to the beam axis, x in the horizontal direction and y in the vertical direction. The origin is defined by the intersection of the beam axis and the mid-plane of D2. The MICE beam line components have been aligned using a laser tracking survey system [174]. Within "Step IV" the upstream of TOF0 is determined as 5263 mm [175], the centre of TOF1 is found to be at a z position of 12922.43 mm [176] and the end of the EMR, at the downstream of the channel, is measured to be at 22446.91 mm [177], all relative to D2.

3.3.3 The Final Channel

Figure 3.5 illustrates the current design for the cooling channel in the final stage of the Muon Ionisation Cooling Experiment; this is the configuration in which the first demonstration of sustainable ionisation cooling could be demonstrated.

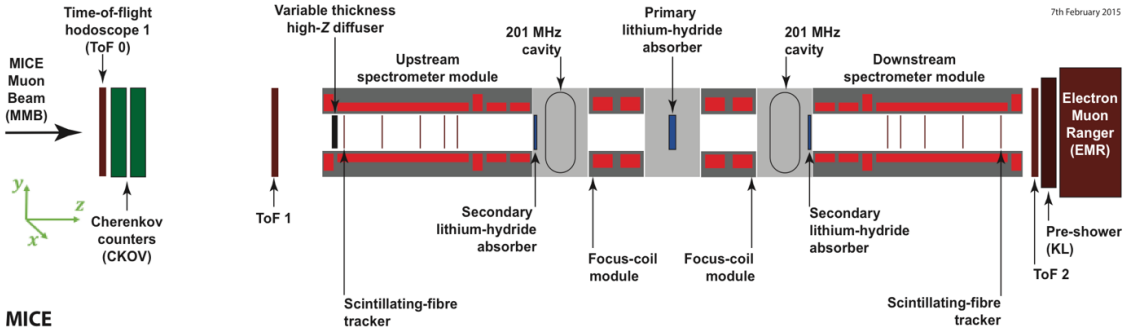

Figure 3.5: Representation of the final design for the MICE cooling channel which aims to conduct the first demonstration of sustainable ionisation cooling. The channel is similar to the "Step IV" configuration, with the addition of two 201 MHz RF cavities. The RF cavities will restore longitudinal momentum. Furthermore, additional secondary absorbers are inserted into the channel. These provide screening between the RF and tracker solenoid. This configuration will permit MICE to attain the sustainable ionisation cooling at the level necessitated by the design goals of MICE as discussed in Section 3.1 [138].

3.4 Cooling Channel Components

3.4.1 The Diffuser

The MICE beam line was designed to produce three different emittance values, nominally: 3,6 and $10 \cdot \pi \cdot$ mm $\cdot$ rad at three different central momenta: 140, 200 and 240 MeV. In order to generate beams of given emittance a diffuser is positioned at the very upstream end of the first spectrometer solenoid; Figure 3.6 shows a schematic of the MICE diffuser [178]. The diffuser consists of a series of 4 irises made of brass and tungsten with varying thicknesses allowing the incoming emittance of the muon beam to be altered.

Each iris possesses a different radiation length; introducing material of larger radiation lengths into the beam increases the amount of Multiple Coulomb Scattering which, by Equation 2.74, results in an increase in the beam emittance.

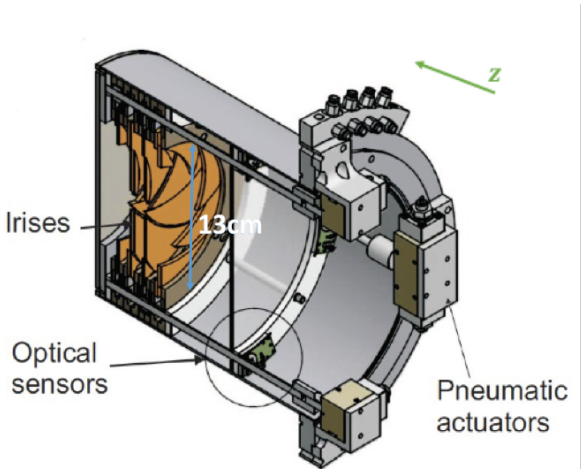

Figure 3.6: Schematic showing the brass and tungsten diffuser placed at the very upstream end of the MICE cooling channel. Each iris has a different radiation length, X_0. Increasing the radiation length by increasing the amount of material through which the muon beam passes will increase the amount of Coulomb scattering and, therefore, the input emittance of the beam. [178].

3.4.2 Absorber Focussing Coil (AFC)

The Absorber Focus Coil (AFC) module comprises of an absorber material housed within a Focus Coil. It is within the AFC that the muons are cooled. Figure 3.7 presents a schematic of the AFC module, designed to hold 21 litres of Liquid Hydrogen (LH_2). During Step IV one AFC is placed in-between the trackers. Throughout the Demonstration of Ionisation Cooling stage, two Focus coils would be placed upstream and downstream of the primary absorber.

The Absorber Material

"Step IV" will test both Liquid Hydrogen and solid Lithium Hydride (LiH) as absorbers. Figure 3.8 shows an image of the Liquid Hydrogen (LH_2) system and Lithium Hydride (LiH) disk. The LH_2 absorber is 35 cm in length, 30 cm in diameter and is contained by two pairs of 250 μm thick Aluminium windows and the MICE LiH disk is 63 mm thick. While LH_2 provides more effective muon cooling due to its lower equilibrium emittance (see Chapter 2), in reality, LiH is a more practical alternative as:

1. There are perceived safety issues associated with the handling and storage of liquid hydrogen;
2. The Liquid Hydrogen absorber tends to be much longer than the focus, so $\beta_\perp$ function is higher; and,
3. The additional windows will introduce additional scattering which degrades performance.

The effort and cost of supporting and maintaining a LH_2 vessel and liquefaction equipment, as well as safety concerns, consequently, mean that LiH will form the primary absorber material within the MICE final stages.

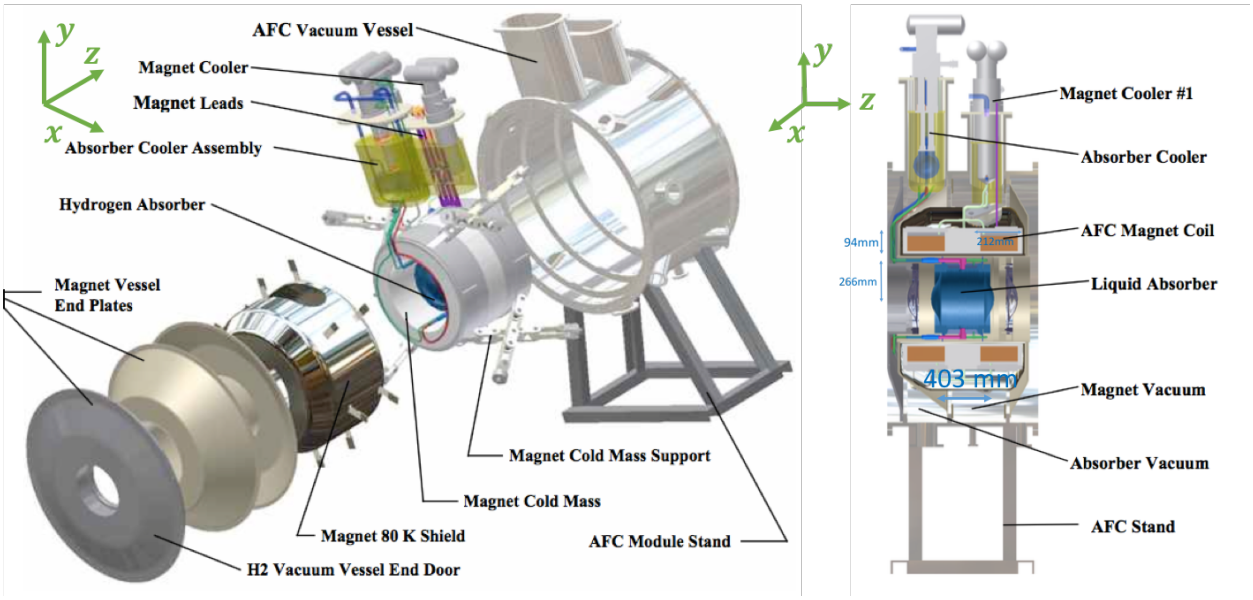

Figure 3.7: (left) A schematic exploded view of the AFC module showing the magnet, the magnet coolers, the absorber, and the absorber cooler. (right) A cross-section view of the MICE AFC module exhibiting the magnet coils, the liquid absorber, the cryostat vacuum vessel and the coolers [179].

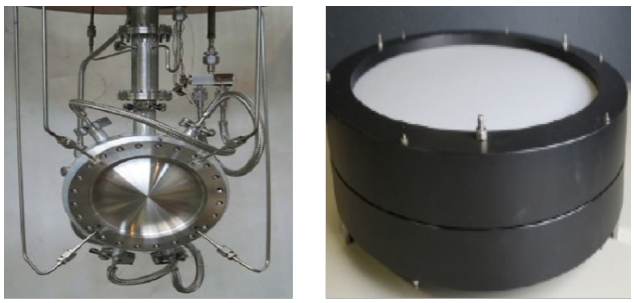

(a) (b)

Figure 3.8: Photographs of two possible MICE absorber materials: (a) 21 Litre Liquid Hydrogen system (b) 63 mm thick Lithium hydride disk [138].

The Focus Coil (FC)

The Focus Coil comprises of two coils bringing the beam to a tight focus by permitting control of the $\beta_\perp$ inside the absorber material. The AFC can be operated in either "flip" or "solenoid" modes. In "solenoid" mode the two coils are powered with the same polarity and in "flip" mode their polarities are in opposing directions. The AFC coils are cooled using cryocoolers. The two coils are a distance 403.78 mm apart, each has a length 212.77 mm, a thickness of 94.16 mm and an inner radius of 266.93 mm. The engineering tolerances of these measurements are considered in [180].

3.4.3 The RF Cavities

The RF cavities [168] are an indispensable part of the final configuration of the MICE cooling channel. If MICE is to ascertain sustainable ionisation cooling the longitudinal momentum of the muons must be restored subsequent to their passage through the absorber material.

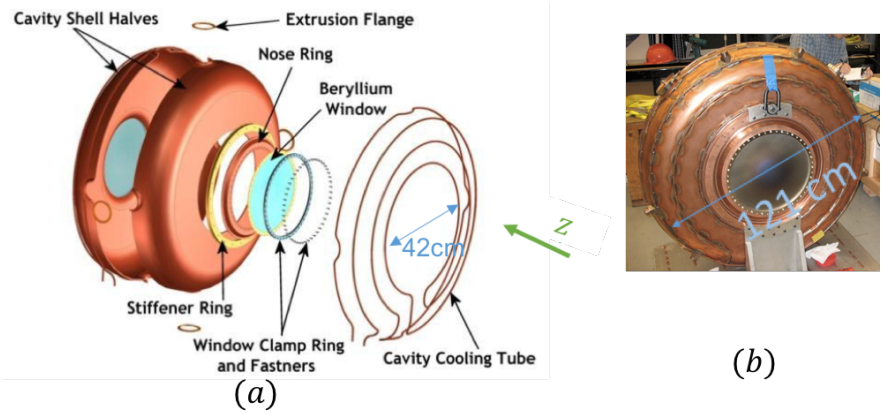

Figure 3.9: RF Cavities are exploited in the final stage of MICE to reaccelerate the muon beam in the longitudinal direction subsequent to its passage though the absorber. (a) A diagram is presented showing various components of the RF cavity including the Beryllium windows. (b) A photograph of the RF as built [138].

Two RF cavities will be in enlisted in the final MICE stage. Figure 3.9 displays a diagram of one of these cavities. Each cavity operates at a frequency of 201 MHz and will be driven by one of two 2 MW amplifier chains. It is anticipated that 10.3 MV/m can be attained over two cavities. The RF cavities have

a round pillbox profile with low peak electric surface field. The RF body consists of two 6 mm thick copper sheet shells welded together with room for four ports around the equator to allow for powering and probing the cavities. The conventional open irises are terminated by curved thin beryllium windows each 42 cm in diameter and 0.38 mm in thickness. Copper stiffener rings are employed around the two windows and they are mounted in the cavity in such a way that the combined slight curvature in the 2 windows acts to minimise cavity frequency shifts.

3.4.4 The Partial Return Yoke (PRY)

The MICE magnets were originally fabricated without a return yoke; however, a partial return yoke (PRY) is crucial to reduce effects of external magnetic fields from 3-4T to < 0.1 mT outside of PRY [181]. The MICE partial return yoke will, in the final configuration, consist of 55t of iron. Figures 3.10 and 3.11 demonstrate how the PRY is constructed around the cooling channel.

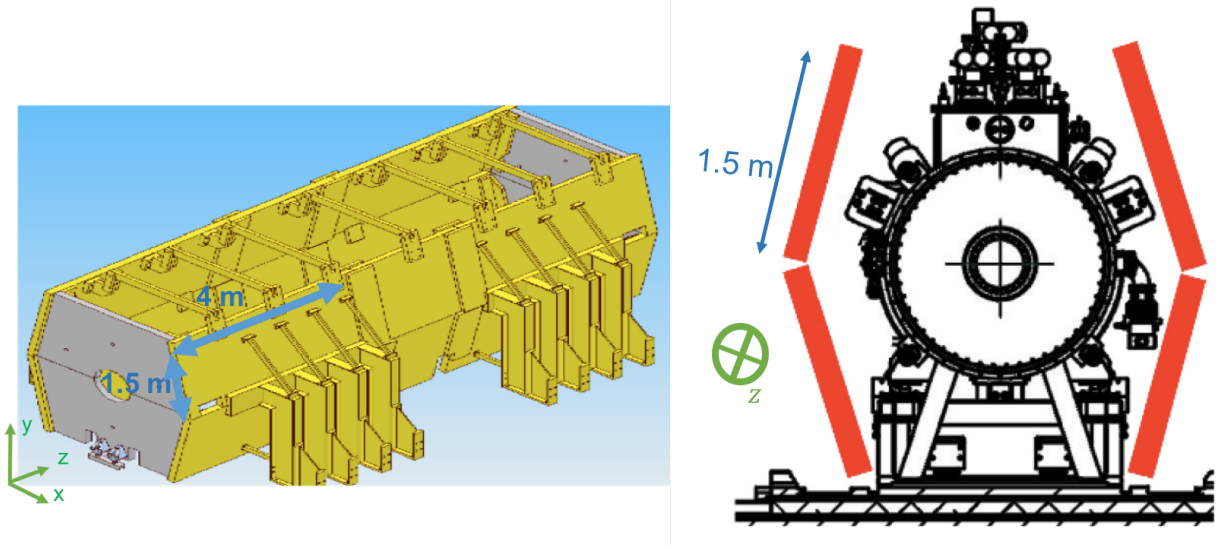

Figure 3.10: (right) An Iron Partial Return Yoke surrounds both the "Step IV" and final step of the MICE experiment. This will act to diminish the external field from 3-4T to < 0.1mT [138]. In practice the MICE PRY consists of eight 1.5m wide and 4 m long iron plates. A nominal thickness of 10 cm is proposed [181]. (left) As shown, the MICE PRY covers an azimuthal angle of about $\pm 60°$ just outside of the cryostats. The remaining parts are left unshielded because of spatial constraints.

3.4.5 The SciFi Trackers

The MICE cooling channel comprises of two identical scintinillator fibre trackers (SciFi trackers) [165], each encased within a 4T spectrometer solenoid. The trackers measure the trace space co-ordinate of every particle in the beam as they traverse the channel. One SciFi tracker is situated just upstream of the absorber and the other just downstream. Cooling will be ascertained through comparison of the beam emittance at the two trackers. Transverse emittance can be measured to an accuracy of $\pm$ 0.06 $\pi\cdot$ mm$\cdot$ rad with the MICE SciFi trackers.

Figure 3.12 exhibits one of the SciFi trackers prior to it being inserted into the spectrometer solenoid.

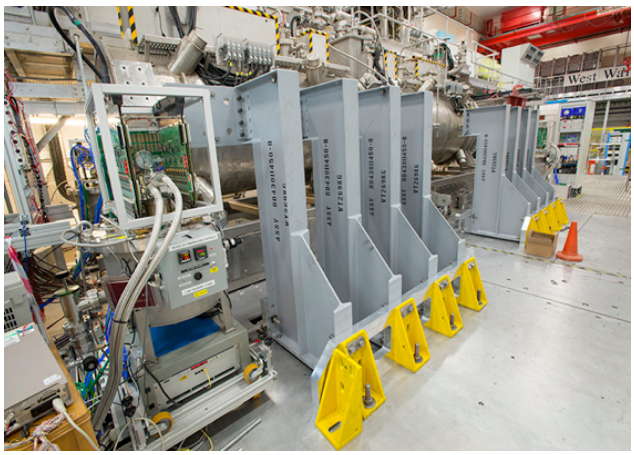

Figure 3.11: Image showing construction of the Step IV partial return yoke around the cooling channel taken during 2014-15 [138].

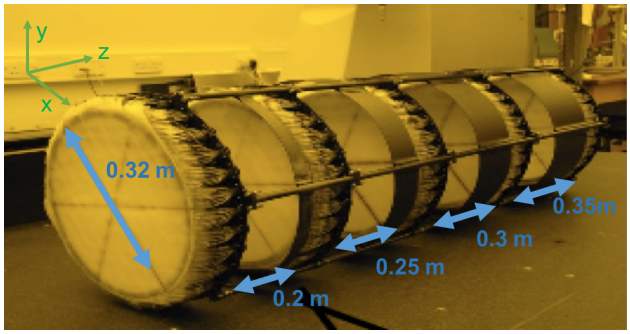

Figure 3.12: A photograph of one of the SciFi trackers before it was placed inside the spectrometer solenoid. Both "Step IV" and the final stage of MICE require two identical scintillator fibre trackers. Each has 5 stations with a diameter of 0.32 m and separated by the values listed in Table 3.2 [138].

The SciFi trackers each comprise of 5 tracker stations of 32 cm in diameter. These stations consist of 3 planes of scintillating fibres constructed using doped polystyrene. The fibres in each plane are placed at an angle of 120° to those in the preceding plane. The spacing between stations is unique in order to account for the turning angles of the particles travelling in the solenoidal field.

As particles pass through the doped polystyrene the fibre emits light; the light produced in the fibres is transported to Visible Light Photon Counters (VLPCs) and is readout. The primary scintillating dopant used in the tracker fibres is polythiophene. The fibres are $350\mu m$ in diameter and are arranged in a doublet layer in each plane. Fibres are grouped into gangs of 7 and individual groups are then readout. A schematic is shown in Figure 3.13 [182].

In order to reconstruct both straight and helical tracks a hit in a single channel will result in a cluster being formed, all adjacent hits are included in the cluster. A Kalman Filter is applied to fitted tracks to account for multiple scattering and energy losses within the tracker materials. The position residuals for the Kalman fit show RMS of the position resolution is 0.31 mm in both transverse position measurements for both trackers [165]. The RMS of the transverse momentum measurements are 1 MeV/c and 1.2 MeV/c in the upstream tracker and downstream trackers respectively for both x and y directions.

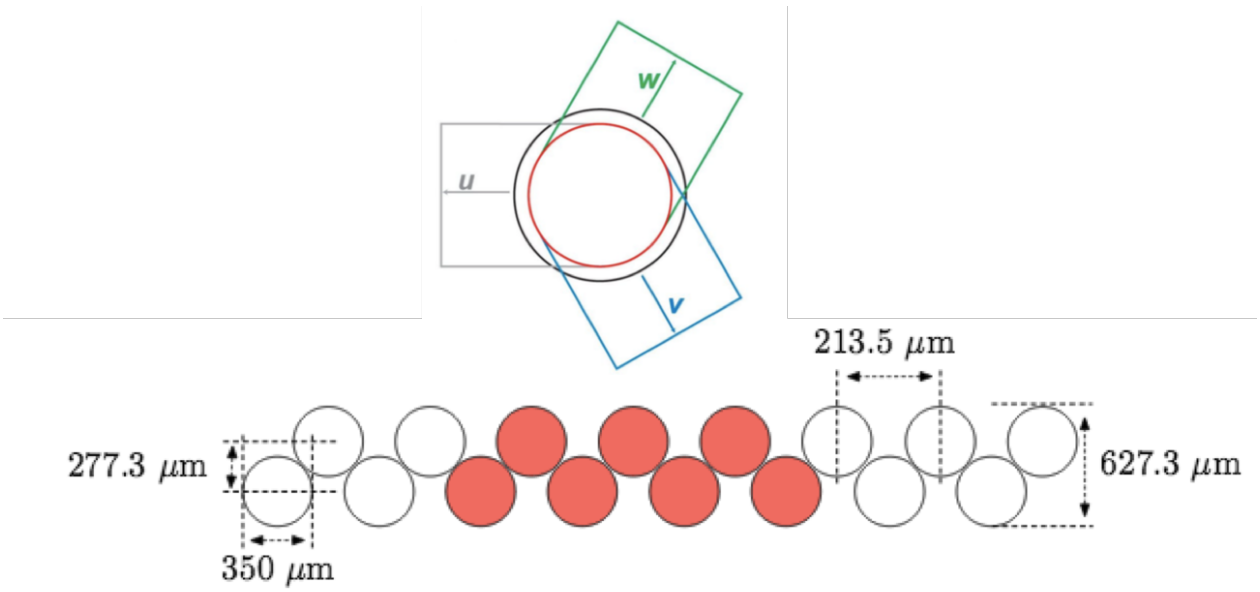

Figure 3.13: Layout of the scintillator fibre trackers. [top]: Beam's eye view of the arrangement of three doublet layers to form a single station. The letters u, v, w denote the three planes. [bottom]: fibre arrangement in each tracker plane. The fibres in red represent a readout channel [182].

Parameter	Value
Number of Stations	5
Diameter of Stations	32 cm
Separation Station 1-2	20 cm
Separation Station 2-3	25 cm
Separation Station 3-4	30 cm
Separation Station 4-5	35 cm
Planes per Station	3
Channels per plane	212-214
Fibre Radius	350 μ m

Table 3.2: Table summarising the tracker specifications [182].

3.5 PID Detectors

3.5.1 Backgrounds in MICE

Particle identification [183] upstream and downstream of the cooling channel is a fundamental to achieving the required precision on the beam emittance measurement. MICE is exposed to several intrinsic background which result in particle contaminants in the channel:

1. Pion Backgrounds - The beam line configuration should produce a relatively pure muon beam. However, due to the similar masses of the charged pions ($m_\pi = 139.57 MeV/c^2$) and muons ($m_\mu = 105.66 MeV/c^2$) some pions may survive the momentum selection in the beam line and enter the cooling channel. Since pions are hadronic and more massive than muons their energy loss and scattering in the absorber and hence their cooling performance differs from muons. Additionally the pions may decay in the channel, meaning the upstream detectors observe a pion and the downstream detectors observe a muon. The muons may be released after cooling and, as a result, would have larger single

particle emittance than the beam line muons. This would affect MICE's cooling performance. The Time-of-Flight (TOF) counters can be utilised to remove pion background.

2. Beam line Electrons and Protons - Pions will predominantly decay to muons with the electronic decay channel heavily suppressed ($R_{\pi\to e} = 1.283\times10^{-4}R_{\pi\to\mu}$ [1]). The transmission rate of these through the channel is small, any remaining particles will be removed by the upstream and downstream calorimeters. When MICE is run in a positive beam mode, protons deflected from the ISIS beam may enter the MICE beam line. A proton absorber is placed upstream of the cooling channel and comprises of borated-polyethylene sheets of varying thickness (15 mm, 29 mm, 49 mm and 54 mm). Protons are stopped, while electrons and muons pass unimpeded. The sheets are combined to the required total thickness depending on the incoming beam momentum placed in the very upstream end of the cooling channel. Any remaining protons can be identified by the Time-of-Flight counters.

3. Dark current - originating from the RF cavities in the final stage of MICE. The RF cavities operate below the Kilpatrick limit but the high electric and magnetic fields may result in electrons being pulled from the cavity surface and accelerated along the cooling channel causing bremsstrahlung. The resulting photons cause a background in the final stages of MICE. This is a source of background in the trackers [184].

4. Electrons resulting from muons decay - Muons have finite lifetimes and can decay throughout the channel. This is an irreducible background, it is the purpose of the the downstream calorimeter (KL and EMR) to aid rejection of this background from the data (Section 3.5.4)

The following section outlines the various upstream and downstream detectors employed by MICE to aid particle identification and background rejection.

3.5.2 Defining Efficiency and Purity

The quality of the muon beam within MICE is quantified in terms of the efficiency of the detectors and selection routines and the muon purity which they can provide within the channel. The efficiency of event type P is the ratio of selected P type events to the total number of P type events in the sample. The purity is the ratio of P type events to all events in the sample.

3.5.3 Upstream Particle Detectors

Upon entering the cooling channel, the muon beam encounters a succession of detectors: 2 Time-Of-Flight detectors alongside a Cherenkov detector. The purpose of this upstream calorimetry system is to help minimise pion and proton contamination in the channel. These detectors produce a 99.9% muon purity in the incoming particle beam.

Time-of-Flight Detectors

MICE employs three Time-of-Flight detectors (TOFs). Two (TOF0 and TOF1) form part of the upstream calorimeter and the third (TOF2) is placed downstream. The detectors are composed of two planes of orthogonally oriented scintillator slabs. Figure 3.14 displays a schematic diagram of TOF1. Within both the TOF0 and TOF1 detectors these slabs are individually wrapped in aluminised mylar to reflect scintillation light originating within the slabs, and black PVC to prevent light being transmitted between adjacent slabs. In addition, each slab has a light-guide and photo-multiplier tube (PMT) at either end. Particles crossing the bar produce scintillation light, which propagates to the PMTs. The time and magnitude of the resultant electron pulse is recorded.

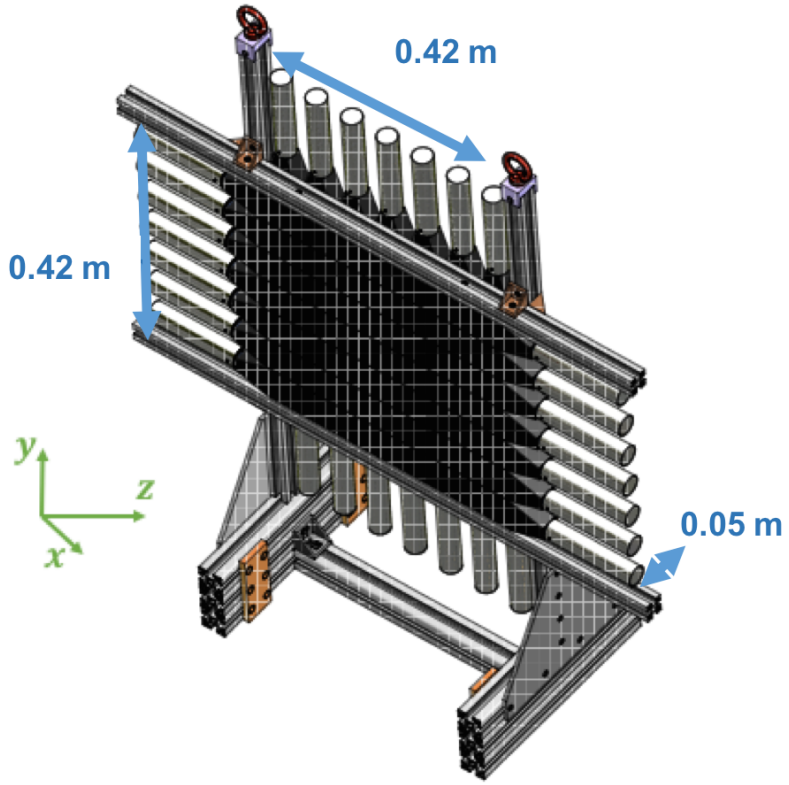

Figure 3.14: Diagram depicting the second of the three time-of-flight detectors present in the final MICE cooling channel, labelled as TOF1. The TOF1 detector is composed of two planes of seven 6 cm × 42 cm × 2.5 cm scintillator slabs and has an active volume of 42 × 42 × 5 cm. Similarly, TOF0 is composed of two planes of ten 4 cm × 40 cm × 2.5 cm scintillator slabs and has an active volume of 40 × 40 × 5cm. Likewise, TOF2, located at the downstream end of the cooling channel, has two planes of ten 6 cm × 60 cm × 2.5 cm. [164].

Figure 3.15 depicts a diagram of a horizontally orientated slab. A charged particle impacts the slab at position x from the bar centre. Light is emitted and travels at speed c_{eff}, assumed constant throughout all bars, to the two PMTs at either end of the bar. The light subsequently arrives at time t_+ at the $x > 0$ PMT and t_- at the $x < 0$ PMT where

$$t_+ = t_x + \frac{l - x}{c_{eff}}, \tag{3.1}$$

and,

$$t_- = t_x + \frac{l+x}{c_{eff}}. \tag{3.2}$$

where c_{eff} is effective speed of light in the material. the The detector measurement of the particles time is taken as an average $t_{x,y} = \frac{t_+ + t_-}{2} - \frac{l}{c_e ff}$. Both the horizontal t_x and vertical t_y are calculated independently for the particle as it traverses the detector as a whole and the time is taken as the average: $\frac{t_x + t_y}{2}$.

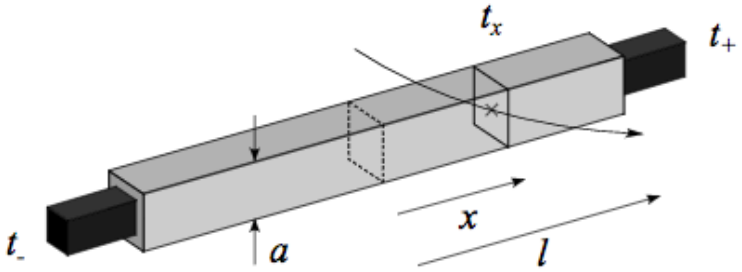

Figure 3.15: Diagram showing a charged particle traversing a horizontally oriented TOF scintillator slab of length $2l$. The particle passes the slab at time t_x at a displacement x from the central "mid-plane." Two PMTs are present at each end of the slab. The light emitted arrives at the $x < 0$ PMT at t_- and in the $x > 0$ PMT at t_+. From these measured times its time-of-flight is established and this may be used for PID purposes [164].

TOF0, TOF1 and TOF2 are found to determine the time at which particles traverse with resolutions of average time resolutions of 52.7 ± 0.9 ps, 59.5 ± 0.7 ps and 52.7 ± 1.1 ps respectively [169]. The slightly worse resolution of TOF1 arises from some of the PMTs used on TOF1 being of slightly poorer quality than those in TOF0 and TOF2. The resolution of the TOF0 station (4 cm wide slabs) and that of the TOF2 (6cm wide) slabs is similar showing the light path length fluctuations are negligible.

Cherenkov Detectors

At higher momenta, muons and pions cannot be easily distinguished by their time of flight. Two aerogel Cherenkov counters, labelled CkovA and CkovB, are placed immediately downstream of TOF0. The two counters have differing thresholds (p^{th}) for light production for both muons and pions. In CkovA: $p_\mu^{th} = 278 MeV/c$ and $p_\pi^{th} = 367 MeV/c$ and in CkovB: $p_\mu^{th} = 210 MeV/c$ and $p_\pi^{th} = 277 MeV/c$. The two counters have densities of 0.225 gcm^{-3} and 0.370 gcm^{-3} and refractive indices of 1.07 and 1.12 respectively [169]. These properties were selected to aid particle identification. For a 140 MeV/c beam neither muons nor pions produce a signal in either counter. At 200 MeV/c muons produce a signal in CkovB but not CkovA but pions produce no signal. At 240 MeV/c muons produce a signal in both while pions produce a signal at only CkovB. The two Cherenkov detectors have been designed to guarantee muon-identification purities better than 99 .7 % in the momentum range 210 MeV/c to 365 MeV/c [169]. At lower momenta, $\pi - \mu$ separation is obtained using the TOF measurement as both Cherenkov detectors cannot detect either.

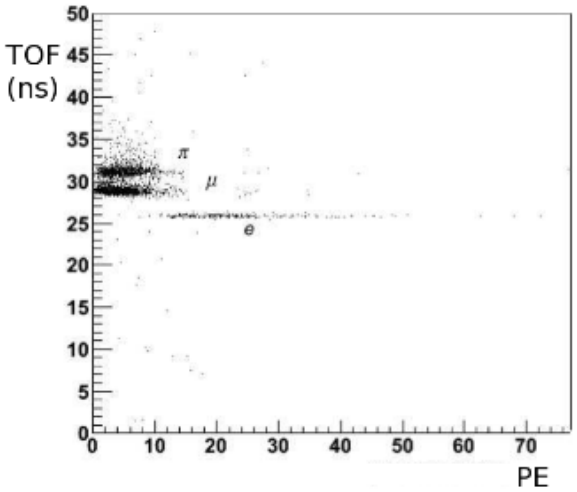

Figure 3.16: The response of the Cerenkov detectors, showing the light yield in photoelectrons (PE) for the Cerenkov detectors and time of flight between TOF detectors. Electrons are seen to be well above threshold while pions and muons are below threshold [169].

3.5.4 Downstream Calorimeter: KL and EMR

Although the upstream calorimetry system provides 99.9% muon purity it is essential to have an additional downstream calorimeter to aid identification of muon decay electrons. The electron backgrounds will occupy the same momentum space as the muons. Figure 3.17(a) shows a historic simulation of momenta distributions in the final cooling channel. In addition, Figure 3.17 (b) shows the simulated single particle emittance distribution for signal (muon) and background (electron) events. The electrons fill a larger phase space volume. This produces a systematic error on the beam emittance measurement. Kinematics cuts can reject about 80 % of electrons, but this is not enough to avoid a lack of accuracy in the beam emittance measurement. Consequently, MICE employs a dedicated downstream calorimeter, comprising of the KL pre-shower and Electron-Muon Ranger (EMR), to separate muons from electrons.

If $\langle \epsilon_\mu \rangle$ denotes the average single particle emittance of the signal (i.e. muon) and $\langle \epsilon_e \rangle$ is that of the background (i.e. electron), the total average single particle emittance is

$$\langle \epsilon_{total} \rangle = \frac{\langle \epsilon_\mu \rangle n_\mu + \langle \epsilon_e \rangle n_e}{n_\mu + n_e}, \tag{3.3}$$

where n_μ and n_e are the numbers of muons and electrons respectively. The relative beam purity, $p = \frac{n_\mu}{n_e + n_\mu}$. The relative systematic error on the measured emittance due to decay electrons is:

$$\delta = \frac{\langle \epsilon_{total} \rangle - \langle \epsilon_\mu \rangle}{\langle \epsilon_\mu \rangle} = (1-p)\frac{\langle \epsilon_e \rangle - \langle \epsilon_\mu \rangle}{\langle \epsilon_\mu \rangle}. \tag{3.4}$$

Assuming an average single particle electron emittance of 50% a minimum purity of 99.8% is required to meet the design goal of $\delta < 0.1\%$ [184]. This corresponds to a signal efficiency requirement of > 99.9 %. The EMR and KL combine to give MICE the purest possible muon beam with high efficiency to limit this error. As the n_e is dependent on muon polarisation (Section 4.2.3), any depolarisation in the cooling channel can

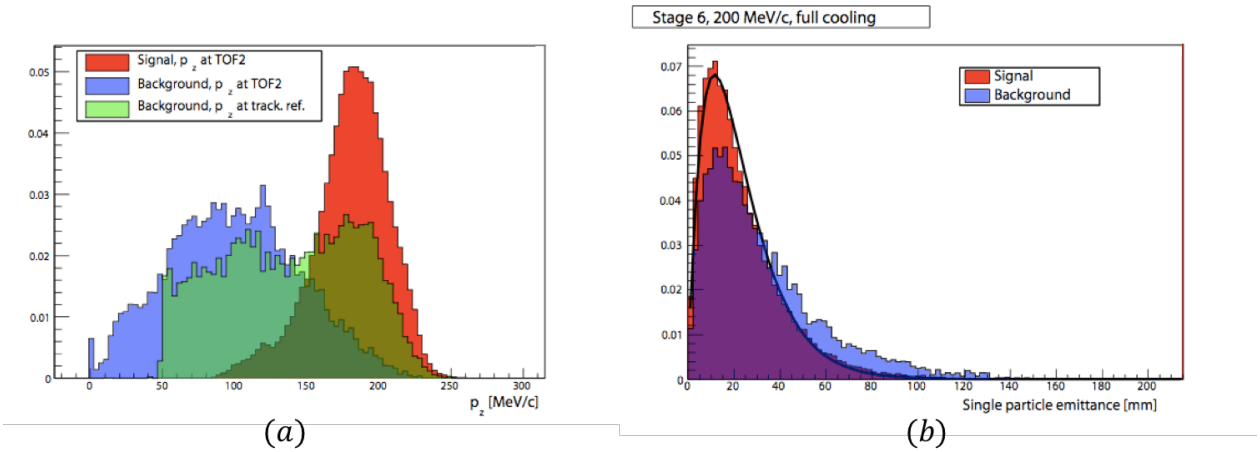

Figure 3.17: These plot are taken from a simulation of an historic version of MICE and are included to aid discussion only. (a) Normalised distributions of p_z. The red distribution shows muons on entrance to TOF2 while blue represents the background causing hits in TOF2. The green area illustrates the momentum of background events measured at the exit of the downstream tracker, significant overlap is observed. (b) Single particle emittance for muon (red) signal and electron (blue) background events [184]. It must be noted that these background electrons are a result of muon decays and backgrounds from the RF cavities in this final stage of MICE.

produce additional uncertainties on the emittance. A measurement of this is presented in Chapter 4.

KL Pre-Shower

The purpose of the KL pre-shower is primarily to provide a separation capability between muons and decay electrons. The KL pre-shower detector is a 2.5X0 Pb scintillating-fibre calorimeter of the type utilised by the KLOE experiment [166]. Consisting of 1 mm diameter scintillating fibres glued between 0.3 mm thick grooved lead plates the aim of the KL calorimeter is to provide a final "muon" tag to aid in MICE achieving $> 99.9\%$ muon purity [185]. An incoming electron will lose most of its energy in the pre-shower layer and generate an electromagnetic shower in the process while muons cross the KL and deposit energy without showering. Consequently, the KL's response to a muon differs from that of the electron. The KL was commissioned, along with the other PID devices, in Step 1 of the MICE implementation. Figure 3.18 shows the energy response of the KL to each particle.

The Electron-Muon Ranger

The Electron-Muon Ranger (EMR) is located at the very downstream end of the cooling channel. Figure 3.19 presents a schematic of the detector. The main objective of the EMR is to help distinguish between muons and decay electrons downstream of the absorber modules. In addition, the EMR will aid exclusion of RF backgrounds in the final stage of the experiment. To accomplish the intended accuracy on the beam emittance measurements a contamination $>1\%$ is essential. The EMR was installed and commissioned in the beam line in Autumn of 2013.

The EMR comprises of 2832 bars, structured into 48 planes, each consisting of 59 triangular scintillator bars, displayed in Figure 3.20. Every bar has a height of 3.3 cm, width of 1.7 cm and length 1.1 m and

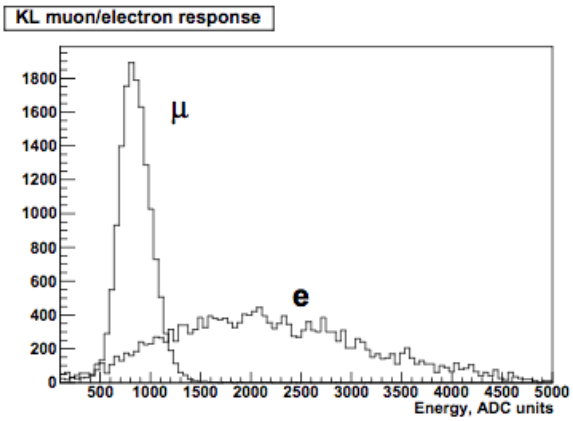

Figure 3.18: KL energy spectrum, in terms of ADC counts, to muons and electrons for a nominal 300 MeV/c beam. The KL has an energy resolution of $\approx 7\%/\sqrt{E(GeV)}$ [183].

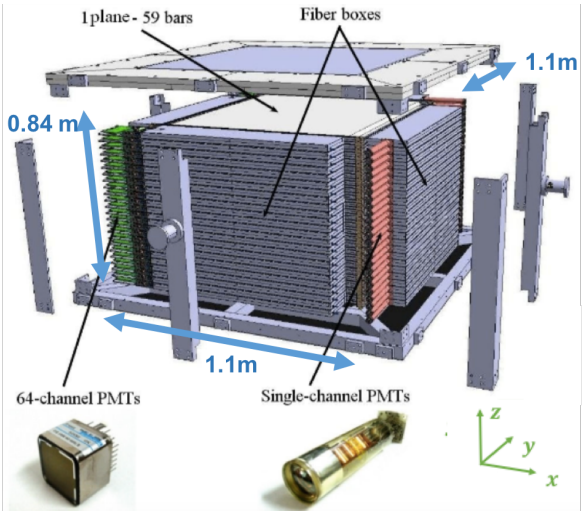

Figure 3.19: Schematic of Electron-Muon Ranger which forms part of the downstream calorimeter in MICE. The detector aims to assist in distinguishing between muons and decay electrons as well as helping to eliminate any RF backgrounds when the cavities are installed in later stages of MICE. The detector consists of 59 polystyrene scintillator bars per plane, with 48 planes in total. Single channel photo-multiplier tubes read out the energy deposited per bar and multi-channel PMTs combine energy form multiple bars [167].

encloses a 1.2 mm diameter polystyrene Wave-Length Shifting Fibre (WLS Fibre) coupled to a 1.5 mm diameter polystyrene light guide. Bars are rotated 180 ° relative to the preceding bar such that the resulting configuration has no dead area for particles traversing a plane with angles less than 45° from the beam axis.

The EMR has dual readout; every plane is equipped with two types of PMTs: single-anode (SAPMTs) and multi-anode (MAPMTs). When particles deposit energy light is produced in a given bar. The single-anode PMT registers light from all the bars in a given plane and provides a signal proportional to the total energy deposited in that plane. 64 channel Multi-anode PMTs read all the bars individually. Eight of the single channel PMTs are readout by one flash Analog to Digital Convertors (fADCs), there are 6 fADCs in total.

The MAPMTs are readout by a Front-End Board (FEB), which amplifies, discriminates and shapes all input signals and Digitiser Buffer Board (DBB), which stores the data and transfers to a PC at the end of

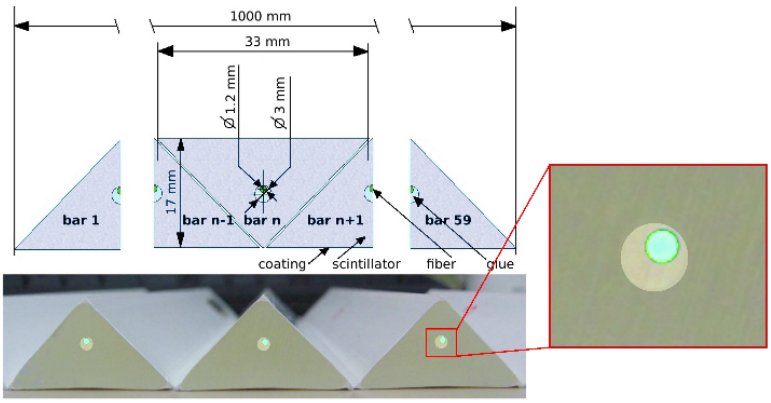

Figure 3.20: EMR bar design: Polystyrene triangular bars are placed in planes of alternate orientation. Each bar is fitted with a WLS fibre down its centre which is read out using PMTs [167].

every spill.

Muons and electrons produce distinct signal patterns in the EMR: muons below a certain energy stop in the detector and the energy deposition exhibits a clear Bragg peak, the position of which defines the range. Electrons shower in KL and exhibit multiple tracks in the EMR.

During "Step 1" it was established that the EMR detector is capable of identifying electrons with an efficiency of 98.6%, providing a purity for the MICE beam that exceeds 99.8%. The detector additionally provided a powerful tool for the reconstruction of muons with momenta in the range 100-280 MeV/c [172].

3.6 Analysis Software

3.6.1 MICE Analysis User Software (MAUS)

The MICE Analysis Users Software (MAUS) [186] is a custom software package with extensive capabilities, especially devised for the requirements of MICE. MAUS is an amalgamation of C++ and python and can produce Monte Carlo simulations and reconstruct both on- and off- line data.

The MAUS simulation tools are based on GEANT4 [153], which incorporates the full range of physical processes and particles that are required for the study of muons in an ionisation cooling channel. GEANT4 is utilised by MAUS to simulate the passing of muons through the experiment, in particular, the passage through the absorbers. This includes simulating both multiple scattering and energy loss. The current version of MAUS is version 2.5, which uses GEANT4.9.6.

MAUS provides the software for the MICE project's particle tracking, detector reconstruction and accelerator physics programs. MAUS is designed to fulfil a number of functions for physicists interested in studying MICE data including:

1. Modelling the behaviour of particles traversing the MICE cooling channels, including all its sub-detectors,

2. Modelling the MICE detector's responses to particles,

3. Performing reconstruction of particle trajectories from the detector responses,

4. Providing a framework for high level accelerator physics analysis,

5. Providing online diagnostics during running of MICE.

3.6.2 The Spill Data Structure

MAUS differs somewhat from the analysis software used in conventional collider particle physics experiments. MAUS exploits a "Map-Reduce" data flow format [187] controlled by the user from a top level Python script along with a configuration file. At this level modules can be interchanged, appended or removed to ease simulation of any particular task which may be desired by an experimenter. The modules come in four types: Input, Output, Map and Reduce. Input modules read in the initial data from ROOT [188], JSON (an ascii data-tree which can be read by any text editor) or binary files from the DAQ. Maps perform most of the simulation and analysis work, including calling the simulation routines and performing the reconstruction. Reducers are used to display output, such as for online reconstruction plots, and are capable of accumulating data sent from maps over multiple spills. Output modules write data in the form of ROOT or JSON allowing them to be analysed both within MAUS or elsewhere.

The top-level data type within the output framework is the "Spill". Each spill is independent and corresponds to a single target dip. Additionally, MAUS can write data into a JobHeader, RunHeader, RunFooter and JobFooter data type. Each "Map" within MAUS modifies the data associated with a given spill, for example, by converting the binary DAQ output to a processable data structure, or performing one of various track fitting methods and routines and appending reconstruction data to the spill data. The spill is separated into three main classes: the MCEventArray contains an array of data, each member of which represents the Monte Carlo of a single primary particle crossing the system; the ReconEventArray contains an array of data, each member of which corresponds to data associated with a DAQ trigger; and the DAQData corresponds to the raw data readout. Additionally, there are branches for reconstructed scalars, which are handled spill by spill and EMR Spill data, which is recorded per spill rather than event by event. The EMRSpillData class will be discussed in detail in Chapter 4. The MAUS top level data structure is documented in the diagram shown in Figure 3.21; the MAUS users guide [186] gives much more information about the data structure and how the software may be utilised.

3.6.3 MCEvents

MAUS is constructed to manage both MC and Recon events on a spill-by-spill basis. The subdivisions of both the MCEvent and ReconEvent level are summarised in Figures 3.23 and 3.22. The MCEvent is split into sensitive detector hits and pure Monte Carlo outputs. The Primary branch holds the primary information which led to the MC data. This includes: the random seed, primary position and momentum. Sensitive detector hits have hit data (energy deposited, position, momentum, etc.) and a detector specific ChannelId

that represents the channel of the detector that was hit - e.g. for TOF this indexes the slab, plane and station. MAUS also stores VirtualHits which are not sensitive detector hits. These hold record of the output position and momenta of particles that cross a particular plane in space, time or proper time.

3.6.4 ReconEvents

Reconstruction information is stored in the ReconEvents. ReconEvents store information in a branch for each detector and combined global reconstruction output, that is the track fitting between detectors. Each ReconEvent pertains to a single trigger.

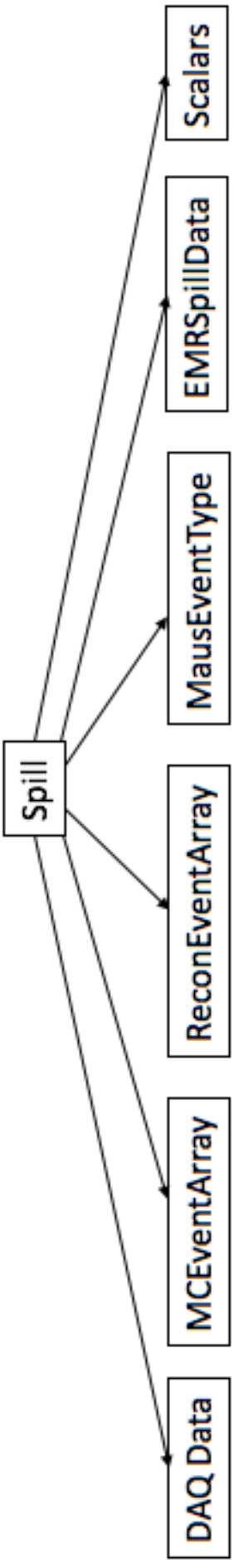

Figure 3.21: Summary of the data structure of a MAUS spill. Each spill describes the events associated with a single target dip in the beam. A MAUS spill contains information on DAQ, MC and Recon events.

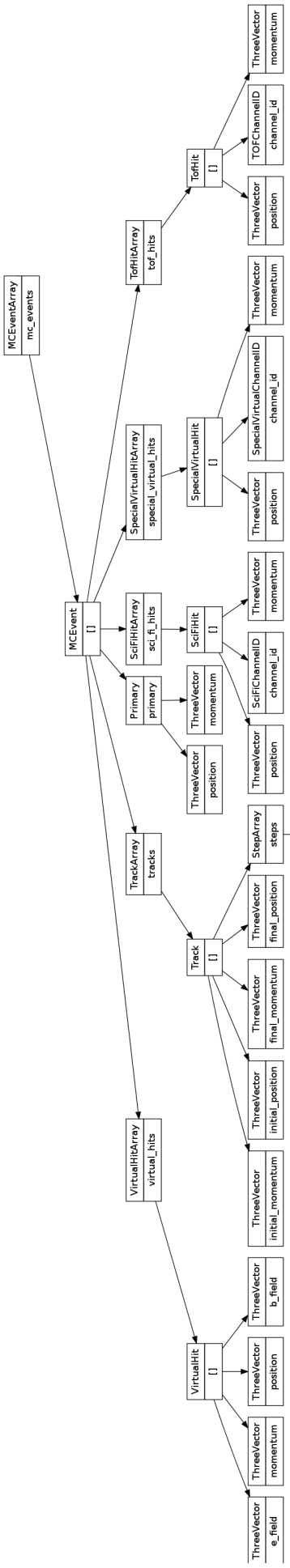

Figure 3.22: Summary of the data structure of a MAUS MCEvent sub structure. [186].

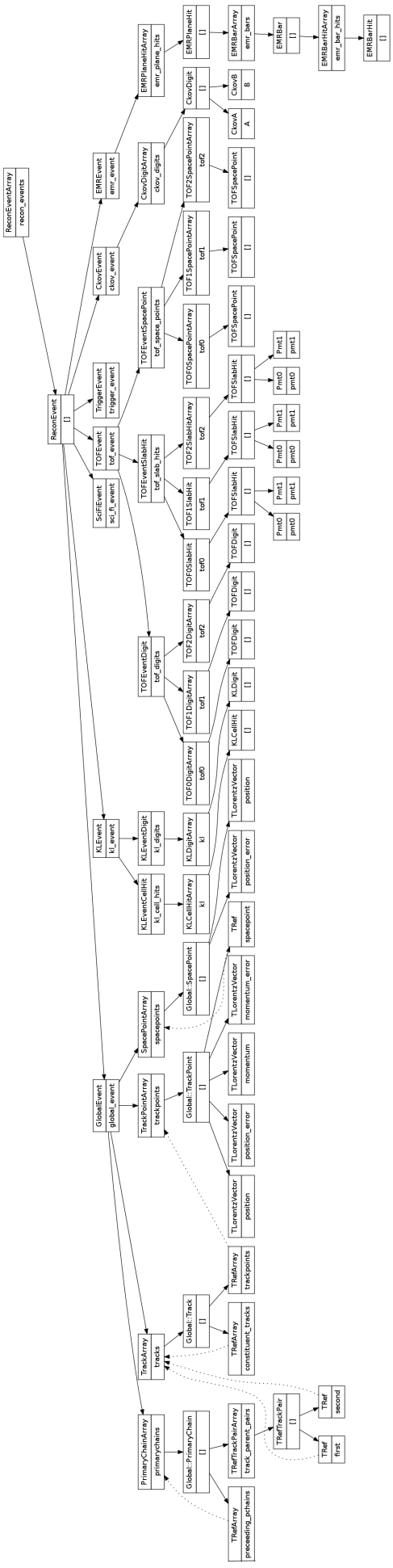

Figure 3.23: Summary of the data structure of a MAUS ReconEvent sub structure. [186].

Chapter 4

A Study of Muon Polarisation in the MICE Cooling Channel

Chapters 1 and 2 outlined the importance of demonstrating the feasibility of ionisation cooling as a means of reducing the emittance of a muon beam. Chapter 3 gave details of the Muon Ionisation Cooling Experiment, MICE, the international effort to conduct the first measurement of sustainable ionisation cooling. MICE is currently in its "Step IV" commissioning stage. During this phase the MICE collaboration seeks to characterise any factors which could enhance beam emittance and, thus, form systematic uncertainties on the cooling measurement.

The presence of decay positrons in the MICE beam can produce uncertainties in the measured beam emittance. Decay processes tend to yield positrons with higher emittance than the incident muon. The energy and angular distribution of the positrons is dependent on muon polarisation. As a result, muon polarisation, at the point of decay, is a systematic uncertainty upon the emittance measurements which it is important to calculate. The polarisation of the muons produced via pion decay is easily deduced from kinematics; however, as the muons traverse the cooling elements, depolarisation may ensue. The level of depolarisation can be computed by making comparisons between the expected muon polarisation and the measured downstream polarisation. This chapter explores the feasibility of using the MICE downstream calorimeter, the EMR, to measure muon polarisation and examine the degree of depolarisation taking place. A unique approach is demonstrated, the decay angle of positron tracks is reconstructed, relative to the initial muon direction, and the muon beam polarisation is determined from the subsequent angular distribution.

4.1 Spin, Helicity, Handedness and Polarisation

The intrinsic angular momentum of a particle is known as its spin. Helicity, h, is defined to be the projection of the particle's spin vector, $\vec{s}$, in the muon rest frame, parallel to its momentum vector, $\vec{p}$, such that

$$h = \frac{\vec{s} \cdot \vec{p}}{|\vec{p}|}, \tag{4.1}$$

where $\vec{s}$ is normalised to 1. Fermions have $h = \pm 1/2$ and bosons $h = \pm 1, 0$. A particle is "right-handed" if the direction of its spin corresponds to the direction of its motion and is "left-handed" if the directions of spin and motion are opposing.

Muon polarisation is commonly defined in terms of the helicity, h, of each muon within a beam. Within an ensemble of muons the average polarisation should be considered instead of the spin of a single muon. A polarisation, $P = |\vec{P}|$, is the magnitude of the average of all polarisations.

$$P = \frac{1}{N} |\sum_{i=1}^{i=N} \vec{s}_i|. \tag{4.2}$$

4.2 Muon Polarisation In MICE

4.2.1 Muon Production via Pion Decay

Section 3.2 explained how MICE obtains its muon beam via pion decay within a decay solenoid. Figure 4.1(a) displays a Feynman diagram for the decay: $\pi^+(u\bar{d}) \rightarrow \mu^+\nu_\mu$, an analogous diagram may be drawn for: $\pi^-(d\bar{u}) \rightarrow \mu^-\bar{\nu_\mu}$. The branching fraction of this decay is ≈ 0.999877 [1] with the positron (or electron) decay mode being heavily suppressed. The pion possesses a spin of zero. The outgoing lepton and neutrino must, consequently, be emitted with opposite spin and opposite linear momenta in the pion rest frame. Given the nature of weak interactions, considered in Section 1.1.2, the neutrino (anti-neutrino) must be left-handed (right-handed) meaning the μ^+ (μ^-) must also be left-handed (right-handed) in the pion rest frame. Consequently, the μ^+ (μ^-) has a polarisation opposite (parallel) to its direction of motion.

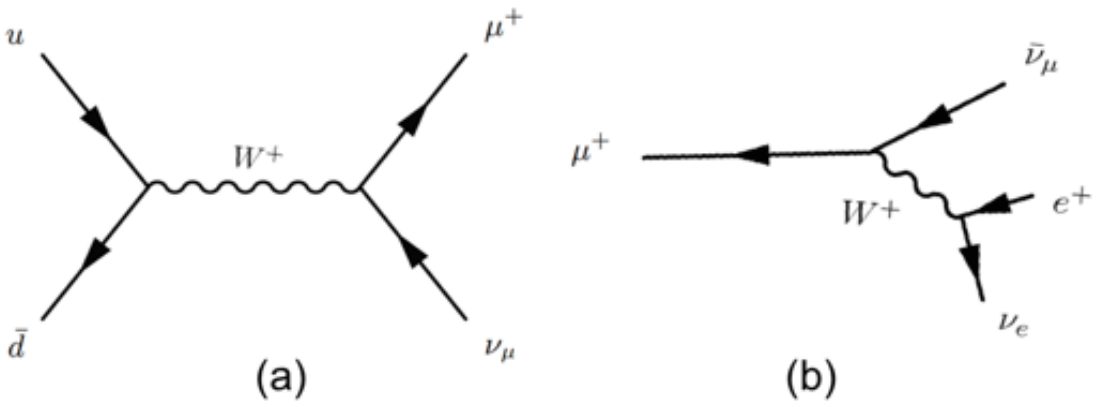

Figure 4.1: Feynman diagrams showing (a) a charged π^+ decaying to anti-muon and muon anti-neutrino. (b) anti-muon decaying to a positron and two neutrinos. Both are mediated by charged W^+ weak boson.

Muons can either be polarised in either "forwards" direction, i.e. polarised along the direction of travel, or "backwards," i.e. polarised in the opposing direction. When muons originate from moving pions the

outgoing muon momenta for "forward" or "backwards" muons differs e.g. for a monochromatic 200MeV/c incoming pion beam a "forward" decay muon has momentum 209MeV/c compared to a "backward" muon with 105MeV/c [189]. By selecting the energy of the incoming beam one can determine the polarisation of the muons in the MICE input beam. This can be accomplished through interplay between the momenta at the two bending magnets, D1 and D2. MICE can discriminate between muons of specific polarisations in the pion rest frame e.g. in normal $\pi \to \mu$ operation D2 can be set to half D1, selecting a beam of almost pure "backwards" going muons in the pion rest frame.

4.2.2 Assumptions

In this analysis the muons from charged pion decay are assumed to be 100 % polarised in a given direction. This ignores:

1. Finite Neutrino Mass - This reduces the neutrino's helicity by a factor of $(1 - \frac{p_\nu}{E_\nu})$. With the most conservative upper mass limit this will contribute a change of 2×10^{-5} [190] in the muon polarisation. This is below the sensitivity of this study.

2. Pion Radiative Decay Modes - The charged pion can also decay radiatively:

$$\pi^+ \to \mu^+ \nu_\mu \gamma, \tag{4.3}$$

   with a branching fraction of $\approx 0.02\%$. In this scenario, the muon's longitudinal polarisation is a function of the photon and muon energies. It is assumed in this study that the polarisation loss due to this mode is negligible.

3. The Existence of Right Handed Neutrinos - The prospect of right handed neutrinos was discussed in Chapter 1. If they were to exist then the muon that produced the associated neutrino would also be right handed. The possibility of such is ignored in this study.

4.2.3 Muon Decay

Figure 4.1(b) depicts a Feynman diagram characterising the purely leptonic three-body decay: $\mu^+ \to e^+ \bar{\nu}_\mu \nu_e$. An analogous diagram can be drawn for the μ^- case.

The matrix element, M, for the most general Lorentz invariant, derivative free expression, is defined by 10 complex, model-independent couplings, g^k_{em}, [190]:

$$M = \frac{4G_F}{\sqrt{2}} \sum_{\substack{e=L,R \\ m=L,R \\ \kappa=S,V,T}} g^\kappa_{ij} \langle \bar{\psi}_{e_\kappa} | \Gamma^\kappa | \psi_{\nu_e} \rangle \langle \bar{\psi}_{\nu_\mu} | \Gamma_\kappa | \psi_{\mu_m} \rangle, \tag{4.4}$$

where L and R are left and right handed leptons, and Γ denotes the decay rate, S, V, and T indicate the scalar, vector, and tensor interactions respectively, G_F is the Fermi coupling constant. In the Standard

Model: $g^V_{LL} = 1$ and $g^{\kappa}_{em} = 0$ otherwise. The decay spectrum of a positron is generally written in terms of four parameters: ρ,δ,($P_\mu\xi$)and η. ρ, δ, ξ and η are the Michel parameters ([191] [192] [193]) and P_μ is the muon polarisation at point of decay. Neglecting neutrino mass, the differential decay rate can be expressed in terms of these parameters, such that

$$\frac{d^2\Gamma}{dxdcos\theta} = \frac{1}{4}m_\mu W^4_{\mu e} G^2_F \sqrt{x^2 - x_0^2} \cdot [\mathcal{F}_{IS}(x,\rho,\eta) + P_\mu cos\theta \cdot \mathcal{F}_{AS}(x,\xi,\delta)], \tag{4.5}$$

with

$$W_{\mu e} = \frac{m_e^2 + m_\mu^2}{2m_\mu} \quad , \quad x = \frac{E_e}{W_{\mu e}} \quad , \quad x_0 = \frac{m_e}{W_{\mu e}} \quad , \quad P_\mu = |\vec{P}_\mu| \quad , \quad cos(\theta) = \frac{\vec{P}_\mu \cdot \vec{p_e}}{|\vec{P}_\mu||\vec{p}_e|} + R.C; \tag{4.6}$$

$$\mathcal{F}_{IS}(x,\rho,\eta) = x(1-x) + \frac{2}{9}\rho(4x^2 - 3x - x_0^2) + \eta x_0(1-x), \tag{4.7}$$

$$\mathcal{F}_{AS}(x,\xi,\delta) = \frac{1}{3}\sqrt{x^2 - x_0^2}\big[1 - x + \frac{2}{3}\delta\big(4x - 3 + \big(\sqrt{1 - x_0^2} - 1\big)\big)\big] + R.C, \tag{4.8}$$

where $R.C$ refers to electromagnetic radiative corrections. The Standard Model predicts $\rho = \delta = 3/4$, $P^\pi_\mu = \xi = 1$ and $\eta = 0$. P^π_μ defines muon polarisation upon production; this may have evolve prior to the muon's subsequent decay. The TRIUMF Weak Interaction Symmetry Test (TWIST) [190] experiment ascertained measurements of the Michel parameters, resulting in improved constraints on extensions to the Standard Model. TWIST obtained the measurements:

$$\rho = 0.74991 \pm 0.00009(stat.) \pm 0.00028(sys), \tag{4.9}$$

$$\delta = 0.75072 \pm 0.00016(stat.) \pm 0.00029(sys.), \tag{4.10}$$

$$P^\pi_\mu \xi = 1.00084 \pm 0.000035(stat.)^{+0.00165}_{-0.00063}(sys.); \tag{4.11}$$

all consistent with the Standard Model. From Equation 4.5 is is apparent that the decay rate is dependent upon the polarisation of the muons at the point of decay Figure 4.2 illustrates the expected differences in particle rates at various muon polarisations.

By Integrating Equation 4.5 with respect to x, and ignoring positron mass, an expression for the angular distribution of the decay positrons, integrated over momentum space, is acquired:

$$\frac{d\Gamma}{d(cos\theta)} \approx 1 \pm \frac{1}{3}P_\mu cos(\theta), \tag{4.12}$$

where P_μ is the relative muon polarisation upon decay. Equation 4.12 implies that the net polarisation of the muon beam upon decay can be calculated from considering the distribution of the cosine of the decay

angle of the decay positron tracks. The aim of the analysis presented here is to make a measurement of the average polarisation of muons which decay in the MICE downstream calorimeter, the EMR, using the decay angle of the reconstructed positron tracks.

Spin evolution due to the presence of electromagnetic fields and scattering from atoms within the absorber material will contribute to a modifications of the beam polarisation as it traverses the cooling channel. The implication is that at the EMR the polarisation P_μ may not be equal to P_μ^π. The amount of depolarisation in MICE can be deduced by comparing the measured downstream polarisation to the expected P_μ^π.

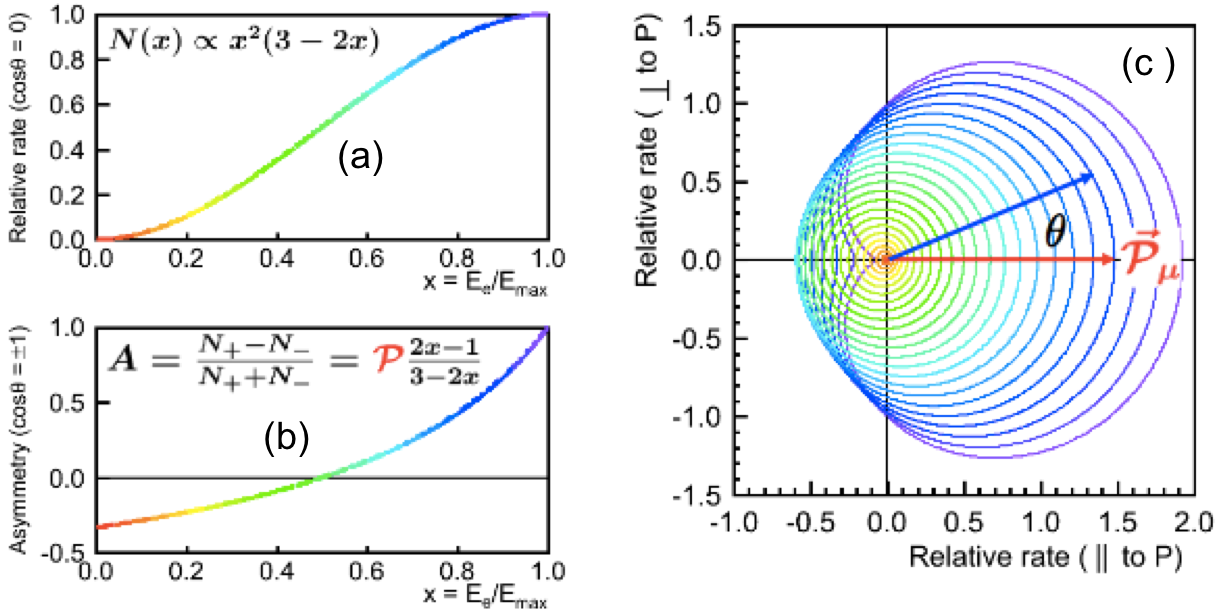

Figure 4.2: From Twist [194]. (a) Rate is maximum at highest energy for unpolarised decays (b) Asymmetry for maximally polarised muons is maximum for higher energy decays (c) A polar-coordinate plot of the rate of positron emission from muon decay as a function of angle from the muon spin θ, at various energies ϵ, represented by each contour. The distribution has axial symmetry about the muon spin polarisation direction, which points toward the right in this plot.

4.2.4 Effects of Muon Polarisation in Neutrino Factories

Figure 1.12 exhibits a schematic of the proposed Neutrino Factory. The objective of such a machine is to yield high intensity neutrino beams via muon decay, permitting accurate measurements of the neutrino oscillation parameters outlined in Chapter 1. Muon polarisation will present a systematic uncertainty on the neutrino flux at such a facility [195] as the angular distribution of neutrinos arising from forward and backward polarised muon beams differ. Considering a μ^+, decaying in the muon centre-of-mass, the neutrino spectra for the ν_μ and $\bar{\nu_e}$ are

$$\frac{d^2N}{dxdcos\theta} = Nx^2[(3-2x) - P_\mu(1-2x)cos\theta], \tag{4.13}$$

and

$$\frac{d^2N}{dxdcos\theta} = 6Nx^2[(1-x) - P_\mu(1-x)cos\theta], \tag{4.14}$$

respectively, where θ is the decay angle of the neutrino relative to the muon direction of travel, P_μ denotes muon longitudinal polarisation at decay and $x = \frac{E_\nu}{m_\mu}$. In order to maximise the neutrino flux whilst minimising systematic uncertainties it is important to understand and monitor P_μ [196]. The analysis presented in this Chapter will deliver insight into how future machines, such as a Neutrino Factory, may measure muon polarisation and thus examine the uncertainty in the neutrino energy spectrum due to beam depolarisation.

4.2.5 Effects of Muon Polarisation in a Muon Collider/Higgs Factory

There are numerous physics benefits of preserving the polarisation of muons in a muon collider Higgs factory [198]. The polarisation of the two muons at point of collision dictates whether a scalar or vector particle is produced. If the two beams have the same polarisation then the $\mu^+\mu^- \rightarrow h \rightarrow f\bar{f}$ occurs. If they have opposing polarisations then the background $\mu^+\mu^- \rightarrow \gamma^*/Z^* \rightarrow f\bar{f}$ dominates. Monitoring and controlling muon polarisation thus assists in improving the signal to background ratio in a Higgs factory.

In addition, a much more accurate determination of the Higgs mass and width, of the order of $\pm$ 100 keV, may be conceivable with the (g - 2) precession of polarised muons and an adequate luminosity [199]. Raia and Tollestrup investigated the feasibility of establishing the precise energy of the circulating muon beams (once accelerated to the final energy of 62.5 GeV) with the turn-by-turn variation of the electron energy spectrum produced by the decay of the muons. This variation is caused by a non-zero value of (g - 2) for the muon and the existence of a finite beam polarisation. The polarisation can also effect the intensity of the beam. Requiring muon beam polarisation results in a lower muon beam intensity, as the momentum range of captured muons from pion decay must be curtailed to select muons from forwards or backwards decay ([197] gives more details). Figure 4.3 shows trade off between beam polarisation choice and the loss in achievable luminosity.

Depolarisations in the muon beam may transpire in the cooling channel of a multi-TeV muon collider. In addition, energy spread in the beam can lead to subsequent depolarisation in the acceleration phase. Within the collider itself there is the possibility of large depolarisation; for 84 turns in a 2 TeV muon collider the beam can become completely depolarised [201]. The muon spin at the interaction points can be altered through use of spin rotators; however, it is still important to characterise and minimise the level of depolarisation occurring in the collider subsystems. Assessing how much depolarisation will ensue in the cooling elements will form an important step in this process.

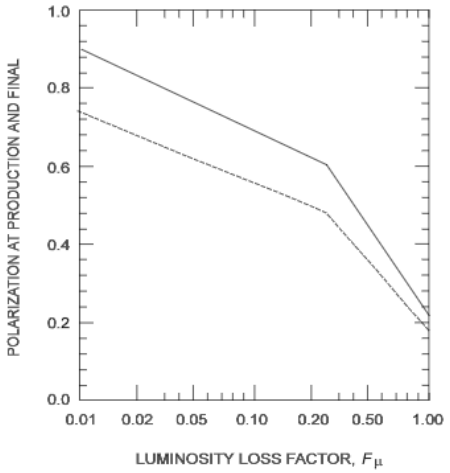

Figure 4.3: Polarisation versus the fraction of muons accepted (solid line: polarisation at source; dashed line: after cooling) [200].

4.3 Sources of Depolarisation in the MICE Channel

4.3.1 Evolution of Particle Spin in Magnetic Fields: The Thomas BMT Equation

Although the polarisation of a muon produced by the pion is easily calculated, the spins of the individual muons in the beam will change as they traverse the MICE electromagnetic fields. Since the spin evolution obeys a different set of equations from the momentum, small depolarisation effects arise, reducing the average polarisation of the muon beam. Consequently, the beam polarisation at the EMR may not be as it was upon entering the cooling channel.

Considering the case of a relativistic particle, of charge e, travelling at velocity $\vec{v}$ where the electric and magnetic fields in the laboratory frame are described by $\vec{E}$ and $\vec{B}$ respectively, the trajectory of the particle is determined by the Lorentz force equation:

$$\frac{d\vec{p}}{dt} = e(\vec{E} + \vec{\beta} \times \vec{B}), \tag{4.15}$$

where $\vec{\beta} = \vec{v}/c$, $\vec{p} = \gamma m \vec{\beta} c$ and γ is the relativistic Lorentz factor. For a relativistic particle Equation 4.15 can be then be rewritten in terms of β such that

$$\frac{d\vec{\beta}}{dt} = \frac{e}{mc\gamma}(\vec{E} - \vec{E} \cdot \vec{\beta}\vec{\beta} + \vec{\beta} \times \vec{B}). \tag{4.16}$$

Using the expression for total rate of change in relativistic energy: $\frac{dU}{dt} = mc^2 \frac{d\gamma}{dt} = ec\vec{E} \cdot \vec{\beta}$.

In an infinitesimal time $t = dt$ the particle will rotate through an angle

$$d\vec{\alpha} = \frac{\vec{\beta} \times d\vec{\beta}}{\beta^2} = \frac{\vec{\beta} \times \frac{d\vec{\beta}}{dt}}{\beta^2} dt \tag{4.17}$$

in the laboratory frame. For the motion in a prescribed external electric and magnetic field and exploiting Equation 4.16 gives

$$\frac{\vec{\beta} \times \frac{d\vec{\beta}}{dt}}{\beta^2} = -\frac{e}{mc\gamma}[\vec{B}_{\perp} - \frac{\vec{\beta} \times \vec{E}}{\beta^2}], \tag{4.18}$$

where

$$\vec{B}_{\perp} = \frac{\vec{\beta} \times (\vec{B} \times \vec{\beta})}{\beta^2} \tag{4.19}$$

is the magnetic field perpendicular to the motion of the particle. Likewise, an expression for the component of the magnetic field parallel to the particles motion ($\vec{B}_{||}$) can also be derived such that

$$\vec{B}_{||} = \frac{(\vec{B}.\vec{\beta})\vec{\beta}}{\beta^2}. \tag{4.20}$$

Applying a Lorentz boost with the relativistic factor γ yields the projection of the magnetic field in the particle's rest frame

$$\vec{B}_{rest} = \gamma(\vec{B}_{\perp} - \vec{\beta} \times \vec{E}) + \vec{B}_{||}. \tag{4.21}$$

A particle's change in spin in its rest frame can be described by the expression ([205]):

$$\frac{d\vec{s}}{dt} = \frac{-ge}{2mc}(\vec{B} \times \vec{s}) \tag{4.22}$$

where all the symbols have their usual meaning, g is the "g-factor" and is a dimensionless quantity that characterises the magnetic momentum and gyromagnetic ratio of the muon; $\vec{s}$ is the particle's spin in the laboratory frame. The spin changes in the proper time interval $d\tau = dt/\gamma$ such that in the inertial frame (moving with the particle velocity $\vec{v}_{t=0}$) :

$$d\vec{s}_{Inertial} = \frac{-ge}{mc}(\vec{B}_{rest} \times \vec{s})d\tau. \tag{4.23}$$

However, the rest frame itself rotates relative to the inertial frame, through an angle $d\phi$, such that

$$d\vec{s} = d\vec{s}_I - d\vec{\phi} \times \vec{s}. \tag{4.24}$$

Given that $d\vec{\phi} = (\gamma - 1)d\vec{\alpha}$ equation 4.24 may be re-written as

$$d\vec{s} = \left[\frac{-ge}{mc\gamma}\vec{B}_{rest} \times \vec{\beta} - \frac{\gamma - 1}{\beta^2}(\vec{\beta} \times \frac{d\vec{\beta}}{dt}) \times \vec{s}\right]dt. \tag{4.25}$$

In another form:

$$\frac{d\vec{s}}{dt} = \vec{\Omega} \times \vec{s}, \tag{4.26}$$

where $\vec{\Omega}$ is the spin precession vector, defined as

$$\vec{\Omega} = -\vec{\mu}\frac{\vec{B}_{rest}}{\gamma} - \frac{\gamma - 1}{\beta^2}(\vec{\beta} \times \frac{d\vec{\beta}}{dt}), \tag{4.27}$$

where $\vec{\mu}$ is the magnetic moment of the particle. In terms of a Hamiltonian, H, one may write:

$$H = -\vec{\mu} \cdot \frac{\vec{B}_{rest}}{\gamma} + \vec{\omega}_T \cdot \vec{s}. \tag{4.28}$$

The first term denotes the magnetic dipole interactions and the second term is referred to as the Thomas Precision [202], $\vec{\omega_T}$ defines the Thomas precession vector. Equation 4.27 can also describe the case of a neutral particle possessing a magnetic moment (for example neutrons). In the case when the particle has charge, for example the muons in MICE, the spin precession vector is more complicated and possesses an additional term proportional to the electric field. The spin precession vector is then

$$\vec{\Omega} = \frac{-e}{mc}[(a + \frac{1}{\gamma})\vec{B}_{\perp} + \frac{1+a}{\gamma}\vec{B}_{||} - (a + \frac{1}{\gamma+1})\vec{\beta} \times \vec{E}], \tag{4.29}$$

where $\vec{B}_{\perp}$ and $\vec{B}_{||}$ are the perpendicular and parallel components of the magnetic field in the laboratory frame and a is known as the magnetic moment anomaly. The values of the magnetic moment anomalies differ for various particles. For $e^{\pm}$, $a = 1.15965218159 \times 10^{-3}$ and for $\mu^{\pm}$, $a = 1.1659208 \times 10^{-3}$ [203]. As a result the effects that this form of depolarisation has on the MICE muon will be small with the change to polarisation being $< 10^{-4} - 10^{-5}$ for a fully polarised muon beam [204]. Depolarisation of this form is therefore expected to be minimal in this analysis.

Equation 4.26 is the Thomas Bargmann-Michel-Telegdi (BMT) equation ([205]) and describes the evolution of the particle's spin $\vec{s}$ in the rest frame as a function of the electric and magnetic field acting upon it. These fields are expressed within the laboratory frame. This parametrisation is natural since the spin is an intrinsic property of the particle and is only truly meaningful in the particle rest frame. The Thomas BMT equation is utilised by the MAUS framework to parametrise the particle's spin evolution as it traverses the cooling channel.

4.3.2 Depolarisation Due to Scattering

Elastic scattering and multiple coulomb scattering in the absorber material and surrounding windows have a finite probability of flipping the muon spin direction and can thus lead to further depolarisation of the muon beam. The polarisation P' following a single muon-nuclear scattering at angle θ is [196]:

$$P' = P_{init.}\big[1 - \frac{2sin^2(\theta/2)}{\gamma^2 cos^2(\theta/2) + sin^2(\theta/2)}\big]. \tag{4.30}$$

Muon-electron scattering results in much smaller deflections. In the case of multiple scattering the total change in polarisation is harder to establish,

$$P' = P_{init.}\big(1 - \sum_i \theta_i^2/2\gamma^2\big), \tag{4.31}$$

where higher order terms are ignored due to θ being small. For muons with $p_z = 200$ MeV/c, it is anticipated that the maximum spin flip probability in an elastic scattering event will be minor ($\approx 5 \times 10^{-3}$) [196]. Hence, the contribution of scattering to the overall MICE beam depolarisation is also expected to be small. The overall depolarisation effect is therefore $\approx 1 \times 10^{-5}$ [204], and is consequently considered negligible in this study.

4.3.3 Depolarisation In Full Cooling Channel

This analysis considers a cooling channel absent of any absorber material. Further depolarisation could ensue within the the absorber material in the final stages of MICE. Simulations of muon beam depolarisation within liquid hydrogen of varying thicknesses are presented in [196]. Depolarisation in a thick absorber material depends on multiple scattering, a process which itself not yet fully understood (Section 2.5.2). It is concluded that within a typical cooling channel depolarisation is very small - at most of order 1%. Consequently, it can either be neglected or it may suffice to calculate average depolarisation and include this as a systematic error. However, further understanding of multiple scattering, and its affect on average beam polarisation in MICE, will be necessary prior to publication of this study.

During continuous energy loss (via the Bethe-Bloch equation) the magnitude of the momentum vector, which corresponds to the kinetic energy available, will be reduced as the beam traverses the absorber. The direction of the momentum is unchanged in this process, and thus the helicity is not altered. As a result energy loss should not depolarise the beam.

4.4 The EMR Software

This analysis is dependent on acquisition and reconstruction of sufficient data at the EMR detector. Within [167] a comprehensive explanation of how the EMR acquires and stores data is presented. This section outlines the tools exploited at analysis level to reduce noise and obtain the final data sample for this study.

4.4.1 The EMR in MAUS

The MICE Analysis Users Software (MAUS) (Section 3.4) serialises Monte Carlo and data for all detector sub-systems within the MICE experiment. The sub-branches applicable to the processing of EMRBarHits are reviewed in Figure 4.4. In addition to the familiar DAQ, MC and Recon, an EMRSpillData branch is also shown; this branch contains raw reconstructed EMRBarHits.

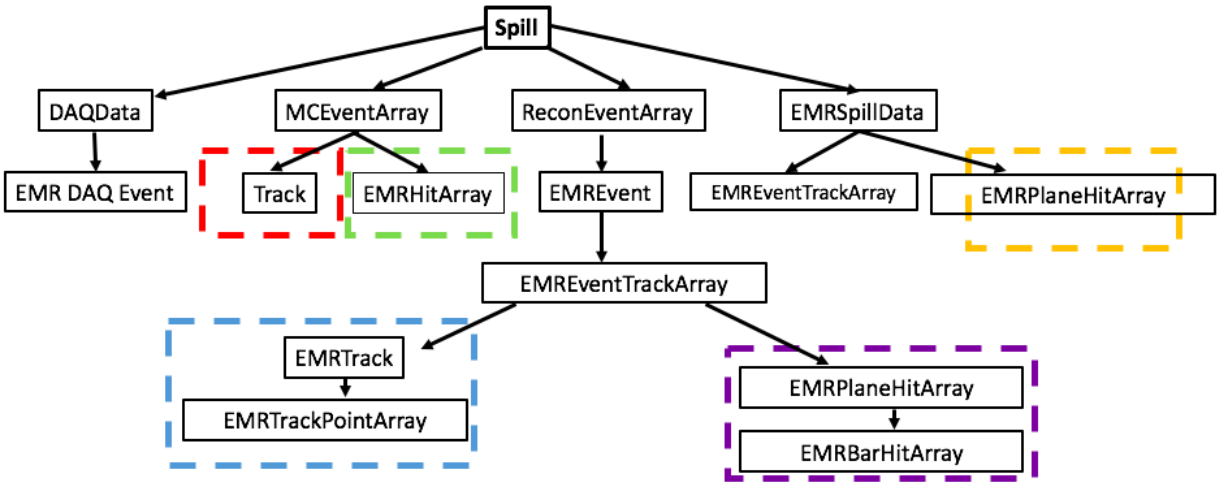

Figure 4.4: Overview of the sub-structure of a Spill within MAUS. For simplicity only branches which correspond to the EMREvents are shown. Each "Spill" corresponds to a dip of the target into the ISIS beam halo. Within MAUS all the DAQ, Recon and MC associated to one spill are stored within that Spill along with a separate list of raw EMRSpillData. True Monte Carlo EMR events are stored in the MCEventArray and are independent of the reconstruction/detector model. EMR hits produced by muons in reconstructed Monte Carlo and data samples are obtained from the ReconEvent EMRBarHitArray. The colours indicate the purpose of each branch in this analysis. Green indicates the location of "true" hits within the data structure. Purple indicates where reconstructed mother tracks are obtained, orange indicates where secondary hits are obtained. The branch indicated in blue is used to link the ReconEvent to the EMRSpillData and is used to associate secondary tracks to their mother track. The MCTrack, outlined in red, denotes a "through channel" MC track. It is from this track that the "true" track angles can be determined. These are then independent of the fitting algorithm derived here and the detector reconstruction employed in MAUS.

All the "true" EMRHits in a given Monte Carlo generated event are stored in the MCEvent, these events are independent of the MAUS reconstruction model and the detector resolution. Within the EMRHitArray each EMRHit has an associated position three-vector. The ReconEvent contains an EMREvent in which tracks are subcategorised into "mother" tracks and their "daughter" tracks. Within the EMREvent hits are stored in EMRPlaneHitArrays. Each EMRPlaneHit contains:

1. The "time-over-threshold" (TOT) i.e. the time during which the shaped ADC signal exceeds pre-defined threshold. The TOT is provided by the Front End Board and is proportional to the charge produced by a BarHit in a given bar. Thus, it is a measure of the energy deposited by a particle in the bar. Figure 4.5 (a) illustrates the exponential relationship between TOT and charge [206].

2. An Integrated charge in ADC counts;

3. A time between trigger and pulse Δt i.e. time selection;

4. A sampled Pulse Shape i.e. output of the fADC;

5. A time stamp in terms of TDC provided by the Digitaliser Buffer Board (DBB);

6. A Channel ID referring to one of 2880 channels of the EMR. With knowledge of the plane ID the bar ID within the plane where the energy is deposited is found. This enables particle tracks to be physically

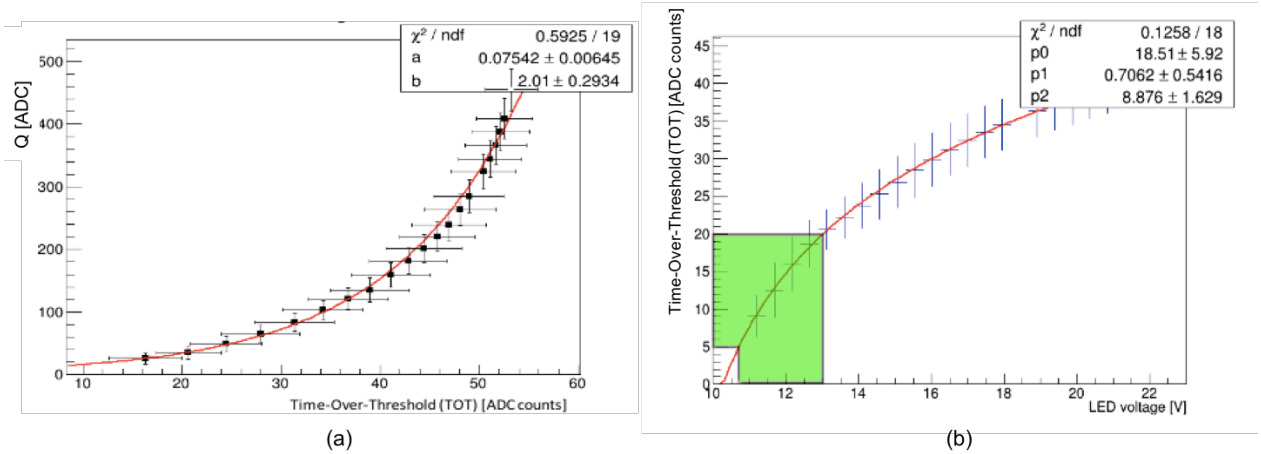

Figure 4.5: Plots from [206]: (a) Plot exhibiting the relationship between the measured time-over-threshold and the charge deposited in a single MAPMT. The units of time-over-threshold are in ADC counts, 1 ADC Count = 2.5 ns. A fit of the form $Q = e^{a \times TOT + b}$ is shown in red. a and b vary for each plane, thus, must be extracted from calibration data for each plane separately. (b) calibration plot obtained by illuminating a plane with light from LEDs of varying driver voltages. The green area corresponds to the TOT in the MAPMT consistent with muons at the energies used within MICE. The fit corresponds to $TOT = p_0 ln[p_1(V - p_2)]$.

reconstructed;

7. A Plane ID which refers to one of the 48 planes of the EMR; and,

8. An array of EMRBarHits each with their own TOT, time stamp, Δt time selection (time between the trigger and the hit) and channel ID.

During implementation of this analysis it was found that the routines within the EMR MAUS framework were unable to reconstruct secondary tracks with large transverse momentum. Therefore, the muon track is obtained directly from the ReconEvent branch but the corresponding daughter track is obtained via the EMRSpillData. An EMREvent within the EMRSpillData contains BarHits obtained from the raw data/reconstructed Monte Carlo, "mother" and "daughter" tracks are not differentiated in this branch. Section 4.7.4 outlines the method of associating muons to their decay particles employed by this analysis. The structure of the EMRSpillData.BarHitArray is analogous to that of the ReconEvent.

4.4.2 TOFEvents in MAUS

Particle velocity can be deduced from knowledge of the time taken for the particle to pass between two TOF detectors; with knowledge of the beam momentum this enables muons, pions and electrons identification. TOFSpacePoints associated with a specific Spill are stored within the ReconEvent giving access to the calibrated time at which a particle passed through each TOF detector relative to a particular trigger along with the overall charge deposited in the PMTs.

4.5 Implementing Polarisation in MAUS

To execute this analysis it was necessary to upgrade MAUS to consider the effects of depolarisation of particles within the cooling channel. MAUS was given the ability to store and precess each particle's spin and establish Monte Carlo beams for pre-defined beam polarisation settings.

Every particle in the MICE beam was assigned a spin three-vector: $\vec{s} = (s_x, s_y, s_z)$, defined and stored in a way analogous to the particle's position and momenta three-vectors which were already implemented in the MAUS framework. The spin components were specified as independent Gaussian distributions in x, y and z, and normalised to unit length. A user interface was constructed permitting the user a choice of initial beam polarisations, configured via adjustment of the mean and RMS of the respective Gaussian distributions. A record of the spin was added to the Monte Carlo data structure. As a result, MAUS gained the functionality required for monitoring the initial and final (i.e. spin at the EMR) of single particles within the beam.

The MAUS simulation tools utilise Geant4 which is capable of implementing the Thomas BMT equation. Consequently, the precession of the individual spin vectors of particles within the beam was included in MAUS via implementation of the Geant4 spin precession, along with the ability of the muon to decay in flight.

Once MAUS had adopted the capability to specify the polarisation of incoming Monte Carlo beams, tests were devised to ensure the spin was both generated and propagated correctly. Figure 4.6 exhibits the angular distribution of decay positrons from two simple Monte Carlo simulations for an initially forwards and initially backward polarised 220MeV anti-muon beam respectively. These help to validate the implementation and prove MAUS can correctly deduced the Michel parameters, within statistical limitations.

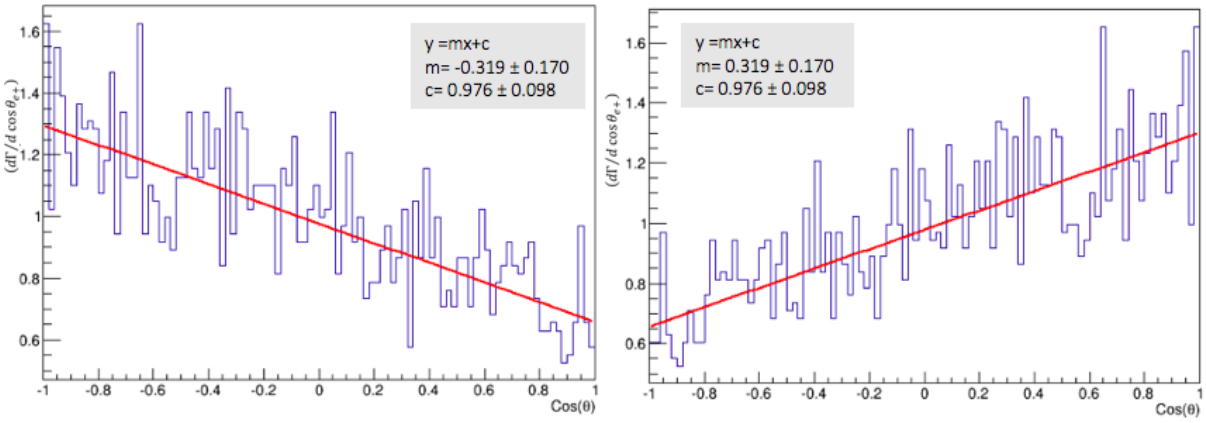

Figure 4.6: The spin tracking implementation is tested for 2 simple Monte Carlo examples of passing both initially (left) backward polarised muons and (right) forward polarised anti-muons of energy 220 MeV through a $1 \times 1 \times 1\ m^3$ polystyrene test volume. The plots show the angular distribution of the resulting decay positrons obtained directly from the resulting MCEvents. Straight lines are fitted to the two distributions and are consistent with the Michel parameters (Equation 4.12), within statistical errors.

4.6 The Data and Monte Carlo Samples

4.6.1 The Data Set: Run 07434

The following analysis uses the Step IV data sample labelled "07434," obtained in September 2015. Throughout this run TOF1 was enlisted as the trigger. A total of 1878 spills were collected with a total of 75403 triggers per spill. A proton absorber of thickness 82 mm was positioned just upstream of D2.

In this configuration the predominant beam line species is the μ^+ and the data sample has an unpolarised mean beam. D1 and D2 were set such that the beam had no overall polarisation in this run i.e. average $P_\mu^\pi = 0$. Therefore, once systematic uncertainties and statistical variations are accounted for it is expected that the measured average muon polarisation, P_μ, at the EMR will be "0". Using data from an unpolarised muon beam allows the fitting routines to be validated as no depolarisation should occur. Subsequent to successfully verifying the method on unpolarised data, polarised data can be considered.

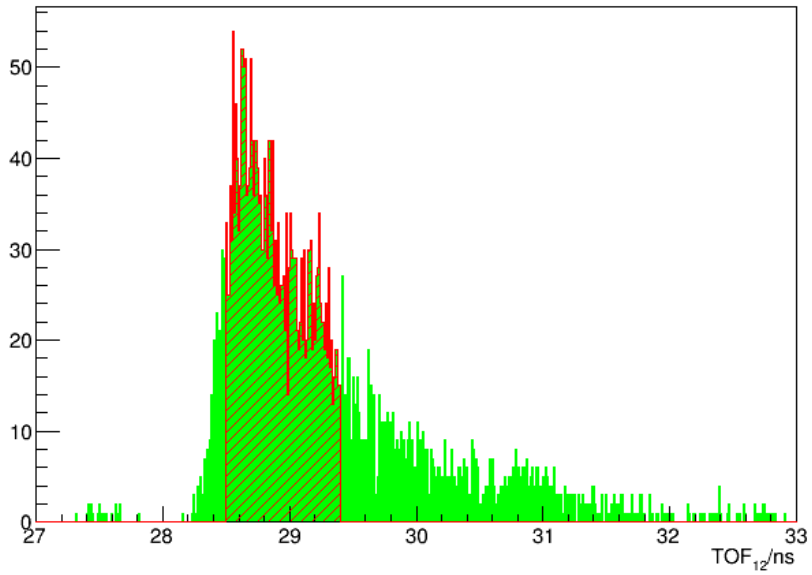

Figure 4.7: Distribution of time taken (TOF_{12}) for particles to pass between the upstream TOF1 detector and downstream TOF2 detector for the data run 07434, obtained as part of the MICE "Step IV" program. TOF_{12} is used to distinguish muons from contaminant particles in the beam. A large -"muon"- peak is observed; some pion contamination is signified by the extended tail at later times and a small decay positron peak, centred around 27.5 ns, is visible. A selection of $28.5 < TOF_{12} < 29.4$ ns ensures a high muon purity in the sample; this is indicated in red.

The distribution of the times taken for each particle to pass from TOF1 to TOF2, prior to the application of particle identification or track resolution cuts, is shown in Figure 4.7. The time taken to traverse the channel will be proportional to the mass of the particle. Thus, TOF_{12} is used to distinguish muons from contaminant particles in the beam. A large "μ^+" peak is evident, centred around 28.6 ns; a significantly smaller "positron" peak, centred around 27.5 ns, is also visible. The extended tail of the "muon" peak and slight shoulder at $\approx$ 29.5 ns indicate some pion contamination. Hence, a TOF_{12} time selection window of $28.5 < TOF_{12} < 29.4$ ns is applied to all primary particles. This ensures a high μ^+ purity in the primary tracks used in the analysis.

4.6.2 Monte Carlo Samples

In order to validate the fitting procedure detailed in this thesis, and evaluate any systematic uncertainties or biases induced by either this analysis procedure or the digitisation/reconstruction algorithms, two Monte Carlo track samples are evaluated:

1. A "true" Monte Carlo sample is generated using a channel geometry comparable to that of run "07434." The "true" Monte Carlo is independent of the detector response model and reconstruction algorithms. Hence, the accuracy of the analysis procedure can be evaluated through applying it to these "true" tracks. Limitations in the track fitting are established via comparisons between the "true" decay angle (θ_{true}), obtained directly from the anti-muon and positron Track vectors stored in the MCEvents, and that derived from the fitting algorithms (θ_{fit}).

2. A "reconstructed, " digitised, Monte Carlo sample is constructed by passing the true Monte Carlo sample through the MAUS reconstruction algorithms. The digitisation process provides a realistic simulacrum of real data and includes knowledge of current calibration quantities and credible noise models. Comparisons between the θ_{fit} derived from the "true" and "reconstructed" Monte Carlo allow any systematic uncertainties in the reconstruction algorithm and errors due to detector resolutions to be quantified.

The focus of Section 4.8 is to quantify any differences between the true track angle, θ_{true}, and that derived from the fitting procedure, θ_{fit}. Subsequent corrections will be applied to the data sample to account for expected systematic inaccuracies. This will permit an accurate measurement of the beam polarisation from the data set.

A distribution of flight-times (TOF_{12}) for particles within the reconstructed Monte Carlo sample, analogous to that presented in Figure 4.7 for data, is displayed in Figure 4.8. The predominant beam line species is the μ^+. A shift, relative to the data, of $\approx 0.8ns$ is evident. This is a result of acknowledged sources of uncertainty in the initial Monte Carlo beam generation emanating from:

1. Uncertainties in the initial pion momentum distribution. The momentum distribution of the pion beam was generated using a Monte Carlo simulation of 800 MeV protons on a titanium target. The data sample was acquired using the protons at an energy of 700 MeV. The transverse distribution was inferred from the geometry of the target, and by assuming that the aperture of Q1 was uniformly illuminated.

2. Uncertainty surrounding the field generated by the dipoles D1 and D2. This leads to an ambiguity in the momentum selection of the initial pion sample.

As a result, a TOF_{12} selection window, differing from that used for data, is enforced. However, to maintain consistency this window is of the same width and is again applied around the maximum of the assumed "μ^+" peak. This corresponds to $29.3 < TOF_{12} < 30.2ns$.

The true Monte Carlo was generated with a fully polarised μ^+ beam. The channel geometry will be identical to that of the data sample; only the beam line magnet settings will differ to allow polarisation selection via momentum selection. Hence, the EMRHit selection criteria, systematic uncertainties and correction factors derived from the Monte Carlo will still apply to the data. The Monte Carlo takes into account the depolarisation due to spin precession and multiple scattering, both effects are expected to be $< 1 \times 10^{-4}$ (Section 4.10.5).

Within MAUS the EMR detector volume is simulated using GEANT4. The MAUS Monte Carlo mimics real data, it contains noise modelling and knowledge of current misalignment limits, connector attenuation and calibration parameters for the EMR SAPMT and MAPMTs. These were obtained from previous physics runs and from the examination of cosmic muon data during the Step 1 stage of MICE. The experimental calibration procedure is detailed in [167] along with the specifics of the EMR simulation in MAUS. The performance of the EMR reconstruction code is examined in [172]. All known, low energy physics processes and interactions were included in the simulation, as were processes for intermediate and high energies for completeness. The digitisation model contains knowledge of the detector response and efficiency.

The G4Beamline [207] package has been used to simulate the beam line. Precision measurements of the beam line magnet and cooling channel detector positions were obtained through surveying of the MICE hall. The MAUS Monte Carlo framework uses the output from G4Beamline to recreate the MICE beam. Within the simulation used in this analysis beam line particles are generated by sampling from a binomial distribution. [186] gives details of the MAUS beam simulation and how this is integrated into the Monte Carlo generator.

Once the method is validated for a polarised Monte Carlo sample it can be applied to the unpolarised data. At the time of this study no polarised data was available, however, if MICE were to continue it would be necessary to study polarised data to complete this study and gain further insight into depolarisation in the channel.

4.7 Reconstructing Tracks in the EMR

The intention of this analysis is to construct a track fitting algorithm capable of deducing the total (3D) decay angle (θ_{fit}) between the incoming anti-muon and outgoing decay positron tracks for a given beam. Equation 4.12 can be utilised to obtain the average effective muon polarisation, P_μ, at the point of decay from a straight line fit to the resulting $(cos(\theta))_{fit}$ distribution for all positrons in the sample.

4.7.1 The Fitting Method

Tracks in the horizontally and vertically orientated bars are reconstructed and fitted independently. Figure 4.9 displays an example 2D ($x - z$) representation of a Monte Carlo decay in the EMR. The axes represent the dimensions of the EMR, where 0 mm is the very upstream of the cooling channel, and the individual points

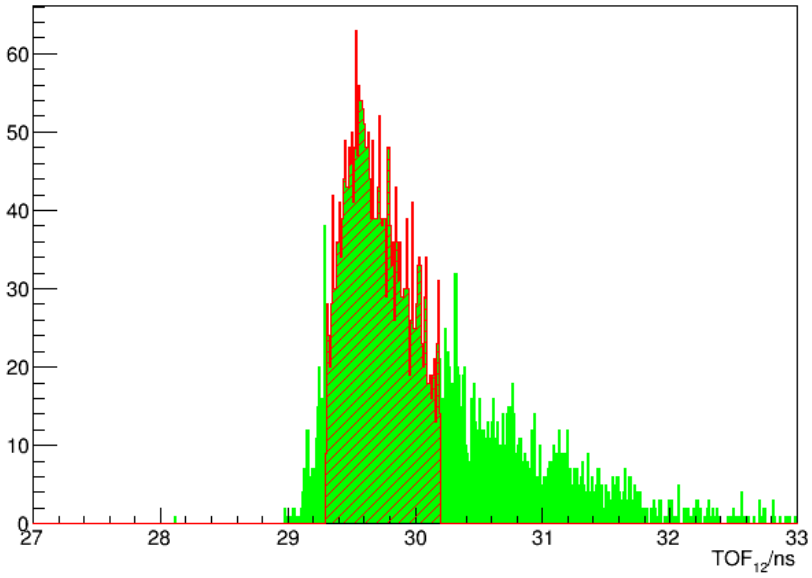

Figure 4.8: Distribution of times taken for single particles to pass from the upstream TOF1 detector to downstream TOF2 detector for the reconstructed (digitised) Monte Carlo. The largest peak corresponds to μ^+ with a smaller pion shoulder evident at ≈ 31.5 ns. A significantly smaller, single bin, of positrons is also apparent at ≈ 28.15 ns. A selection window (shaded red) is applied such that only particles falling in the centre of the largest ("muon") peak are used (i.e. $29.3 < TOF_{12} < 30.2ns$), providing a good simulacrum of the real data.

signify bar hits. The colour of each hit in the plot is proportional to the time-over-threshold, a measure of the energy deposited by that hit in the EMR bar (see Figure 4.5). A well-defined anti-muon track, parallel to the beam axis (z), is evident. A large energy deposit (the "Bragg" point) is observed at the point of decay and a subsequent decay positron track proceeds from that point at an angle (θ_x) relative to the anti-muon's initial direction. The same track will have an equivalent representation for the vertically orientated bars; an accompanying θ_y angle will be reconstructed. In order to reconstruct the total decay angle a track must be reconstructed in both orientations. A combined "3D" decay angle is then established using the method to be outlined in Section 4.7.9.

To ascertain the 2D decay angle of a specific positron track a "vector fit" method is utilised. The muon decay point (i.e. vertex) is determined and a vector is drawn between this point and each subsequent bar hit. The angles of each of these "vectors," relative to the initial muon vector, is established and placed in a histogram with each hit weighted according to the energy it deposits. The overall track angle is assumed to be the $\theta_{x,y}$ value of the bin possessing the most hits. Figure 4.10 gives a pictorial description of this method.

4.7.2 Dealing with Non-Axial Muon Tracks

Given the MICE muon beam has a non-zero angular divergence, some muons may arrive downstream slightly off-axis. To account for non-axial muons a separate fit is performed on the primary track to obtain the initial μ^+ track direction relative to the beam axis. The overall angle between the incoming μ^+ and outgoing positron is then deduced from the scalar product of the two fitted lines. The fitting procedure for the incoming track is identical to that for the decay track except that instead of using decay vertex as the seed point, the

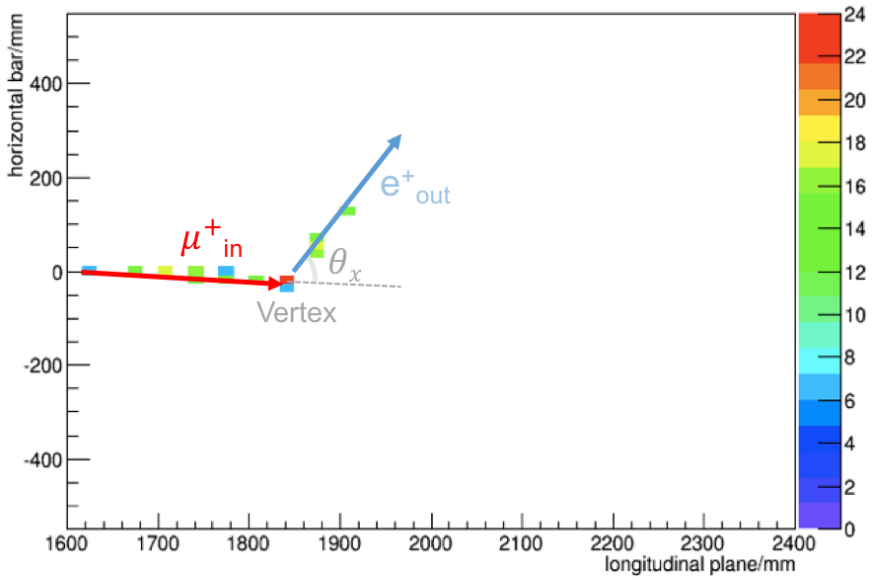

Figure 4.9: An example 2D visualisation from a reconstructed Monte Carlo sample showing muon decay within EMR. The bars are visualised as squares for simplicity here. A muon enters from the right and travels almost parallel to the axis before decaying at a point. The resulting decay positron then proceeds a short distance before being captured. Each point is an individual bar hit and the colour is proportional to the time-over-threshold of the hit. This example shows only the hits observed within horizontally orientated bars.

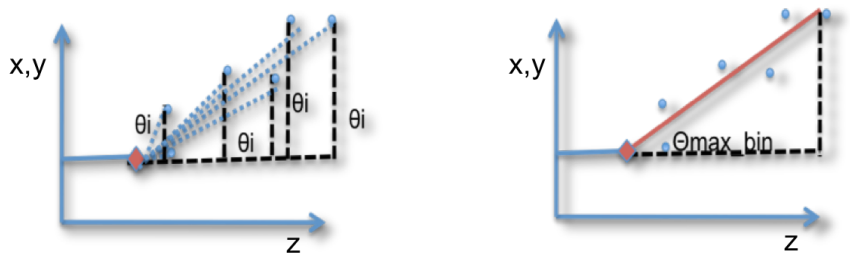

Figure 4.10: Pictorial depiction of fitting method: a vector is drawn from the muon decay point to each subsequent bar hit within both the vertical and horizontal orientated planes separately. An angle θ_x or θ_y is determined between the vector and the initial muon direction. These angles are then placed in a 1D histogram and the overall track angle is taken to be the bin-centre of the theta bin containing the most hits.

first point on the line is taken to be the first "muon" EMR hit.

4.7.3 Accounting for the triangular bars

The EMR bars are triangular in cross-section. In this analysis the co-ordinates of a given bar hit are the assumed centre-of-gravity of the triangular cross-section. This is located one third of the bar's height from its base, bisecting its width.

4.7.4 Separating Muon and Associated Electron Tracks

The EMR reconstruction code routines within the MAUS framework were unable to reconstruct secondary tracks with large transverse momentum. This would induce a bias into the angular measurements; therefore, this analysis develops a unique fitting routine using EMR hits from the raw data (EMRSpillData). Prior to

applying the fitting algorithms two lists are complied from the output data files, one encompassing all μ^+ tracks and a second containing the associated decay positron tracks. The splitting of the events into these two lists is done differently depending on whether the tracks are from true, i.e. MCEvents, or reconstructed, i.e ReconEvents, samples:

For True Monte Carlo

The EMRTracks within the "true" MCEvent contain a particle ID identifying tracks as either "positron" or "anti-muon." Any MCEvent which does not possess both tracks is removed from the analysis. In addition, the EMRTracks contains a list of EMRHits including both EMRHits resulting from primary μ^+s and their decay positrons. These are separated initially by placing a timing cut on the arrival times of the hits. Figure 4.11 displays the distribution of arrival times of all EMRHits in the simulated Monte Carlo relative to the time at which the primary particle was generated i.e. EMR Hit Time $= t_{hit} - t_{primary}$.

Figure 4.12 shows how the relative composition of particle tracks varies as a function of EMR Hit time. Any hits recorded with $t > 100$ ns are tagged as positron candidates. Anything arriving prior to $t < 80$ns is tagged as a possible muon. The muon arrival at the EMR is at ≈ 60 ns, relative to the primary muon generation. This arises due to the time-of-flight of muons from the generation point to the EMR. An incoming muon can have some contamination associated with it (e.g. knock-on electrons), consequently, a 20 ns "safety window" is employed. Particles observed after 100 ns are assumed to be the outcome of a decay, however, come contamination may be present. The muons which remain at $t > 100$ns will have deposited most of their energy and are not likely to produce digits. Only tracks which have successfully produced reconstructed digits will be used in this analysis.

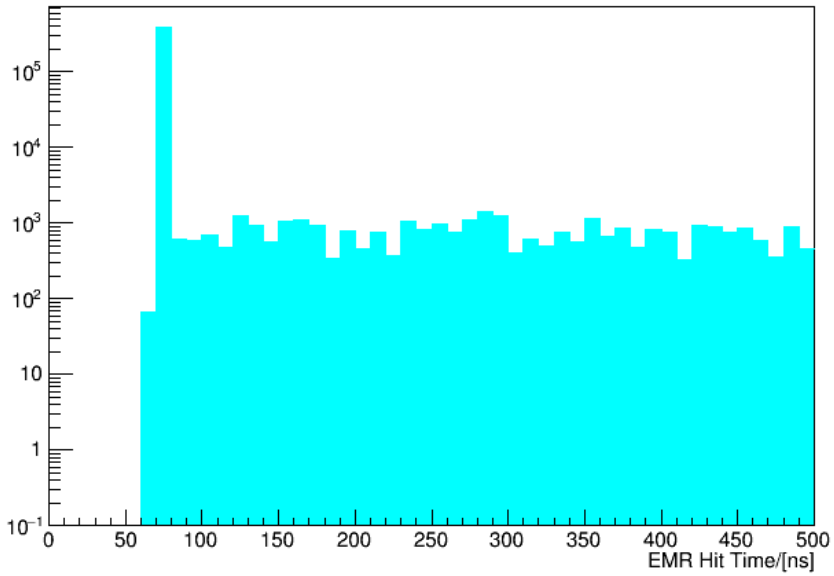

Figure 4.11: Distribution of arrival times of all the hits at the EMR for all MCEvents in all Spills of the true Monte Carlo sample. These times are relative to the time at which the primary particle was generated. Hits arriving at time < 80 ns are assumed to be muons.

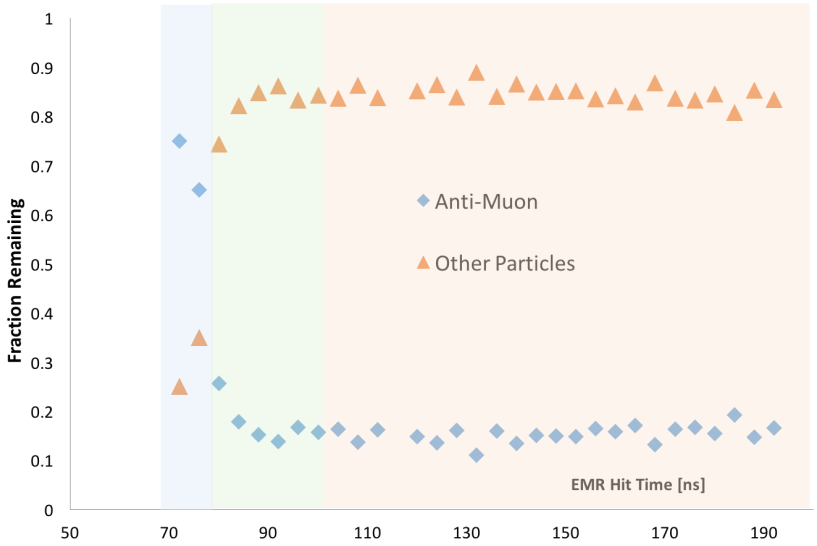

Figure 4.12: Plot displaying the fraction of particle tracks which are muon (blue) and non-muon (orange). The green region corresponds to the "safety window." Hits recorded with $t > 100$ ns are identified as possible positrons but further cuts are required in both regions to reduce contamination. Hits with $t < 80$ns are assumed to be muon.

To improve sample purity in both regions, a track energy deposit density factor, ρ_{Edep}, is calculated to aid further separation of muon and electron tracks. ρ_{Edep} is defined such that:

$$\rho_{Edep} = \frac{E_{dep}}{z_f - z_i}, \tag{4.32}$$

where E_{dep} describes the total energy deposited throughout the track in terms of the EMRHit time-over-threshold and $z_f - z_i$ denotes track length. Figure 4.13 shows the energy deposited by particles in the $t > 100$ "positron" region. It is necessary when enforcing any cut on ρ_{Edep} that, not only is muon contamination reduced, but that the loss of true positrons is minimised. A selection criterion of $\rho_{Edep} > 0.0026$ removes 99.8% of muon impurities with a loss of $< 1\%$ of viable positron tracks. However, some pion contaminants remain. These will not form viable track candidates and will fail the necessary "mother+daughter" criteria to reconstruct a decay.

Figure 4.14 shows an analogous plot for the selected "muon" region. Here a cut of $\rho_{Edep} < 0.012$ is used to reduce positron and pion contamination. The muon purity in the remaining tracks is 98.02%. Some viable muon tracks are lost by this strict cut, however, these correspond to only 2% of total muon with $t < 80$ns.

An electron-muon separation efficiency $\epsilon_{\mu+e}$ is defined as the probability that a MCEvent, which is known to have both mother and daughter MCEvent Tracks, is successfully found to have both when applying the algorithm to true MCEvent EMRHits. A $\epsilon_{\mu+e} = 90\%$ is derived, with applicable selection criteria enforced, showing the algorithm has good efficiency for identifying the primary and secondary particles. The main source of the loss of viable candidate events is the use of the 20 ns "safety window" employed here to avoid contamination from knock-on electrons. This is, however, an essential restriction as the accidental inclusion of these events will have detrimental effects on the analysis.

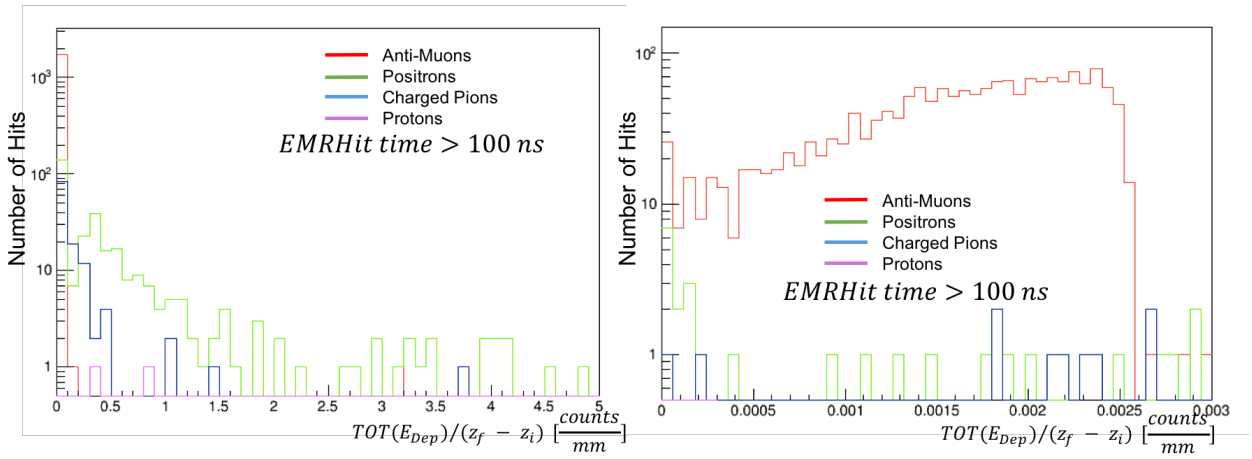

Figure 4.13: Plot shows distribution of the energy deposit density (ρ_{Edep}) taken from true Monte Carlo Tracks for muons, positrons, pions and protons in the "positron" region. Clear shape differences are visible. A selection cut of $\rho_{Edep} > 0.0026$ is applied to remove remaining undecayed muons from the sample. Some pions remain, these will produce different event signatures from the muon decay positrons and will be removed later in the analysis.

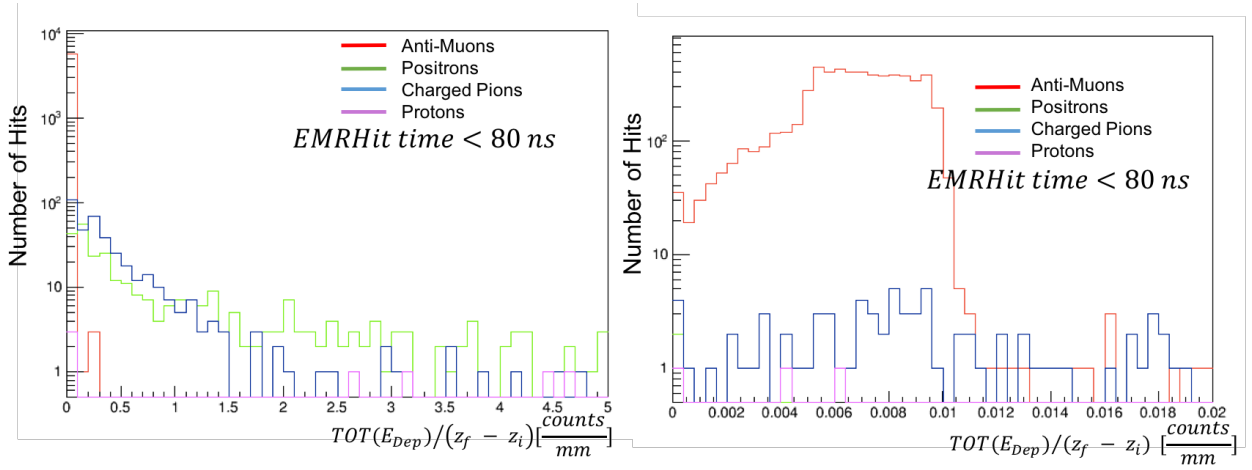

Figure 4.14: Plot shows distribution of the energy deposit density (ρ_{Edep}) taken from true Monte Carlo Tracks for muons, positrons, pions and protons in the "positron" region. Clear shape differences are visible. A selection cut of $\rho_{Edep} < 0.012$ is applied to remove positron contaminants from the sample. Some pions remain, these will produce different event signatures from the muons and will be removed later in the analysis.

For Reconstructed Monte Carlo and Data

Finding the separate anti-muon and decay positron tracks within the ReconEvent data structure is more complicated:

1. A primary "μ^+ list" is compiled by looping over all the EMREvents in a given ReconEvent in a specific Spill. For each EMREventTrackArray the first EMRTrack will be the mother particle and the hits associated with this track can be directly added to a "μ^+ list". A separate timing list is compiled to be used later to associate secondaries to the correct primary μ^+; this list is index by Spill and ReconEvent number.

2. A "positron list" is subsequently accumulated using the information stored in the EMRBarHitArray of the EMRSpillData branch. The arrival time of each EMRBarHit is retrieved and compared to the time of the "mother" track in that event using timing information amassed in the preceding step. EMRBarHits with time later than the last muon hit in the event and earlier than the first muon hit in the next event are then attributed to "positron" tracks and added to the list. They are numbered and tagged accordingly.

A reconstruction efficiency, $\epsilon_{\mu+e}$, can be calculate for reconstructed Monte Carlo and is established as 89%. This is the probability that a event which is known, from MC Track information, to contain both mother (muon) and daughter (positron) tracks is successfully identified has having both.

4.7.5 Example tracks: True and Reconstructed MC

Figures 4.15 and 4.16 display examples of the differentiated μ^+ and decay e^+ tracks in both horizontal and vertical planes in the EMR for the same event.

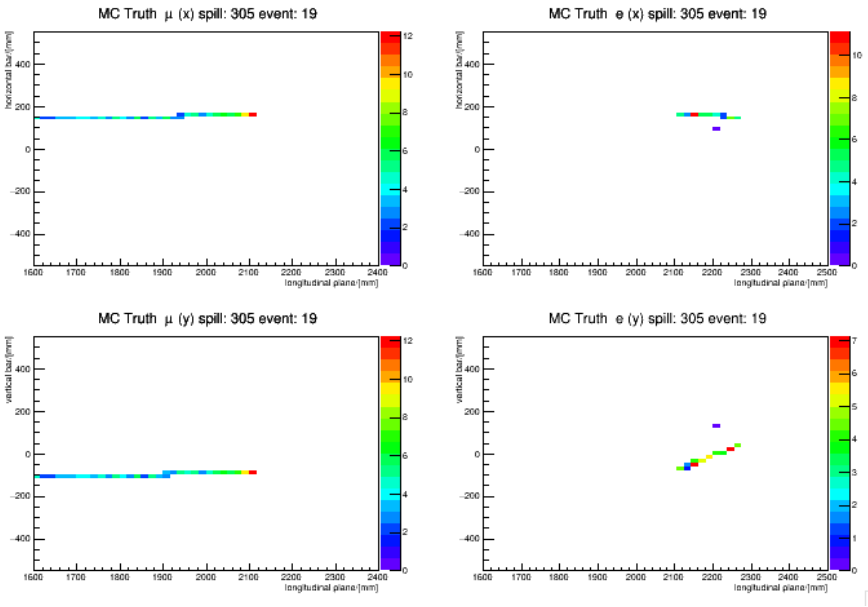

Figure 4.15: Four 2-D histograms (weighted by time of arrival) showing visualisations of event displays for the primary muon track (left panel) and decay positron track (right panel) in the EMR in both the horizontal (top) and vertical (bottom) orientations. These hits are derived from "true" Monte Carlo EMRHits, so are independent of the detector resolution.

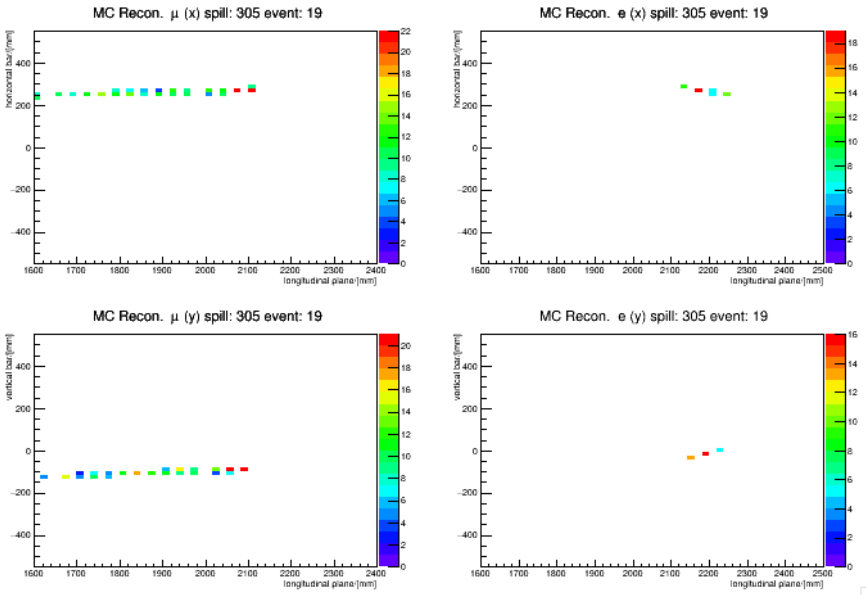

Figure 4.16: Four 2-D histograms (weighted by time of arrival) showing visualisations of event displays for the primary muon (left panel) and decay positron (right panel) in the EMR in both the horizontal (top) and vertical (bottom) orientations This plot shows the bar hits from reconstructed Monte Carlo bar hits for the same event as displayed in Figure 4.15 for true Monte Carlo. The reconstructed Monte Carlo has been digitised to imitate real data and include knowledge of the detector geometry and reconstruction models. There is an offset in x co-ordinate as can be seen from comparison between these plots and those in Figure 4.15. This is a result of a known misalignment in x relative to the beam centre and will not effect the results of this analysis.

4.7.6 Track Selection

Prior to fitting the EMR hits resulting from both data and Monte Carlo samples a number of selection criteria are enforced. These help to improve the accuracy of the derived θ_{fit} and remove impurities emanating from noise or contaminant particles. In the following discussion the track selection criteria are separated according to there purpose:

Producing a Viable Muon and Positron Track

1. **"Mother + Daughter" Cut** : Ensures both a "mother" (μ^+) primary track and an associated "daughter" positron are present. This is a definitive criterion for a viable analysis of hits derived from "data", "MC truth" and "MC Recon."

2. **"Digits Cut"**: Horizontal and vertical orientations are reconstructed and fitted separately. A requirement of ≥ 3 bar hits in both the orientations is applied. This removes events in which the particle travels down a bar and thus cannot be reconstructed in both directions. Inclusion of such events leads to singularities in the fit. This also aids reduction of cosmic muon background which have higher fluxes in the vertical direction.

Improving Track Resolution

1. **Goodness-of-Fit ("Window Cut")**: The fitting procedure is outlined in Section 4.7.1. For a given track a distribution of hit angles, θ_i, is expected around a mean angle, θ_{fit}. Examples of two tracks, and their corresponding hit angle distributions, are shown in Figure 4.18. One limitation inherent in this vector fitting method is the finite bin width in these plots. In the following study 100 bins are used across a 4π angular spread, giving a bin width of $4\pi/100$ (=0.125 rad).

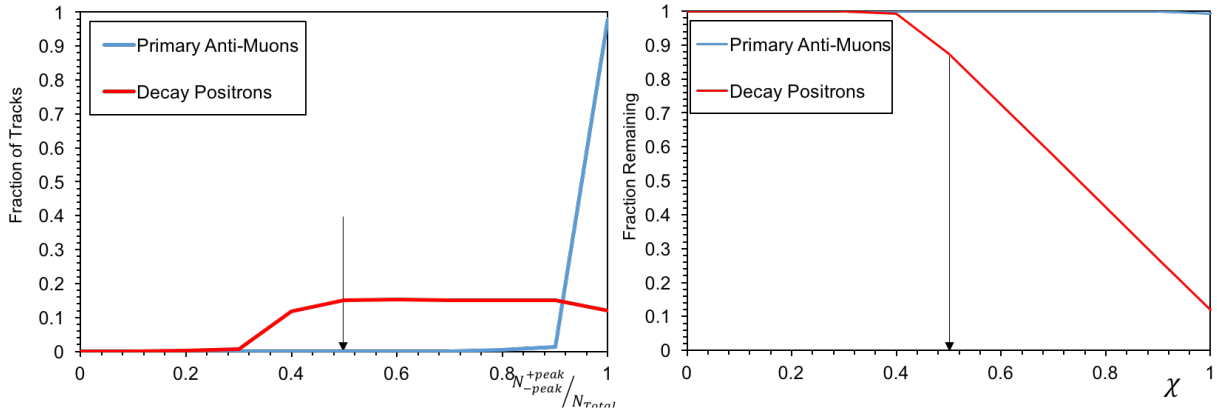

Figure 4.17: (left)Distribution of fraction of reconstructed Monte Carlo tracks (vertical axis) as a function of fraction of tracks in selection region of $N_{peak} \pm 2$ bins (horizontal axis) (right) Tracks remaining when a cut of $N^{n_{peak}+n}_{n_{peak}-n}/N_{Total} \geq \chi$ is placed on the same sample. The distributions for the decay positron and the primary μ^+ are presented. The primary muons follow very straight tracks with the majority remaining on-axis. The decay positrons have a larger angular spread and may shower in the detector. Hence the cut, indicated by the arrow, is imposed upon all positron tracks in this analysis.

A "goodness of fit" criteria will be enforced on the average deviation from θ_{fit} permitted in each track. A parameter is defined, such that

$$\frac{N^{n_{peak}+n}_{n_{peak}-n}}{N_{Total}} \geq \chi \tag{4.33}$$

where $N^{n_{peak}+n}_{n_{peak}-n}$ is the bin content in the range $\pm n$ bins from the peak bin n_{peak} and N_{Total} is the total number of hits in the track. Thus, 2 parameters, χ and n must be chosen and optimised to ensure θ_{fit} is a good representation of the track angle. In the following analysis $\chi = 0.5$ and $n = 2$ bins corresponding to tolerance of $\pm$ 0.3 rad from $(\theta_{fit})_{x,y}$. This provides a resolution of $(5 \times 0.125)/4\pi = 0.05$ rad on the measured decay angle. Section 4.8.3 presents justification for these in terms of the resulting track resolutions. Figure 4.17 shows the distribution of track $\frac{N^{n_{peak}+n}_{n_{peak}-n}}{N_{Total}}$ as well as the cumulative effect enforcing varying values of χ has on the reconstructed Monte Carlo.

The fitting algorithm is set-up such that it is always the smallest angle between the two tracks which is chosen as the "decay angle." To account for the periodicity of the angular range in the vector angle plot, the bin content of the 2 bins preceding and including $+\pi$ and the bin including $-\pi$ and the following 2 bins are combined and considered together. This is to avoid vetoing viable tracks in that region. Figure 4.19 shows an example event display for a backwards going positron track along with

the associated vector angle plot.

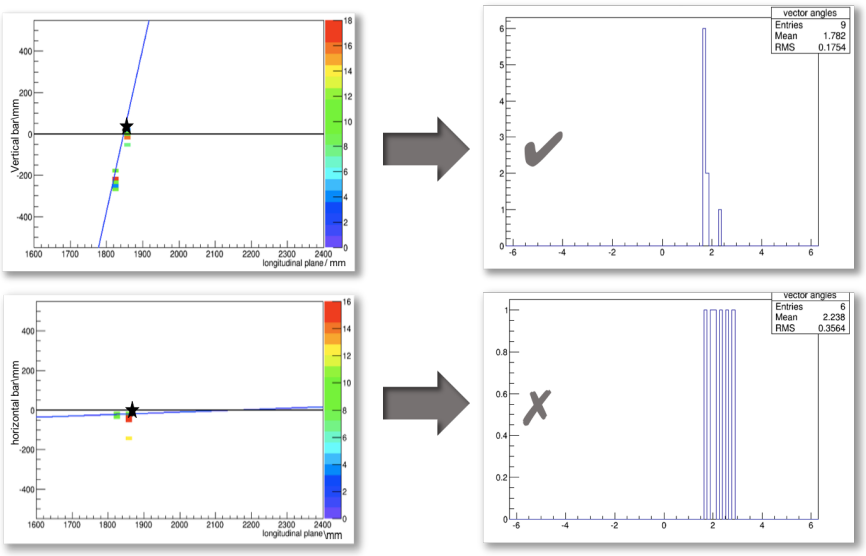

Figure 4.18: Two example decay positron tracks, taken from digitised Monte Carlo, with the track fit shown in blue; the derived vertex is represented as a black circle. The distribution of vector angles is presented in the adjacent plots. In the top example the track is well-defined and the fit line is a good representation. This track passes the "window cut," a measure of the goodness of the fit. For the bottom track the overall track angle is harder to deduce; this track rejected by the "window cut."

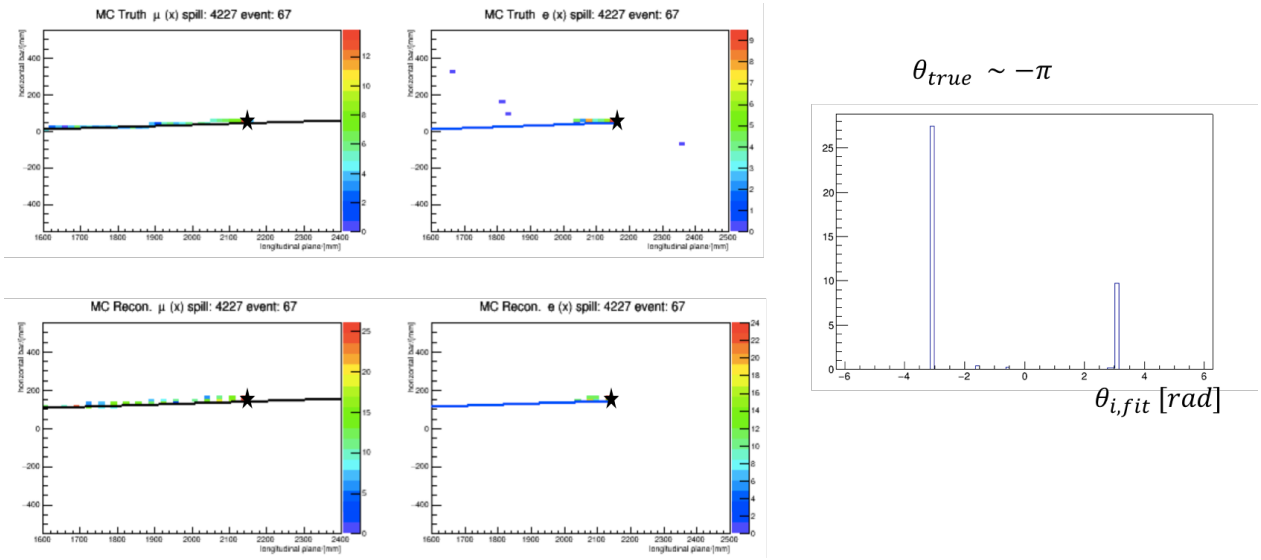

Figure 4.19: An example of a backwards going positron produced nearly on-axis. The track hit angles plot is also shown. There are two peaks visible at $\approx \pm\pi$. These two bins and those ± 2 bins either side of $\mp\pi$ are combined and the contents are considered together within the "window cut." This track is successfully reconstructed without this correction.

2. **"Fiducial Cut"**: It is required that the μ^+ decays at least 5 bars from the edge of the EMR. Attempting to fit positron track initiated too close to the edge of the fiducial volume of the detector may bias the measurement as the complete track would not be visible. Figure 4.20 shows an example of a subset of the true Monte Carlo derived vertex (decay point) positions for horizontal planes. Tracks with vertices outside of the orange square are not fitted. Section 4.8.3 indicates a considerable improvement

in track resolution is achieved through imposing this criterion.

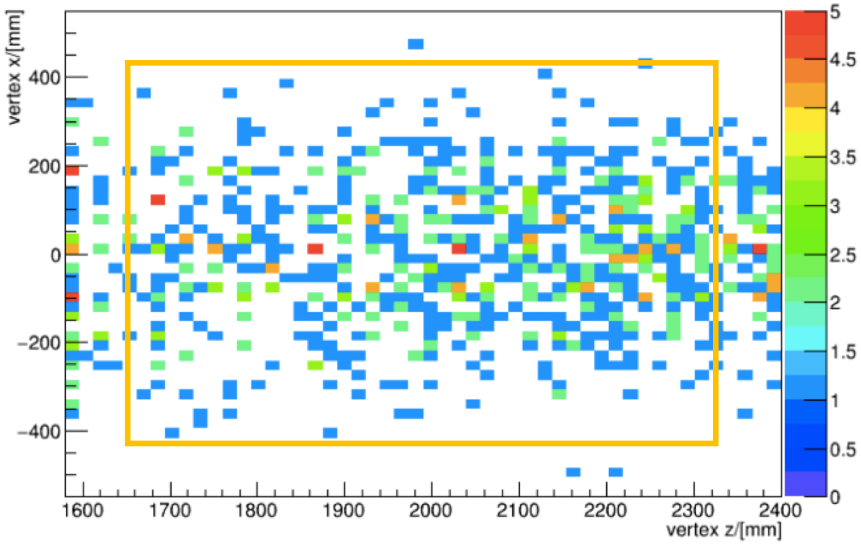

Figure 4.20: Subset of derived vertex positions. A fiducial cut is placed such that anything outside of the orange square is rejected from the analysis.

Noise Rejection in Positron Tracks

Electron contaminants, resulting from noise or early muon decays, will produce electromagnetic showers in the EMR. The resulting hits will have disconnected and multiple tracks widely spread throughout the detector, possibly appearing far downstream in the fiducial volume, without any visible tracks upstream. Muons, on the other hand, exhibit uniformly deposit significant amounts of energy along its trajectory prior to stopping or exiting the detector. There is also the possibility of cosmic muons entering, and decaying within the EMR. Two selection criteria are enforced to enhance the fitting algorithm's capability for noise rejection:

1. A selection criterion is applied to the distance (Δr_{hit}) between positron hits deemed consecutive in time such that: $\Delta r_{hit} = \sqrt{\Delta x^2 (\text{or} \Delta y^2) + \Delta z^2} < 45$ mm, for hits in either horizontal (or vertical) planes. The combined distribution of Δr_{hit} for both transverse directions (x and y), for all particles in the reconstructed Monte Carlo set, is presented in Figure 4.21. This cut acts to increase the accuracy of noise rejection and is applied to all samples.

   Figure 4.21 shows the distribution of all "decay positron" hit candidates in the reconstructed Monte Carlo sample (purple) along with the true Monte Carlo distribution for a pure decay positron sample (green). The reconstructed Monte Carlo contains a noise model and aims to mimic the data.

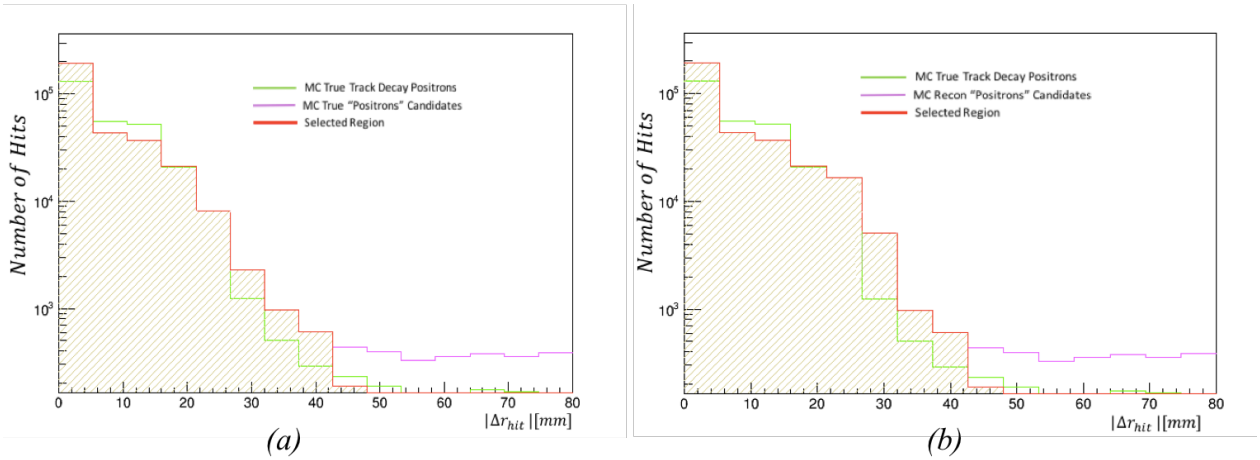

Figure 4.21: Distribution of distances between hits deemed consecutive in time for all hits in "positron" candidate tracks in the (a) true Monte Carlo EMRHits and (b) reconstructed Monte Carlo BarHits samples. The green line represents the true Monte Carlo distribution for a positron only sample selected via matching the spill and event numbers to the MC True Track. This plot is made after e/μ separation but prior to any other selection criteria. The Monte Carlo contains a noise model which mimics data. The reconstructed Monte Carlo contains knowledge of the detector response and geometry. A requirement of $|\Delta r| < 45mm$ is enforced.

2. Additional selection criteria are applied to the time difference between all consecutive hits: $|(\Delta t_{hit_{i,i-1}})| < 2.5ns$ and $|(\Delta t_{hit_{i+1,i}})| < 2.5ns$ (i.e. 1 ADC count). The aim being to reject noise initiated by cosmic muons and their decay products or other particles arriving significantly later (or earlier) than the assumed μ^+ or decay positron track could have. Figures 4.22(a) and 4.22(b) display the distribution of $|(\Delta t_{hit_{i\pm1,i}})|$ for true Monte Carlo and reconstructed Monte Carlo respectively following the application of the Δr_{hit} cut. The green line represents the true Monte Carlo distribution for a pure decay positron sample.

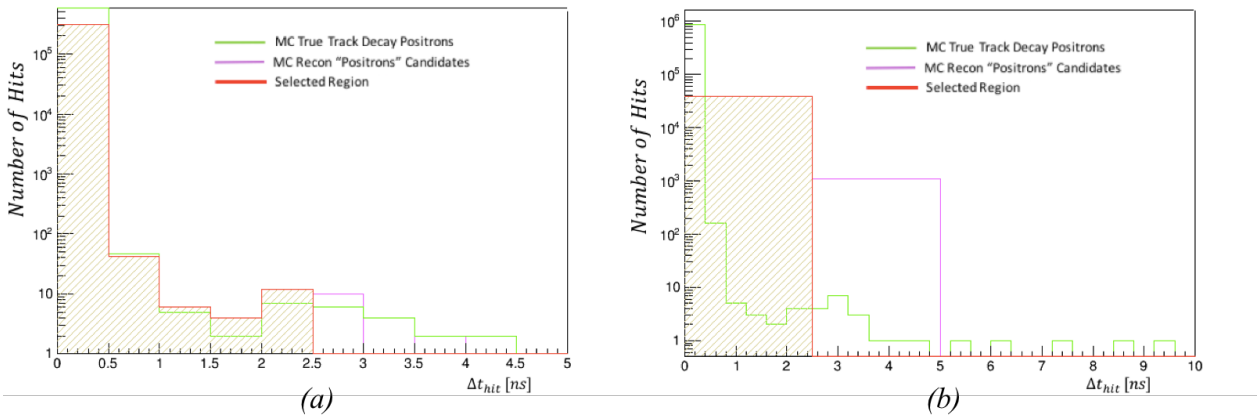

Figure 4.22: Distribution of time difference for consecutive EMR hits from (a) Monte Carlo true EMRHits and (b) reconstructed Monte Carlo EMR BarHits for all "positron" candidates found using the e/μ tagging and separation methods in the samples. The green line represents the true Monte Carlo distribution for a positron only sample selected via matching the spill and event numbers to the MC True Track. Some noise/contamination is removed from the tails of both sample by enforcing that $|(\Delta t_{hit_{i,i-1}})| < 2.5ns$ and $|(\Delta t_{hit_{i+1,i}})| < 2.5ns$.

The combination of these two criteria removes 10.4% of tracks which pass the initial e/μ separation cuts.

Limiting Particle Contaminants

1. **Time-of-Flight cut**: The preceding list of track selection criteria mainly focus on ensuring accuracy in the fitting procedure, i.e. by removing any poorly reconstructed or noisy tracks. It is also necessary to remove any remaining pions from the selected primary particles list; this is done via the TOF_{12} cut. The specific criterion imposed is dependent upon the input beam momentum, thus, it differs for Monte Carlo and data samples. Justification for the choice of time-of-flight window for the data and Monte Carlo was presented in Sections 4.6.1 and 4.6.2 respectively. TOF1 and TOF2 are separated by 9.4 m and a minimum ionising muon will lose $\approx$ 2 MeV/c i.e. $\approx$ 1% [172] of its momentum in between the TOFs. The use of the TOF_{12} time as a form of PID is based on the assumption that momentum remains approximately constant and that the path length is given by the orthogonal distance between the two TOF detectors. A sample purity can be calculated from comparison between the reconstructed and true Monte Carlo samples. This allows the amount of electron/pion contamination which exists in the selected region to be calculated. A purity of 99.58% is achieved. Given the respective TOF_{12} cuts for data and Monte Carlo were chosen to select analogous regions it is assumed that purity attained in the data through enforcing the TOF_{12} criterion will, therefore, be 99.58%. This is after all preceding selection criteria have been enforced.

Table 4.1 documents how each selection criterion effects the total number of "use-able" tracks in the samples. Additionally, the impact on fitted track resolution which results from imposing each cut is discussed in Section 4.8.3.

Cut	MC Truth	$-\Delta\%$	MC Recon.	$-\Delta\%$	Data (07417)	$-\Delta\%$
Has TOF_{12}	N/A	N/A	1034	N/A	1652	N/A
Passes TOF_{12} muon selection	N/A	N/A	606	41.4	1193	26.4
has muon+positron+vertex	924	N/A	606	41.4	1193	26.4
$\Delta r_{hit} < 45mm$	875	5.3	554	46.4	987	39.1
$\Delta t_{hit} < 2.5ns$	869	5.9	548	47.0	968	40.2
passes "digits cut"	858	7.1	521	49.3	944	41.8
passes "fiducial cut"	829	10.3	463	55.2	732	54.8
passes "window cut" in x	824	10.8	449	56.5	698	56.9
passes "window cut" in y	822	11.0	443	57.1	652	59.8
Total selected	**822**	**11.0**	**443**	**57.1**	**652**	**59.8**

Table 4.1: Table documenting the effect imposing the selection criteria outlined has on the number of positron events remaining in each sample for the data, true and reconstructed Monte Carlos. Different TOF cuts were used for MC and Data due to different beam line settings. The total percentage decrease is also detailed with similar performance observed in reconstructed MC and data. A factor of 2 difference between True and Reconstructed MC is to be expected as a consequence of the True sample having no knowledge of the detector geometry.

4.7.7 Finding the Vertex

The vertex (μ^+ decay point) is reconstructed in the $x-z$ and $y-z$ planes independently and is taken as the centre of the EMRBarHit in the μ^+ track with the greatest time-over-threshold i.e. energy deposit. Once a vertex is found in both orientations, the z positions are combined and the furthest downstream value is taken to be the z co-ordinate of the vertex in both planes. Figure 4.23 shows an example decay obtained from the true Monte Carlo EMRHits. The fit to the off-axis primary μ^+ and to the decay e^+ are presented. The derived decay point is indicated by the star.

.

4.7.8 Vertex Resolution

A "vertex resolution," denoted as δ_x for the transverse co-ordinate and δ_z for the longitudinal co-ordinate, may be computed, such that,

$$\delta v_x = x_{true}^{vertex} - x_{fit}^{vertex} \tag{4.34}$$

and

$$\delta v_z = z_{true}^{vertex} - z_{fit}^{vertex}. \tag{4.35}$$

These provide a measure of how accurate the method, outlined in Section 4.7.7, calculates the decay

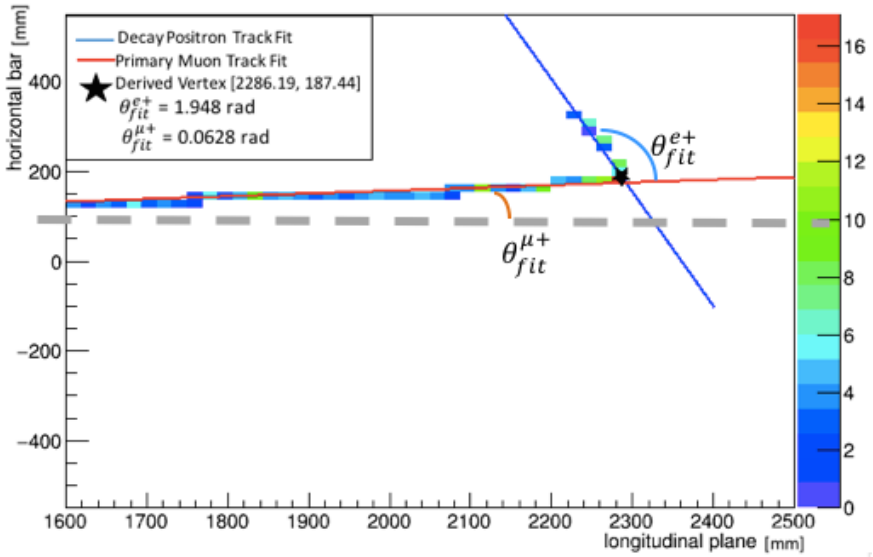

Figure 4.23: Example of a non-axial muon decaying to a positron in the fiducial volume of the EMR detector. The incoming μ^+ and outgoing positron are fitted independently and the derived vertex position, assumed to be the bar in which the muon deposits its maximum energy, is represented by the star. The legend presents the two derived fit angles. The μ^+ angle is taken relative the the z axis and the e^+ angle is taken relative to the μ^+ track fit line.

point, v, in a given orientation, where $v = [z^{vertex}, x^{vertex}]$ or $v = [z^{vertex}, y^{vertex}]$. x^{vertex}_{true} and z^{vertex}_{true} are taken directly from the initial position of the positron Track within the MCEvents. The fit method outlined is then applied to the EMRHits associated with that same MCEvents; x^{vertex}_{fit} and z^{vertex}_{fit} are the vertex co-ordinates derived.

Figures 4.24a and 4.24b display distributions of the vertex resolution for transverse (x or y) and longitudinal (z) co-ordinates respectively for the true Monte Carlo sample. The transverse co-ordinate (Figure 4.24a) is symmetric and centred around 0 mm with an RMS of 1.2 mm. Given that an EMR bar spans 33 mm in the transverse direction, this is well within the limits of the detector, implying a good level of accuracy can be achieved with this method of vertex reconstruction.

The distribution of the longitudinal vertex position resolution (Figure 4.24b) is asymmetric as a result of the triangular bar geometry. The distribution is centred on the geometric centre of the triangular cross-section of the EMR bar (5.7 mm). An RMS of 4.11 mm is measured. The thickness of the each EMR bar in the longitudinal direction is 17 mm; suggesting the vertex reconstruction used in the analysis is accurate, within the limits of the detector.

Figures 4.25a and 4.25b show how the vertex resolution, δv_x and δv_z, vary with θ_{true}. Both plots show flat distributions, within the statistical errors. Thus, the vertex finding algorithm will not introduce any systematic angular bias in the accuracy of the track fitting.

4.7.9 Finding the Total Decay Angle

The particle tracks are reconstructed and fitted separately in both the horizontal and vertical orientations. A combined 3D $(cos(\theta))_{fit}$ can then be derived. The effective muon beam polarisation upon decay will be

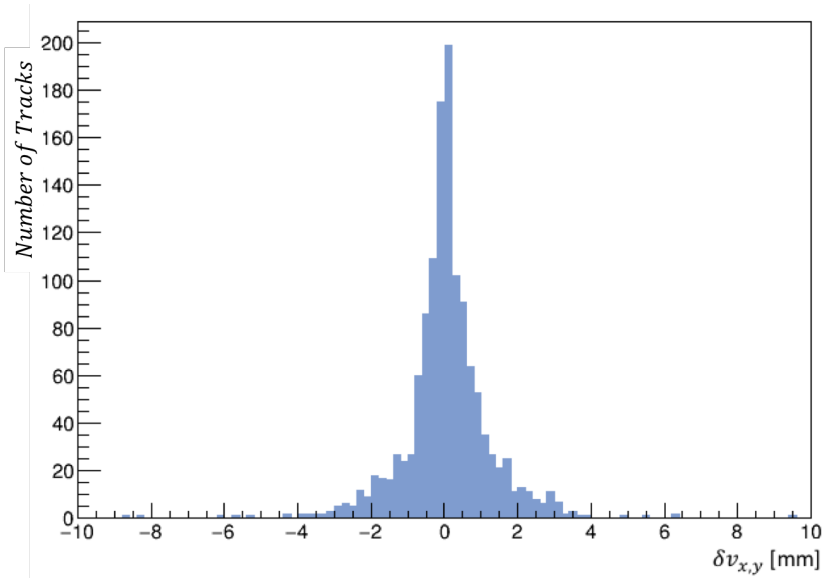

(a)

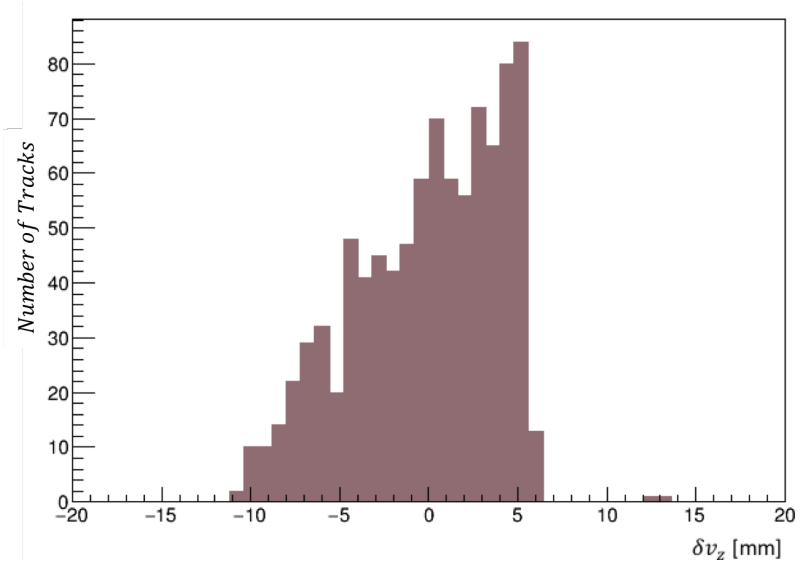

(b)

Figure 4.24: Distribution of the calculated differences in (a) the transverse position (x or y) and (b) longitudinal (z) position of the derived vertex as calculated by the method outlined in this thesis and that obtained directly from the true MCEvent Tracks. In (a) the distribution is symmetric and centred at ≈ 0 mm suggesting no obvious bias and the RMS of ≈ 1.2 mm indicates that given the dimensions of the EMR bars, the method accurately predicts the vertex position within the detector limits. In (b) the distribution is asymmetric it is centred around the geometric centre of the triangular bar (5.7 mm) ; an RMS of ≈ 4.1 mm is calculated. Given the dimensions of the EMR bars, the method can accurately predicts the vertex position, within the detector limits. The distribution is asymmetry due to the triangular geometry of the bars

determined by fitting a straight line to the resulting distribution and applying Equation 4.12. Figure 4.26 gives a pictorial representation of the reconstruction for an example decay in 3D.

This overall track angle is found by calculating the scalar product of the track fits to the positron and anti-muon tracks. For a given track, fitted in both x and y with derived angles θ_x and θ_y, a track vector, $\vec{r}_{track}$, can be computed:

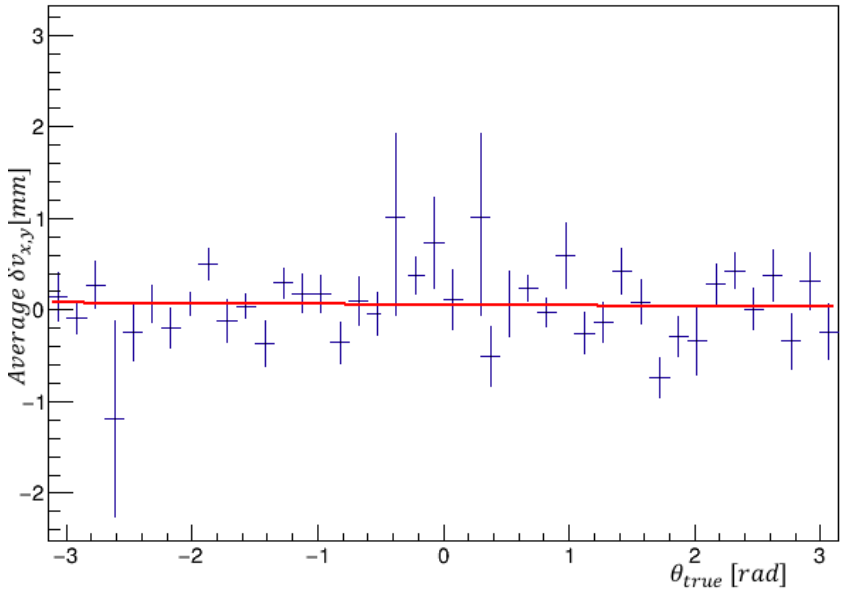

(a)

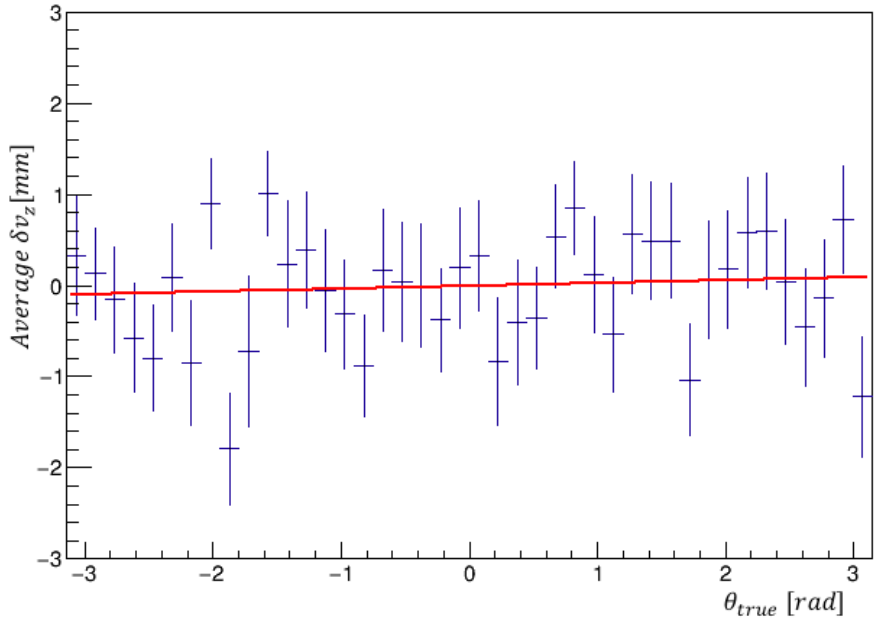

(b)

Figure 4.25: Profile plots showing the average vertex residuals in the (a) transverse and (b)longitudinal vertex co-ordinates against θ_{true} for both $x-y$ orientations. Line fits of the form $y = mx + c$ have been fitted to each. For: (a) values of $m = -0.0611 \pm 0.07$ and $c = 0.0083 \pm 0.0013$ and is consistent with a flat line with $\chi^2/ndf = 1.0$. For (b) $m = 0.04 \pm 0.044$ and $c = -0.00756 \pm 0.01956$ with $\chi^2/ndf = 1.47$.

$$\vec{r}_{track} = [sin\theta_x \cdot cos\theta_y, sin\theta_y \cdot cos\theta_x, cos\theta_x \cdot cos\theta_y]. \tag{4.36}$$

The scalar product between the two fitted particle tracks, $\vec{r}_\mu$ and $\vec{r}_e$, is then

$$\vec{r}_\mu \cdot \vec{r}_e = |\vec{r}_\mu||\vec{r}_e|(cos(\theta))_{fit}, \tag{4.37}$$

rearranging to find an expression for $(cos(\theta))_{fit}$, gives:

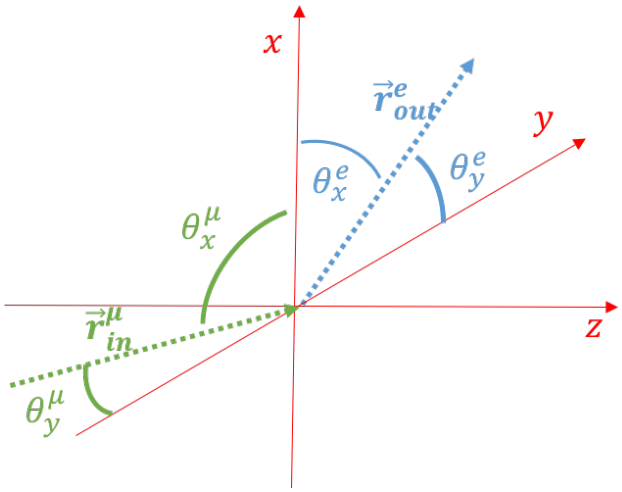

Figure 4.26: Diagram defining the various angles in 3D space required for 3D reconstruction of the track in the EMR.

$$\frac{\vec{r_\mu} \cdot \vec{r_e}}{|\vec{r_\mu}||\vec{r_e}|} = (cos(\theta))_{fit}. \tag{4.38}$$

This corresponds to the cos(θ) described in Equation 4.12.

4.8 Angular Fit Quality

The preceding sections outlined a technique for fitting both the primary μ^+ and decay positron tracks as well as establishing the point at which the decay took place. The technique intends to derive the 3D cos(θ) of the outgoing positrons, relative to their "mother" μ^+ tracks and establish the muon beam polarisation at decay. Prior to doing so the limitations in the fitting algorithms must be evaluated. Comprehension and correction of the underlying systematics, inefficiencies and possible biases is essential in order to obtain an accurate measure of P_μ for real data (Section 4.9).

4.8.1 Definitions

Throughout this analysis three terms are used to indicate the origin of a quantity or parameter:

1. "True" - defines an angle or track parameter obtained directly from the Monte Carlo Track information. If a parameter is referred to as "true" it is independent of both the fit and the digitisation/detector model.

2. "Fit-True" - the "true" value as detailed in the preceding definition, however, this term denotes a "true" value of a successfully fitted track. This is used when comparing a "true" parameter with the corresponding parameter for the fit to the EMR hits and is useful when quantifying accuracy and efficiency of the fitting algorithm.

3. "Fit" - This refers to a track parameter or angle which is derived purely from the fitting algorithms outlined in this analysis. The fitting method can be applied to tracks comprising of both true MCEvent EMRHits or reconstructed BarHits.

4.8.2 Track Resolution

The track angular resolution ($\Delta\theta^{track}$) is defined as the difference between the true angle $(\theta^{track})_{true}$, as calculated directly from the Tracks in the Monte Carlo MCEvents, and that derived from fitting to EMR hits using the procedure presented in the preceding section, $(\theta^{track})_{fit}$:

$$\Delta(\theta^{track})_{x,y} = (\theta^{track}_{fit} - \theta^{track}_{true})_{x,y}. \tag{4.39}$$

Figure 4.27a and Figure 4.27b show the distribution of the $\Delta\theta^{track}$ resulting from fits to true MCEvent EMRHits, for horizontally and vertically orientated EMR planes respectively. Gaussian fits were performed on the distributions; means consistent with 0 are obtained for both orientations. σ_x is found to be 0.133 $\pm$0.003 rad and σ_y is 0.133 $\pm$ 0.004 rad; these are equivalent, within derived errors. Consequently, no bias, in terms of angular resolution, towards a given orientation is anticipated.

Figures 4.28a and Figure 4.28b display the resulting $\Delta\theta^{track}$ distribution for tracks derived from reconstructed Monte Carlo BarHits, in x and y orientations respectively. Gaussian fits are performed on both distributions and means consistent with 0 and measurements of $\sigma_x = 0.224 \pm 0.015$ rad and $\sigma_y = 0.209 \pm 0.012$ rad are obtained. These track resolutions, although larger than those associated with the true Monte Carlo sample, are still consistent with each other. The resolutions in both orientations are equal, within the statistical errors. As a result, no bias in the accuracy of the reconstruction towards given orientation is expected.

As stated in Section 4.6.2 the true Monte Carlo sample has no dependence upon the digitisation/reconstruction model or detector resolution. Therefore, the non-perfect resolution in the fit to the true Monte Carlo EMRHits is a consequence of decay positrons scattering in the detector. Comparing the resolution obtained for true Monte Carlo tracks to that for reconstructed Monte Carlo implies that the effect of scattering on the track resolution is roughly as significant as the contribution due to limitations which result from detector geometry, assuming a track 10 bars in length and a resolution of $\tan(\theta) = 1/10 \approx \theta \approx 0.1$ rad. The RMS values calculated for the reconstructed Monte Carlo tracks are, therefore, consistent with the expected resolution given the restrains of the EMR geometry and the resolutions obtained for the true Monte Carlo.

Sample	σ_x/[rad]	σ_y/[rad]
MC True	0.133 $\pm$ 0.003 rad	0.133 $\pm$ 0.004
MC Recon.	0.224 $\pm$ 0.015	0.209 $\pm$ 0.012

Table 4.2: Summary of measured track resolutions for both true Monte Carlo, i.e. fitting algorithm is applied to EMRHits from MCEvents, and reconstructed Monte Carlo, i.e. fits to BarHits derived from digitised Monte Carlo ReconEvents, relative to the true angle of the track, a measure independent of the fitting algorithms and MAUS reconstruction.

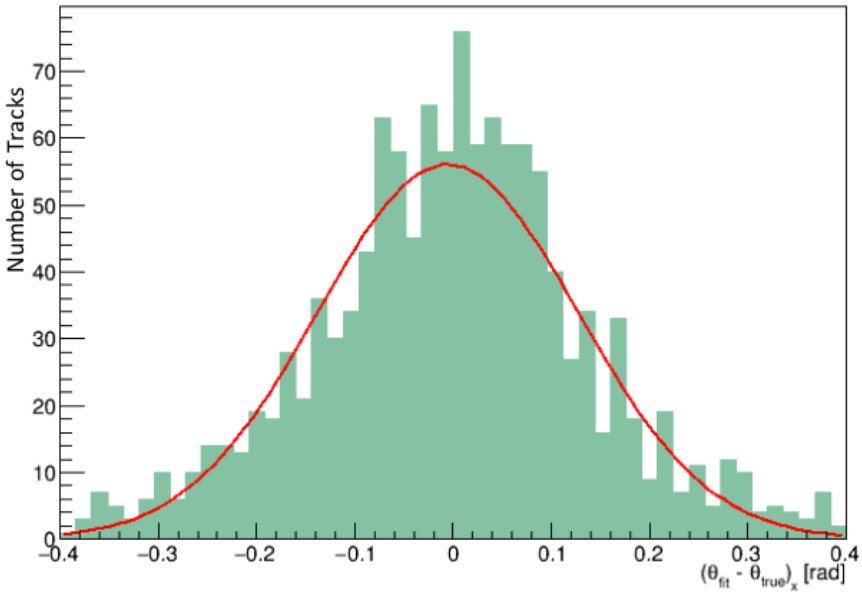

(a)

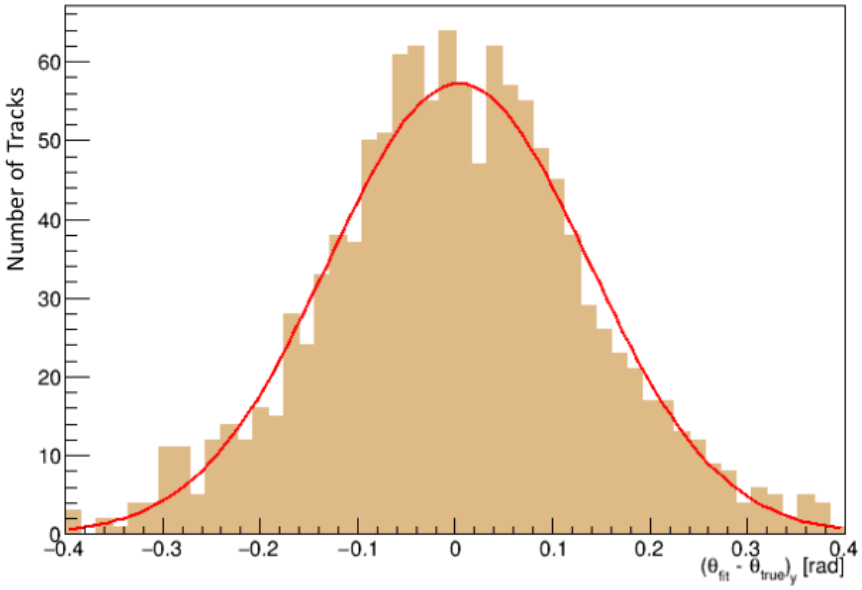

(b)

Figure 4.27: Distribution of track resolutions achieved when the fitting algorithm is performed on true Monte Carlo EMRHits for horizontally (a) and vertically (b) orientated planes. Both distributions are fitted. The resulting Gaussians have, in (a) a mean of -0.0005 ± 0.0004 rad and σ of 0.133 ± 0.003 rad with a χ^2/ndf = 1.83 and in (b) a mean of 0.004 ±0.004 rad (i.e. consistent with 0) and σ of 0.133 ± 0.004 rad with a χ^2/ndf =1.79

4.8.3 Justification and Optimisation of Track Resolution Cuts

Section 4.7.6 outlined a number of selection criteria imposed upon the track samples to improve the accuracy of the resulting fit. This section quantifies the effects of these cuts on the final fitted horizontal track resolution of the reconstructed Monte Carlo sample. The exclusion of the "digits cut" will result in singularities, as the algorithm cannot compute a track, therefore, this cut is never disregarded. Likewise, the effects of removing the "Mother+Daughter" cut is not evaluated here as the lack of secondary track nullifies such events.

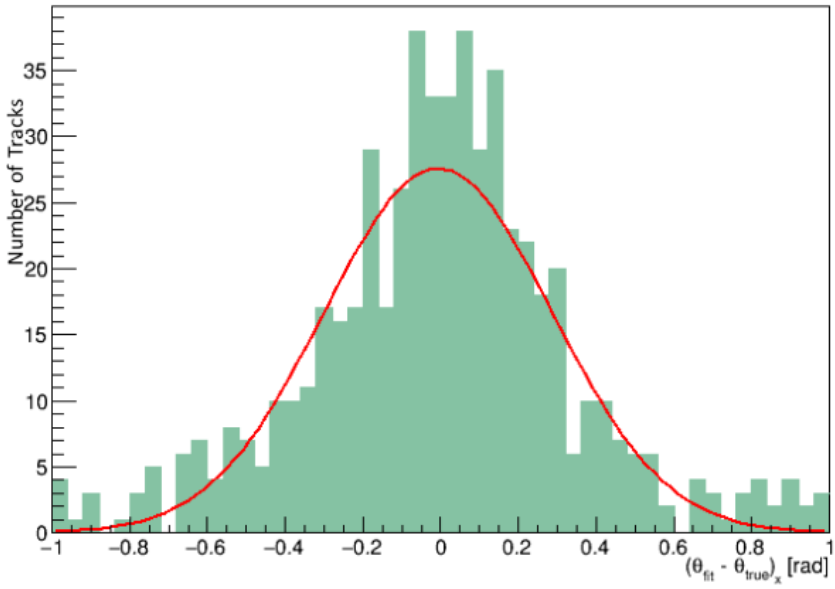

(a)

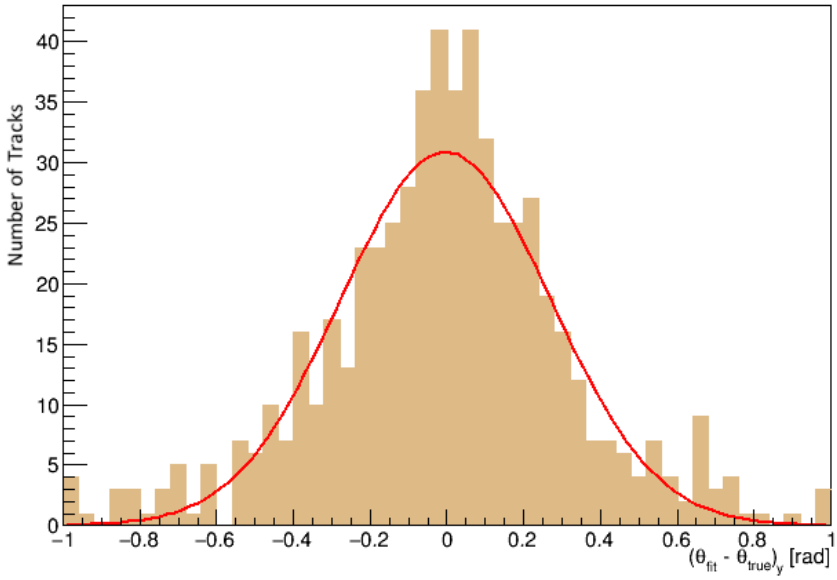

(b)

Figure 4.28: Distribution of track resolutions achieved when the fitting algorithm is applied to BarHits derived from reconstructed Monte Carlo for horizontally (a) and vertically (b) orientated planes. Both distributions are consistent with Gaussians scented upon 0, in (a) a mean of 0.010 ±0.013 rad and σ of 0.224 ± 0.015 rad. with a χ^2/ndf =1.52 and in (b) a mean of 0.006 ±0.011 rad and σ of 0.209 ± 0.012 rad. with a χ^2/ndf = 1.23.

1. **"Window Cut"**

   Figure 4.31a shows the distribution of track resolutions, obtained from fits to reconstructed Monte Carlo BarHits, when the "window cut," outlined in Section 4.7.6, was ignored. All other cuts remained in place. This criterion is enforced as a measure of the "goodness-of-fit" of the track and excluding it will result in less accurately fitted tracks been included in the analysis. The resulting track resolution distribution remains fairly consistent with the Gaussian fit, having a χ^2/ndf of 1.65 and mean consistent with 0, however, σ is changed by +32.6%, a considerable increase. The resolution of the fit is thus

decreased by excluding this cut, as is to be expected.

Figure 4.29 shows calculated RMS of track resolutions for varying "window" sizes in terms of the fraction of events in the window (i.e. χ for a constant bin number of n=2) and tolerance in terms of number of bins from the peak (i.e. n with constant $\chi = 0.5$). It is evident that the stricter either parameter choice is, the better the resolution. Changing the window size does not improve the resolution below ≈ 0.22 rad, which is a result of the detector geometry and scattering effects. In the following analysis tracks with 50% of their hits with angles ± 2 bins from the θ_{fit} are selected.

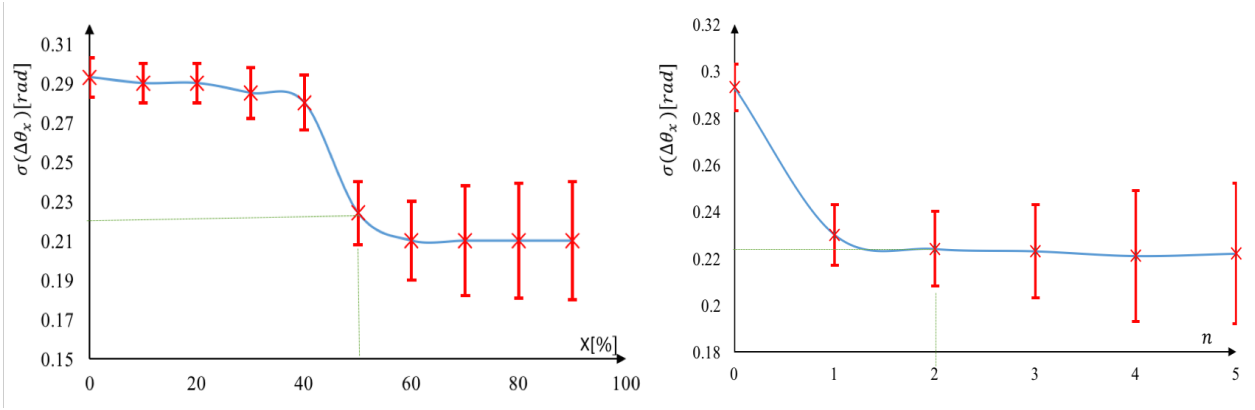

Figure 4.29: Plots showing the deviations in track resolution on fits to digitised Monte Carlo bar hits when parameters of the goodness-of-fit criterion (Equation 4.33) are altered. In (a) χ is varied but bin tolerance remains at n=2. In (b) the size of the window, quantified in terms of $\pm n$ bins from peak (centred on θ_{fit}), is altered, χ remains at 0.5. Each bin corresponds to 0.125 rad. Error bars are statistical and weighted by $1/\sqrt{N_{total}}$.

2. **"Fiducial Cut"**

Figure 4.31b displays the distribution of track resolutions for the scenario in which the "fiducial cut" is ignored, yet all other criteria are imposed. Disregarding this cut allows positron tracks produced on the edges of the detector to be incorporated into the analysis. It is anticipated such tracks will be less accurately fitted due to the limited information received regarding their subsequent trajectories. The distribution remains consistent with a Gaussian centred on 0 rad, however, there is a significant increase in the angular spread of the track resolution of +38.4% suggesting a larger number of badly fitted tracks are now included in the sample. Figure 4.30 shows how the resolution increases with increasingly stricter cuts. A criterion of $v \geq 5$ bars from the edge is enforced. Cuts stricter than this did not improve resolution and became increasingly more dominated by statistical errors.

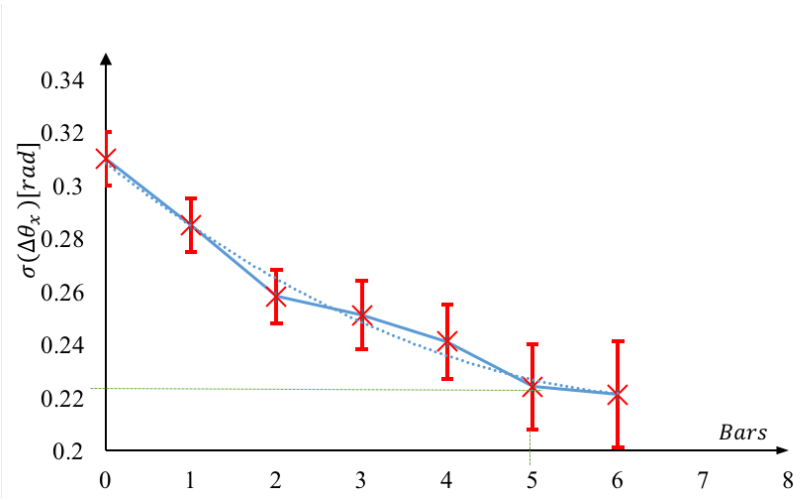

Figure 4.30: (left) Plot showing the deviations in track resolution on fits to digitised Monte Carlo bar hits when the "fiducial cut" is varied to exclude positron tracks produced a given number of bars from the edges of the detector in both directions hence the quadratic decrease observed. A criteria of $v \geq 5$ bars from the edge in either direction is imposed. This keeps resolution high without statistical uncertainties dominating. Error bars represent statistical variations existing in the sample and are weighted by a $1/\sqrt{N_{Total}}$ factor.

3. **"$\Delta t_{hit_{i,i-1}}$" Cut**

   Figure 4.31c shows the horizontal track resolution when the "$\Delta t_{hit_{i,i-1}}$ cut" is removed but all other cuts are imposed. This denotes a criterion enforced upon the time between consecutive hits in a track. The cut is expected to aid rejection of "noisy" tracks (see Section 4.7.4). A Gaussian fit provides a mean of 0.0197 ±0.0114 rad and σ of 0.245± 0.011 rad. The centre of the distribution has a slight offset from 0 rad and the angular spread of the distribution has increased by 9.3 %. This is still a relatively large percentage increase this, coupled with the apparent offset in the mean, indicates significant noise is now present in the fitted tracks. It is, therefore, deemed that the cut is necessary to improve track resolution.

4. **"$\Delta r_{hit_{i,i-1}}$" Cut**

   Figure 4.31d shows the distribution of track resolutions when the "$\Delta r_{hit_{i,i-1}}$ cut" alone is removed. This cut is imposed to remove "noisy" tracks from the sample and to aid background rejection. The Gaussian fit provides a mean of 0.005 ± 0.012 (stat.) rad and σ of 0.262 ± 0.012 (stat.) rad with χ^2/ndf of 1.58. Thus, excluding this cut has again increased the width of the track resolution distribution and reduced the accuracy of the fitted angle.

In conclusion, although these criteria do not remove any obvious, visible, bias in the track resolution distribution, or alter the overall shape, they do help to reduce angular spread and therefore improve the accuracy of the track fitting method. This will result in a more precise polarisation measurement.

Cut Removed	σ_x/[rad]	% change
"Window Cut"	0.297 ± 0.016	+32.6
"Fiducial Cut"	0.310 ± 0.017	+38.4
"$\Delta t_{hit_{i,i-1}}$" Cut	0.245 ± 0.011	+9.3
"$\Delta r_{hit_{i,i-1}}$" Cut	0.262 ± 0.012	+17.0
All Removed	0.377 ±0.041	+41.0

Table 4.3: Summary of measured RMS of track resolutions for horizontal tracks in the reconstructed Monte Carlo sample for several scenarios in which the selection criteria, outlined in the first column, are removed. The third column illustrates the effect each cut has on improving the RMS of the track resolution distribution in terms of the % change relative to the case in which all criteria are enforced. A total combined change, i.e. if all 4 cuts are removed, is also detailed.

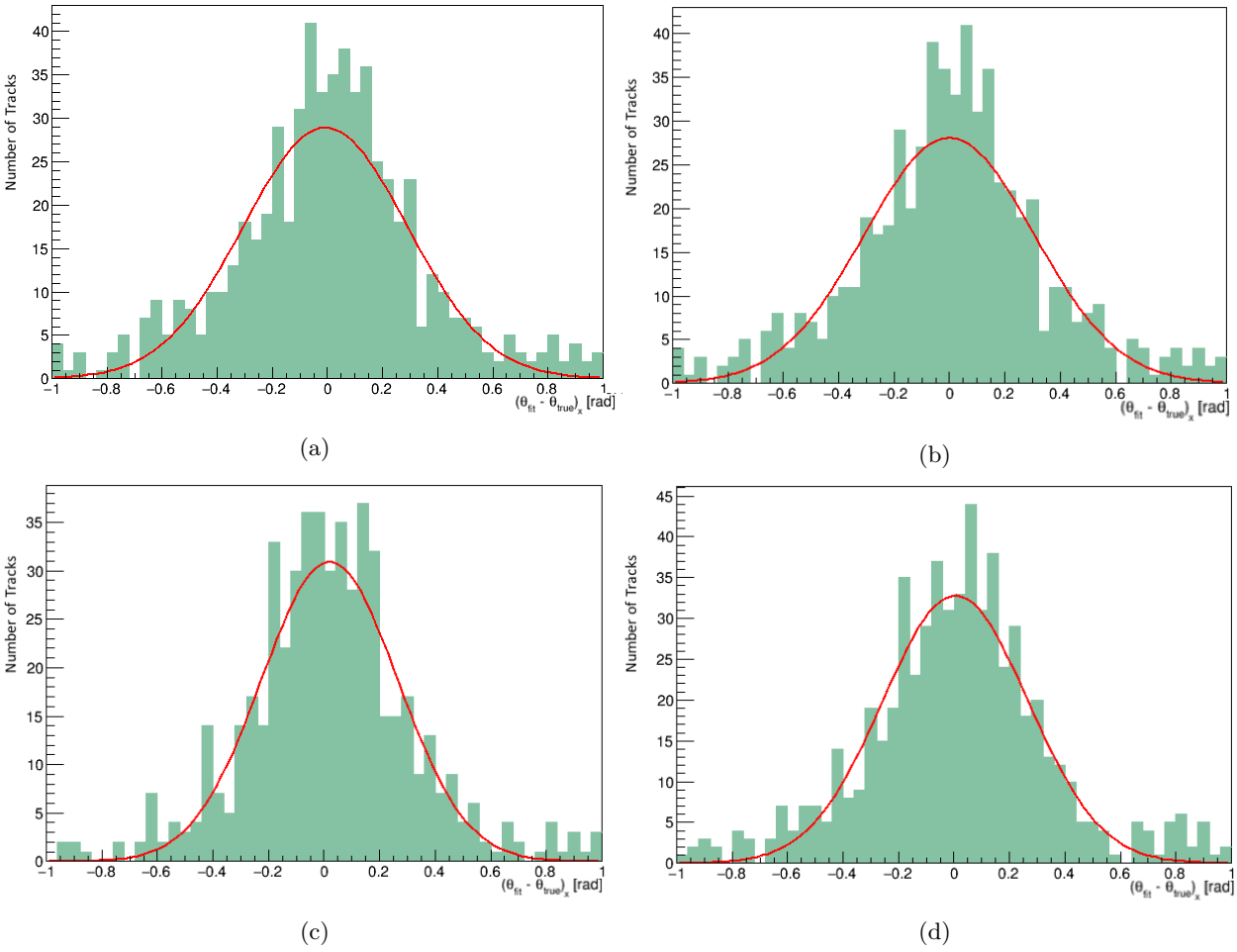

Figure 4.31: Distribution of track resolutions achieved by applying the fitting algorithms to BarHits derived from reconstructed Monte Carlo for the horizontal (x) orientation when the (a) "window cut" is removed the mean, μ, is -0.0076 ± 0.0134 rad and RMS, σ, is 0.297 ± 0.016 rad is measured with $\chi^2/ndf = 1.65$. The resolution is worsened by +32.6% when disregarding this criterion. When fiducial cut is removed (b) $\mu = -0.0011 \pm 0.0137$ rad and $\sigma = 0.310 \pm 0.017$ rad with a $\chi^2/ndf = 1.60$. The resolution is worsened by +38.4% from disregarding this criterion. When (c) "$\Delta t_{hit_{i,i-1}}$" cut is removed $\mu = 0.0197 \pm 0.0114$ rad and $\sigma = 0.245 \pm 0.011$ rad with a $\chi^2/ndf = 1.39$. The mean has shifted away from 0 in the positive direction. The resolution is worsened by 9.3%. When (d) the "$\Delta r_{hit_{i,i-1}}$" cut is excluded. $\mu = 0.005 \pm 0.012$ rad and $\sigma 0.262 \pm 0.012$ rad with a $\chi^2/ndf = 1.58$. The resolution is worsened by +17%

4.8.4 Track Residuals

For a given bar hit, i, within the track a "residual", r_i, can be derived, such that

$$r_i = \theta_i - \theta_{fit}, \tag{4.40}$$

were θ_i is the angle, relative to the initial muon direction, of the vector drawn from the muon decay point to bar hit i and θ_{fit} is the overall fitted angle for the whole track. For a track of N points an averaged track residual r_{track} can be characterised as:

$$r_{track} = \frac{\sum_{i=1}^{N}(\theta_i - \theta_{fit})}{N}. \tag{4.41}$$

The distributions of these averaged track residuals for the fitted tracks derived from the true Monte Carlo EMRHits, in both the horizontal and vertical orientated planes, are presented in Figures 4.32a and 4.32b respectively. Means of -0.0008 ± 0.032 rad (x) and -0.0022± 0.032 rad (y) and RMS values of 0.178 ± 0.052 rad (x) and 0.168 ±0.054 rad (y) are measured. The averaged track residual is consistent with the track resolution (outlined in Section 4.8.4) and the overall fitted track angle θ_{fit} is assumed to be an accurate representation of the angle of the track.

Similarly, Figures 4.33a and 4.33b present distributions of the averaged track residuals for fits to the reconstructed Monte Carlo bar hits for the x and y orientations respectively. The distributions have means of 0.012 ± 0.032 rad (x) and 0.015± 0.032 rad (y) and RMS values of 0.097 ± 0.050 rad (x) and 0.099 ±0.050 rad (y). They are consistent with the limitations which exist due to the geometry of the detector and no bias towards a particular orientation is observed.

4.8.5 Reconstruction Efficiency For $\theta_{x,y}$

A reconstruction efficiency, ϵ^{recon}, can be calculated, such that

$$\epsilon^{recon}_{\theta_{x,y}} = \frac{n^{fit,true}}{n^{true}}. \tag{4.42}$$

This is a measure of how likely the fitting procedure is to reconstruct a track of true angle θ_{true}. $n^{fit,true}$ is the number of tracks at a given θ_{true}, which pass all the selection criteria outlined in Section 4.7.6 and n^{true} is the total number of tracks prior to applying the fitting algorithms. $n^{fit,true}$ and n^{true} are acquired directly from the MCEvents Tracks, therefore, ϵ^{recon} acts only as a means of gauging any geometric bias in the likelihood of reconstructing a track with given θ_{true}, it has no information on the accuracy to which θ_{fit} was determined.

Figures 4.34a and 4.34b show the reconstruction efficiency achieved when the fitting algorithms are applied to the true MCEvent hits for both x and y orientations respectively. The points are consistent with straight lines with a $\chi^2/(ndf)$ of 1.14 for x and 0.83 for y. It is concluded, therefore, that the efficiency is constant, within statistical errors, with an average efficiency of $\approx 80\%$. A slightly lower efficiency is observed for bins incorporating the tracks at $\theta_{true} \approx \pm\frac{\pi}{2}$. This is a consequence of the selection criteria as cuts are applied to

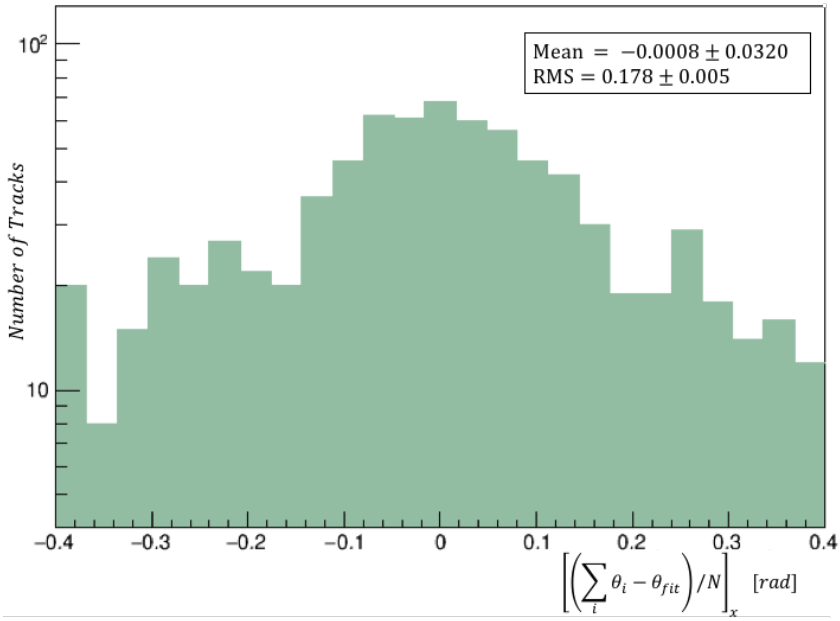

(a)

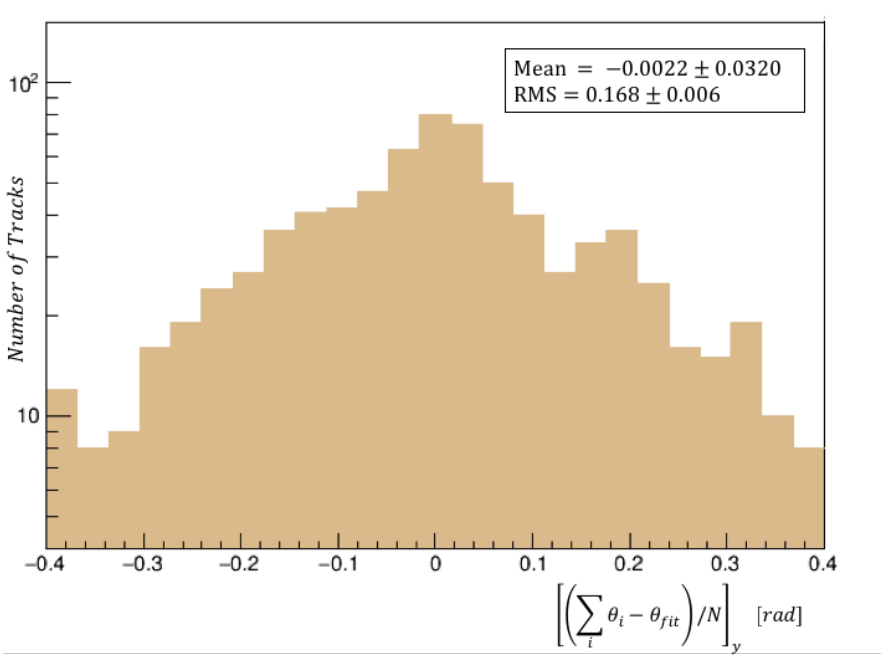

(b)

Figure 4.32: Distribution of averaged individual EMRHit residuals in the horizontal, (a) and vertical (b) orientations for fits to tracks obtained from the true Monte Carlo sample. This denotes the average difference between angles deduced from individual vectors traced from the decay point to the individual hit, θ_i, and the angle measured from the fit to the overall track angle, θ_{fit}. In (a) a mean of -0.0008 ± 0.0320 rad and an RMS of 0.178 ± 0.005 rad are found. This deviation is a result of scattering of the particles in the EMR material. In (b) a mean of -0.0022± 0.032 rad and an RMS of 0.168 ±0.006 rad is measured. This is consistent with the analogous distribution in x within calculated errors.

avoid singularities when particles are travelling directly along a bar.

The reconstruction efficiency achieved when applying the fitting algorithms to reconstructed Monte Carlo hits is presented in Figures 4.35a and 4.35b. Although, these plots and those for true Monte Carlo have the same n^{true} value for each bin, the $n^{fit,true}$ obtained is now dependent on the limitations of the recon-

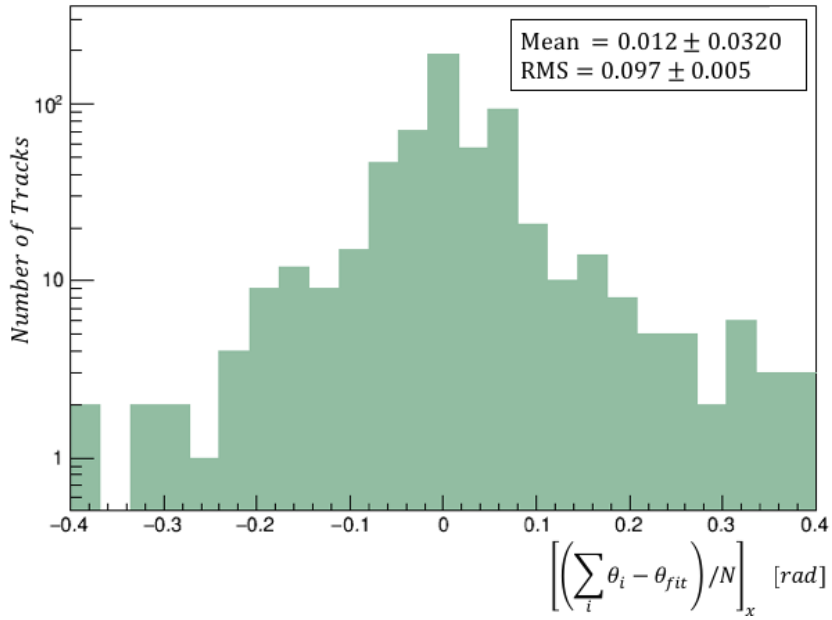

(a)

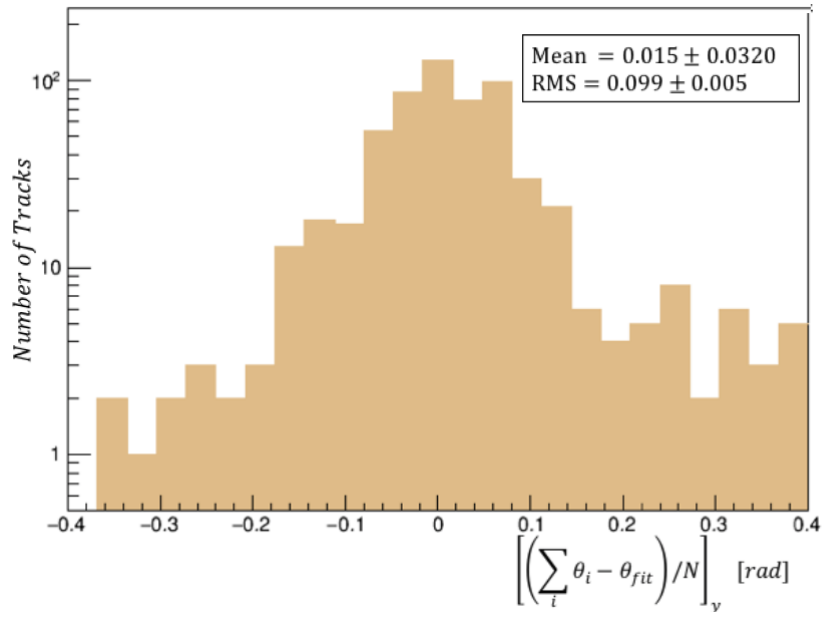

(b)

Figure 4.33: Distribution of averaged individual EMR BarHit residuals in the horizontal, (a) and vertical (b) orientations for fits to tracks obtained from the digitised Monte Carlo sample. This denotes the average difference between angles deduced from individual vectors traced from the decay point to the individual hit, θ_i, and the angle measured from the fit to the overall track angle, θ_{fit}. In (a) a mean of 0.012 ± 0.032 and an RMS of 0.097 ± 0.005 rad.are found. In (b) a mean of 0.015± 0.032 rad (y) and an RMS of 0.099 ±0.005 rad is calculated. This is consistent with the analogous distribution in x within calculated errors.

struction/digitsation algorithms too, hence, some differences from the preceding plots are observed. Straight lines are fitted to the plots, the $\chi^2/(ndf)$ values suggest a constant efficiency, within the available statistics, implying no obvious geometric bias. An average $\epsilon^{recon} \approx 80\%$ over all bins is obtained.

The computed reconstruction efficiencies are sufficiency high to allow the analysis to provide a high precision measurement of the polarisation of the beam.

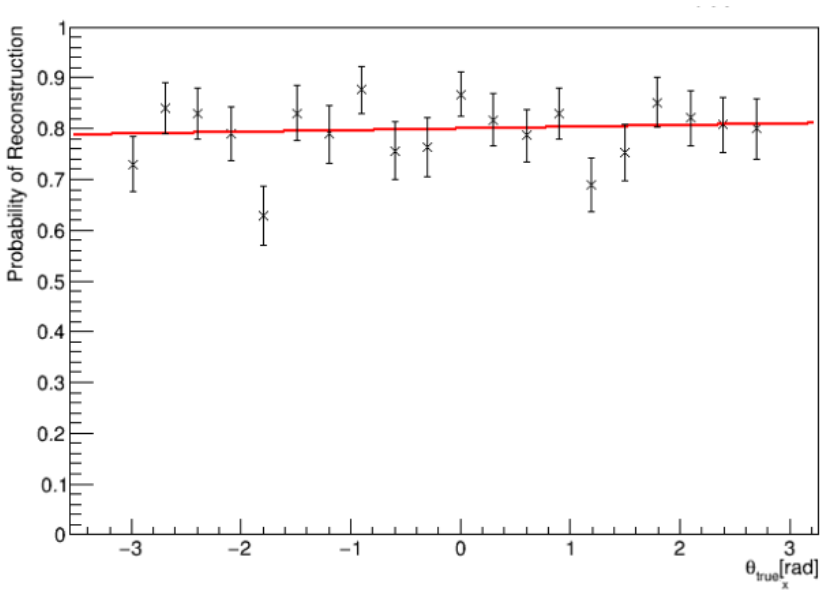

(a)

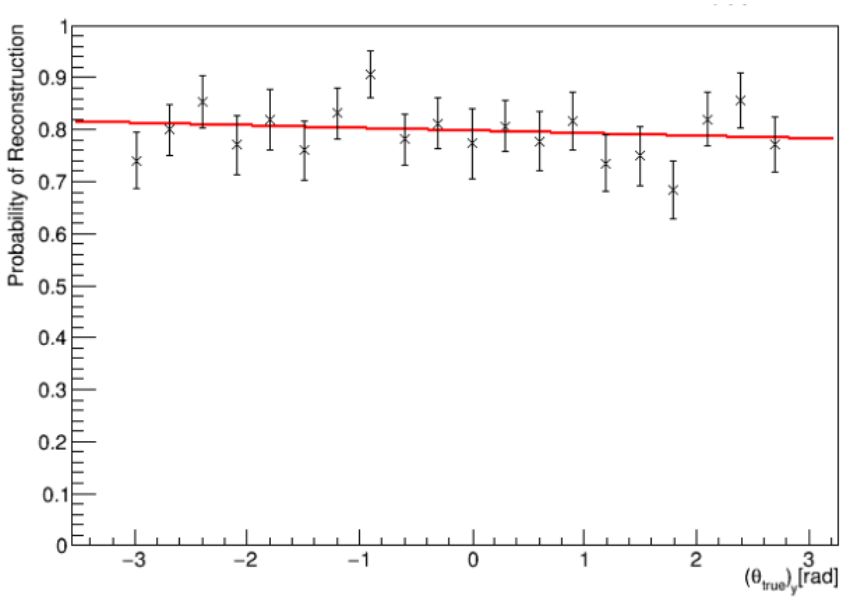

(b)

Figure 4.34: Reconstruction efficiency achieved when applying the fitting algorithms to true EMRHits obtained from MCEvents for planes orientated in the horizontal (a) and vertical (b) directions. Value describes how likely a given θ_{true} is to be reconstructed. This is not a measure of accuracy of the fit. Straight line fits are applied to both and presented in red. In (a) a gradient corresponding to the average reconstruction efficiency of 80.0 ± 1.2 %. is obtained with $\chi^2/ndf = 1.14$. Some deviation from the straight line is observed around $\pm\frac{\pi}{2}$, this was less apparent in the y direction. In (b) a gradient (average efficiency) of 79.7± 1.2 % is obtained with a $\chi^2/ndf = 0.83$ suggesting a good fit. The reconstruction efficiency is consistent with that for the horizontal planes.

4.8.6 Reconstruction Efficiency for Track cos(θ)

In Section 4.8.5 a reconstruction efficiency was defined describing the likelihood of reconstructing a given θ_{true} for the individual horizontal (x) and vertical (y) angles. By analogy, a reconstruction efficiency may also be calculated in terms of how likely you are to reconstruct a given overall $(cos(\theta))_{true}$ value such that

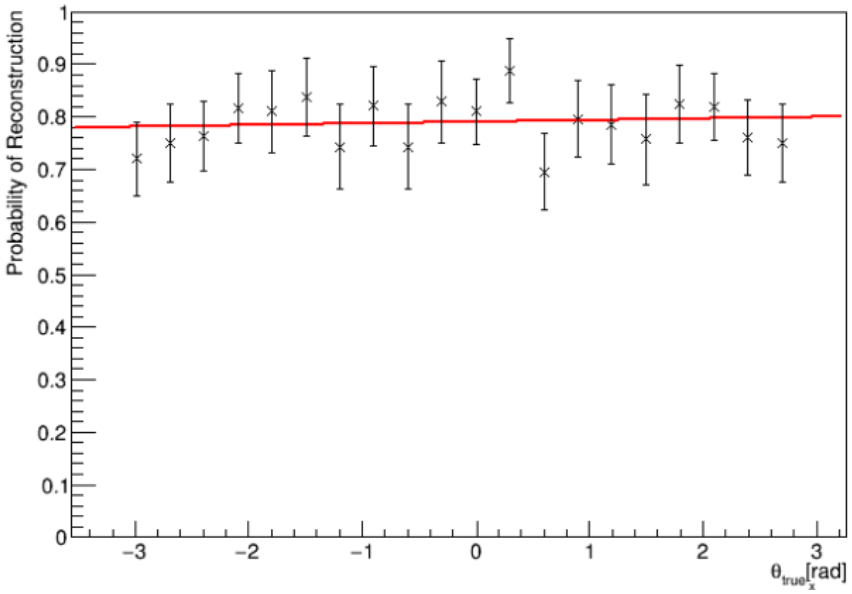

(a)

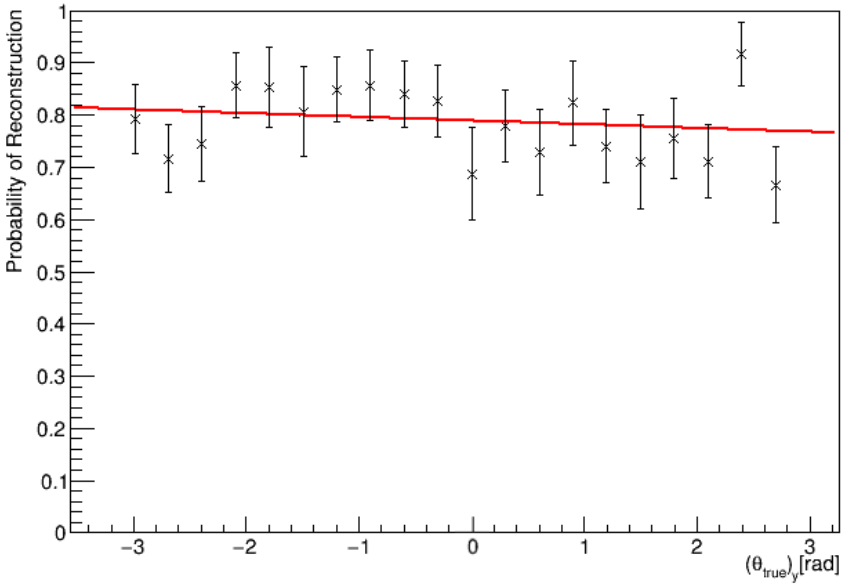

(b)

Figure 4.35: Reconstruction efficiency achieved when applying the fitting algorithms to reconstructed, digitised, Monte Carlo EMR BarHits for planes orientated in the horizontal (a) and vertical (b) directions. The probability presented describes the likelihood that a track with θ_{true} is to be reconstructed in the method. There is now a dependence on the digitisation model and detector geometry. Straight line fits are applied to both and presented in red. In (a) a gradient (average reconstruction efficiency) of 79.0 $\pm$ 1.6 % with $\chi^2/(ndf) = 0.43$ suggesting a good fit. In (b) a gradient (average efficiency) of 79.8 $\pm$ 1.6% is obtained. The fit has a $\chi^2/(ndf) = 0.85$ suggesting a good fit to this line and consistency with that for the horizontal direction and that for true Monte Carlo.

$$\epsilon_{cos\theta} = \frac{n_i^{fit,true}}{n_i^{true}} \tag{4.43}$$

where these are now numbers of events in the i-th $(cos(\theta))_{true}$ bin. It is expected that this too will be $\approx 80\%$ given the derived efficiencies in Section 4.8.5. This is confirmed by Figures 4.36a and 4.36b.

The reconstruction efficiency is constant, within statistical limitations, suggesting that no overall bias

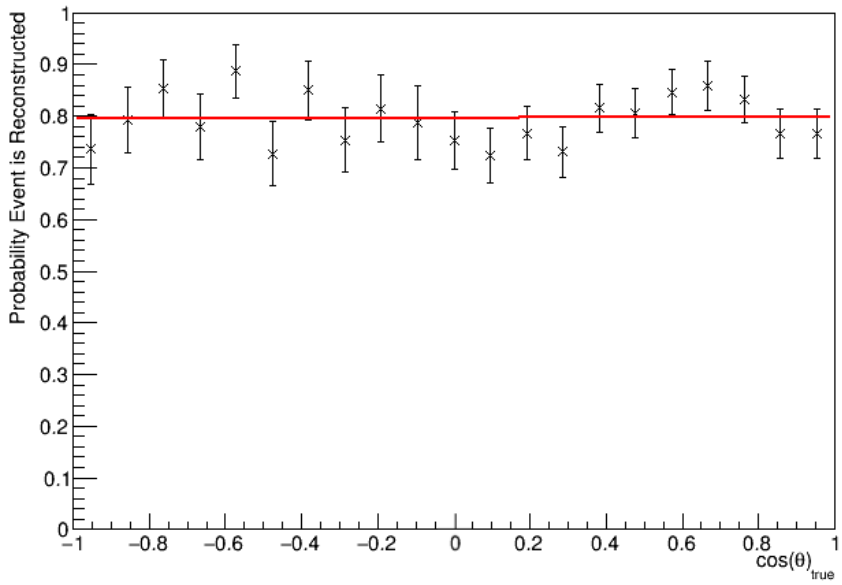

(a)

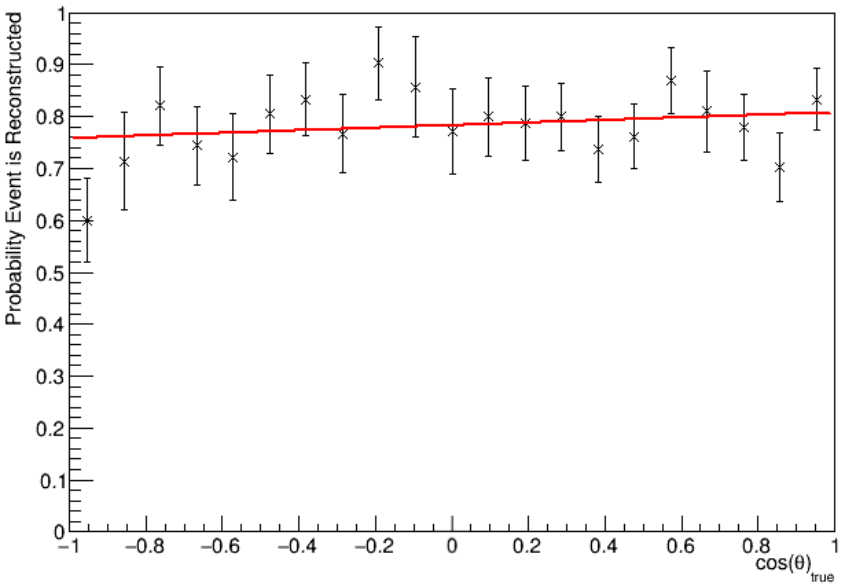

(b)

Figure 4.36: Probability of reconstructing a track at a given total true $(cos(\theta))_{true}$ for tracks obtained from (a) fitting to the EMRHits derived from the true MCEvents. This seems to be constant between 70-90% within statistical errors. A fit is performed and an average efficiency of 79.6 ± 1.2 % is calculated with a $\chi^2/(ndf) = 0.8$. And (b) from fitting to the BarHits taken from the digitised Monte Carlo. This seems to be constant between 60-90% within statistical errors. A fit is performed giving an average efficiency of 78.3 ± 1.6 % with a $\chi^2/(ndf) = 0.71$

is induced by the fitting method. Additionally, the reconstruction efficiencies for tracks derived from true MCEvent and from digitised Monte Carlo ReconEvents are consistent with one another implying the digitisation has not introduced any large geometric bias whereby the likelihood of the track being reconstructed is dependent on its true angle.

4.8.7 Checking For Geometrical Bias in Track Resolution

Figures 4.37a and 4.37b characterise any dependence the average angular resolution, in x and y respectively, may have on the true angle, θ_{true}, when the fitting algorithm is applied to EMRHits derived from true MCEvents. This is a good indicator as to whether the accuracy of the fitting method has any inherent bias towards a given true angle. A fit of the form $[\theta_{fit} - \theta_{true}]_{x,y} = m(\theta_{true})_{x,y} + c$ is fitted to the distributions. If no average angular bias were present then $m = 0$ and $c = 0$.

The distribution for y is shown to be consistent with a flat, straight line, symmetrical about $\Delta\theta = 0$ rad. There is a slight negative gradient observed for the x orientation.

Figures 4.38a and 4.38b show the analogous plots for the reconstructed EMR BarHits. Again the distributions are relatively consistent with straight line fits. However, the statistical deviations are larger than those for true Monte Carlo EMRHits. Given the relative statistical errors this small offsets from the unbiased, m=0, case should not provide a significant bias within the limits of this analysis. Section 4.8.12 presents a discussion of the effects of systematic bias on the combined $(cos(\theta))_{fit}$ along with a correction calculation which will be applied to reconstructed tracks in the data sample.

4.8.8 Measuring Polarisation from True MC

The Monte Carlo sample used throughout the study has an initially fully polarised muon beam with $P_{\mu}^{\pi} = 1$. Figure 4.39a shows the distribution of the calculated $(cos(\theta))_{fit}$ derived from applying the fitting algorithm, presented in this thesis, to the true MCEvent EMRHits. The true Monte Carlo is independent of the MAUS reconstruction code and detector resolution. As a result, evaluating the effect of the fitting method on the calculated beam polarisation of the true Monte Carlo helps to isolate systematic errors resulting from the fitting routines from those which result from errors in the MAUS digitisation/reconstruction algorithms or the detector resolution.

By fitting a straight line to the distribution and exploiting Equation 4.12 a normalised gradient of $+0.377 \pm 0.057$ is obtained. This corresponds to a measure of $P_{\mu} = 1.131 \pm 0.171(stat.)$. Although the overall direction of the distribution still indicates a "+" polarisation, this deviation from the expected value of 1 indicates a systematic error in the method. Correcting for systematic errors is discussed in Section 4.8.12. A systematic error of ± 0.128 is calculated from comparison to the derived polarisation from True Monte Carlo Tracks.

4.8.9 Measuring Polarisation for Reconstructed MC

Figure 4.39b shows the distribution of derived $(cos(\theta))_{fit}$ values for track fits obtained from the reconstructed, digitised, Monte Carlo bar hits. Fitting a straight line to the distribution provides a normalised gradient of $+0.305 \pm 0.081$ and offset 0.933 ± 0.048 with a $\chi^2/(ndf)$ of 2.46. These values are consistent with those obtained from the fits to true Monte Carlo EMRHits (Figure 4.39a), within the respective errors. However, there are obvious differences, most notably, the deficit of tracks at $(cos(\theta))_{fit} = 0$ and the subsequent excess of events in the two adjacent bins.

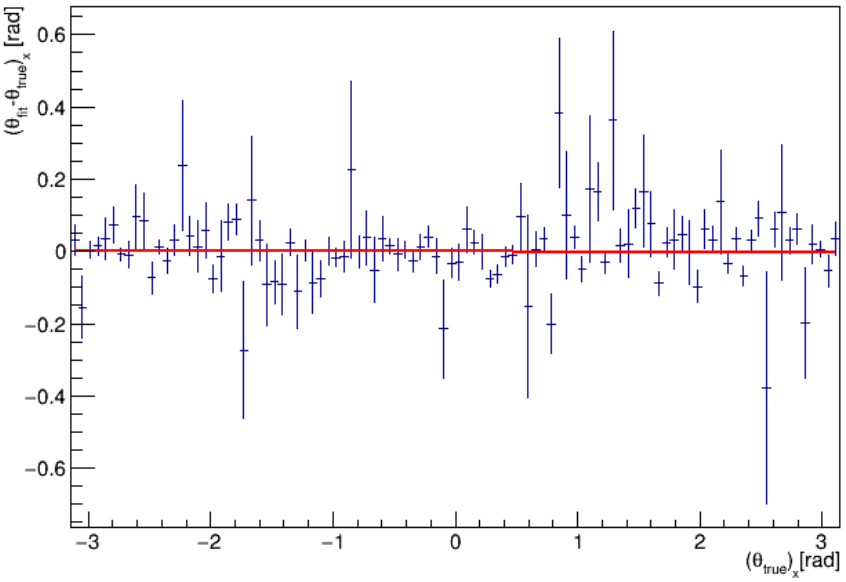

(a)

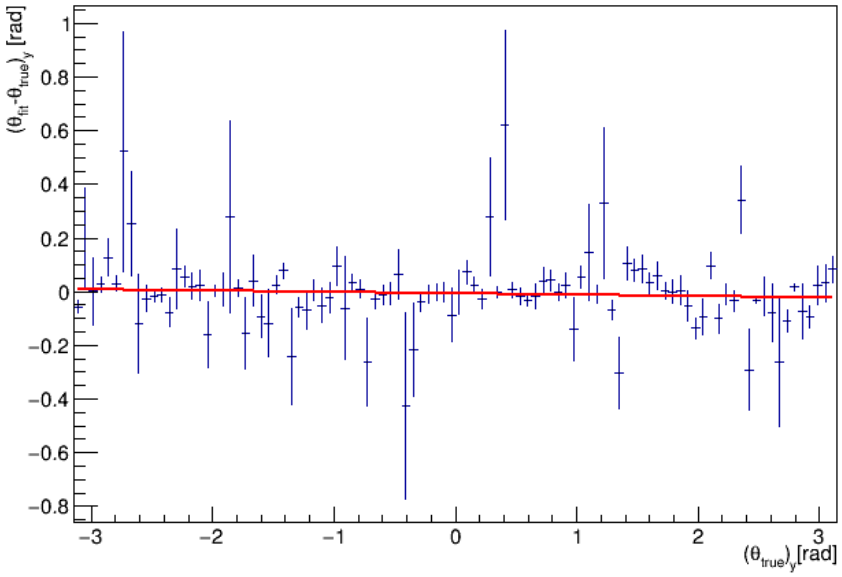

(b)

Figure 4.37: Profile histograms showing the mean of the fit x (a) and y (b) angular resolution, achieved when applying the fitting algorithms to true MC EMRHits, as a function of the decay angle derived directly from the true Monte Carlo Track (θ_{true}). The error bars represent the RMS of the track resolution in each point. A linear fit is performed, the fit line (red) gives (a) A gradient of -0.0021 ± 0.0017 and vertical axis intercept of 0.032 ± 0.0022 with a $\chi^2/n = 2.3$ for the x orientation. And (b) a gradient of -0.0008 ± 0.0004 and vertical axis intercept of -0.00016 ± 0.000212 with $\chi^2/n = 1.4$ for y orientated planes.

The "digits cut" could have some bearing on this deficit given it removes tracks which propagate along a bar i.e at θ_x or $\theta_y = \pm\frac{\pi}{2}$ and thus results in slightly lower reconstruction efficiency in that region. However, this large deficit is not solely the result of an inherent systematic in the fitting algorithm as it is absent in Figure 4.39a. Given that, in addition, the two bins either side of the dip have a considerably larger than expected number of tracks suggests there is some larger systematic effect induced by the detector geometry. There also appears to be some excess of events at $((cos(\theta))_{fit}$ = -1. This may be a result of events having an incorrectly assigned direction.

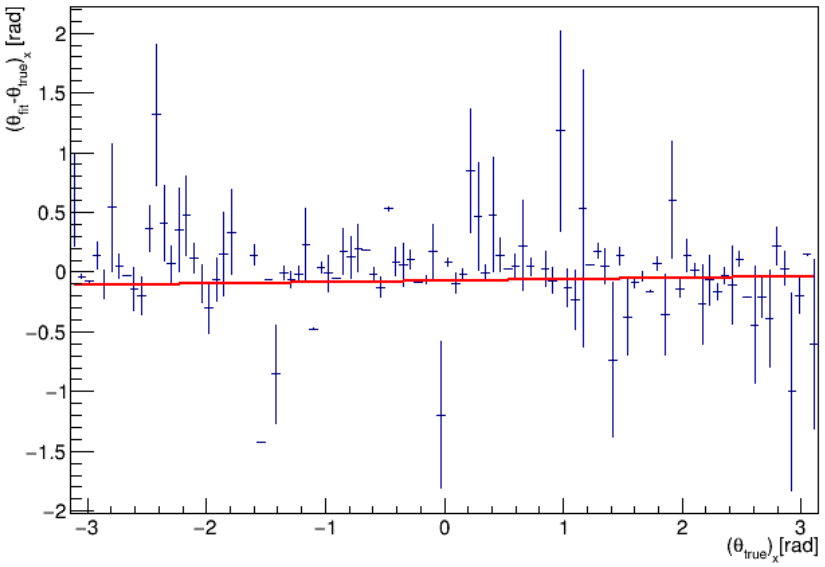

(a)

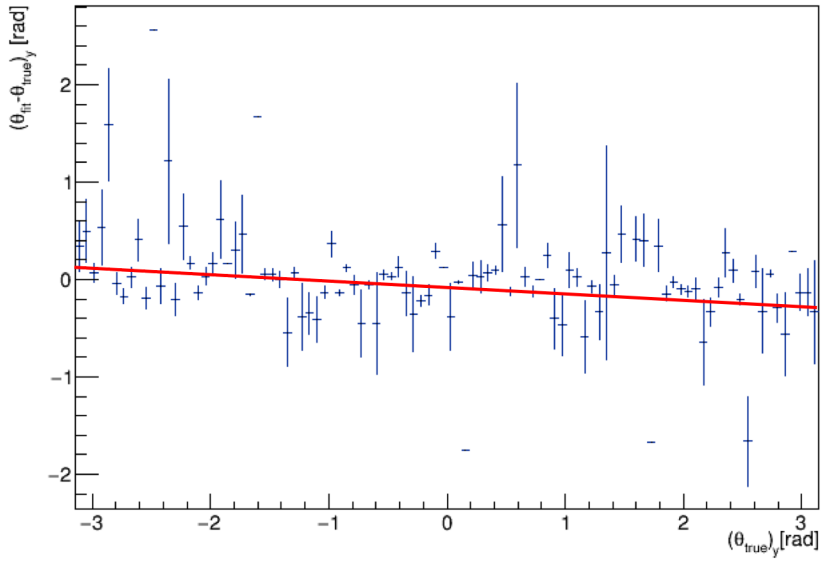

(b)

Figure 4.38: Profile histograms showing the mean of the fit x (a) and y (b) angular resolution, achieved when applying the fitting algorithms to reconstructed BarHits, as a function of the decay angle derived directly from the true Monte Carlo Track (θ_{true}). The error bars represent the RMS of the track resolution in each point. A linear fit is performed, the fit line (red) gives (a) A gradient of -0.0741 ± 0.0021 and vertical axis intercept of -0.012 ± 0.019 with a $\chi^2/n = 2.36$ for the x orientation. And (b) a gradient of 0.022 ± 0.005 and vertical axis intercept of -0.015 ± 0.019 with $\chi^2/n = 2.61$ for y orientated planes.

Further analysis of these systematic features is presented in Section 4.8.12, including details of a Monte Carlo driven "correction factor" for each $(cos(\theta))_{fit}$ bin.

4.8.10 Possible Cause of $(cos(\theta))_{fit} = 0$ Deficit

The deficit of reconstructed tracks at $(cos(\theta))_{fit} = 0$ is a result of the detector geometry. However, it is important to explain how the fitting method could have contributed to this and the subsequent excess of events in the adjacent bins. Figure 4.40 shows a schematic of 4 possible muon decays which result

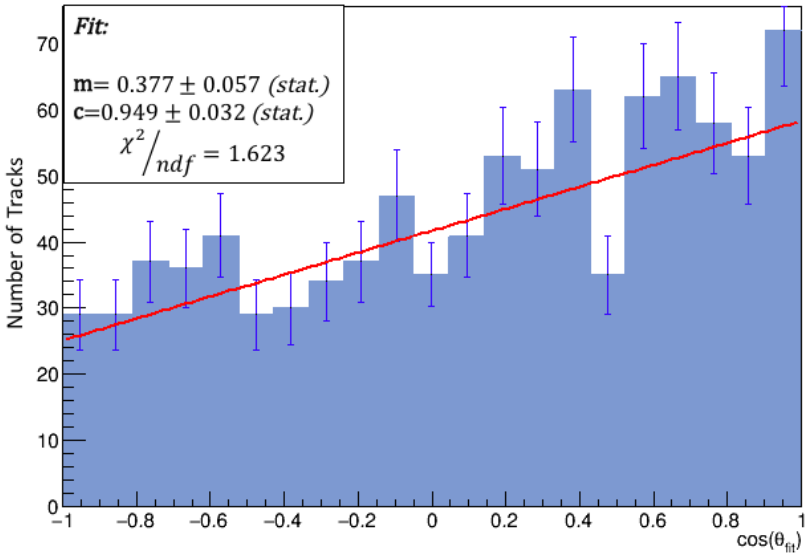

(a)

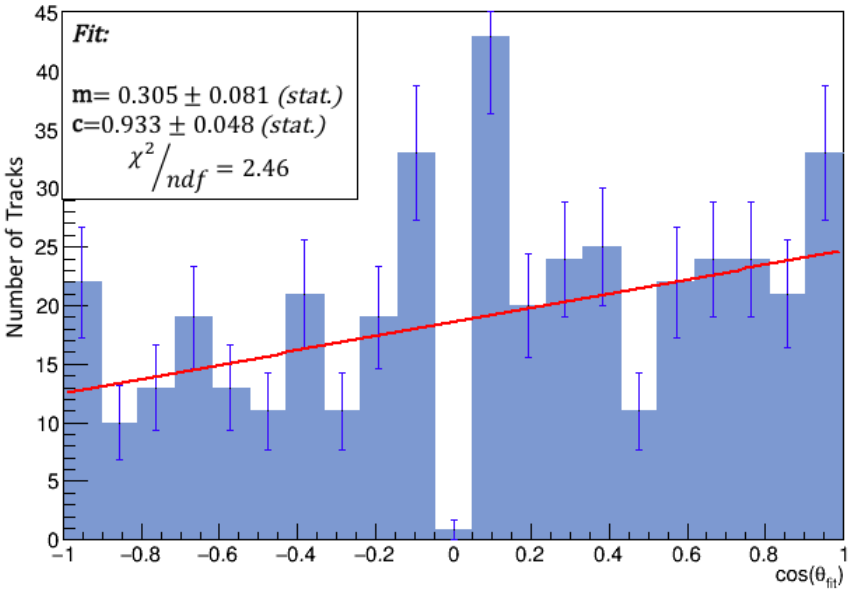

(b)

Figure 4.39: Distribution of $(cos(\theta))_{fit}$ as derived from applying the fitting algorithm to the (a) true Monte Carlo EMRHits (b) Reconstructed Monte Carlo BarHits. A straight line has been fitted to both distributions. Once normalised (through multiplying by a factor of number of bins/total number of tracks) the gradient of this line is a measure of $\frac{1}{3}P_\mu$. Both distributions show positive gradients. For (a) a normalised gradient of $+0.377 \pm 0.047$ and offset of 0.949 ± 0.032 are obtained with $\chi^2/(ndf) = 1.623$, corresponding to a polarisation of 1.131 ± 0.171. This is consistent with a fully polarised muon beam but this is not exact. The line seems to parameterise the distribution fairly well with most bins being within $1\sigma_{stat.}$ of the fitted line. For (b) a normalised gradient of $+0.305$ ($P_\mu = 0.915$) with a $\chi^2/(ndf) = 2.46$ is obtained. A systematic effect is observed in the central bins. The error bars represent only statistical errors only which correspond to $\sqrt{n_{bin}}$, where n_{bin} is the number of events in each bin. Systematic errors can be corrected in the real data using the technique outlined in Section 4.8.12

$(cos(\theta))_{fit} \approx 0$.

In the scenario labelled "Decay 1" the positron is produced at $\approx \pi/2$ rad from the muon trajectory. The track is rejected by the "digits cut" in this analysis as it only imparts energy in one transverse orientation. Thus, the observed deficit of tracks at $(cos(\theta))_{fit} = 0$ is produced. The angular size of this dip is dependent

upon the detector dimensions and the size of, and separation between, each transverse plane.

The other 3 scenarios on Figure 4.40 help explain the apparent excess of events in the adjacent $(cos(\theta))_{fit}$ bins:

- Decay 2 - The positron is produced nearly vertically. In this scenario the decay manages to make sufficient hits in both orientations to pass the "digits cut." However, the track is reconstructed better in the one orientation than the other as more hits are available to fit. The result is that the derived $(cos(\theta))_{fit}$ gets pulled towards "0."
- Decay 3, Decay 4 - In these tracks the positron will traverse enough planes such that viable tracks are produced in both orientations. These tracks will be reconstructed effectively, hence, the derived $(cos(\theta))_{fit}$ now converges on its true value.

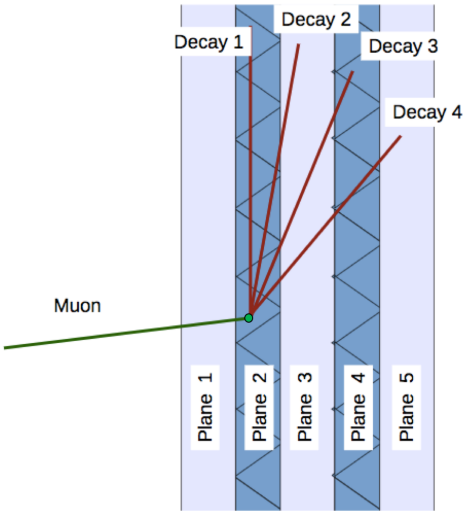

Figure 4.40: Schematic showing decay positron tracks (red) which result in the angle "Plane 2" being close to vertical. In "Decay 1" the positron travels down the plane and the track fails the "digits cut." This produces the deficit of tracks at $(cos(\theta))_{fit} = 0$ observed in figure 4.39b

4.8.11 Deviations at $(cos(\theta))_{fit} = \pm 1$

In Figure 4.39b an apparent excess of events is observed at $(cos(\theta))_{fit} = -1$, relative to the immediately preceding bin. In addition the penultimate $(cos(\theta))_{fit}$ bin also appears to have a deficit when compared to the fit line. Given that the reconstruction efficiency is approximately constant throughout (Section 4.8.5) this may signify a systematic pulling of tracks close $(cos(\theta))_{fit} = -1$ bin into the final bin.

Figure 4.41 displays a schematic of 2 scenarios in which the decay positron is produced along the direction of the muon travel. In "Decay 1," the positron is emitted along the direction of the original muon track. These tracks should traverse a number of transverse planes, in both orientations, thus, they will result in a high number of hits per track and will be well reconstructed. In "Decay 2" the positron travels anti-parallel

to the muon track, i.e. in the opposing direction. It is possible that an event of type "Decay 2" could be mis-identified as "Decay 1" or vice versa if, for instance, the track was short or the vertex is poorly reconstructed. The "window cut" will help minimise this effect. This could occur in true and reconstructed samples but has most affect in the reconstructed Monte Carlo due to the digitisation and detector geometry. In the following section a correction matrix will be derived in order to countervail this type of mis-binning of tracks.

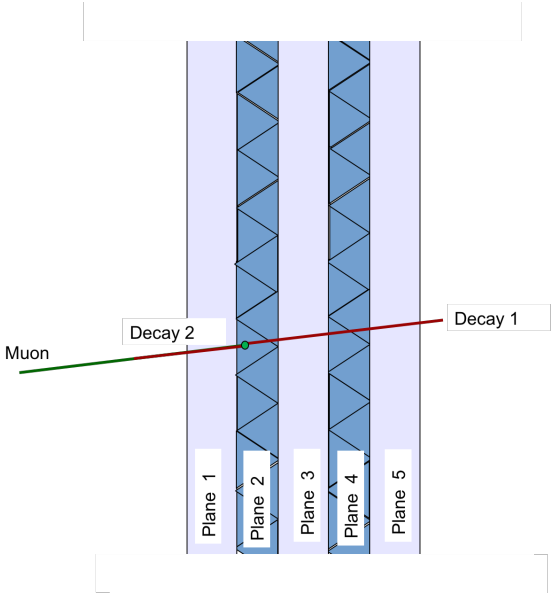

Figure 4.41: Schematic showing decay positron tracks (red) which result in the outgoing track being close to parallel with the incoming muon track. A mis-assigned direction could produce a slight excess $(cos(\theta))_{fit} \approx -1$ in Figure 4.39b. Tracks can be incorrectly assigned a direction if the track is short or the vertex is badly reconstructed. This could occur in true and reconstructed Monte Carlo but has most effect in the reconstructed Monte Carlo due to the digitisation and detector geometry.

4.8.12 Calculating and Correcting Bias and Systematic Errors

Figure 4.42a displays the relationship between the derived $(cos(\theta))_{fit}$ and that taken directly from MCEvent Track, labelled $(cos(\theta))_{fit,true}$, for fits to the true MC EMRHits[1]. This sample is independent of the detector reconstruction algorithms and geometry, therefore, this plot demonstrates that the method, derived in this study, does not induce any systematic bias in the fit. Some off-diagonal track angles are observed which are a result of the finite resolution of the fit algorithms but in general most tracks remain $\pm$ 1 or $\pm$ 2 bins from the $(cos(\theta))_{fit} = (cos(\theta))_{fit,true}$ diagonal. Figure 4.42b exhibits the analogous plot for $(cos(\theta))_{fit}$ values derived from digitised Monte Carlo ReconEvents. In this case the plot has a similar diagonal, yet a larger amount of off-diagonal "noise" is apparent. The main feature, in comparison to Figure 4.42a, is the deficit of events at $(cos(\theta))_{fit} = 0$; to be anticipated considering Figure 4.39b. It is expected that this deficit will be present for any tracks derived from ReconEvents, including the real data. Consequently, it is vital to remove this systematic uncertainty induced from the detector reconstruction model in order to correctly determine beam polarisation.

[1]note that the term "fit-true" represents the "true" angle, derived from MCEvent Tracks for tracks which make it through the selection criteria of the fitting algorithms and, therefore, have a corresponding $(cos(\theta))_{fit}$. Any deficiencies/excesses in these plots are not a simply result reconstruction inefficiencies in the fit algorithm. They represent a more systematic effect .

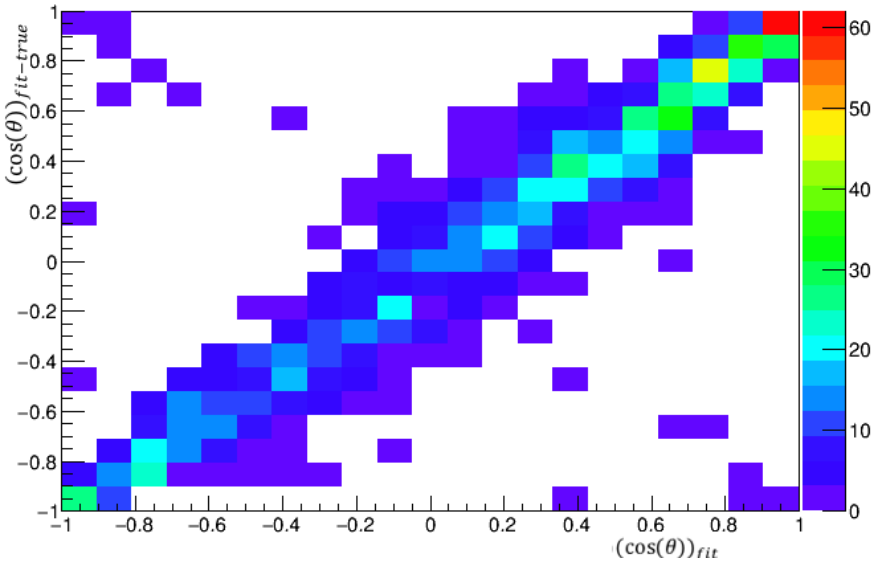

(a)

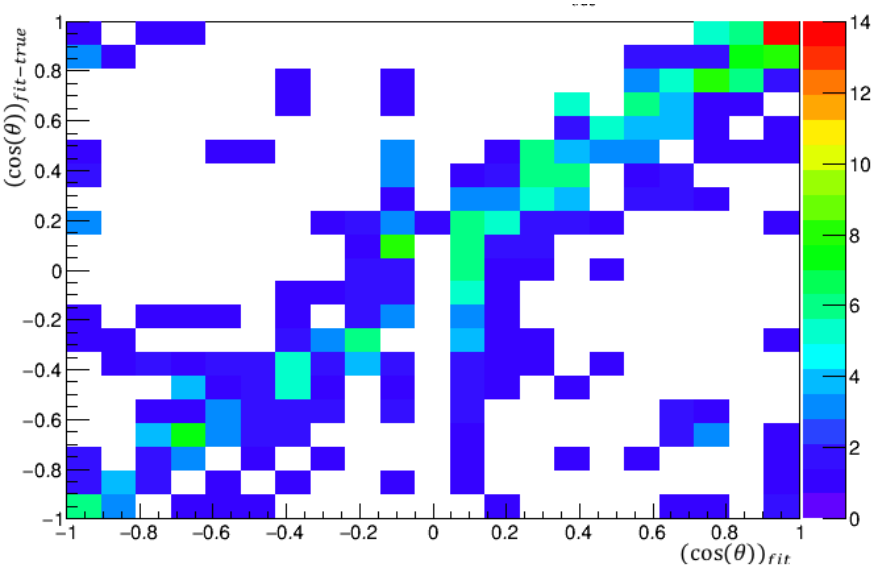

(b)

Figure 4.42: Relationship between $(cos(\theta))_{fit-true}$, taken directly from the Monte Carlo Track information and the $(cos(\theta))_{fit}$ obtained from applying the fitting algorithm to (a) true MCEvent EMRHits or (b) reconstructed Monte Carlo BarHits. The term "fit-true" is defined in Section 4.8.1. In (a) a diagonal line is apparent, corresponding to $cos(\theta))_{fit} = (cos(\theta))_{fit-true}$. A smaller density of tracks ± 1 or 2 bins from the diagonal line is evident; a result of the finite resolution of the fit. No large geometric bias is observed when fitting to the true Monte Carlo i.e. to tracks independent of the detector model. In (b) a densely populated diagonal line is evident at $cos(\theta))_{fit} = (cos(\theta))_{fit-true}$ but this is less well-defined than in (a). Additionally, a deficit of events is evident at $(cos(\theta))_{fit} \approx 0$; suggests a bias is present resulting in tracks along the transverse plane, i.e. $\theta_{true} = \pm\frac{\pi}{2}$, being poorly reconstructed. This effect is largely due to the detector reconstruction algorithm and not solely a consequence of fitting method outlined in this thesis hence the differences between (a) and (b). A correction factor, derived from Monte Carlo, will be applied to data to correct for this effect.

In Section 4.8.6 the probability of reconstructing a given $(cos(\theta))_{true}$ was defined in terms of the reconstruction efficiency, $\epsilon_{cos\theta}$. $\epsilon_{cos\theta}$ is simply the probability of an event in $(cos(\theta))_{true}$ bin i being reconstructed in the equivalent $(cos(\theta))_{fit}$ bin. It doesn't take into account any bias whereby an event, which should be in bin i, is instead reconstructed in bin j. To account for such bias a $m \times n$ matrix, $\underline{\underline{M}}_{bias}$, can be expressed, where m is the number of true bins and n is the number of fit bins (these must be the same), such that

$$\underline{\underline{M}}_{bias} = \begin{pmatrix} a_{1,1} & a_{1,2} & \cdots & a_{1,n} \\ a_{2,1} & a_{2,2} & \cdots & a_{2,n} \\ \vdots & \vdots & \ddots & \vdots \\ a_{m,1} & a_{m,2} & \cdots & a_{m,n} \end{pmatrix}.$$

Each element, a_{ij}, is given by:

$$a_{ij} = \frac{n_j^{fit}}{n_i^{fit,true}}, \tag{4.44}$$

where n_j^{fit} defines the number of tracks in the $(cos(\theta))_{fit}$ bin j and $n_i^{fit,true}$ is still number of tracks in the $(cos(\theta))_{true}$ bin i. The total number of events reconstructed in bin i is

$$n_i^{fit} = \sum_j a_{ij} \epsilon_i^{recon} n_i^{true}, \tag{4.45}$$

where a_{ij} is the ij-th element of $\underline{\underline{M}}_{bias}$, ϵ^{recon} is the reconstruction efficiency for bin i, i.e. $n_i^{fit,true}/n_i^{true}$. n^{true} is the total amount of events in i if no bias or inefficiency were present, found using Monte Carlo truth Track information. $\underline{\underline{M}}_{bias}$ can be derived from Figure 4.42b. A correction can be applied to the $(cos(\theta))_{fit}$ distribution, taking into account the systematic bias and reconstruction inefficiency in the fitting method. A corrected bin content, $n^{corrected}$, can be determined:

$$n_i^{fit,corrected} = \sum_j a_{ji} (\epsilon_i^{recon})^{-1} n_j^{fit,raw}. \tag{4.46}$$

The systematic error, σ^{sys}, on the content of given $cos(\theta))_{fit}$ bin k is then, simply,

$$\sigma_k^{sys} = n_k^{raw} - n_k^{corrected}. \tag{4.47}$$

Equation 4.46 can be utilised to correct for systematic biases, which result from the detector model, and reconstruction inefficiencies, which result from the fitting algorithms, for real data. ϵ^{recon} and $\underline{\underline{M}}_{bias}$ are derived using the Monte Carlo samples.

4.8.13 Conclusions from Monte Carlo

Section 4.7 outlined a unique fitting algorithm which can derive the angle at which positrons are produced when a muon decays in the MICE EMR. Section 4.8 examined the accuracy of this method and measurements of the effective beam polarisation where presented for tracks derived from true and reconstructed Monte Carlo EMR hits. Fit angular resolutions are shown to be consistent with the spatial resolution of the detector. Reconstruction efficiencies, defining the likelihood of a track at a given true track angle being reconstructed, are found to be $\approx$ 80% with no geometric bias. Chosen selection criteria improve the residuals without biasing the measurement and aim to pre-select less noisy, more easily reconstructed tracks, ensuring a more

accurate determination of the track angle is achieved. All selection criteria outlined in Section 4.7.6 will be applied to the data.

The fitting algorithm successfully predicts the direction of the beam polarisation, within statistical errors, for hits derived from true Monte Carlo events. However, systematic errors are apparent when it is applied to reconstructed, digitised, Monte Carlo tracks and a large deficit at $\cos(\theta_{fit}) \approx 0$ is exhibited. A method for correcting for this bias has been outlined. A Monte Carlo driven "correction factor" will be applied to the $(cos(\theta))_{fit}$ on a bin-by-bin basis using Equation 4.46. The reconstruction efficiency and bias matrix are obtained from comparison of the true MCEvent Track angle and that obtained from fitting to the digitised Monte Carlo ReconEvent hits. These corrections take into account both the systematic bias, induced by the detector geometry, and reconstruction inefficiencies inherent in the fitting algorithm. Once corrected the reconstructed Monte Carlo sample has a measured polarisation of 0.933 ± 0.243 (stat.) ± 0.194 (sys.) which is both consistent with that derived from the true Monte Carlo sample (1.131±0.171 (stat.) ± 0.128 (sys.)) and the expected value of $P_\mu = 1$.

4.9 Deriving Polarisation for Step IV Data

This section presents analysis of real data run 07434. This run was set up with an initially unpolarised muon beam, therefore, it is expected that $P_\mu = 0$ if the systematic errors are correctly accounted for.

4.9.1 Track Residuals

Figures 4.43a and 4.43b show the distribution of track hit residuals calculated as described in Section 4.8.4. For both x and y the distributions have small RMS values of 0.0885 ± 0.005 rad (x) and 0.0992 ± 0.0061 rad (y) and means consistent with 0 rad. This suggests no obvious bias towards a given orientation or angular direction relative to the muon decay point. The RMS values are consistent with the reconstructed Monte Carlo tracks presented in Section 4.8.4.

4.9.2 Fitting cos(θ) For Data

Figure 4.44 displays the raw $(cos(\theta))_{fit}$ distribution obtained from applying the fitting algorithm to data set 07434 and prior to correcting for systematic bias or inefficiencies. An obvious deficit at $(cos(\theta))_{fit} \approx 0$ is again apparent, with excesses in the two adjacent bins.

The selection criteria employed by the fitting procedure may have contributed to this deficit as tracks at $\theta_{x,y} \approx \pm\frac{\pi}{2}$ were deliberately excluded from the analysis. However, this feature was observed for both data and digitised Monte Carlo (Figure 4.39b), but is less apparent in the true Monte Carlo (Figure 4.39a). This implies that an inherent feature of the detector reconstruction is culpable. Section 4.8.12 outlined a method of correcting for this systematic bias on a bin-by-bin basis. For each uncorrected (raw) $(cos(\theta_{fit})$ bin the corrected content is given by Equation 4.46, the bias matrix elements, a_{ji}, and efficiency, ϵ, are computed

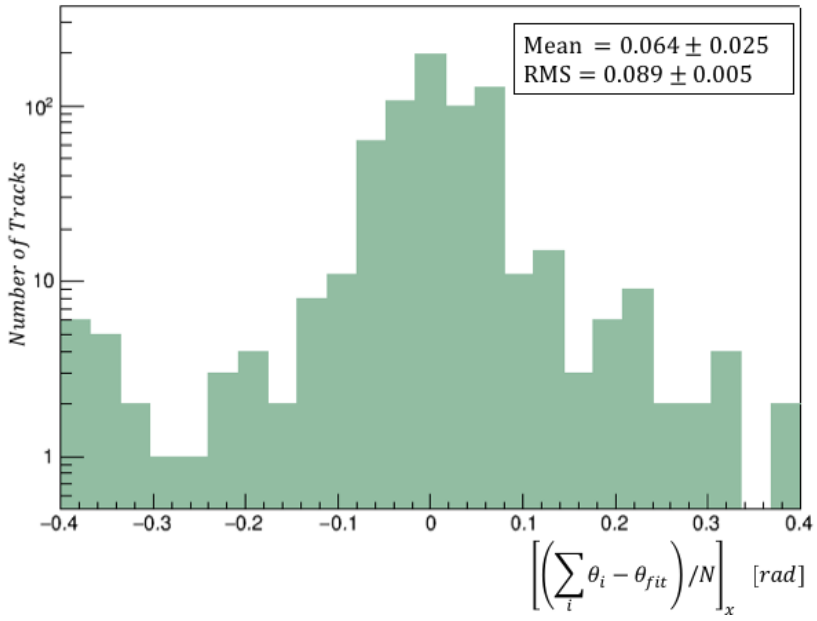

(a)

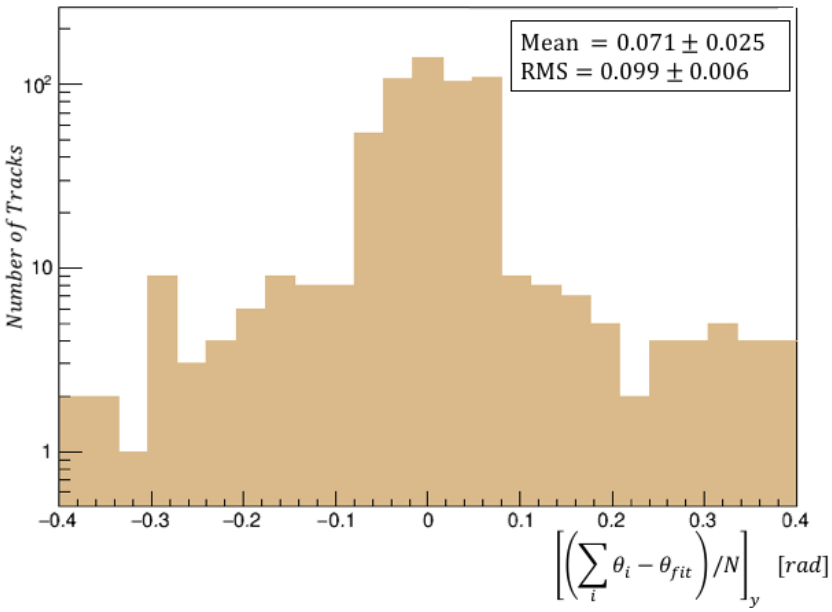

(b)

Figure 4.43: Distribution of the track residuals for data set 07434 for EMR hits in the x (a) and y (b) planes. This represents the average difference between angle of a vector drawn from the vertex to a given hit and the overall, fitted, track angle for each track. In (a) A mean of 0.0064 ± 0.025 rad and RMS of 0.0885 ± 0.005 rad is obtained. In (b) A mean of 0.0071 ±0.025 rad and RMS is 0.099 ± 0.006 rad is obtained. This is consistent with the y distribution and the analogous value for reconstructed Monte Carlo.

using Monte Carlo samples.

Figure 4.45 shows the distribution of $(cos(\theta))_{fit}$ after this correction has been applied. Fitting a straight line to the distribution and utilising Equation 4.12 will give a measure of the effective beam polarisation. The data set is unpolarised so a gradient consistent with 0 is expected if depolarisation in the cooling channel is negligible, which should be the case for an unpolarised beam. A normalised gradient of -0.00713± 0.07312(stat.) ± 0.06181 (sys.) is obtained, where the total systematic error is computed via comparison of

fits to the corrected and uncorrected distributions. This corresponds to a muon beam polarisation of -0.02139 ± 0.21936 (stat.) ± 0.18543 (sys.). The data is consistent, within $\pm 1\sigma_{stat+sys}$, with an unpolarised beam suggesting the method has can correctly measure the beam polarisation at the EMR.

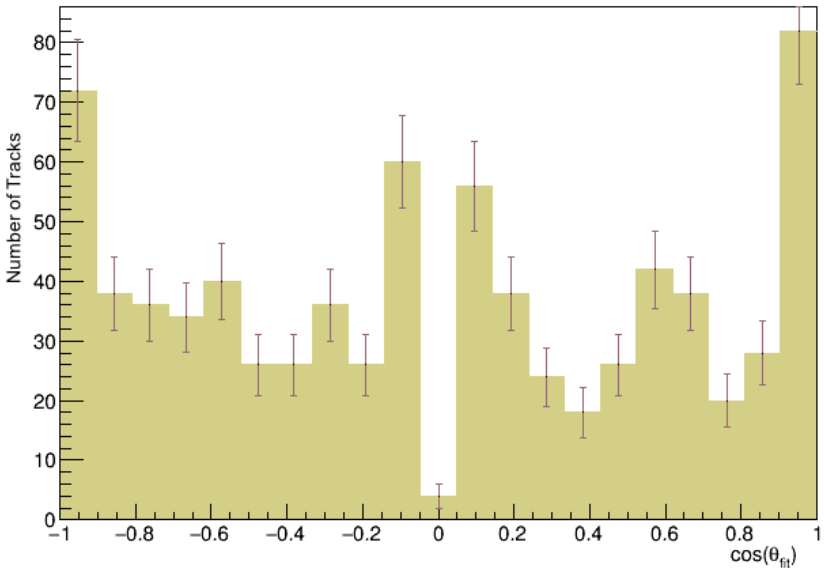

Figure 4.44: Distribution of raw $(cos(\theta))_{fit}$ for data set 07434 derived using the method outlined in this thesis. A systematic effect is observed and is corrected for using Equation 4.46, the resulting distribution is presented in Figure 4.45. The error bars exhibited here are purely statistical and are taken as $\sqrt{n_{bin}}$, where n_{bin} is the bin content.

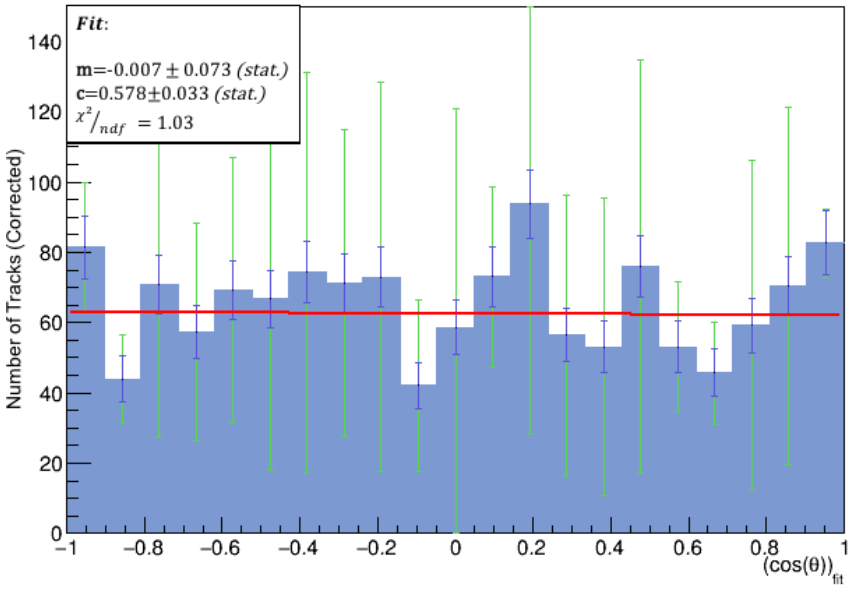

Figure 4.45: Distribution of corrected $(cos(\theta))_{fit}$ for the data set 07434 found using Equation 4.46. The raw bin content, obtained from Figure 4.44 is multiplied by "correction factors" derived from Monte Carlo (explained in Section 4.8.12). These correct for systematic errors and inefficiencies in the fitting procedure. A linear fit is performed, using Equation 4.12, the gradient is a measure of the beam polarisation at decay. A polarisation of -0.02139± 0.21936 (stat.) ± 0.18543 (sys.) is obtained, consistent with an unpolarised beam. The blue error bars represent the statistical errors and the green error bars represent the difference in the systematic correction (i.e. difference in bin content of corrected and raw distributions). The $\chi^2/(ndf)$ for the fit is 1.03, showing agreement with the linear fir.

4.9.3 Polarisation Sensitivity to Selection Criteria

In Section 4.7.6 a number of track selection criteria were outlined. These were optimised to increase purity and improve angular resolution of the fitting routine. Table 4.4 characterise the changes in the derived polarisation if each cut is disregarded.

For the Monte Carlo samples the derived polarisation values all remain "+." For the true Monte Carlo sample, some variation is observed and the derived values shift away from the expected polarisation for the fully polarised beam. However, the altered polarisation do not differ significantly ($> 1\sigma$) from the final (all cuts enforced) value.

For reconstructed Monte Carlo the deviations are larger and, when all cuts are removed, a significant difference is observed from the polarisation derived when all selection cuts were enforced. This is also the case for the data. In reconstructed Monte Carlo and data the derived polarisation differ by 21% and 26% respectively. In the case when the data is being considered the bias matrix has been recalculated and the same cut has been removed from both Monte Carlo derivations.

The fact that both Monte Carlo and data maintain their expected polarisation, even when all track selection cuts are removed, shows that the fitting method is able to correctly identify the beam polarisation. Although, the cuts help to improve the accuracy of the polarisation measurement by removing noise or poorly reconstructed tracks they do not cause significant depolarisation or remove the directionality of the beam's polarisation.

Cut Removed	MC Recon.	MC True	Data (Corrected)
All Cuts Enforced	**0.915±0.243**	**1.131±0.171**	**-0.02139± 0.21936**
"Window Cut"	0.891 ± 0.231	1.132 ±0.191	-0.02241±0.21122
"Fiducial Cut"	0.732 ±0.211	1.138±0.188	-0.02315±0.24311
"$\Delta t_{hit_{i,i-1}}$" Cut	0.876 ±0.243	1.132 ±0.177	-0.02211±0.16713
"$\Delta r_{hit_{i,i-1}}$" Cut	0.786 ± 0.211	1.135±0.178	-0.02511±0.27613
All Removed	0.719 ±0.211	1.139±0.189	-0.02715±0.15614

Table 4.4: Table summarising the change in derived polarisation if the various track selection criteria are removed. Statistical error on the fit line are also exhibited.

4.10 Systematic Error Discussion

This section summarises several sources of uncertainty which may exist in the polarisation measurement and attempts to quantify their impact on the final result.

4.10.1 Bin Widths in "Vector Angle" Plot

A systematic error exists on all angular measurements in this study which is due to the resolution of the "vector angle" plot used to derive the fitted value, θ_{fit}. The uncertainty on both θ_x and θ_y is ±0.05 rad. As a result each $\vec{r}_\mu$ and $\vec{r}_e$ has an associated tolerance emanating from this resolution. This systematic error is removed via the application of the correction factors.

4.10.2 Random "Noise"

The EMR readout, the Digital Buffer Board, stores all TDC and ADC information, this includes information associated with the trigger and all that happens between triggers i.e. every hit which occurs during the time of a specific spill (up to $3ms$). This information may include electrons resulting from the decays of both muons and pions, cosmic muons and electronic noise. Noise separation and rejection is, therefore, essential in order to achieve accurate event reconstruction.

Timing information is utilised to reject electronics noise arising in the EMR readout. This will typically come $\approx$100 ns after the corresponding hits associated to the trigger. Decay electrons and noise from comic muons are harder to differentiate as they are not coincident with the trigger, arriving randomly throughout the spill. Consequently, it is difficult to fully exclude random noise. However, the cuts on the time between, and relative positions of, consecutive hits, outlined in Section 4.7.4, help limit the impact it will have on this analysis.

The effect of noise on the calculated track residuals can be inferred by removing all resolution cuts and recalculating the track residuals. By doing so the RMS was seen to increase by 41 % in both orientations. Given that the RMS of the track residuals, presented in Section 4.9.1, are consistent with the detector limits and reconstructed Monte Carlo, it is assumed that the contribution of cosmic muons and random noise on the measured beam polarisation is negligible, once the track resolution criteria, outlined in Sections 4.7.4 and 4.7.6, were applied.

4.10.3 "Cross-Talk" between EMR Channels

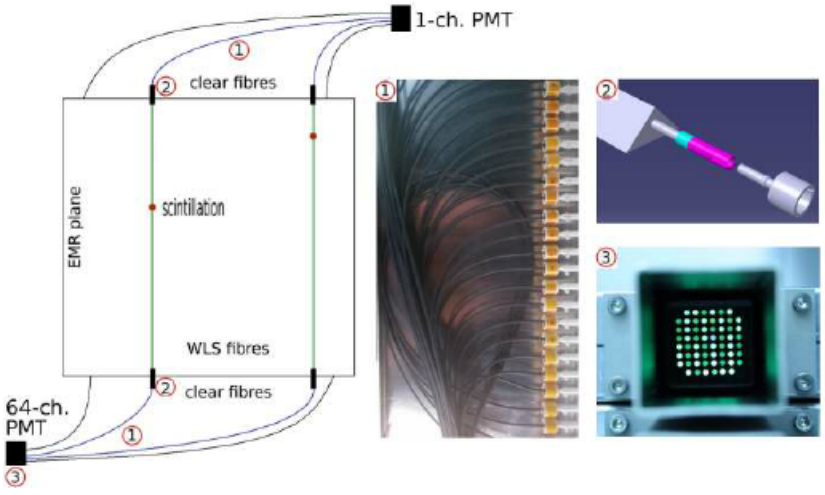

Figure 4.46: A schematic of the EMR readout taken from [206] showing how light is transported in a plane of the EMR. After scintillation, light is transported by the WLS fibre to the connectors on each end of the bar. This optical connector is shown in (2). The light is then transmitted through the clear fibres (1) to finally reach the fibre mask (3) that is fitted against the PMT. The mask shown here is the MAPMT fibre mask.

Figure 4.46 presents a schematic of the EMR read-out. Scintillation light is transported via Wavelength-Shifting-Fibres (WLS) to connectors at the end of each bar. Clear fibres then transmit the light to the PMTs.

There is the possibility of cross-talk between adjacent channels; this is studied in detail in [206]. The main source of this cross-talk occurs at the MAPMT which is where all the fibres coming from the 59 bars come together in one place. The cross-talk could be a result of optical cross-talk, when a single fibre of the bundle shines on more than one channel of the MAPMT mask. Figure 4.47 shows a schematic representation of how optical cross-talk can occur between adjacent channels.

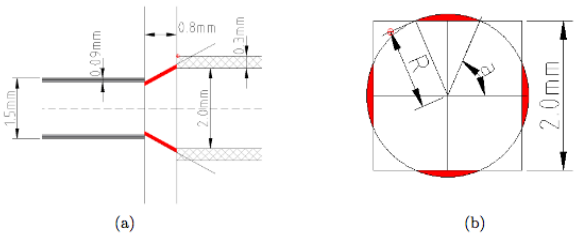

Figure 4.47: Schematics showing optical cross-talk taken from [206]. Both show how light can leak into the wrong MAPMT channel. a) shows a side view of a clear multi cladding fibre shining on one channel of the MAPMT and b) shows a circle of light coming from the clear fibre and shining on the MAPMT channel.

Another possible source of cross-talk is anode crosstalk, when a photo-electron leaks from a dynode to an adjacent accelerating structure generating a signal in another channel. The study presented in [206] concludes that the probability of cross-talk is mostly under 0.5 % and, even when present the signal recorded in the adjacent channels only represents 4.5 ± 1.5 % of the expected signal. Therefore, cross-talk will be ignored in this analysis as it is assumed negligible.

4.10.4 Finite Bin Width in cos(θ) and Efficiency Plots

Both the $(cos(\theta))_{fit}$ plot, used to derive the polarisation of the beam, and the efficiency and bias plots, used to derive the correction matrix, have finite bin widths; 21 bins were used for a $-1 \leq cos\theta \leq 1$ range. Reducing the number of bins will remove some of the cos(θ) plot's sub-structure, thus, reducing the accuracy of the fit. Doubling the number of bins produced a change in the derived polarisation of -2% for fit to the true Monte Carlo EMRHits, making the derived polarisation closer to the expected polarisation. However, increasing the number of bins means statistical errors on each bin becoming increasingly more significant. The choice of 21 bins is used as a compromise between accuracy in the fit and reduced statistical errors per bin.

4.10.5 Depolarisation due to Material in The EMR

Several processes may contribute to the depolarisation of muons as they come to a stop within a material. A concise summary of these processes is presented in [208]; two main sources of depolarisation applicable to decelerating, positively charged muons are identified as:

1. Depolarisation from Multiple Coulomb Scattering

   The most frequently occurring form of depolarisation, for both positive and negative charged muons,

results from multiple Coulomb scattering; discussed in Section 4.3.2. The mean angle, through which the muon rotates, will be small, even for high energy muon beams, consequently, depolarisation resulting from scattering is considered negligible in this analysis.

2. Depolarisation of Positive Muons via Muonium Formation

   Following multiple scattering and as the muon slows and eventually comes to a rest in a material it will reach a speed comparable to that of the electron in the medium, many short-lived muonium atoms may then form, resulting in depolarisation of the beam. The effects of muonium formation on beam polarisation are studied in [208]. It is found that when a magnetic field is applied along the beam trajectory, restoring the muon's velocity, a μ^+ beam retains 93.4 ± 4.8 % of its initial polarisation. Therefore, the beam will preserve almost all of its polarisation, within the experimental limits, when a magnetic field is applied along the direction of travel; depolarisation will be minimal in such a set-up. Nevertheless, in the absence of a magnetic field the polarisation was found to be altered by 42%. This result is, however, averaged over several different materials, many of which will not be present in the MICE channel.

   Direct measurements of the muon residual polarisation after traversing different target materials immersed in varying external magnetic fields are examined in [209] , [210] and [211]. The level of depolarisation is observed to depend considerably on the material. It is essential that all possible outcomes for the various materials present in the EMR are considered in order to ascertain the uncertainty which exists on the measured polarisation. The fiducial volume of the EMR comprises primarily of polystyrene scintillator bars, for which no direct measurement is available; it is assumed that this material behaves like polyethylene which is examined in [210]. When no magnetic field is applied a residual polarisation of 67.1 ± 2 % is reported, reaching ≈ 100% as the field is increased as is expected given [208]. Data presented in [211] corroborates that in sufficiently large magnetic fields parallel to the direction of travel this depolarisation is "quenched." However, evidence is again presented suggesting muons become partially depolarised when no magnetic field is present.

4.10.6 Particle Detector Efficiency and TOF_{12} assumptions

On average, muons lose ≈ 30± 3 MeV/c in the KL and TOF2 detectors. In addition, the TOF detectors have a resolution of $\sigma_t^{TOF} \approx 70$ ps and $\sigma_z^{TOF} \approx 1$ cm [172]. Although, this could lead to mis-identification of particles, given the strict TOF_{12} selection window imposed and the calculated selection efficiencies (Section 4.7.6) it is unlikely it has has too much impact. In addition the EMR has a longitudinal position resolution of $\sigma_z^{EMR} \approx$5 mm [172]. To calculate the effect of the detector resolutions the particle TOF_{12} and z positions are corrected to the extreme of the respective tolerances and the polarisation recalculated. The total difference in calculated polarisation was $< 0.001\%$.

4.10.7 Implications on the Calculated Polarisation

Before reaching the EMR muons traverse several materials within the various cooling channel elements. Given the high magnetic field throughout the channel it will be assumed that no depolarisation emanating from muonium formation occurs prior to the beam entering the EMR. However, the EMR is not within a magnetic field. It is must, therefore, be anticipated that some depolarisation may occur in the plastic bars of the detector. Utilising the result of [210] the beam may only retain 67.1± 2 % of its initial polarisation. It is necessary to take this into account as a systematic uncertainty on the polarisation measurement obtained in this analysis. An upper limit of 32.9% will be used to characterise this effect and will be quoted along with the polarisation in further discussion. This corresponds to $\pm - 0.02139 \times 0.329 = 0.00721$ for the polarisation measurement of -0.02139± 0.21936 (stat.) ± 0.18543 (sys.) ± 0.00721 (depol.) obtained from the data sample. In addition, depolarisation from the sources described in 4.10.5 accounts for a much smaller change in polarisation, with an upper estimate of 0.01%.

Table 4.5 summarises the various sources of systematic uncertainties which are a result of limitation in the measurements available. In addition to the reconstruction/fitting bias correction and depolarisation uncertainties a total detection method systematic uncertainty of ± 0.00120 (det.) is calculated.

Systematic	Value
PID	$\epsilon_{TOF_{12}PID} \approx 0.42\%$
TOF resolution	$\sigma_t^{TOF} \approx 70$ps, $\sigma_z^{TOF} \approx 1$ cm
TOF2+KL momentum loss	$\sigma_{p_z}^{KL} \approx 30 \pm 3$ MeV/c
EMR z resolution	$\sigma_z \approx 5$ mm
$(cos(\theta))_{fit}$ bin width	2%
Depolarisation (Channel)	$< 0.01\%$
Depolarisation (EMR)	32.9 %
Cross-Talk	Negligible
$\theta_{x,y}$ resolution	±0.05 rad per $\theta_{x,y}$ (Corrected)
Electronics Noise/Cosmic Background	Removed
Recon./Fit Algorithm Bias/inefficiency	Corrected

Table 4.5: Table summarising sources of systematic uncertainties in the method presented in this thesis. Those which are a result of the fit/reconstruction bias and inefficiencies have been corrected via the MC driven correction factors.

4.11 Conclusions

A complete analysis has been presented in which a fitting algorithm is derived possessing the ability to fit particle tracks at the EMR and obtain a measurement of the effective muon beam polarisation upon decay.

The vertex, or decay point, of the incoming muon is identified as the EMR bar in which the muon deposits the most energy. The incoming μ^+ and outgoing e^+ tracks are separated and fitted independently in the two transverse planes. The angle between the two tracks is determined and a combined $(cos(\theta))_{fit}$ is then obtained from the scalar product of "mother" and "daughter" fitted tracks.

The algorithm was verified for both true and digitised Monte Carlo, track resolutions were shown to

provide fitted track angles consistent with the limits of the geometry of the detector and reconstruction efficiencies of $\approx 80\%$ where obtained. This was deemed sufficient to produce an accurate calculation of the polarisation.

The algorithm was applied to both true and digitised Monte Carlo samples with an initial polarisation of $P_\mu = 1$. The Monte Carlo takes into account the depolarisation due to spin precession and multiple scattering. Both effects are expected to be $< 1 \times 10^{-4}$ (Section 4.10.5). A measured polarisation of 0.915 $\pm$ 0.243 (stat.) $\pm$ 0.194 (sys.) was obtained from the digitised Monte Carlo which accounted for the finite size of the EMR bars and the effects of the digitisation of the detector. This is both consistent with that derived from the true Monte Carlo sample (1.131$\pm$0.171 (stat.) $\pm$ 0.128 (sys.)) and the expected value. Therefore, the algorithm presented in this thesis was proven to have the ability to successfully identify the polarisation of a muon beam using positron tracks at the downstream calorimeter, within acknowledged errors. A systematic bias was observed and a correction matrix derived from Monte Carlo. This was later applied to the data.

After correcting for the observed geometric bias and measured inefficiencies in the fitting method, the overall muon beam polarisation for an initially unpolarised data sample, obtained during the Step IV running of MICE, was calculated as: -0.02139$\pm$ 0.21936 (stat.) $\pm$ 0.18543 (sys.) $\pm$ 0.00721 (depol.) $\pm$ 0.00120 (det.). This is consistent with an unpolarised beam within $\pm 1\sigma_{TOTAL}$. Once again, the fitting algorithm has been shown to accurately determine the polarisation of the muon beam at the EMR. The technique can now be employed by MICE, and future facilities, to monitor beam polarisation thus allowing accurate determination of the systematic uncertainty on the beam emittance resulting from positron backgrounds.

In addition, both the Neutrino Factory and Muon Collider will require the functionality to be able to monitor and control muon polarisation throughout their sub-systems. This study could have some impact on how such facilities may do so.

Chapter 5

A Measurement of the Focus Coil Alignment using Transfer Matrices

Chapter 3 outlined the design goals of MICE. MICE is currently operational in its "Step IV" configuration. During this stage it is necessary to characterise any sources of errors within the beam line. Misalignment in the Focus Coil's magnetic axis relative to the beam axis as well as the misalignment of the various beam line detectors relative to one another will introduce non-linear effects which cause emittance growth. It is, therefore, essential that any Tracker-Tracker or Tracker-Focus Coil misalignment is measured [212].

This chapter presents a unique analysis using single particle transfer matrices at the Focus Coil to place limits on the presence of transverse (x, y) translational or rotational offsets relative to the global beam axis (longitudinal z axis). The analysis presented in this chapter is unique, there are no known previous studies which have used single particle transfer matrices in this way. Magnet alignment is important in any accelerator or collider facility and this novel technique can be adapted to any multi-magnet particle machine in which a particle's co-ordinates are measured upon entrance and exit of a component magnet. Consequently, this study is an important reference point for accelerator physics as a whole.

5.1 Measuring Transfer Matrices

When a charged particle travels along an accelerator beam line, through the various magnetic fields, its path will be altered. The particle beam may be focused, defocused or bent about the beam axis. Chapter 2 introduced the use of transfer matrices as a means of describing the propagation of a single particle within an accelerator beam line. Transfer matrices are utilised to describe the effects of the magnetic fields on a particle's path in a way analogous to how they may be used in optical physics to explain the effects of a lens on a ray of light [213] . Transfer matrices allow the beam line magnets to be described independently from the input beam and can be exploited to provide a measurement of the various lattice parameters defined in

Section 2.3.8.

Within the geometry of the Step IV cooling channel (Figure 3.4) the MICE experiment employs two identical scintillator fibre trackers to measure the 4-D co-ordinates, (x, x', y, y') of a specified particle both upstream and downstream of the Focus Coil. It is conceivable to utilise these two measurements to derive a 4×5 transfer matrix, including a constant offset term, for muons that pass through the Focus Coil. This chapter presents a measurement of this transfer matrix and uses it to place limits on any transverse misalignment of the coil's magnetic axis relative to the beam axis.

The Focus Coil module comprises of two focusing coils (Section 3.4.2). These can be set to have the same polarity, in which case the Focus Coil acts like a solenoid, or opposing polarities ("Flip mode"). The Focus Coil can be regarded as one solenoidal magnet within this analysis.

5.2 Alignment in MICE

Misalignment in MICE can originate from two independent sources [212]:

1. **Magnet-Axis : Beam-Axis Misalignment** - The alignment of the axes of the various superconducting magnets with respect to the beam axis. An exaggerated representation of magnetic axis misalignments of both tracker Spectrometer Solenoids and the Focus Coil in the Step IV geometry is shown in Figure 5.1.

2. **Detector : Detector Misalignment** - The alignment of the detectors with respect to each other and to the global co-ordinate system. Misalignment of the various detectors relative to one another will not affect beam emittance; nevertheless, it will affect the emittance measurement if not properly corrected for i.e. if the detector position is not well enough known.

This analysis is concerned with the former of these two potential sources of misalignment, specifically, any misalignment of the Focus Coil's magnetic axis, relative to the beam axis, in the Step IV configuration. Misalignment of this sort will introduce an additional transverse field resulting in the displacement of the beam from the central axis. The amount of displacement will depend on magnet current, beam polarity and momentum and whether the Focus Coil is in Flip or Solenoid mode.

Any displacement of the magnetic axis will not affect the measurement of the emittance as the difference in centre-of-gravity of the beam distribution can easily be corrected for in the calculation of the covariance matrix used for emittance measurement. Nevertheless, displacement of the beam axis can be indicative of issues in the diagnostics; isolating this effect from magnet misalignment enables better studies of the detector diagnostics. MICE is designed to have an on-axis magnetic field, as would be necessary for a real cooling channel. Consequently, misalignment of this type will define how well the cooling channel can perform and the amount of ionisation cooling MICE can achieve will be directly affected by beam-axis misalignment. It is, therefore, essential that it is quantified and corrected for.

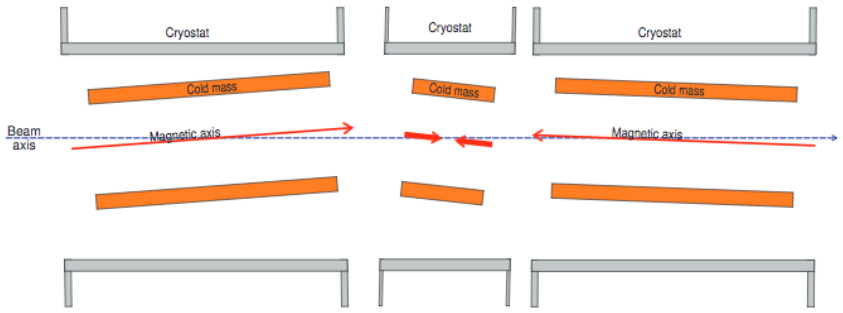

Figure 5.1: Simple, but exaggerated, representation of how magnetic misalignment may cause the magnetic axis of the Step IV beam line magnets to differ from the beam axis (SciFi Tracker Spectrometer Solenoids and Focus coil are depicted) [212]. The Focus Coil here is represented in "flip" mode (Section 3.4.2 discusses the various operational modes of the Focus Coil).

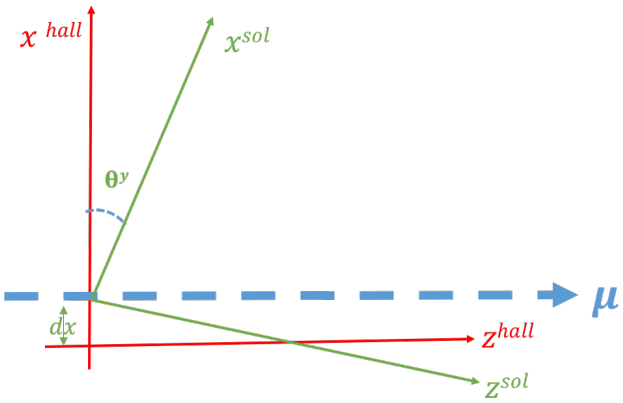

Figure 5.2: Simple representation of how the coil axis may be offset in the x-z plane relative to the beam ("hall") axis.

If the Focus Coil's magnetic axis is misaligned from the beam axis then an additional field, perpendicular to the motion of travel, will be acting on the muons. Figure 5.2 shows a simple representation of such an offset in the transverse, x-z, plane. If a muon passes through the coil aperture, in the case of an ideal solenoid, i.e. no misalignment, the transverse magnetic field experienced by that particle at position (z, x) will be [214]

$$B_x^{ideal} = -\frac{1}{2}\frac{\partial B_z}{\partial z}x, \tag{5.1}$$

assuming the paraxial approximation and where B_z is the longitudinal field on the axis. Considering the misaligned case presented in Figure 5.2, θ_y is a rotational offset around the y axis in the x-z plane, dx is the offset of the coil axis is x and L is the length of the coil in z. In this scenario the misalignment produces bending dipole terms to leading, linear optic order such that the transverse magnetic field experienced by the muon is now

$$B_x' = B_x^{ideal} + B_z\theta_y + \frac{dx}{2}\frac{\partial B_z}{\partial z} + \frac{L}{2}\theta_y\frac{\partial B_z}{\partial z}. \tag{5.2}$$

An analogous equation can be derived for B_y'.

These additional transverse fields cause the shift in the centre-of-gravity of the beam from the beam axis. Further discussion of higher order dispersion and bending effects of an off-axis beam in a solenoid is given in [214] and [215].

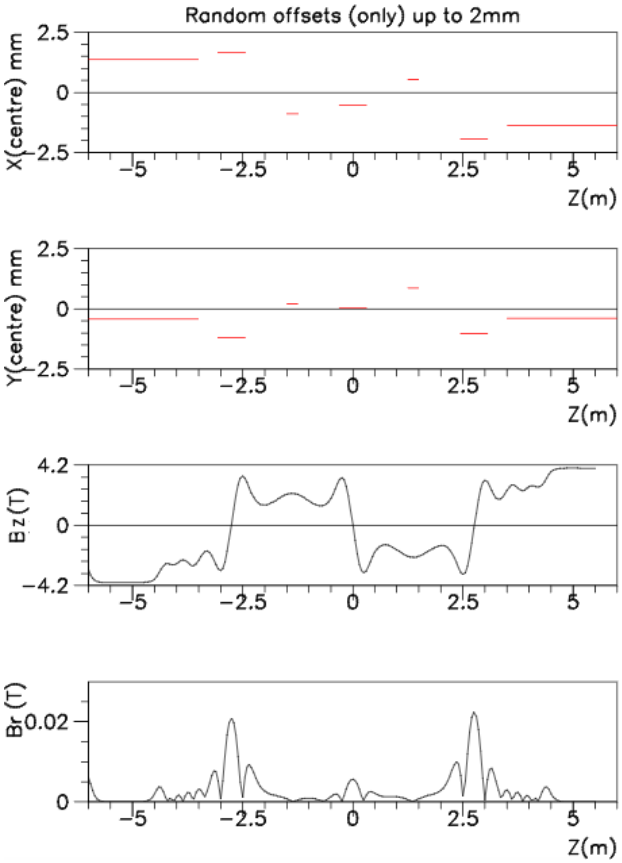

Figure 5.3: Elements across the whole of MICE are randomly offset. Upper pair: Positions in x and y of the bobbin axes (red lines) of the seven modules with respect to the beam axis. The offsets of the axes were randomised within a 2 mm radius cylinder about the beam axis. Lower pair: Effect on B_z and combined B_r (total radial field) on beam as a result of offsets [212]. This study took place on a simulated version of MICE's final stage channel configuration, not "Step IV."

Within [212] a comprehensive Monte Carlo study is presented and MICE's tolerances to transverse translational and rotational offsets are calculated. Figure 5.3 illustrates the effect of small, random, transverse misalignments of various elements throughout the length of the cooling channel on the longitudinal and radial magnetic fields. A displacement of $dx, dy > 0.5mm$ is found to cause measurable dispersion. A preceding study, presented in [216], demonstrates that a transverse total rotational offset of $\theta_{x,y} > 24$ mrad is sufficient to produce significant beam losses for a Focus Coil in solenoid mode.

5.3 Measuring Misalignment

There are numerous approaches presently employed within accelerator physics to obtain direct alignment measurements of the magnetic axes of accelerator components. In [217] a review of 19 different beam alignment methods is presented and detailed discussion of the performance of each is given.

The entire MICE cooling channel, including the Focus Coil, has been surveyed, and alignment measurements of the beam line components performed, during the Step IV commissioning of the experiment [218]. Although useful, these direct measurements are dependent on the accuracy of the measuring instrumentation. Consequently, using measurements from the survey alone is insufficient; there are many motivations for utilising additional "beam-based alignment" techniques as a consistency check of the detector survey, most notably:

1. When MICE is in operation large forces will act upon the Focus Coil, and the entire cooling channel. The effect of the Partial Return Yoke (PRY) on the Coil is unknown. An asymmetry of the lateral placing, with respect to the beam axis, could introduce not-yet-measured error fields which could result in displacement of the beam from the centre.

2. The magnets are made by suspending the cold mass inside a vacuum vessel on a pre-tensioned strap. There exists some uncertainty on the alignment of this cold mass. In addition, when the magnets are in operation the large magnetic forces between the cold masses of the modules will cause them to move. The cold mass suspensions have been designed to support the maximum expected longitudinal forces, but, a misalignment of the magnetic axes of the modules will produce an additional torque which will tend to rotate the modules.

3. There exists some engineering uncertainty about the winding and number of turns (i.e. effective current) within the coils. Further discussion of how the method presented here can be exploited to obtain a measurement of the effective Coil current is given in Section 5.3.6.

There are again many techniques employed to provide "beam based alignment" measurements and some of these make use of transfer matrices. Prior studies usually assume a transfer matrix established from an analytical formula, checking these against the beam distribution rather than using a measurement based transfer matrix calculation for single particles. This analysis is, therefore, thought to be the first of its kind and a novel way of measuring misalignment. The technique can be utilised by MICE to provide consistency checks to the existing direct alignment methods or as an alternative, in future.

5.3.1 Summary of Method

The process of obtaining the transfer matrices and measured misalignment can be divided into 4 distinct tasks:

1. Set up a linear fitting routine which takes two sets of trace space co-ordinates of a given particle, one at the upstream tracker, and one at the downstream tracker, and calculates a transfer map between the two.

2. Apply the analysis and fitting routines to straight track data, i.e. data taken when the Focus Coil is switched off, and use this to quantify any systematic errors as well as justify any selection criteria

required to improve the resolution and accuracy of the measurement.

3. Use the analysis with these optimised selection criteria and knowledge of the limits of the method to calculate the transfer matrix for data taken when the Focus Coil is switched on.

4. Iterate through a series of sample Monte Carlo lattices, starting from perfect alignment, and use MINUIT to compare the results to the data. The objective is to obtain the Focus Coil position and effective current which minimises the total χ^2 value between the measured transfer matrix of the data and that of the Monte Carlo. Each iterative Monte Carlo then becomes more "data-like." This total χ^2 will take into account fits to the x and x' and y and y' components of the matrix as well as the focusing terms, which are current dependent. The aim being to establish a fitted coil position which accounts for misalignment of all 5 parameters (x, x', y, y' and coil current, I).

5.3.2 Definition of the Transfer Matrix

When the MICE SciFiTracker spectrometer solenoids are switched off, as is the case during this analysis, the trackers measure only the 4 transverse trace space co-ordinates, (x, x', y, y'), of the particles in the beam. As a result, only the transverse component of the transfer matrices are considered here.

The transfer matrix ($\underline{\underline{M}}$) at the Focus Coil defines a linear relationship between the trace space co-ordinates of a muon at the upstream tracker ($\vec{u} = (1, x_u, x'_u, y_u, y'_u)$) and the downstream tracker ($\vec{d} = (1, x_d, x'_d, y_d, y'_d)$) such that

$$x_d = M_{00} + M_{01}x_u + M_{02}x'_u + M_{03}y_u + M_{04}y'_u, \tag{5.3}$$

$$x'_d = M_{10} + M_{11}x_u + M_{12}x'_u + M_{13}y_u + M_{14}y'_u, \tag{5.4}$$

$$y_d = M_{20} + M_{21}x_u + M_{22}x'_u + M_{23}y_u + M_{24}y'_u \tag{5.5}$$

and

$$y'_d = M_{30} + M_{31}x_u + M_{32}x'_u + M_{33}y_u + M_{34}y'_u \tag{5.6}$$

where the M_{ij} are the elements of the transfer matrix such that

$$\underline{\underline{M}} = \begin{pmatrix} M_{00} & M_{01} & M_{02} & M_{03} & M_{04} \\ M_{10} & M_{11} & M_{12} & M_{13} & M_{14} \\ M_{20} & M_{21} & M_{22} & M_{23} & M_{24} \\ M_{30} & M_{31} & M_{32} & M_{33} & M_{34} \end{pmatrix}.$$

Any misalignment will become apparent when the constant terms, i.e. M_{i0}, deviate from 0 (red). Here x' and y' are the trace space co-ordinates outlined in Section 2.1.2 and describe the particle's momenta in x and y relative to the z component. The elements highlighted in green are the transverse focusing terms, these relate the (x_d, x'_d) to (x_u, x_u) (upper left) and (y_d, y'_d) to (y_u, y'_u) (lower right). These terms describe the effect the Focus Coil has on compressing the beam in the (x, x') and (y, y') trace space planes respectively. The terms highlighted in purple are angular momentum terms - often referred to as the "defocussing" terms. These relate (x_d, x'_d) to (y_u, y'_u) and vice versa. These terms represent the coupling between motion in the two directions, if x and y are decoupled these terms vanish. In this analysis the entire matrix is calculated and used to place limits on the Focus Coil's misalignment relative to the beam axis.

5.3.3 Transfer Matrices for "Straight Tracks"

When the Focus Coil magnets are switched off, and perfect alignment in the trackers is assumed, Equations 5.3 to 5.6 can be simplified to describe the muon's "straight track" through a drift space of length L, L being the distance between the last station of the upstream tracker and the first of the downstream tracker. In this scenario $M_{02} = M_{24} = L$ and the downstream co-ordinates can be expressed in terms of the upstream co-ordinates such that

$$x_d = x_u + Lx'_u, \tag{5.7}$$

$$x'_d = x'_u, \tag{5.8}$$

$$y_d = y_u + Ly'_u \tag{5.9}$$

and

$$y'^d = y'_u. \tag{5.10}$$

These "straight tracks" can be used as a test setup allowing the accuracy of the fitting method to be established and any systematic errors to be quantified.

5.3.4 Translational and Rotational Misalignments

Consider a general case of a solenoid placed in the MICE cooling channel. A particle has a 3D cartesian spatial co-ordinate in the solenoid (sol) and reference ($hall$) frames defined as

$$\vec{r}^{sol} = (x^{sol}, y^{sol}, z^{sol}), \tag{5.11}$$

and

$$\vec{r}^{hall} = (x^{hall}, y^{hall}, z^{hall}), \tag{5.12}$$

respectively.

If there exists some transverse misalignment $\vec{dr} = (dx, dy, 0)$ between the axis of the solenoid and the reference co-ordinate system, the co-ordinate system in which z is assumed to be the beam axis, then these two points are related to one another by the expression

$$r_{sol} = \underline{\underline{R}}_{x,y}(\vec{r}_{hall} + \vec{dr}) = \underline{\underline{R}} \begin{pmatrix} x^{hall} + dx \\ y^{hall} + dy \\ z^{hall} \end{pmatrix}, \tag{5.13}$$

where $\underline{\underline{R}}_{x,y}$ describes the total rotational transformation of the transverse plane and $\vec{dr}$ is the translational misalignment vector.

Assuming a rotation of the axes about the x axis in the $x-z$ and the y axis $y-z$, relative to the hall co-ordinates, denoted as $\underline{\underline{R}}_x$ and $\underline{\underline{R}}_y$ respectively, the total rotational matrix $\underline{\underline{R}}_{x,y}$ for the transverse plane is then given by:

$$\underline{\underline{R}}_{x,y} = \underline{\underline{R}}_x . \underline{\underline{R}}_y = \begin{pmatrix} 1 & 0 & 0 \\ 0 & cos\theta_x & -sin\theta_x \\ 0 & sin\theta_x & cos\theta_x \end{pmatrix} \begin{pmatrix} cos\theta_y & 0 & sin\theta_y \\ 0 & 1 & 0 \\ -sin\theta_y & 0 & cos\theta_y \end{pmatrix} \tag{5.14}$$

$$= \begin{pmatrix} cos\theta_y & 0 & sin\theta_y \\ sin\theta_x sin\theta_y & cos\theta_x & -sin\theta_x cos\theta_y \\ -cos\theta_x sin\theta_y & sin\theta_x & cos\theta_x cos\theta_y \end{pmatrix}. \tag{5.15}$$

Assuming that the angular displacements are small and therefore $cos(\theta_{x,y}) \approx 1$ and $sin(\theta_{x,y}) \approx \theta_{x,y}$, and ignoring any second order terms, gives

$$\underline{\underline{R}}_{x,y} = \begin{pmatrix} 1 & 0 & \theta_y \\ 0 & 1 & -\theta_x \\ -\theta_y & \theta_x & 1 \end{pmatrix}. \tag{5.16}$$

By substituting Equation 5.16 back into Equation 5.13 the hall co-ordinates can be related to the rotated solenoid co-ordinates by

$$x^{sol} = x^{hall} + dx + z^{hall}\theta_y, \tag{5.17}$$

$$y^{sol} = y^{hall} + dy - z^{hall}\theta_x \tag{5.18}$$

and

$$z^{sol} = (y^{hall} + dy)\theta_y - (x^{hall} + dx)\theta_x + z^{hall}. \tag{5.19}$$

Rearranging Equation 5.19 gives

$$z^{hall} = z^{sol} - (x^{hall} + dx)\theta_x - (y^{hall} + dy)\theta_y. \tag{5.20}$$

Substituting this expression for z^{hall} back into those for x^{sol} and y^{sol}, and assuming all second order terms are negligible, gives:

$$x^{sol} \approx x^{hall} + dx + z^{sol}\theta_y \tag{5.21}$$

$$y^{sol} \approx y^{hall} + dy - z^{sol}\theta_x. \tag{5.22}$$

These expression describe the transformation a particle's 2D position co-ordinates from the hall frame into the solenoid frame, which is rotated and offset from this reference hall frame. The transformed gradient projections in the x-z and y-z planes (x' and y') can be found by differentiating these expressions with respect to z such that

$$x'^{sol} \approx x'^{hall} + \theta_y \tag{5.23}$$

and

$$y'^{sol} \approx y'^{hall} - \theta_x. \tag{5.24}$$

Equations 5.21 - 5.24 can, therefore, be used to transform a particle's tracker co-ordinates (x, x', y, y') from a situation in which the Focus Coil and Tracker are aligned to system in which the Focus Coil is displaced. The overall effect that translational and rotational offsets have on the derived transfer matrices will be discussed in Section 5.3.5.

5.3.5 Misalignment and the Transfer Matrix

Two transfer matrices, $\underline{\underline{M}}^{sol}$ and $\underline{\underline{M}}^{hall}$, can be defined describing the particle transportation in the Focus Coil (solenoid) frame and hall (lab) frames respectively. In the hall frame the particle has co-ordinates:

$$u^{hall} = (1, x_u^{hall}, x_u'^{hall}, y_u^{hall}, y_u'^{hall}), \tag{5.25}$$

$$d^{hall} = (1, x_d^{hall}, x_d'^{hall}, y_d^{hall}, y_d'^{hall}), \tag{5.26}$$

where the u denotes its upstream co-ordinate and d denotes its downstream co-ordinate. The first term is used to help derive the constant, offset, terms in this analysis. Likewise, the corresponding particle's co-ordinates in the solenoid, Focus Coil, frame can be denoted as:

$$u^{sol} = (1, x_u^{sol}, x_u'^{sol}, y_u^{sol}, y_u'^{sol}), \tag{5.27}$$

and

$$d^{sol} = (1, x_d^{sol}, x_d'^{sol}, y_d^{sol}, y_d'^{sol}). \tag{5.28}$$

u and d can be written as 5×1 column vectors, $\vec{u}$ and $\vec{d}$, related to one another by the respective transfer matrices such that

$$\vec{d}^{hall} = \underline{\underline{M}}^{hall} \vec{u}^{hall}, \tag{5.29}$$

and

$$\vec{d}^{sol} = \underline{\underline{M}}^{sol} \vec{u}^{sol}. \tag{5.30}$$

One can transform between the two frames using a transformation matrix, $\underline{\underline{T}}$, which will contain terms corresponding to the translational offsets, dx and dy, as well as the rotational offsets, θ_y and θ_x, outlined in Section 5.3.4 such that,

$$\underline{\underline{T}} = \begin{pmatrix} 1 & 0 & 0 & 0 & 0 \\ dx + L\theta_y & 1 & 0 & 0 & 0 \\ \theta_y & 0 & 1 & 0 & 0 \\ dy - L\theta_x & 0 & 0 & 1 & 0 \\ -\theta_x & 0 & 0 & 0 & 1 \end{pmatrix}. \tag{5.31}$$

The particle's co-ordinates in the solenoid and hall frames are therefore related by

$$\vec{u}^{sol} = \underline{\underline{T}}\vec{u}^{hall}, \tag{5.32}$$

and

$$\vec{d}^{sol} = \underline{\underline{T}}\vec{d}^{hall}. \tag{5.33}$$

Substituting these into Equation 5.30 gives

$$\underline{\underline{T}}\vec{d}^{hall} = \underline{\underline{M}}^{sol}\underline{\underline{T}}\vec{u}^{hall}. \tag{5.34}$$

Using Equation 5.29

$$\underline{\underline{TM}}^{hall}\vec{u}^{hall} = \underline{\underline{M}}^{sol}\underline{\underline{T}}\vec{u}^{hall}. \tag{5.35}$$

Multiplying out the LHS of 5.35 gives:

$$\begin{pmatrix} 1 & 0 & 0 & 0 & 0 \\ dx + L\theta_y & 1 & 0 & 0 & 0 \\ \theta_y & 0 & 1 & 0 & 0 \\ dy - L\theta_x & 0 & 0 & 1 & 0 \\ -\theta_x & 0 & 0 & 0 & 1 \end{pmatrix} \cdot \begin{pmatrix} 1 & 0 & 0 & 0 & 0 \\ M_{00}^{hall} & M_{01}^{hall} & M_{02}^{hall} & M_{03}^{hall} & M_{04}^{hall} \\ M_{10}^{hall} & M_{11}^{hall} & M_{12}^{hall} & M_{13}^{hall} & M_{14}^{hall} \\ M_{20}^{hall} & M_{21}^{hall} & M_{22}^{hall} & M_{23}^{hall} & M_{24}^{hall} \\ M_{30}^{hall} & M_{31}^{hall} & M_{32}^{hall} & M_{33}^{hall} & M_{34}^{hall} \end{pmatrix} \cdot \begin{pmatrix} 1 \\ x_u^{hall} \\ x_u'^{hall} \\ y_u^{hall} \\ y_u'^{hall} \end{pmatrix} \tag{5.36}$$

$$= \begin{pmatrix} 1 & 0 & 0 & 0 & 0 \\ dx + L\theta_y + M_{00}^{hall} & M_{01}^{hall} & M_{02}^{hall} & M_{03}^{hall} & M_{04}^{hall} \\ \theta_y + M_{10}^{hall} & M_{11}^{hall} & M_{12}^{hall} & M_{13}^{hall} & M_{14}^{hall} \\ dy - L\theta_x + M_{20}^{hall} & M_{21}^{hall} & M_{22}^{hall} & M_{23}^{hall} & M_{24}^{hall} \\ -\theta_x + M_{30}^{hall} & M_{31}^{hall} & M_{32}^{hall} & M_{33}^{hall} & M_{34}^{hall} \end{pmatrix} \cdot \begin{pmatrix} 1 \\ x_u^{hall} \\ x_u'^{hall} \\ y_u^{hall} \\ y_u'^{hall} \end{pmatrix}. \tag{5.37}$$

$$= \begin{pmatrix} 1 \\ [(dx + L\theta_y) + M_{00}^{hall}] + M_{01}^{hall} x_u^{hall} + M_{02}^{hall} x_u'^{hall} + M_{03}^{hall} y_u^{hall} + M_{04}^{hall} y_u'^{hall} \\ [\theta_y + M_{10}^{hall}] + M_{10}^{hall} x_u^{hall} + M_{11}^{hall} x_u^{hall} + M_{12}^{hall} x_u'^{hall} + M_{13}^{hall} y_u^{hall} + M_{14}^{hall} y_u'^{hall} \\ [(dx - L\theta_y) + M_{20}^{hall}] + M_{21}^{hall} x_u^{hall} + M_{22}^{hall} x_u'^{hall} + M_{23}^{hall} y_u^{hall} + M_{24}^{hall} y_u'^{hall} \\ [-\theta_x + M_{30}^{hall}] + M_{30}^{hall} x_u^{hall} + M_{31}^{hall} x_u^{hall} + M_{32}^{hall} x_u'^{hall} + M_{33}^{hall} y_u^{hall} + M_{34}^{hall} y_u'^{hall} \end{pmatrix}. \tag{5.38}$$

Similarly, the RHS of 5.35 can be written as:

$$\begin{pmatrix} 1 & 0 & 0 & 0 & 0 \\ M_{00}^{sol} & M_{01}^{sol} & M_{02}^{sol} & M_{03}^{sol} & M_{04}^{sol} \\ M_{10}^{sol} & M_{11}^{sol} & M_{12}^{sol} & M_{13}^{sol} & M_{14}^{sol} \\ M_{20}^{sol} & M_{21}^{sol} & M_{22}^{sol} & M_{23}^{sol} & M_{24}^{sol} \\ M_{30}^{sol} & M_{31}^{sol} & M_{32}^{sol} & M_{33}^{sol} & M_{34}^{sol} \end{pmatrix} \cdot \begin{pmatrix} 1 & 0 & 0 & 0 & 0 \\ dx + L\theta_y & 1 & 0 & 0 & 0 \\ \theta_y & 0 & 1 & 0 & 0 \\ dy - L\theta_x & 0 & 0 & 1 & 0 \\ -\theta_x & 0 & 0 & 0 & 1 \end{pmatrix} \cdot \begin{pmatrix} 1 \\ x_u^{hall} \\ x_u'^{hall} \\ y_u^{hall} \\ y_u'^{hall} \end{pmatrix} \tag{5.39}$$

$$= \begin{pmatrix} 1 & 0 & 0 & 0 & 0 \\ [M_{00}^{sol} + (dx + L\theta_y)M_{01}^{sol} + M_{02}^{sol}\theta_y + M_{03}^{sol}(dy - L\theta_x) - M_{04}^{sol}\theta_x] & M_{01}^{sol} & M_{02}^{sol} & M_{03}^{sol} & M_{04}^{sol} \\ [M_{10}^{sol} + (dx + L\theta_y)M_{11}^{sol} + M_{12}^{sol}\theta_y + M_{13}^{sol}(dy - L\theta_x) - M_{14}^{sol}\theta_x] & M_{11}^{sol} & M_{12}^{sol} & M_{13}^{sol} & M_{14}^{sol} \\ [M_{20}^{sol} + (dx + L\theta_y)M_{21}^{sol} + M_{22}^{sol}\theta_y + M_{23}^{sol}(dy - L\theta_x) - M_{24}^{sol} - \theta_x] & M_{21}^{sol} & M_{22}^{sol} & M_{23}^{sol} & M_{24}^{sol} \\ [M_{30}^{sol} + (dx + L\theta_y)M_{31}^{sol} + M_{32}^{sol}\theta_y + M_{33}^{sol}(dy - L\theta_x) - M_{34}^{sol}\theta_x] & M_{31}^{sol} & M_{32}^{sol} & M_{33}^{sol} & M_{34}^{sol} \end{pmatrix} \cdot \begin{pmatrix} 1 \\ x_u^{hall} \\ x_u'^{hall} \\ y_u^{hall} \\ y_u'^{hall} \end{pmatrix}. \tag{5.40}$$

Multiplying through gives:

$$\begin{pmatrix} 1 \\ [M_{00}^{sol} + (dx + L\theta_y)M_{01}^{sol} + M_{02}^{sol}\theta_y + M_{03}^{sol}(dy - L\theta_x) - M_{04}^{sol}\theta_x] + M_{01}^{sol} x_u^{hall} + M_{02}^{sol} x_u'^{hall} + M_{03}^{sol} y_u^{hall} + M_{04}^{sol} y_u'^{hall} \\ [M_{10}^{sol} + (dx + L\theta_y)M_{11}^{sol} + M_{12}^{sol}\theta_y + M_{13}^{sol}(dy - L\theta_x) - M_{14}^{sol}\theta_x] + M_{11}^{sol} x_u^{hall} + M_{12}^{sol} x_u'^{hall} + M_{13}^{sol} y_u^{hall} + M_{14}^{sol} y_u'^{hall} \\ [M_{20}^{sol} + (dx + L\theta_y)M_{21}^{sol} + M_{22}^{sol}\theta_y + M_{23}^{sol}(dy - L\theta_x) - M_{24}^{sol}\theta_x] + M_{21}^{sol} x_u^{hall} + M_{22}^{sol} x_u'^{hall} + M_{23}^{sol} y_u^{hall} + M_{24}^{sol} y_u'^{hall} \\ [M_{30}^{sol} + (dx + L\theta_y)M_{31}^{sol} + M_{32}^{sol}\theta_y + M_{33}^{sol}(dy - L\theta_x) - M_{34}^{sol}\theta_x] + M_{31}^{sol} x_u^{hall} + M_{32}^{sol} x_u'^{hall} + M_{33}^{sol} y_u^{hall} + M_{34}^{sol} y_u'^{hall} \end{pmatrix}. \tag{5.41}$$

Focussing just on the second row, i.e. the 'x' term, for simplicity, and equating the second rows of the matrices in Equations 5.41 to 5.38 gives

$$\begin{aligned} &[(dx + L\theta_y) + M_{00}^{hall}] + M_{01}^{hall} x_u^{hall} + M_{02}^{hall} x_u'^{hall} + M_{03}^{hall} y_u^{hall} + M_{04}^{hall} y_u'^{hall} \\ &= [M_{00}^{sol} + (dx + L\theta_y)M_{01}^{sol} + M_{02}^{sol}\theta_y + M_{03}^{sol}(dy - L\theta_x) - M_{04}^{sol}\theta_x] + M_{01}^{sol} x_u^{hall} + M_{02}^{sol} x_u'^{hall} + M_{03}^{sol} y_u^{hall} + M_{04}^{sol} y_u'^{hall}. \end{aligned} \tag{5.42}$$

Using the transformation equations in Section 5.3.4 this may be written as:

$$x_d^{sol} = M_{00}^{sol} + [(dx + L\theta_y)M_{01}^{sol} + M_{02}^{sol}\theta_y + M_{03}^{sol}(dy - L\theta_x) - M_{04}^{sol}\theta_x] + M_{01}^{sol}x_u^{hall} + M_{02}^{sol}x_u'^{hall} + M_{03}^{sol}y_u^{hall} + M_{04}^{sol}y_u'^{hall}. \tag{5.43}$$

Hence there is an additional offset in the derived x_d^{sol} co-ordinate, Δx_d, due to the transformation between hall and solenoid frames:

$$\Delta x_d^{sol} = (M_{01}^{sol} - 1)dx + (M_{02}^{sol} + LM_{01}^{sol} - L)\theta_y + M_{03}^{sol}dy - (M_{04}^{sol} + LM_{03}^{sol})\theta_x. \tag{5.44}$$

By analogy offsets in the other 3 co-ordinates can be written, such that:

$$\Delta x_d'^{sol} = (dx + L\theta_y)M_{11}^{sol} + M_{12}^{sol}\theta_y + M_{13}^{sol}(dy - L\theta_x) - M_{14}^{sol}\theta_x, \tag{5.45}$$

$$\Delta y_d^{sol} = (dx + L\theta_y)M_{21}^{sol} + M_{22}^{sol}\theta_y + M_{23}^{sol}(dy - L\theta_x) - M_{24}^{sol}\theta_x, \tag{5.46}$$

$$\Delta y_d'^{sol} = (dx + L\theta_y)M_{31}^{sol} + M_{32}^{sol}\theta_y + M_{33}^{sol}(dy - L\theta_x) - M_{34}^{sol}\theta_x. \tag{5.47}$$

This shows that the transfer matrix can be used to directly provide information regarding coil translational and rotational misalignments. If no misalignment is present in the Focus Coil and the measurement of $\underline{\underline{M}}$ was exact and the transport perfectly linear then the derived co-ordinate would be equal to the measured value at the downstream tracker. In that case $\Delta x_d^{sol} = \Delta x_d^{sol} = \Delta y_d^{sol} = \Delta y'^{sol}_d = 0$. However, there will be some systematic and statistical uncertainty in the measured transfer matrix which will be discussed in the following sections. These uncertainties arise due to imperfections in the model (due to non-linear terms in the transport) and imperfections in the data (due to detector resolution and scattering in the beam line). Once these errors have been taken into account, then, any misalignment would become apparent in the derived co-ordinates. To place limits on the misalignments in x and x' in the hall frame the main components to consider are the calculated constant terms: M_{00} and M_{10}. Likewise, any misalignment in the measured hall y and y' will be most apparent through the M_{02} and M_{03} terms. However, the above discussion shows the importance of considering the matrix as a whole.

5.3.6 Fitting Focusing terms for Effective Current

The displacement of the a coil relative to the beam axis by (dx, θ_y, dy, θ_x) results in the on-axis muon receiving a momentum kick in either transverse direction, $\Delta p_\perp$, such that

$$\Delta p_{\perp} = k \int (\vec{v} \times \vec{B}) dz, \tag{5.48}$$

where k is a constant. Looking first at the x component and using the expressions for the B_x and B_y, derived in Section 5.2, the kick in x is

$$\Delta p_x = k \int_{-\infty}^{\infty} \big[B_z + \frac{1}{2}(dy - z\theta_x) \frac{\partial B_z}{\partial x} \big] dz, \tag{5.49}$$

$$\Delta p_x = k\theta_x \int_{-\infty}^{\infty} B_z dz + 0 - \frac{k}{2}\theta_x \int_{-\infty}^{\infty} z \frac{\partial B_z}{\partial z} dz. \tag{5.50}$$

Integrating the last term by parts gives

$$-\big[\int z \frac{\partial B_z}{dz} dz \big] = -\big[[zB_z]_{-\infty}^{\infty} - \int_{-\infty}^{\infty} B_z dz \big] = \int_{-\infty}^{\infty} B_z dz. \tag{5.51}$$

Assuming that B_z falls faster than z^{-1} the first term becomes 0. On the axis of a cylindrical coil Ampere's law gives $\int_{-\infty}^{\infty} B_z dz = \mu_0 NI$ where NI is the magnetising current in the coil. The net p_x imparted on the muons due to coil misalignment is therefore:

$$\Delta p_x = \frac{K\theta_x}{2} \int_{-\infty}^{\infty} B_z dz, \tag{5.52}$$

$$\approx \frac{K\mu_0 NI}{2} \theta_x. \tag{5.53}$$

A similar expression can be obtained for Δp_y. Dividing these expressions by the constant p_z shows that $\Delta x' \propto NI\theta_x$ and $\Delta y' \propto NI\theta_y$. The change in transverse momentum of the muon depends only on the rotational offsets, not the displacement in x or y of the coil centre.

The focusing terms of the transfer matrix, i.e. the M_{01}, M_{02}, M_{11} and M_{12} quadrant and the M_{23}, M_{24}, M_{33} and M_{34} quadrant, will be directly affected by any miscalculation in the effective current of the coils. Miscalculating the coil current results in a miscalculation of the effective magnetic field acting on the particle at the Focus Coil. The effect of the coil axis misalignment on the measured misalignment terms is current dependent, and, as such, it is important to understand the effective current acting on the beam. If coil effective current is not understood, it becomes a systematic uncertainty on the derived misalignment measurements. The fitting routine will, not only, take into account differences in the constant terms of the matrix, i.e. (M_{i0}), the terms directly affected by transverse "kicks," but it will also take into account these focusing terms. This will permit the fit to provide an evaluation of the effective current that is acting within the Focus Coil.

It is necessary to cross-check the effective current in the Focus Coil with the expected coil current as there are a number of reasons why it may differ from the set current, namely:

1. The magnet contains a quench protection system [219] which acts to protect the coil from over heating if the current becomes too high. If the magnet's temperature goes above a given value it will cease superconducting. The quench protection system acts to prevent this from occurring. The presence of the numerous diodes and resistors in the protection system could modify the effective current of the Coil.

2. The magnetic field of the Coil is proportional to the product of the number of turns N in the Coil and the current I. Therefore, if the number of turns has been miscounted then the magnetic field produced by the Focus Coil will differ from the expected magnetic field.

3. Within Chapter 3 the need for the addition of a "partial return yoke" (PRY) was discussed (Section 3.4.4). The PRY will consist of 55t of iron in the final stage and acts to shield the hall from the MICE magnets. Encasing the Focus Coil inside large quantities of iron could affect the effective on-axis magnetic field. Simulations of this effect have been carried out ([220], [221]). These indicate "no measurable effect" on the field as a result of the presence of the PRY. The calculations are, however, quite complicated and a direct measurement of any misalignment of the axes would help reassure the collaboration that the PRY has no effect on the on-axis field experienced at the Focus Coil.

5.4 Obtaining the Transfer Matrix

5.4.1 Fitting Method: Linear Least Squares in 1D

The method of least squares fitting is a simple and commonly used form of regression analysis [222]. The overall solution acts to minimise the sum of the squares of the offsets of each point from the fit (i.e. the sum of the squared point residuals).

Taking a simple 1-dimensional case where each data point in the set of length n is measured at a point d_i, u_i a linear relationship can be established between d_i and a fit to the data denoted here as $f(u_i)$ such that

$$d_i = \sum_i a_i f_i(u_j). \tag{5.54}$$

Taking $f_0 =$ constant and $f_1 = u_i$, as is the case for a simple straight line fit, this becomes

$$d_i = a_0 + a_1 u_i. \tag{5.55}$$

Then, in least squares fitting, the vertical deviation, r_i, from the fitted line, f, for the i-th point can be expressed as:

$$r_i = (d_i - f(u_i)) = d_i - (a_0 + a_1 u_i) \tag{5.56}$$

and the sum of the squares of these measured vertical residuals can be given by S such that

$$S = \sum_i r_i^2 = \sum_i [d_i - (a_0 + a_1 u_i)]^2 = \sum_i (d_i - \sum_j a_j f_j(u_i))^2. \tag{5.57}$$

In the least squares method the aim is to minimise S with respect to each a_i meaning

$$\frac{\partial S}{\partial a_0} = 0 \tag{5.58}$$

$$\frac{\partial S}{\partial a_1} = 0. \tag{5.59}$$

Given that

$$S = \sum_i^n [d_i - (a_0 + a_1 u_i)]^2 \tag{5.60}$$

it can be shown that

$$\frac{\partial S}{\partial a_0} = -2 \sum_i^n [d_i - (a_0 + a_1 u_i)] = 0 \tag{5.61}$$

and

$$\frac{\partial S}{\partial a_1} = -2 \sum_i^n [d_i - (a_0 + a_1 u_i)] v_i = 0 \tag{5.62}$$

which leads to

$$n a_0 + a_1 \sum_i^n u_i = \sum_i^n d_i \tag{5.63}$$

and

$$a_0 \sum_i^n u_i + a_1 \sum_i^n u_i^2 = \sum_i^n u_i d_i \tag{5.64}$$

for a data set of length n.

This may be re-arranged and generalised to give expressions for each measured fit co-efficient a [222]

$$a = \frac{\sum_i^n u_i d_i}{\sum_i^n u_i^2}. \tag{5.65}$$

5.4.2 Parameterising Fitting Errors in 1D

Taking the true data co-ordinate to be (u_i^t, d_i^t) and the measured (i.e. fitted) data point to be (u_i^m, d_i^m), and assuming any difference in these measured and true values is small and denoted by $\delta_i^{u,d}$, then the measured particle co-ordinates can be written in terms of the true co-ordinates such that

$$u_i^m = u_i^t + \delta_i^u \tag{5.66}$$

$$d_i^m = d_i^t + \delta_i^d. \tag{5.67}$$

Using Equation 5.65 the expressions for the fit parameters for the measured data (a^m) and true data (a^t) can be written as

$$a^m = \frac{\sum_i^n u_i^t d_i^t - \delta_i^d u_i^t - \delta_i^u d_i^t + \delta_i^v \delta_i^d}{\sum_i^n (u_i^t)^2 - (2u^t)_i \delta_i^u + \delta_i^u \delta_i^u} \tag{5.68}$$

$$a^t = \frac{\sum_i^n u_i^t d_i^t}{(\sum_i^n u_i^t)^2} \tag{5.69}$$

respectively. Assuming errors are relatively small and using $\frac{1}{1+u} \approx 1 - u$ for $u \ll 1$ then the expression for a^m may be re-written as

$$a^m \approx \frac{\sum_i^n [d_i^t u_i^t - \delta_i^d u_i^t - \delta_i^u d_i^t + \delta_i^d \delta_i^u + 2u_i^t \delta_i^u - (\delta_i^u)^2]}{\sum_i^n (u^t)^2}. \tag{5.70}$$

The error on the measurement can therefore be defined as the difference in the measured and true fit parameter and denoted as e^a where

$$e^a \approx a^m - a^t = \frac{\sum_i^n [-\delta_i^d u_i^t - \delta_i^u d_i^t + \delta_i^d \delta_i^u + 2u_i \delta_i^u - (\delta_i^u)^2]}{\sum_i^n (u_i^t)^2}. \tag{5.71}$$

5.4.3 Statistical and Systematic Errors in 1D

Statistical errors can be introduced into the system by the presence of non-zero covariances. The mean of v may be denoted in moment notation as $\langle u \rangle = \sum_i^n u_i/n$ and the variance may be expressed as $\langle u^2 \rangle = \frac{1}{n} \sum_i^n (u_i - \langle u \rangle)^2$.

Assuming that errors e^a are not correlated with each other or with the truth variables the mean of the error distribution e^a is given by the expression:

$$\langle e^a \rangle = -\frac{\langle (\delta^u)^2 \rangle}{\langle (u^t)^2 \rangle}. \tag{5.72}$$

This mean value can be taken as a systematic error within the sample.

Assuming that the errors are small it can also be seen that the variance of the error distribution is

$$\langle (e^a)^2 \rangle - \langle e^a \rangle^2 = \frac{1}{N} \frac{\langle (\delta^d)^2 \rangle \langle u^t \rangle}{\langle (u^t)^2 \rangle}, \tag{5.73}$$

where N is the total number of particles in the sample.

5.4.4 Application to Higher Dimensional Cases

In order to derive a measurement of a particle's 4×5 transfer matrix it is necessary to carry out linear fits between the particle's measured upstream and downstream trace space co-ordinates. This can be done using linear least squares fitting. The discussion in the preceding section focussed on a simple 1D mapping. In order to derive the higher dimensional mapping necessary for this analysis, the method must be extended.

Consider mapping from one trace space co-ordinate $\vec{u}$ to another $\vec{d}$, in this case Equation 5.54 becomes

$$d_i = \sum_i a_{ij} f_j(\vec{u}) \tag{5.74}$$

where d_i are the elements of $\vec{d}$ and $f_j(\vec{u})$ are a set of functions mapping vector spaces $\vec{u}$ to $\vec{d}$. a_{ij} are the coefficients which are found via the linear least squares fitting.

In the case where $\vec{u}$ and $\vec{d}$ are a particle's upstream and downstream tracker co-ordinates respectively. a_{ij} are the elements of the single particle transfer matrix $\underline{\underline{M}}$. For a linear transfer matrix in x and y, f_j are the constant and first order polynomial terms i.e. $(1, x^u, x'^u, y^u, y'^u)$. The error vectors $\vec{\delta}^u$ and $\vec{\delta}^d$ on the measured $\vec{u}^m$ and $\vec{d}^m$ can now be defined by

$$\vec{u}^m = \vec{u}^t + \vec{\delta}^u \tag{5.75}$$

and

$$\vec{d}^m = \vec{d}^t + \vec{\delta}^d. \tag{5.76}$$

By analogy to Equation 5.57, an expression for the sum of the squares of the residuals, S, for this higher order case can be derived such that

$$S = \sum_i [d_i - \sum_j a_{ij} f_j(\vec{u})]^2. \tag{5.77}$$

The aim of the linear least squares method is then to minimise this expression as was done in the 1D case. The expressions 5.61 and 5.62 can be generalised in this higher order case and the linear least squares system of simultaneous equations are now defined as

$$0 = \sum_i d_{ki} f_{kj} - \sum_j a_{ij} f_{kj} f_{kl}. \tag{5.78}$$

This can be written more concisely in matrix notation, such that $0 = \underline{\underline{F_D}} - \underline{\underline{M}} \cdot \underline{\underline{F_F}}$ where $\underline{\underline{F_D}}$ has elements $\sum_i d_{ki} f_{kj}$ and $\underline{\underline{F_F}}$ has elements $\sum_j f_{kj} f_{kl}$, the transfer matrix, $\underline{\underline{M}}$, contains elements a_{ij}.

Solving the matrix equation for $\underline{\underline{M}}$ gives

$$\underline{\underline{M}} = \underline{\underline{F_D}} \cdot \underline{\underline{F_F}}^{-1} \tag{5.79}$$

The aim of the analysis presented in this Chapter is to find the matrix $\underline{\underline{M}}$ which maps a single particle's upstream trace space co-ordinate to its downstream trace space co-ordinate.

5.4.5 Errors for Higher Dimensional Fitting

To consider the overall errors on the elements of $\underline{\underline{M}}$ it is necessary to calculate, or at least consider, the errors on each of the matrix elements of $\underline{\underline{F_D}}$ and $\underline{\underline{F_F}}$. Firstly, considering the elements of $\underline{\underline{F_D}}$, $d_{ik} f_{jk}$; there are two cases for f_{ji}: the constant terms ($f_{jk} = 1$) and the linear terms ($f_{jk} = u_{(j-1)k}$). The measured elements of $\underline{\underline{F_D}}$ are then

$$F^m_{D,ij} = F^t_{d,ij} + \begin{cases} \sum\limits_k \delta^d_{ik} & \text{j = 0} \\ \sum\limits_k [u^t_{(j-1)k}\delta^d_{ik} + d^t_{ik}\delta^u_{(j-1)k} + \delta^u_{(j-1)k}\delta^d_{ik}] & \text{j > 0,} \end{cases} \tag{5.80}$$

where k represents the particle number in the set.

Similarly, for $\underline{\underline{F_F}}$ where the elements are $\sum_j f_{ik} f_{jk}$, the errors are given by

$$F^m_{F,ij} = F^t_{F,ij} + \begin{cases} 0 & \text{i=j=0} \\ \sum\limits_k \delta^u_{ik} & \text{i=0, j>0} \\ \sum\limits_k \delta^u_{jk} & \text{i>0, j=0} \\ \sum\limits_k [u^t_{(j-1)k}\delta^u_{(i-1)k} + u^t_{(i-1)k}\delta^u_{(j-1)k} + \delta^u_{(i-1)k}\delta^u_{(j-1)k}] & \text{i>0, j>0.} \end{cases} \tag{5.81}$$

Propagating these errors into Equation 5.79 is complicated by the necessary matrix inversion. Instead the errors on the matrix elements are considered. in particular we are interested in the mean of the error i.e. the systematic error on the difference between the measured and true elements of $\underline{\underline{F_D}}$ and $\underline{\underline{F_F}}$. So for $\underline{\underline{F_D}}$

$$\langle F^m_{D,ij} - F^t_{d,ij} \rangle = \begin{cases} \langle \delta^d_{ik} \rangle & \text{j = 0} \\ [\langle u^t_{(j-1)k}\delta^d_{ik} \rangle + \langle d^t_{ik}\delta^u_{(j-1)k} \rangle + \langle \delta^u_{(j-1)k}\delta^d_{ik} \rangle] & \text{j > 0} \end{cases} \tag{5.82}$$

and for $\underline{\underline{F_F}}$

$$\langle F^m_{F,ij} - F^t_{F,ij} \rangle = \begin{cases} 0 & \text{i=j=0} \\ \langle \delta^u_{ik} \rangle & \text{i=0, j>0} \\ \langle \delta^u_{jk} \rangle & \text{i>0, j=0} \\ [\langle u^t_{(j-1)k} \delta^u_{(i-1)k} \rangle + \langle u^t_{(i-1)k} \delta^u_{(j-1)k} \rangle + \langle \delta^u_{(i-1)k} \delta^u_{(j-1)k} \rangle] & \text{i>0, j>0} \end{cases} \tag{5.83}$$

In Section 5.8.7 a covariance matrix will be derived and utilised to correct for systematic errors induced by the fitting procedure. $\langle u^t_{(j-1)k} \delta^d_{ik} \rangle$, $\langle d^t_{ik} \delta^u_{(j-1)k} \rangle$,$\langle \delta^u_{(j-1)k} \delta^d_{ik} \rangle$, $\langle u^t_{(j-1)k} \delta^u_{(i-1)k} \rangle$ and $\langle u^t_{(i-1)k} \delta^u_{(j-1)k} \rangle$ should all be 0 as the residuals should not be correlated to the upstream particle co-ordinates. The mean of the covariance between the "truth residuals" i.e. $\langle \delta^u_{(i-1)k} \delta^u_{(j-1)k} \rangle$, can be calculated using two Monte Carlo samples, one "true" and one "digitised." The differences between the true and reconstructed co-ordinates for each particle can be calculated and the covariance established. Once the covariances have been measured they can be corrected for within the fitting procedure.

5.5 The SciFi Trackers in MAUS

As discussed in Chapter 3 the MICE experiment has its own purpose built analysis software, MAUS. MAUS provides all the sub-detectors and sub-systems within the cooling channel a joint platform for storing and reconstructing events on a Spill-by-Spill basis. Each Spill corresponds to a dip of the MICE target into the ISIS beam. Figure 5.4 presents a simplified schematic of the MAUS data structure associated with the storing of tracker events from both true Monte Caro (MC) events and reconstructed (Recon) events. The reconstruction code makes no direct reference to the Monte Carlo information and has no way to distinguish real from simulated data, thus ensuring that they are treated equally.

5.5.1 SciFi Track Reconstruction Algorithms

Within [165] a detailed discussion of the algorithms employed by the MAUS SciFi track reconstruction is provided. MAUS has the capability to reconstruct both straight (field-on) and helical (field-off) particle tracks. An examination of the performance of the MAUS track reconstruction is also given in [165].

Prior to the analysis of either MCEvents or ReconEvents there are several stages within the MAUS track fitting procedure which must take place in order to reconstruct, and pre-select, the SciFi tracks. Specifically:

1. Data Digitisation - Raw electronics data (from both trackers) is converted into the MAUS data structure.

2. MC Digitisation - Monte Carlo simulated energy deposits are converted into electronics signals. Dead

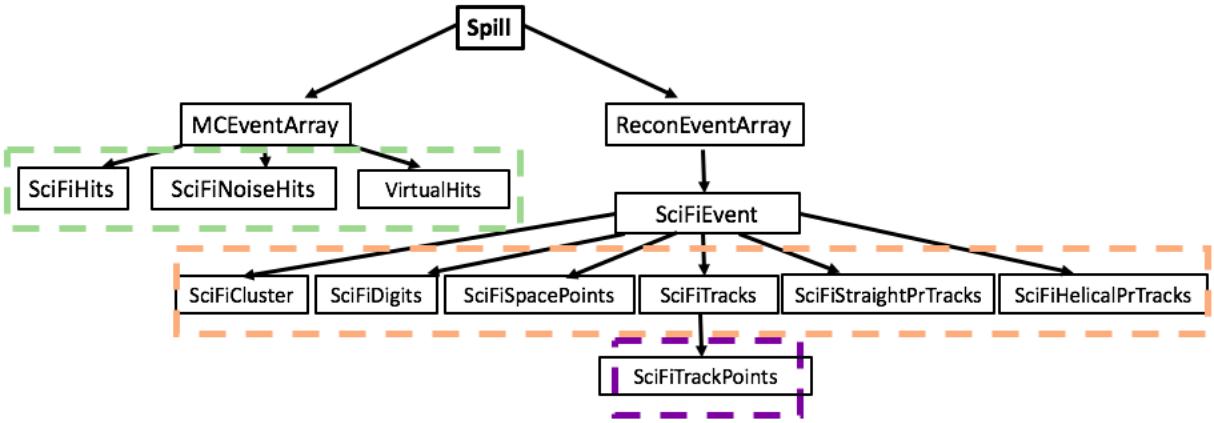

Figure 5.4: Summary of the data structure corresponding to the storing of tracker hits in both the Monte Carlo and reconstruction branches of the Spill. Each "Spill" represents a target dip, and each ReconEvent contains all of the SciFiTracks associated with a particular trigger. Indicated in orange are the various parameters associated with each reconstructed SciFiEvent, these can be utilised to aid track resolution, these are defined in Section 5.5.2. The information associated with true, un-digitised, Monte Carlo data is shown in green. The reconstructed SciFiTrackPoints are shown in purple, it is from here that this analysis will retrieve the information required to fit particle tracks from data.

channels and noise are added into the Monte Carlo based on a data-derived model to improve the Monte Carlo's verisimilitude to real data.

3. Cluster Finding - Neighbouring digits are associated into single clusters in order to account for particles crossing more than one fibre.

4. Space-point Finding - Clusters found within a particular station are associated into a single space-point.

5. Pattern Recognising - A track is formed from the space-points using a linear-least-squares technique. There are separate algorithms for the straight tracks and the helical tracks.

6. Kalman Filtering - The Kalman filter attempts to find a best fit "track," accounting for energy loss and expected scattering introduced by materials in the detector.

5.5.2 Reconstructing SciFiEvents

Within the reconstruction code, the SciFiEvent class represents the highest level and contains within it C++ standard library vectors of the following container classes:

1. SciFiDigits - contains the analogue-to-digital converter (ADC) counts (real or simulated) from the readout of a single channel in response to an incident track.

2. SciFiClusters - a cluster represents a group of neighbouring digits which are assumed to arise from the same particle crossing multiple channels.

3. SciFiSpacePoints - a real space 3D position co-ordinate which is produced from the grouping clusters from adjacent detector planes.

4. SciFiStraightPrTracks - these straight pattern recognition tracks group together space-points from the different tracker stations according to the particle track which generated them. In the case of "straight tracks" the track is either that of a neutral particle or any particle if the solenoidal fields are switched off.

5. SciFiHelicalPrTracks - group together space points from different tracker stations when the track that produced the hits was helical. Helical tracks are found by fitting a helix to the space points.

6. SciFiTracks - The SciFiTrack holds the χ^2 and p-value associated with the particle track. The SciFiTrack points to a vector of SciFiTrackPoints that store the position, momentum and estimated errors at each tracker plane for the SciFiTrack.

These are highlighted in orange in Figure 5.4. The data, presented in this thesis, will be retrieved directly from the SciFiTrackPoints of each reconstructed SciFiTrack. The SciFiTrackPoint holds the fit parameters at each detector plane, including the momentum and position of the track. The analysis strategy is detailed in Section 5.6.

5.5.3 SciFiHits from MC Events

The MCEvent class holds "truth" Monte Carlo for SciFiHits produced by tracks passing through sensitive volumes (the tracker fibre planes) and any associated SciFiNoiseHits originating in those planes. This produces a Monte Carlo digit interface which is identical to that for real digits with some reasonable noise model providing a verisimilitude that will allow direct comparisons between truth Monte Carlo and reconstructed hits. Once understood, the anticipated systematic effects can then be countervailed. The MCEvent class structure is highlighted in green in Figure 5.4.

5.5.4 Transfer Matrices in MAUS

Once the upstream and downstream particle co-ordinates have been established and the relevant selection criteria applied, the method of multi-dimensional linear least squares fitting, documented in Section 5.4.1, will be exploited to derive the particle transfer matrices. When no magnetic field is present at the Focus Coil, muons travel in straight tracks between the trackers. These "straight tracks" can be utilised to verify the fitting algorithms and test their accuracy before applying them to more complicated magnetic setups. Within MAUS the reported tracker co-ordinates, X' and Y', are defined relative to a beam at a nominal beam momentum of 200 MeV/c , such that:

$$X'_u = 200x'_u \quad , \quad Y_u = 200y'_u. \tag{5.84}$$

Thus, Equations 5.3 and 5.5 becomes:

$$x_d = x_u + \frac{L}{200} X'_u, \tag{5.85}$$

$$y_d = y_u + \frac{L}{200} Y'_u \tag{5.86}$$

where $M_{01} = M_{12} = M_{23} = M_{34} = 1$ and M_{02} and M_{24} are related to the drift space length between the two trackers. This factor of $p_z = 200$ is inherent throughout the tracker reconstruction within MAUS and remains in all quoted measurements of the trace space co-ordinates. In this arrangement the co-ordinates x' and y' are dimensionless.

5.6 Analysis Strategy

In the subsequent analysis the SciFiTracks associated with each tracker must be identified. For a given data sample all Spills must be looped over and each ReconEvent identified. TOF1 is used as the trigger meaning every ReconEvent is initiated by a TOF1 hit and all hits in subsequent detectors are timed relative to that initial trigger hit.

For the analysis of reconstructed data in this study a "data loader" class is developed which will search through the SciFiTracks accompanying each ReconEvent. For each SciFiTrack within the ReconEvent the SciFiTrackPoints will be retrieved and SciFiTrackPoints associated with the first station on either tracker identified. The tracker stations within both the upstream and downstream tracker are labelled $1 - 5$. If a track point is found at the first station of both trackers then the positions and momenta co-ordinates of these track points will be added to a list of "analysable data" which will be loaded and analysed accordingly once all Spills and all ReconEvents have been obtained. At this point a number of selection criteria will be imposed on the tracks. These are outlined in Section 5.6.1 and help aid background and noise rejection and ensure the highest muon purity in the end data.

A similar loader will be used to load the associated MCEvents which uses the VirtualHits position and momenta, again creating a list of "analysable Monte Carlo tracks" which can then be passed to the analysis code to continue the study and measurement of the transfer matrix.

Once the list of analysable SciFiTrackPoints has been compiled it is split into upstream and downstream co-ordinates, a polynomial map can then be created between these two sets of co-ordinates with the coefficients of the transfer matrix subsequently being calculated via the method outlined in Section 5.4.1.

5.6.1 Track Selection

It is vital that any tracks in the data which do not originate from muons produced within the MICE beam line are eliminated prior to the transfer matrix calculation. The presence of track impurities would be detrimental to the analysis and produce inaccurate misalignment calculations. It is essential to limit contamination from: random electronics noise; decay electrons and pions; knock-on electrons, which can be emitted from a tracker

plane due to the ionising effect of the primary track; and secondary tracks due to multiple muons within the same event.

A series of cuts are applied to the data and reconstructed Monte Carlo to ensure the list of SciFiTrackPoints being analysed has the highest muon purity achievable. The subsequent track selection criteria were imposed upon reconstructed tracks prior to the matrix calculations in this analysis:

Tracker Resolution Cuts

1. There must be at least 1 SciFiDigit associated with a known SciFiTrack in both trackers.

2. There must be at least 2 SciFiTrackPoints in each upstream and downstream SciFiTrack. This will allow for an accurate derivation of the mapping between the two. There must be at least 2 points in each track to allow the matrix calculation to take place.

3. At least one SciFiSpacePoint in each of the 5 tracker stations in both trackers must be observed in a given SciFiTrack. This helps to reduce "noise" from possible secondary particle tracks produced within the tracker which could become included in the fitting. This criterion will also aid rejection of electronics noise. It is highly unlikely that electronics"noise" would produce corresponding space points in all stations and therefore be classed as a viable track.

4. Each upstream track must contain 15 SciFiClusters. There are 3 planes and 5 stations so in order to improve noise rejection as well as improve general accuracy and resolution of the track it is required that the particle passes through all planes and all stations for both upstream and downstream tracker tracks. The average fibre has a better than 99% probability of producing a digit above background noise [223].

   Although items 1-4 may appear to overlap it is important to enforce all 3 criterion as consistency checks and to improve accuracy of the end matrix calculation by ensuring poorly reconstructed tracks are removed from the "analysable data" set.

5. A P-Value is defined within the MAUS tracker data structure describing a "goodness-of-fit" based on the track residuals at the tracker reconstruction level of the MAUS algorithms (a detailed derivation and justification of this value is given in [165]). In the following analysis it is required that the P-Value of a track is > 0.1. Discussion of, and justification for, this criterion is presented in Section 5.9.3. This cut will remove any badly reconstructed tracks which could be a result of hard scatters or noise.

6. A "scraping cut" is derived to eliminate tracks with a high probability of striking an aperture between the two tracker. The justification for, and optimisation of, this cut is given in Section 5.9.2 and its effectiveness is analysed.

Particle Identification Cuts

7. Each selected track must have at least one TOFSpacePoint in both the TOF1 and TOF2 detector meaning it passes the whole length of the channel.

8. A Time-of-Flight selection window is applied. This is momentum dependent so will differ for each data/MC sample. Particles must be in the central region of the "muon peak." In this study the cut is enforced upon the time a particle takes to traverse from upstream Time-of-Flight detector (TOF1) to downstream Time-of-Flight detector (TOF2). Figures 5.6 and 5.28 display example distributions with the selected regions are shown in red.

The effects of each of these selection criteria on the data samples, in terms of total track number remaining, are presented in Tables 5.2 and 5.4.

5.7 Dead Channels

The SciFiTrackers were installed and commissioned during 2016 in preparation for Step IV. During this installation a study was conducted which aimed to identify any "dead channels." Figure 5.5 exhibits 5 representations of particle SciFiSpacePoint triplets, one for each downstream tracker station, obtained from the tracker commissioning data. A vertical stripe is apparent in the 1st station and a diagonal stripe in the 5th station. These correspond to dead channels in the tracker. The study presented in this chapter is reliant on the presence of a SciFiTrackPoint in the 1st station of the downstream tracker. Given the existence of dead channels in this station it is expected that there will be a deficit of tracker points around $x \approx 90$ mm in the distribution of particles' reconstructed downstream x co-ordinate. This is a result of particle tracks in this region failing the required selection criteria outlined in Section 5.6.1.

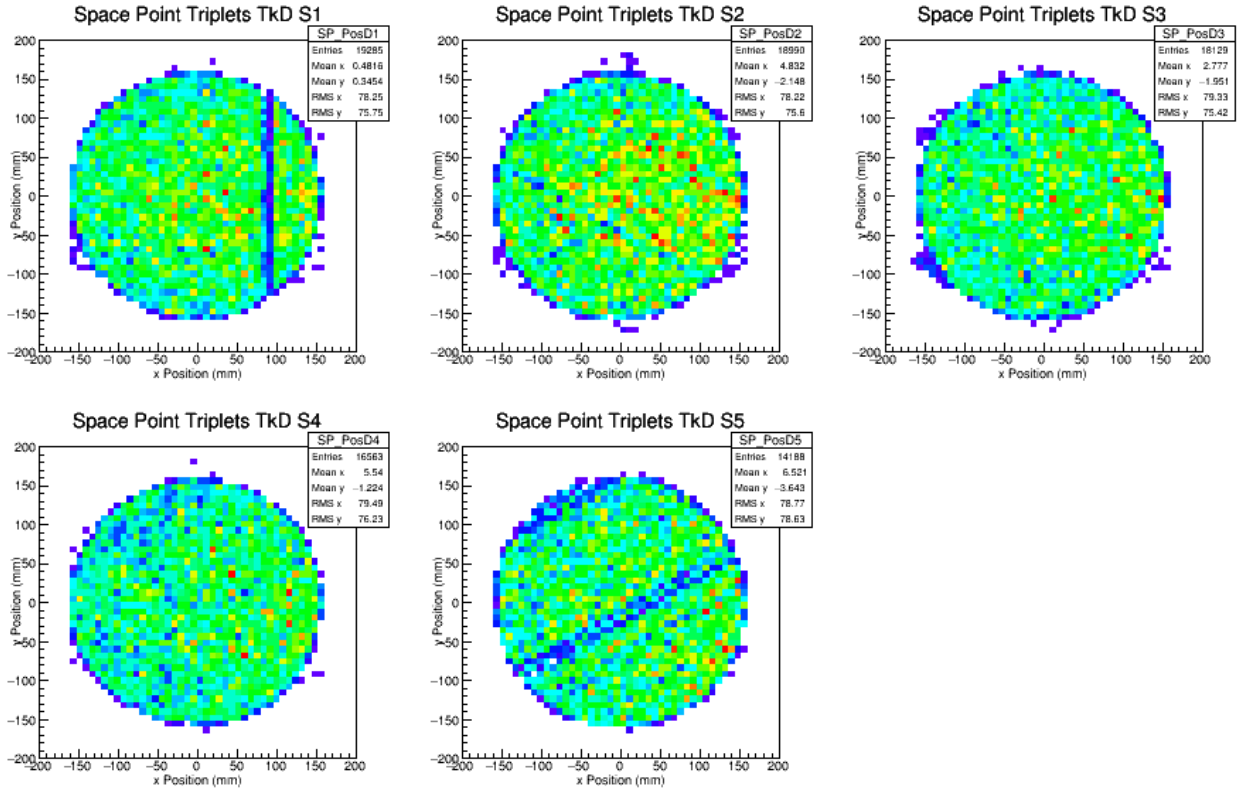

Figure 5.5: Plots produced by the MICE Tracker group showing evidence of dead channels in the first station of the downstream tracker at $x \approx 90mm$. Additional dead channels are observed in the 5th station, however, the analysis presented in this chapter only relies on SciFiTrackPoints being identified in the 1st downstream tracker station. As a result, a deficit of SciFiTracks is anticipated at $x \approx 90mm$ [223].

5.8 Validation Using Straight Tracks Data

5.8.1 Data Sample 07417

The following analysis uses the Step IV data sample labelled "07417", obtained in September 2015. Throughout this run no current is applied to the Focus Coil, consequently, no magnetic field is present between the trackers and the muons follow "straight tracks."

Run 07417 enlisted TOF1 as the initial trigger; as a result, all timing information is relative to the particle's arrival at TOF1. A proton absorber of thickness 82 mm was positioned just downstream of D1. The beam line magnet settings for this run are listed in Table 5.1. The final data set has 12346 total spills with 612484 triggers.

The distribution of time taken for all particles in this sample to transit from upstream time-of-flight detector, TOF1, to downstream time-of-flight detector, TOF2, is exhibited in Figure 5.6. A large "μ^+" peak is evident, centred around 31 ns; a significantly smaller "positron" peak, centred around 27 ns, is also visible. The extended tail of the "muon" peak and slight shoulder at $\approx$ 33 ns indicate some pion contamination. Hence, a TOF_{12} time selection window of $31 < TOF_{12} < 32.5$ ns is applied to all primary particles. This ensures a high muon purity in the primary tracks used in the analysis.

Magnet	Current/[A]
D1	323.2
D2	94
DS	445
Q1	102.4
Q2	127.9
Q3	89.0
Q4	158.2
Q5	212
Q6	140.6
Q7	138.7
Q8	209.8
Q9	179.2
FC	0

Table 5.1: Table listing settings of the MICE beam line for run "07417" on which the analysis will be conducted. Current setting of the 9 quadruples (Q1-9), 2 dipoles (D1-2) as well as the decay solenoid (DS) are detailed. These are labelled according to the schematic of the MICE beam line in Figure 3.2. The Focus Coil (FC) current is also included. This is 0A hence the FC is treated as a drift space for this "straight track" run.

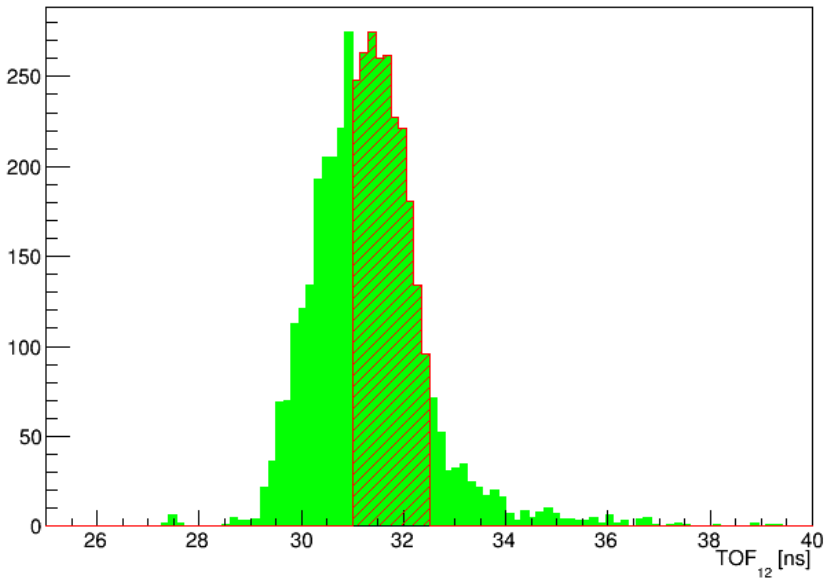

Figure 5.6: Distribution of the time taken for particles in data run 07417 to travel between upstream TOF1 and downstream TOF2, labelled as TOF_{12} time. A large peak is visible, centred around 31 ns, with a small shoulder present around 33 ns. The majority of particles in this region will be muons with the sloped tail > 33 ns suggesting some pion contamination. A significantly smaller electron peak is also visible at ≈ 27 ns. In the following analysis a selection cut of $31 < TOF_{12} < 32.5$ ns is applied to keep muon purity in the data sample high and to coincide with the Monte Carlo peak muon region.

5.8.2 Monte Carlo Simulation For Straight Tracks

Two Monte Carlo samples, truth and reconstructed ("digitised"), are produced in MAUS for a MICE cooling channel geometry comparable to that in run 07417. This incorporates the upstream and downstream PID detectors, and all materials in the beam line. The simulation will take into account any measured tracker-to-tracker misalignment, to the accuracy it is known at the time of its formulation. In order to produce a realistic reconstructed Monte Carlo, the digitisation model mimics the real data and includes knowledge of the current tracker calibration and models of noise and dead channels for verisimilitude. This should produce

track resolutions similar to those in the real data reconstruction.

The physics processes and channel detectors are modelled using GEANT4 within MAUS. The G4Beamline [207] package has been used to simulate the beam line. Precision measurements of the beam line magnet and cooling channel detector positions were obtained through surveying of the MICE hall. The MAUS Monte Carlo framework uses the output from G4Beamline to recreate the MICE beam. All known, low energy physics processes and interactions were included in the simulation, as were processes for intermediate and high energies for completeness.

Comparisons between the two Monte Carlo samples and the real data will permit examination of the accuracy of the fitting algorithms. Any systematic uncertainties or biases will be evaluated and countervailed within the "field-on" study. In addition, comparisons between the two Monte Carlo samples allows the fitting covariance matrix (derived in Section 5.4.1) to be measured and the resulting systematic error in the transfer matrix corrected for. Any mis-alignments at the Focus Coil will become apparent through comparing the calculated matrix elements.

There are still some limitations in the tracker simulation within the MAUS Monte Carlo generator. These include the need for an improved model of multiple Coulomb scattering and energy loss within the tracker materials (see Section 2.5). In addition, there are some known geometric discrepancies, detailed in [224], which arise from the fact that the nominal centre of an ideal tracker hit is not in the true centre of the individual channel. This has been amended within the upstream channel, however, it is remains necessary to build a more accurate simulation of the downstream channel. The Monte Carlo simulation can naively model dead channels, hence, the effect of the dead channel (outlined in Section 5.7) is included in the simulation. The selection criteria outlined in Section 5.6.1 will be applied to both Monte Carlo and data.

Figure 5.7 displays the TOF_{12} distribution containing all particles within reconstructed Monte Carlo sample. A TOF_{12} selection window of $31 < TOF_{12} < 32.5$ ns is used for both data and Monte Carlo to permit direct comparison. The same cut is applied to the true Monte Carlo in which case the time is obtained by matching each MCEvent to the corresponding ReconEvent.

There is a small ($\approx 0.5ns$) offset between data maximum i.e centre of the "muon peak," and the corresponding region in the reconstructed Monte Carlo distribution. This is a result of a known problem within the MAUS Monte Carlo beam line settings, discussed in Section 4.6.2. The dipoles are set too low in MAUS Monte Carlo generator. This has been resolved in new versions of MAUS. A TOF_{12} cut is chosen which coincides with the Monte Carlo peak muon region. This offset should not effect the end conclusions as sufficient muon content will be present in the selection window for data. Pion contamination in the chosen region is expected to be minimal. The only errors which arise due to this slightly off-peak TOF_{12} selection will be increased statistical errors in the data sample. The impact of statistical errors on the calculated transfer matrices can easily be accounted for using the method discussed in detail in Section 5.8.8.

The purity (ϵ_{TOFPID}) of the particle tracks selected using the TOF_{12} criterion for this straight track sample can be evaluated using the true Monte Carlo (MCEvents) in the region analogous to the selected

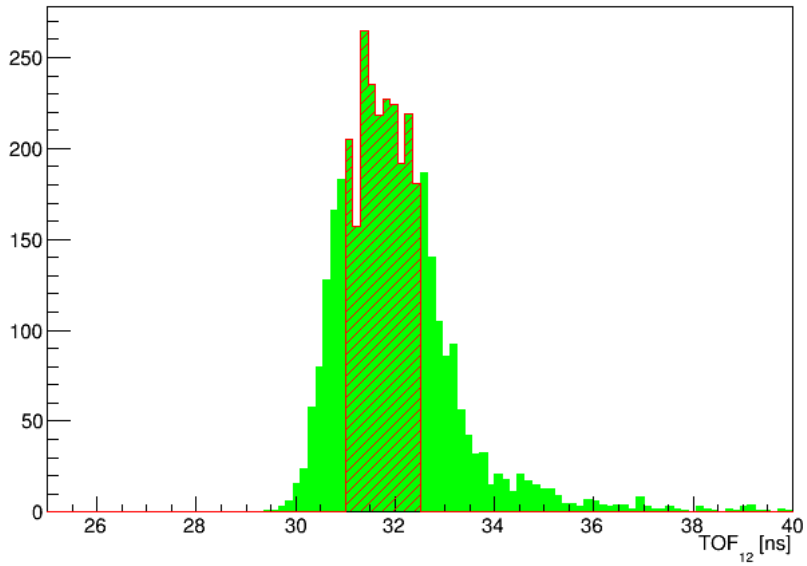

Figure 5.7: Distribution of the time taken for particles in the reconstructed Monte Carlo sample to travel between upstream time-of-flight counter, TOF1, and downstream time-of-flight counter,TOF2. To ensure the Monte Carlo provides good simulacrum of the real data a geometry comparable to that in run 07417 is used. A selection cut of $31 < TOF_{12} < 32.5$ ns is applied to tracks in the Monte Carlo to keep muon purity in the sample as high as possible. The same window is used for data, this selected region is shown in red.

data region i.e. the region shifted + 0.5 ns from the peak ($31.5 < TOF_{12} < 33$ ns). The purity of selected tracks in this region is:

$$\epsilon_{TOFPID}^{31.5<\delta t_{12}<33} = \left(\frac{N_{\mu}^{true}}{N_{e+\mu+\pi}^{true}} \right)_{31.5}^{33} \tag{5.87}$$

where N^{true} describes the number of events of each particle type which remain after the TOF_{12} cut is applied. TOF_{12} time is obtained from matching the true track to its corresponding reconstructed Monte Carlo track. Therefore, this should be a direct measure of the cut's efficiency. The calculated contamination is small. In total only 0.167 % of particles in this region were found to be non-muon with 0.028% being mis-identified electrons and 0.139 % being pions. The ϵ_{TOFPID} in this region is 99.833%. It is therefore assumed, that the chosen TOF_{12} selection criteria is sufficient and that any bias due to particle mis-identification will be minimal in the data sample despite being offset from maximum.

5.8.3 Dependence on Longitudinal Momentum

In the solenoid Focus Coil it is the transverse momentum which affects the focusing. Equation 2.28 displays the general relationship between the transverse components of the transfer matrix and the longitudinal momentum. The factor of $\frac{1}{p}$ means the transfer matrix method of mapping a particle trace space at one point in a lattice to another is dependent upon the presence of constant longitudinal momentum. Throughout this analysis the Monte Carlo and data samples are divided into 5, equally sized, bins in TOF_{12} time. This assumes that any deviations from the axis are small. The matrix is then calculated for each TOF_{12} bin separately. The choice of 5 bins over a range of $31 < TOF_{12} < 32.5$ corresponds to a momentum spread

of 5.4 [MeV/c]/bin. In reality a larger number of bins would be advantageous especially in samples with a larger momentum spread in order to determine any p_z dependent variations. Due to the limited sample and relatively small momentum spread of the beam with the TOF_{12} selection criterion enforced the choice of 5 bins is sufficient for the scope of this study. Figure 5.8 shows the relationship between TOF_{12} and p_z for particles in the true Monte Carlo sample in the selected region; it is linear. It is expected therefore that the transfer matrix is approximately constant throughout the TOF_{12} space, within the statistical limits.

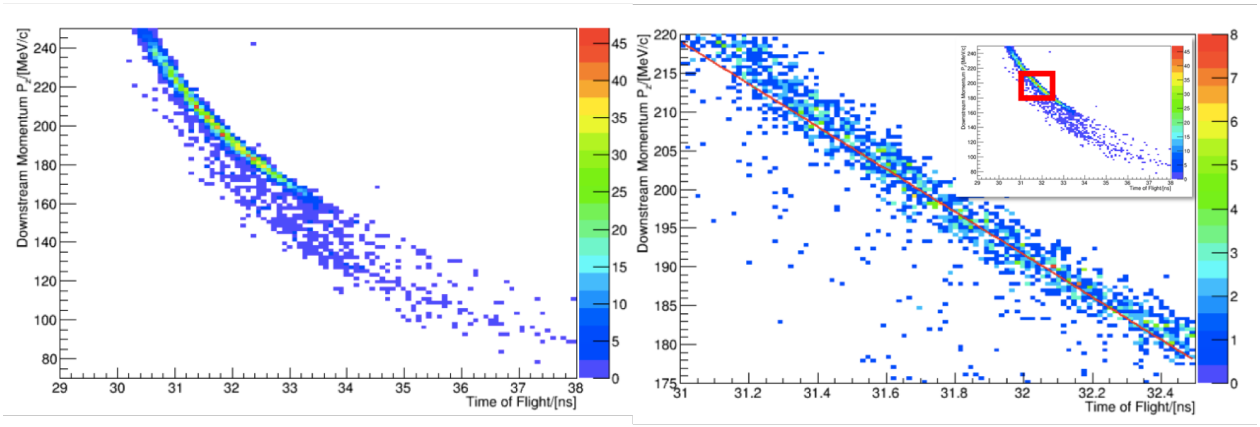

(a) (b)

Figure 5.8: (a) Distribution of longitudinal momentum, p_z, and TOF_{12} for all particles in true Monte Carlo (b) Plot shows relationship between longitudinal momentum, p_z, and TOF_{12} for tracks in the true Monte Carlo sample for run 07417. The top plot is presented only to give perspective of the non-linear relationship observed when plotting of the full range of TOF_{12} times, the main plot magnifies the selected region. The relationship is linear, a fit line is fitted with gradient = -27.42 ± 0.31 [MeV/c]/ns.

5.8.4 Track Cut-flow for Straight Tracks

Section 5.6.1 outlined a number of selection criteria imposed on tracks prior to the transfer matrix calculation. The majority of these cuts permit preselection of the particles entering into the fitting algorithm. In addition, the scraping cut, discussed in Section 5.9.2, eradicates tracks likely to be "scraped out" at the tracker aperture due to multiple scattering by the beam line materials. The combined effect of these cuts is to reject noise and background events, helping to reduce the pion and electron contamination in the final sample, and as a result, improving the accuracy of the calculated transfer matrices and, ultimately, the measured misalignment.

Table 5.2 gives a break-down of the effect each selection criterion has on the number of track points remaining in the final data and digitsed Monte Carlo samples.

Criterion	Data	Recon. MC
Has Space Points in Tracker 0 and 1	19059	9038
Has hits in both TOF1 and TOF2	18851	8969
Has space points in all 5 stations of tracker 0	18290	8917
Has space points in all 5 stations of Tracker 1	15817	7921
Has 15 clusters in Tracker 0	11802	6965
Has 15 clusters in Tracker 1	6949	5105
Is in assumed muon peak in TOF_{12} time	4018	2123
Passes P Value Cut > 0.1	3474	2085
Has- 10 track points in both trackers	1858	2069
$\sqrt{(x+\sigma_x)^2+(y+\sigma_y)^2} < 150$	1088	1149
After all Cuts applied	**1088**	**1149**

Table 5.2: Break down of cumulative effect on total number of SciFiTracks remaining in both the data sample (07417) and the corresponding reconstructed Monte Carlo as each of the selection criteria, outlined in Section 5.6.1, is applied.

5.8.5 Beam Distributions for 07417

Figures 5.9a to 5.12a show distributions of the individual trace space co-ordinates, at both the upstream and downstream trackers, for the particles within the 07417 data sample. These were produced after all track selection criteria, outlined in Section 5.6.1, with the exception of the "scraping cut", were applied. In order to calculate the tracks most likely to be "scraped" out of the beam it is necessary to first establish the total transverse spread of the beam, hence ignoring that cut at this point in the analysis.

It is evident that the transverse position distributions, x and y, are much narrower at the upstream tracker than at the downstream tracker. Between the upstream and downstream trackers the transverse spread of the beam in both x and y increases by $\approx 45\%$. However, little change is observed in the distributions of the momentum correlated co-ordinates, x' and y', as particles pass between the upstream and downstream trackers. This is to be expected given the absence of a magnetic field. The particles traverse the drift space between the two trackers continuing on their initial momentum trajectory unimpeded. The effect in trace space is then to stretch the beam in position, x and y, while the distributions in x' and y' remain constant. Correlations between x and x' and y and y' are introduced as particles with the largest momentum are moved further from the centre of the position axis while the distribution of x' remains constant.

Figure 5.9b shows an apparent deficit of tracks with positions $x \approx 90$ mm in the downstream tracker. This is a result of the dead channel in the tracker (Section 5.7). Tracks in this region fail the track selection, outlined in Section 5.6.1, as no SciFiTrackPoint can be found in the first station of the downstream tracker due to the presence of this dead channel. The MAUS Monte Carlo generator includes a crude model of the dead channel, therefore, there is no need to countervail this deficit for the purpose of this thesis.

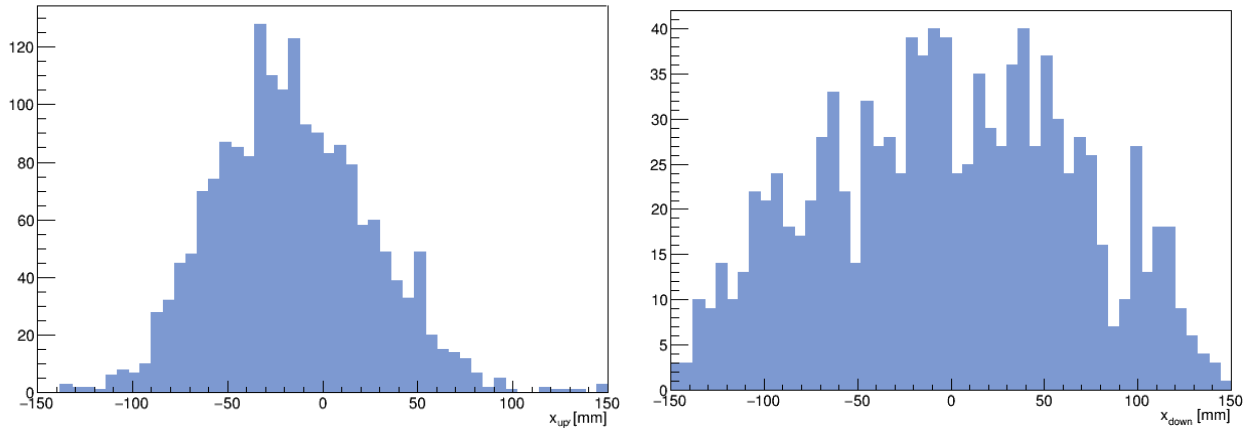

(a) (b)

Figure 5.9: Distribution of x for data sample 07417 prior to the application of the "scraping cut" but after all other selection criteria, outlined in Section 5.6.1, were imposed. (a) Upstream: The distribution has mean of $= -10.50 \pm 1.25$ mm and RMS $= 39.19 \pm 0.87$ mm. (b) Downstream: The distribution has mean of $= -4.80 \pm 2.03$ mm and RMS $= 71.88 \pm 2.15$ mm, with the errors being purely statistical. There is a deficit of tracks at ≈ 90 mm. This is a result of the dead channel in the first station of the downstream channel, outlined in Section 5.7. A selection criteria is enforced such that a track must have a track point in this station. As a result of the dead channel, tracks which happened to have $x_d \approx 90$ mm are removed. Thus, a deficit of tracks is observed in that region

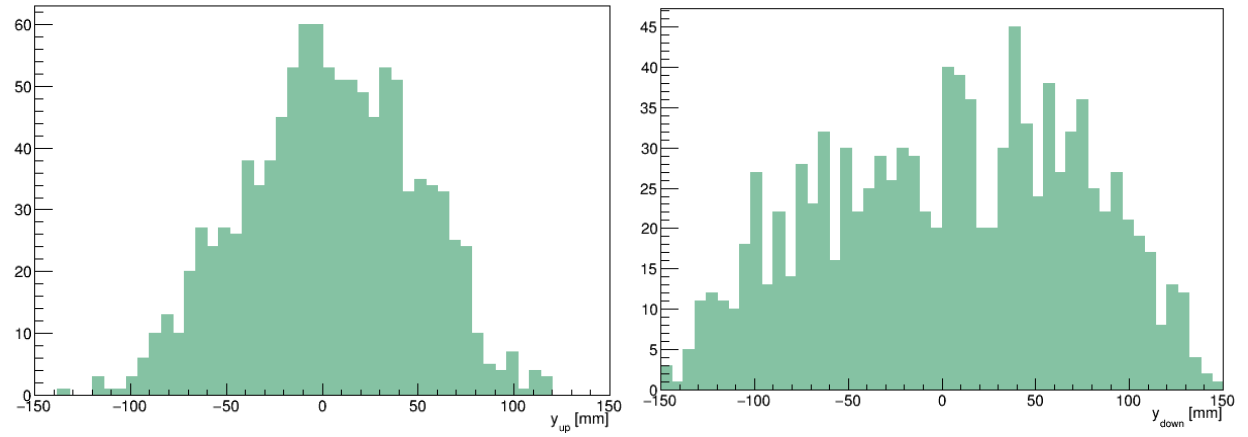

(a) (b)

Figure 5.10: Distribution of y for data sample 07417 prior to the application of the "scraping cut" but after all other selection criteria, outlined in Section 5.6.1, were imposed. (a) Upstream: The distribution has mean $= 3.21 \pm 1.39$ mm and RMS $= 43.05 \pm 0.895$ mm. (b) Downstream: The distribution has mean $= 4.59 \pm 2.10$ mm and RMS $= 77.02 \pm 1.88$ mm. All quoted errors are statistical.

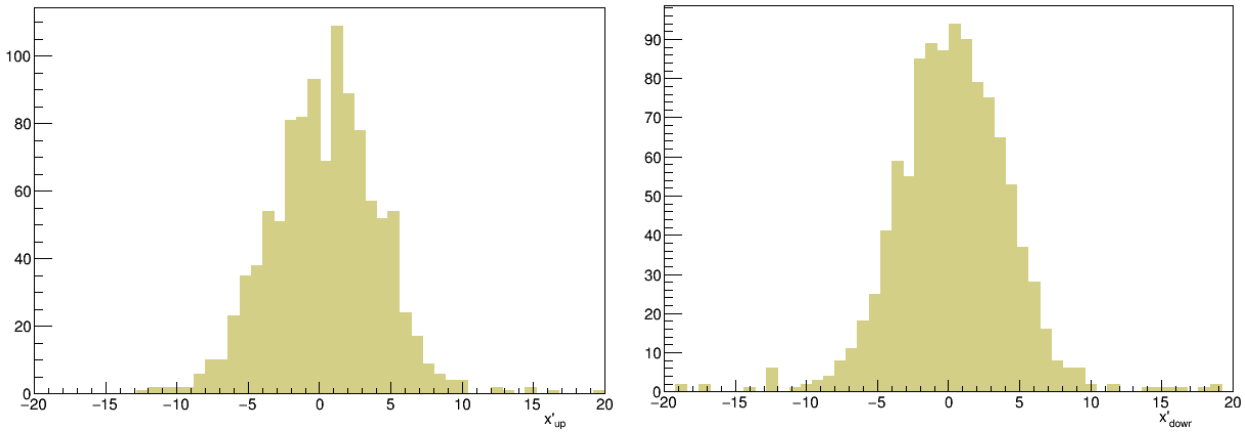

(a) (b)

Figure 5.11: Distribution of x' for data sample 07417 prior to the application of the "scraping cut" but after all other selection criteria, outlined in Section 5.6.1, were imposed. The distributions have (a) Upstream: a mean $= 0.023 \pm 0.11$ and RMS $= 3.310 \pm 0.075$. (b) Downstream: a mean of $= 0.32 \pm 0.11$ and RMS of $= 3.52 \pm 0.08$. Where all errors are purely statistical.

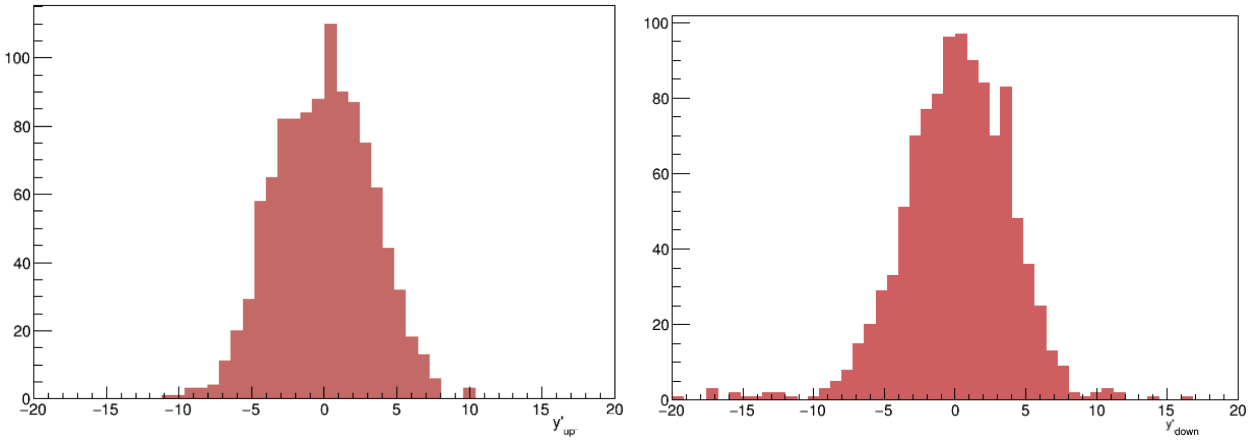

(a) (b)

Figure 5.12: Distribution of y' for data sample 07417 prior to the application of the "scraping cut" but after all other selection criteria, outlined in Section 5.6.1, were imposed. The distributions have (a) Upstream: a mean $= 0.023 \pm 0.11$ and RMS $= 3.38 \pm 0.08$ and (b) Downstream: a mean$= 0.16 \pm 0.11$ and RMS $= 3.37 \pm 0.08$. Errors are again statistical.

5.8.6 Track Residuals

A "track residual" is derived through comparison of the true Monte Carlo tracks, i.e. those obtained from MCEvents, and the reconstructed Monte Carlo ReconEvents tracks, i.e. Monte Carlo simulated events which have been passed though the MAUS reconstruction/digitisation model to simulate how the data would be reconstructed in the software.

This "track residual," $(0, \delta x^t, \delta x'^t, \delta y^t, \delta y'^t)$, is the difference between the upstream trace space co-ordinate of the particle, $\vec{u}^{true} = (1, x_u^{true}, x_u'^{true}, y_u^{true}, y_u'^{true})$, taken directly from MCEvents and the upstream trace space co-ordinates of the same particle taken directly from reconstructed Monte Carlo, $\vec{u}^{MCreco} = (1, x_u^{MCreco}, x_u'^{MCreco}, y_u^{MCreco}, y_u'^{MCreco})$, such that:

$$\delta x^t = x_u^{MCreco} - x_u^{truth}, \tag{5.88}$$

$$\delta x'^t = x_u'^{MCreco} - x_u'^{truth}, \tag{5.89}$$

$$\delta y^t = y_u^{MCreco} - y_u^{truth} \tag{5.90}$$

and

$$\delta y'^t = y_u'^{MCreco} - y_u'^{truth}. \tag{5.91}$$

The "track residuals" are independent of the transfer matrix fitting procedure and help characterise the systematic uncertainty which exists due to the detector (tracker) resolutions.

Figures 5.13a to 5.13d show the distributions of these residuals for each of the four trace space co-ordinates. These distributions are all symmetric about 0, within statistical errors, and are found to be consistent with Gaussian distributions. Therefore, no systematic bias or other underlying issues are introduced within the reconstruction algorithms as a result of the detector geometries. Any tracker-tracker misalignment has been correctly characterised in the Monte Carlo.

5.8.7 Track Residuals Covariance Matrix

To account for the inherent errors which will be induced via the linear least squares fitting method due to the finite detector resolution, detailed by Equations 5.80 to 5.83, a "covariance matrix", $\underline{\underline{C}}_{cov}$, can be derived, such that

$$C_{cov} = \begin{pmatrix} 0 & 0 & 0 & 0 & 0 \\ 0 & c_{\delta x^t,\delta x^t} & c_{\delta x^t,\delta x'^t} & c_{\delta x^t,\delta y^t} & c_{\delta x^t,\delta y'^t} \\ 0 & c_{\delta x'^t,\delta x^t} & c_{\delta x'^t,\delta x'^t} & c_{\delta x'^t,\delta y^t} & c_{\delta x'^t,\delta y'^t} \\ 0 & c_{\delta y^t,\delta x^t} & c_{\delta y^t,\delta x'^t} & c_{\delta y^t,\delta y^t} & c_{\delta y^t,\delta y'^t} \\ 0 & c_{\delta y'^t,\delta x^t} & c_{\delta y'^t,\delta x'^t} & c_{\delta y'^t,\delta y^t} & c_{\delta y'^t,\delta y'^t} \end{pmatrix}.$$

with elements, $c_{i,j}$, being the mean of the covariance between the tracker residuals of corresponding trace space co-ordinates denoted in sub-script. The first row and column of $\underline{\underline{C}}_{cov}$ ($i = 0$ or $j = 0$) are 0, representing the mean of the distributions in Figures 5.13a to 5.13d. There remains a non-zero 4×4 matrix. The diagonal terms, $c_{i,i}$ represent the variance of each of the track residuals and the off-diagonal terms, $i \neq j$, represent the covariance between the track residuals $\delta\vec{u}_i^t$ and $\delta\vec{u}_j^t$. In a perfect case all the matrix elements of C_{cov} would be 0, meaning that the reconstructed and true distributions are identical.

For data set 07417 the covariance matrix is found to be:

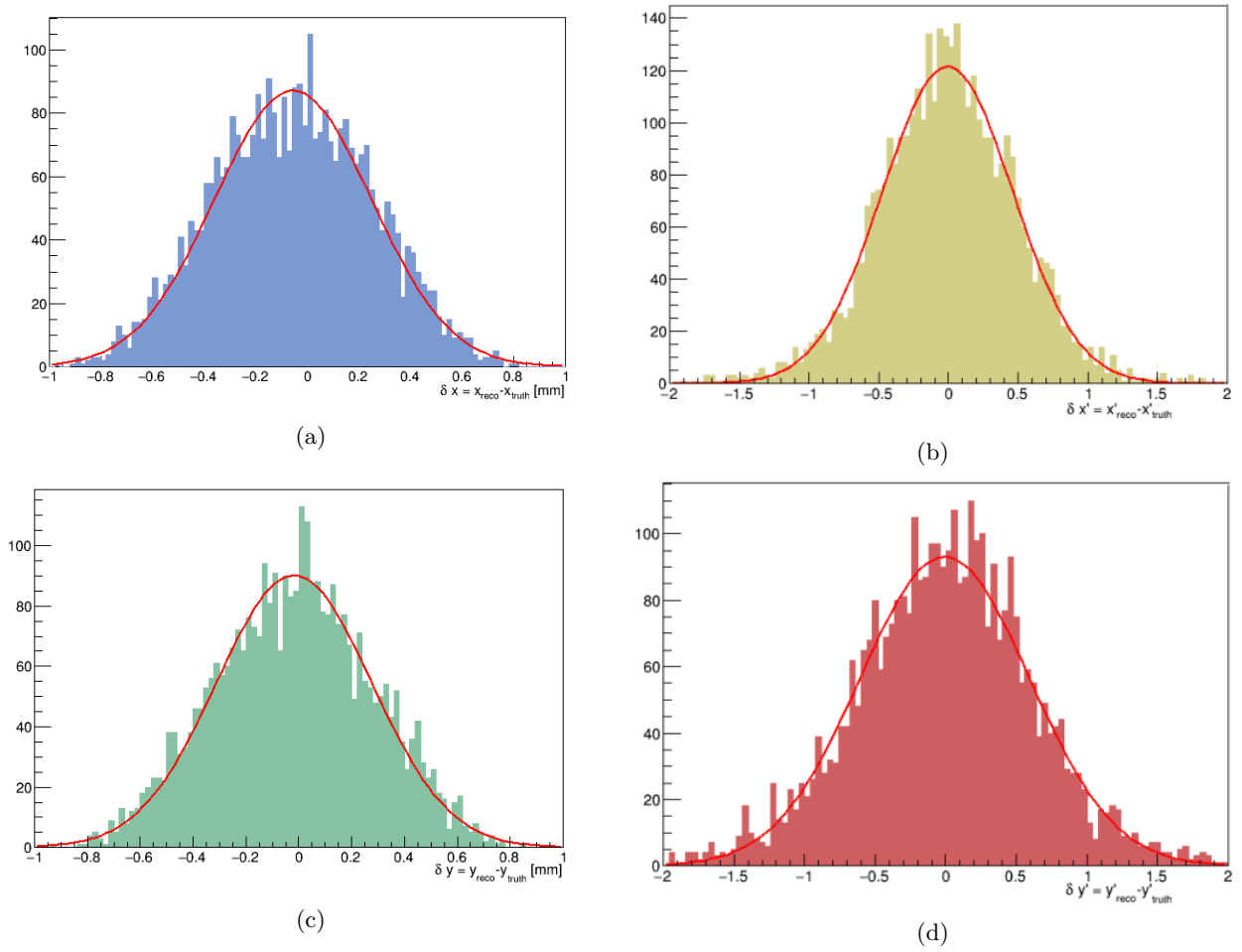

Figure 5.13: Distributions of particle "track residuals," defined as the difference in the particle's true (derived from MCEvents) co-ordinate and that from the digitised Monte Carlo (derived from MC ReconEvents) for run 07417. The 4 truth residuals are fitted with Gaussian curves. For (a) x - $\mu = 0.0014 \pm 0.005$ mm and $\sigma = 0.305 \pm 0.0034$ mm with $\chi^2/ndf = 1.03$ (b) x' - $\mu = -0.007 \pm 0.007$ and $\sigma = 0.467 \pm 0.006$ with a $\chi^2/ndf = 1.19$. (c)y - $\mu = 0.005 \pm 0.005$ mm and $\sigma = 0.295 \pm 0.0032$ mm with a χ^2/ndf1.34.(d) y' - $\mu = 0.0065 \pm 0.01$, and $\sigma = 0.6 \pm 0.0085$ with a $\chi^2/ndf = 1.32$. All 4 distributions are, therefore, consistent with Gaussian distributions centred upon $\delta^t = 0$. Suggesting no systematic bias is apparent in any of the 4 co-ordinates. Finite widths are observed representing the resolution of the reconstruction process. The resolutions in x and y are equivalent, within respective errors.

$$C_{cov} = \begin{pmatrix} 0 & 0 & 0 & 0 & 0 \\ 0 & 0.27 \pm 0.05 & 0.2 \pm 0.02 & 0.07 \pm 0.07 & 0.02 \pm 0.08 \\ 0 & 0.2 \pm 0.02 & 0.38 \pm 0.02 & 0.02 \pm 0.08 & 0.01 \pm 0.07 \\ 0 & 0.07 \pm 0.07 & 0.02 \pm 0.08 & 0.36 \pm 0.1 & 0.22 \pm 0.07 \\ 0 & 0.02 \pm 0.02 & 0.01 \pm 0.07 & 0.22 \pm 0.07 & 0.57 \pm 0.04 \end{pmatrix}.$$

The matrix is symmetric. The variances correspond, within errors, to the width of the track residual plots, as expected. The covariance terms between the residuals of x and y or x' and y' are small, suggesting little correlation, and the covariance between the residuals in x and x' or y and y' are comparable to the diagonal variances, again as is expected.

Figures 5.14a to 5.14d display examples of the calculated values of 4 matrix elements. The green points in each plot represent the transfer matrix calculated when the covariance matrix is assumed to be 0, i.e. it

is assumed the detector has perfect resolution, and the dark blue points represent the case when the method is assumed to have a resolution as measured by the covariance matrix. This covariance is then corrected for, and the transfer matrix recalculated.

Figure 5.14a displays the effect that correcting for this covariance has on the calculated matrix element M_{00}, the term describing x offset between the two trackers, as a function of TOF_{12}. For all but the latest TOF_{12} point, accounting for the covariance matrix moved the calculated value of M_{00} closer to the expected, aligned, value of 0. Likewise, Figure 5.14b shows an analogous plot for the matrix element M_{02}, the mapping between downstream x^d and upstream x'_u. For all TOF_{12} values it is clear that correcting for the covariance matrix shifts the calculated matrix element, in many cases by over 1σ, closer to the expected value.

Figures 5.14c and 5.14d exhibit the effect that the correction has on transfer matrix elements M_{10} and M_{11} respectively. M_{10} describes the rotational x' offset and M_{11} denotes the mapping between x'_d and x_u. Here the shift is less apparent, this is to be expected given the relative size of the calculated corresponding elements in C_{cov}.

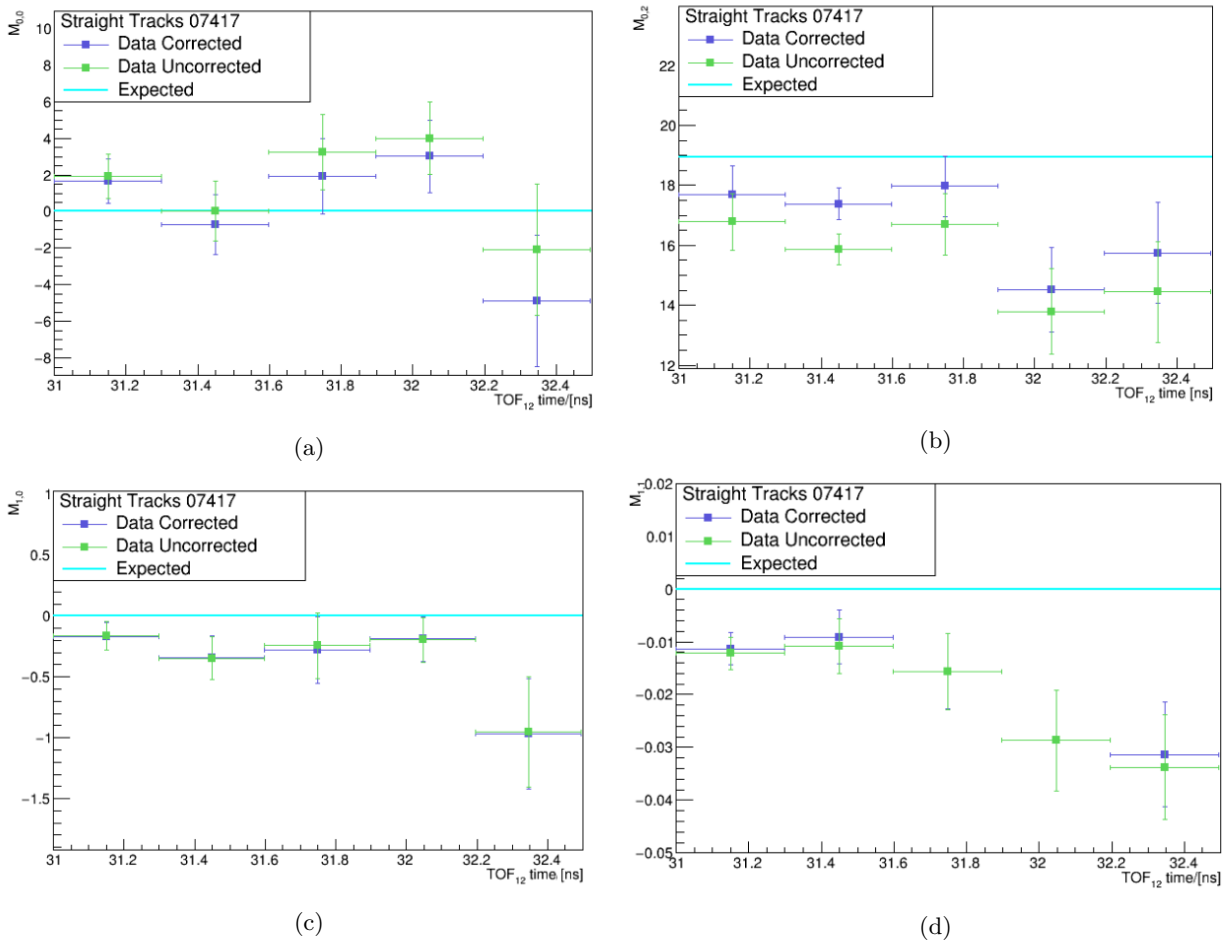

Figure 5.14: Plots show examples of how transfer matrix elements: (a) $M_{0,0}$ (b) $M_{0,2}$ (c) $M_{1,0}$ (d) $M_{1,1}$ vary as functions of binned particle TOF_{12} times for the case where the systematic error due to the covariance between truth residuals in Equation 5.83 is ignored (in green) and the case where it is accounted for (in dark blue). It is seen that in (a) and (b) this brings the calculated value closer to the expected case (blue line) these plots show the elements corresponding to the x offset and drift space length respectively. This is less apparent in (c) and (d) which correspond to the angular x' offset and $x_u \to x'_d$ mapping element respectively.

5.8.8 Calculated Transfer Matrix Elements

Figure 5.15 displays the derived transfer matrix elements for the data sample alongside those obtained from the true and reconstructed Monte Carlo samples, each as a function of the time taken for particles to traverse from the TOF_1 and TOF_2 detectors. The position of the plot in this array of figures corresponds to the matrix element it represents. These were produced after accounting for the covariance systematic error in the fitting procedure, discussed in Section 5.8.7, and after all tracker resolution and particle identification section criteria, outlined in Section 5.6.1, had been applied. The corresponding numerical values and their respective errors are displayed in Table A.1.

The selected TOF_{12} (shown in red in Figures 5.7 and 5.6) has been subdivided into 5 discrete TOF_{12} bins of equal widths, in time, and the transfer matrix has been calculated separately for each of these 5 sub-samples. The error bars represent purely statistical errors which are calculated by sub-sampling each of the 5 TOF_{12} bins: each of the 5 bins is split into a further 5, and the transfer matrix elements re-calculated. The statistical error on each bin is then taken to be:

$$\sigma_{stats} = \frac{\sigma_{var}}{\sqrt{n}}, \tag{5.92}$$

where (σ_{var}) is the variance of the distribution of the calculated matrix elements for the 5 sub-bins and n is the number of events in each bin. The TOF_{12} selection window discussed in Section 5.6.1 helps limit the impact of statistical errors on the derived matrix elements analysis as it ensures the fit is carried out in a densely populated TOF_{12} region.

Both true Monte Carlo (MCEvents) and reconstructed Monte Carlo (ReconEvents) are compared to the data. The "expected" line describes the expected ("field-off") value of the matrix elements given Equations 5.7 to 5.10. For this Focus Coil "field-off" study it is essential that, within statistical errors, the matrix elements for each of the 5 TOF_{12} bins are consistent with one another, ensuring no bias in the method to a given particle momentum. In order to establish that there is no tracker-tracker misalignment in the data it is also essential that the data and Monte Carlo samples are consistent with the expected, straight track, matrix, within accountable errors, both statistical and systematic.

The plots in Figure 5.15 show that for the majority of matrix elements and the majority of TOF_{12} bins the true and reconstructed Monte Carlo samples are consistent, within their respective statistical errors. This suggests that any systematic bias introduced by the intrinsic detector reconstruction algorithms have been properly accounted for. The data has more substantial variations from the expected line, this is a result of statistical variations and in most cases the data lies within $\pm 1\sigma_{stat}$ from expectation and the Monte Carlo simulations. Any offsets may arise due to residual asymmetries that are not completely removed by the "scraping cut."

MC True
MC Recon
Data
Expected
TOF12 [ns]

Figure 5.15: Array of transfer matrix elements plotted as functions of TOF_{12}. The position of each plot corresponds to its position in the transfer matrix. Error bars show statistical errors. The yellow line represents the constant expected value given straight muon tracks in the 07417 geometry in a completely aligned system. The exact values are shown in Table A.1. The selected TOF_{12} region was chosen to exclude pion and decay electrons. This region was then subdivided into 5 equal-width bins. The transfer matrix was subsequently calculated for particles in each bin separately. Any bin-to-bin variation is a result of statistical variations.

5.8.9 Trace Space Projections

Figures 5.16a to 5.16d and 5.17a to 5.17d show examples of the resulting correlation between the upstream and downstream co-ordinates for the "focussing" and "defocussing" quadrants associated with the $x_d - x'_d$ co-ordinates respectively. These terms are used in analogy to their purpose in a solenoidal field. In this straight tracks run the Focus Coil acts as a drift space, $B_0 = 0$. Consequently, x and y are decoupled. The Equations 5.3 to 5.6 can be expressed in terms of 4 lines given by Equations 5.7 to 5.10.

The 2-D "sub-plots" presented in Figures 5.16a to 5.16d and 5.17a to 5.17d are derived from a multi-dimensional fitting routine which takes into account the two sets of 4D co-ordinates of each particle in the sample in order to derive the full 4×5 transfer map transporting the particles between the two trackers. The fitted matrix is a result of an optimisation which takes into account all permutations of the 2 sets of 4D co-ordinates to provide the best fit to the data, it does not simply fit the two co-ordinates shown.

There are 5 coloured fit lines presented on each plot. Each line corresponds to a separate independent fitted transfer matrix to the particles with times corresponding to the 5 discrete TOF_{12} bins. The coloured lines are 2D projections of the total fitted matrix, and are not direct fits to the histograms presented. The fit lines are presented here for illustrative purposes only. It is evident that there is some differences between the transfer matrix elements calculated for each of the 5 TOF_{12} bins; small variations between different TOF_{12} bins are observed in all plots. These are a result of the differing statistical errors in each TOF_{12} bin.

In the case of the "focussing" quadrant which describes the relationship between $x_d, x'_d \rightarrow x_u x'_u$, all 5 lines in all 4 "sub-plots" have finite, positive gradients. The distributions are $\approx$ symmetric about the mean of the fit lines. The angular-momentum generating quadrant ("defocussing") quadrant describes the relationship between $x_d, x'_d \rightarrow y_u y'_u$. Here the gradients of the lines are much smaller and average ≈ 0 for each set of 2D combination. This is to be expected as the x and y co-ordinates are decoupled in the drift space. In a "field-on" study this may not be the case.

5.8.10 Method Residuals

A "method residual" can be calculated such that

$$\delta_x^m = (x_d)_m - M_{00}^m - \sum_{j=1}^{j<5} M_{0,j}^m (u_j)_m, \tag{5.93}$$

$$\delta_x^m = (x'_d)_m - M_{10}^m - \sum_{j=1}^{j<5} M_{1,j}^m (u_j)_m, \tag{5.94}$$

$$\delta_y^m = (y_d)_m - M_{20}^m - \sum_{j=1}^{j<5} M_{2,j}^m (u_j)_m \tag{5.95}$$

and

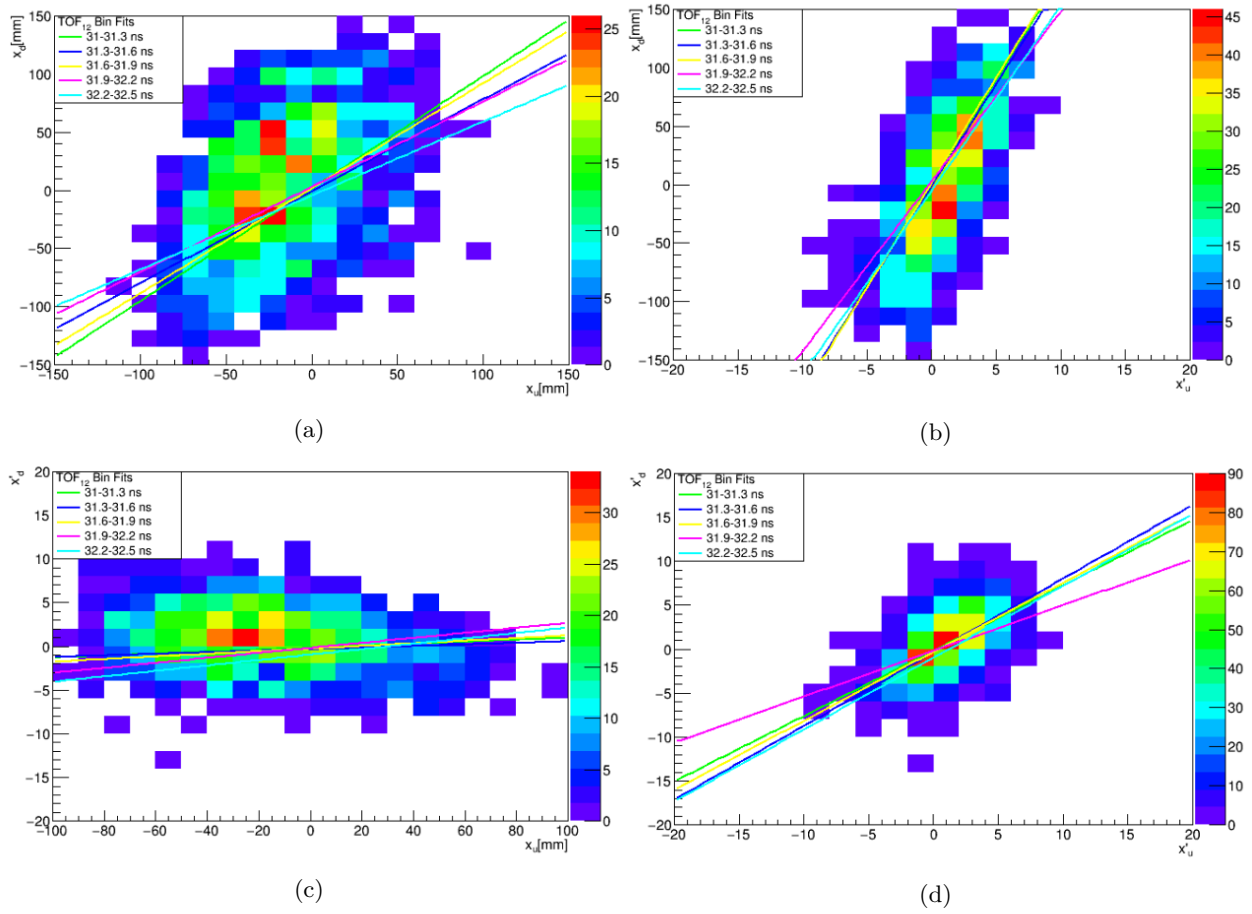

Figure 5.16: "Focussing" quadrant in x: Plots showing correlations between particle co-ordinates in the data sample 07417. The fit lines correspond to fits to the total data sample and take into account the whole transfer matrix. The data has been split into 5 TOF_{12} bins and the matrix calculated for each. These 5 lines have been projected on to the 2D plots simply for visualisation purposes. The lines are not direct fits to the two co-ordinates alone. Some variation can be seen between the 5 separate fits. Plots show (a) downstream particle x position and upstream particle x position. The gradient of these lines corresponds to the matrix element M_{01} and any offset is due to M_{00}. (b) downstream x' and upstream x'. The gradient of these lines corresponds to matrix element M_{02} and any offset due to constant term M_{00}. (c) downstream x' and upstream x. The gradient of these lines corresponds to the matrix element M_{11} and any offset is due to constant term M_{10}. (d) downstream x' and upstream x'. The gradient of these lines correspond to matrix element M_{12} and any offset corresponds to M_{10}.

$$\delta_y^m = (y'_d)_m - M_{30}^m - \sum_{j=1}^{j<5} M_{3,j}^m (u_j)_m; \tag{5.96}$$

where $(\vec{d})_m$ is the particle's measured downstream trace space coordinate and $(\vec{u})_m$ is the measured upstream co-ordinate. The matrix elements M_{nj}^m correspond to the elements of the measured transfer matrix. For the case when $j = 0$ the matrix element is simply the offset between the two trackers.

These residuals are therefore the difference in the actual downstream value, as measured by the trackers and stored in the SciFiTrack, and the predicted value, extrapolated using the fitted transfer matrix elements and the measured upstream tracker. The distributions of these "method residuals" for true Monte Carlo (i.e. MCEvents) are shown in Figures 5.18a to 5.18d. Figures 5.19a to 5.19d and Figures 5.20a to 5.20d show analogous distributions for the reconstructed Monte Carlo and data sample respectively.

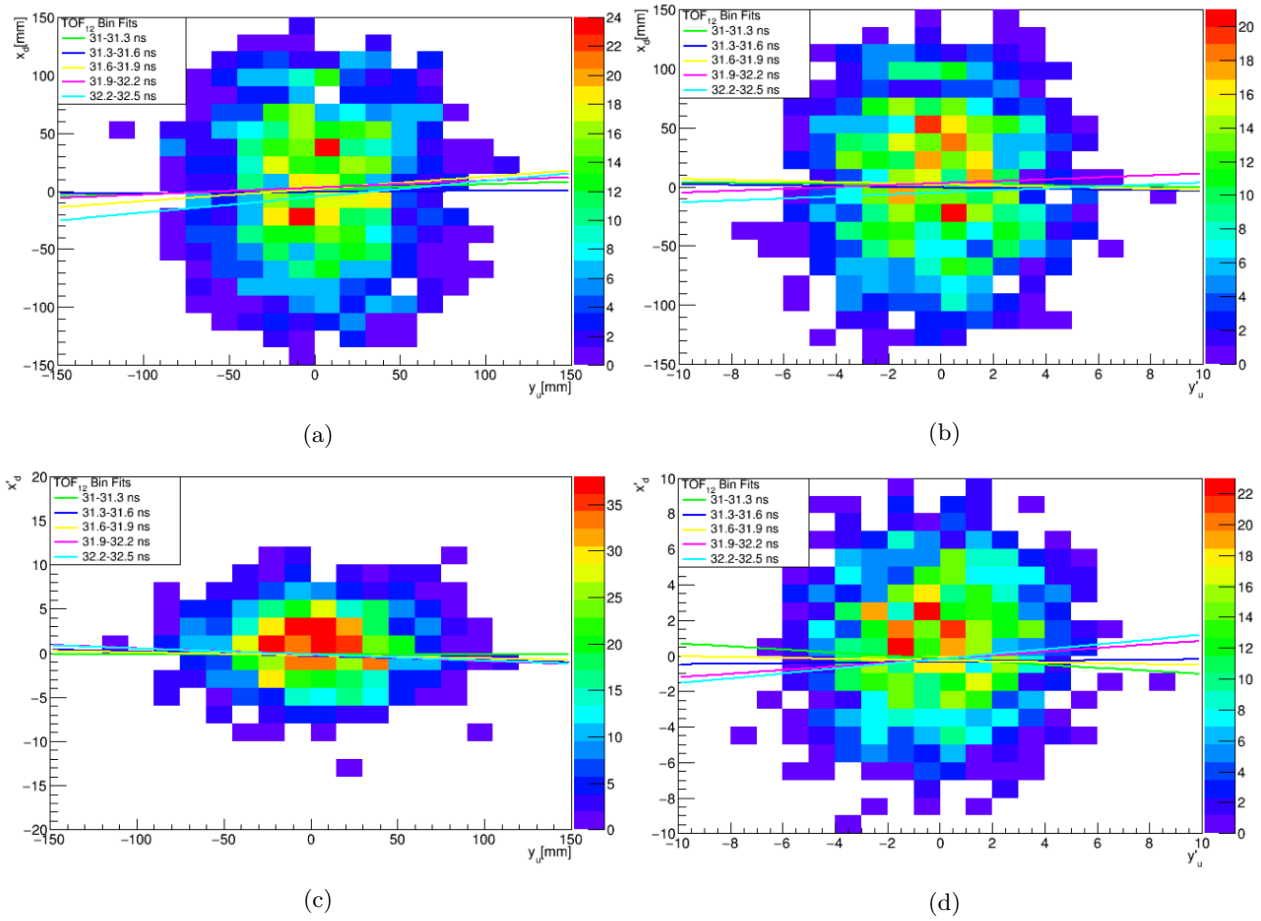

Figure 5.17: "Defocussing" quadrant in $x - y$: Plots showing correlations particle co-ordinates in the data sample 07417. The fit lines correspond to fits to the total data sample and take into account the whole transfer matrix. The data has been split into 5 TOF_{12} bins and the matrix calculated for each. These 5 lines have been projected on to the 2D plots simply for visualisation purposes. The lines are not direct fits to the two co-ordinates alone. Some variation can be seen between the 5 separate fits. Plots show (a) downstream particle x position and upstream particle y position. The gradient of these lines corresponds to the matrix element M_{03} and any offset is due to M_{00}. (b) downstream x and downstream y'. The gradient of these lines corresponds to matrix element M_{04} and any offset due to constant term M_{00}. (c) downstream x' and upstream y. The gradient of these lines corresponds to the matrix element M_{11} and any offset is due to constant term M_{13}. (d) downstream x' and upstream y'. The gradient of these lines correspond to matrix element M_{14} and any offset corresponds to M_{10}.

All 3 samples are shown to have Gaussian residual distributions for all co-ordinates, within available statistical errors, suggesting no bias or large misalignment is present in the trackers. The resolution in the position co-ordinates (x, y) is found to be slightly better for the Monte Carlo simulations, both truth and reconstructed, at $\approx$ 22 mm compared to $\approx$ 28 mm for the data. The correlated momentum resolutions (x', y'), for all three samples, are shown to be consistent with one another.

5.8.11 Correlations between Method Residuals and Particle Co-ordinates

Figures 5.21a to 5.22b display the relationship between the method residuals, δx and $\delta x'$, and the corresponding upstream and downstream co-ordinate for track points obtained from data run 07417. Such distributions help assert that there is no hidden curvature or inherent correlations that have not yet been taken into

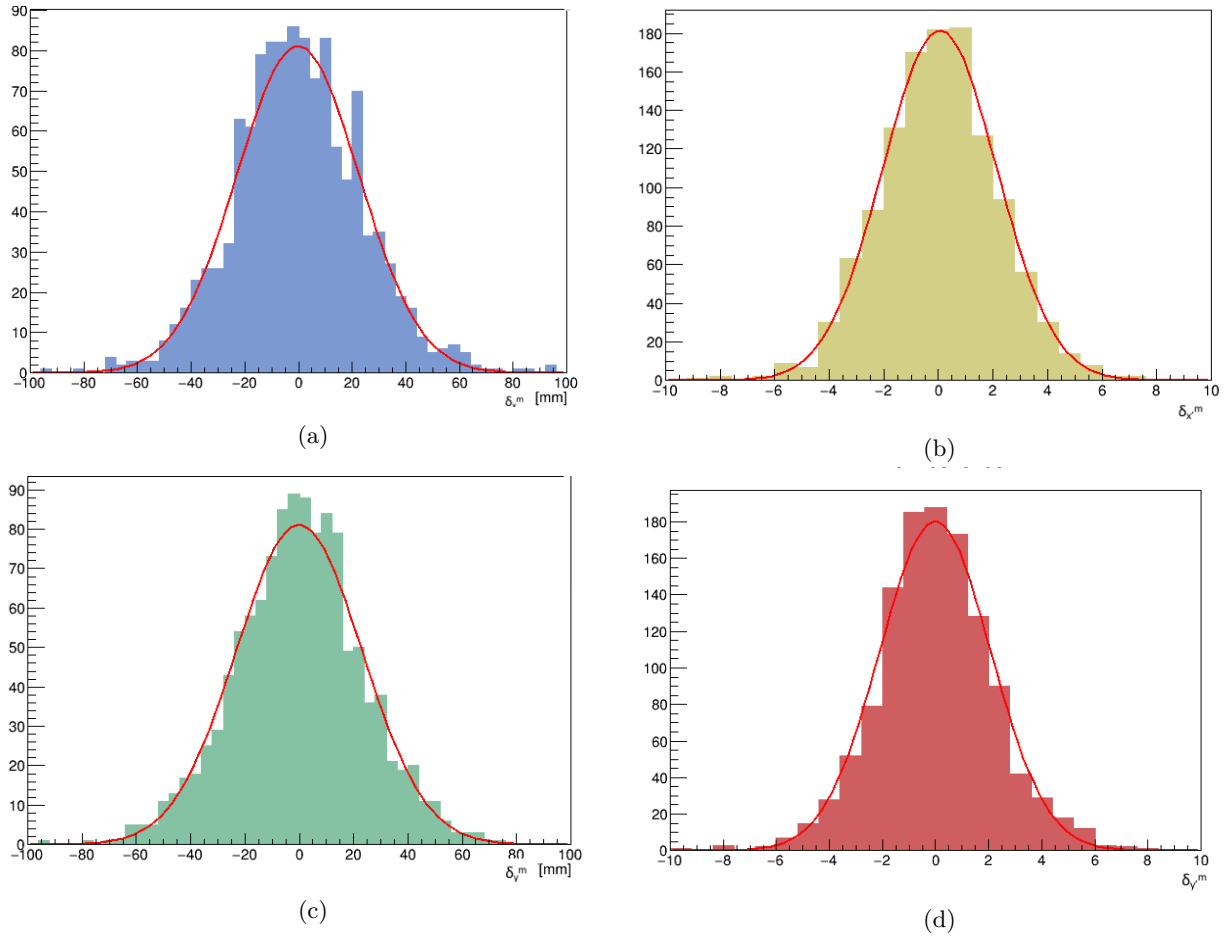

Figure 5.18: Distributions of particle "method residuals" for tracks in true Monte Carlo sample in which particles traverse a cooling channel with a geometry comparable to data run 07417. This residual denotes the difference between the measured (x, x', y, y') and that extrapolated from the upstream data through exploiting the matrix elements calculated in this analysis. Each distribution is fitted with a Gaussian curve: For (a) x - $\mu = -0.2 \pm 0.5$mm and $\sigma = 22.3 \pm 0.4$ mm with a $\chi^2/ndf = 1.14$. For (b) x' - $\mu = 0.023 \pm 0.05$ and $\sigma = 2.1 \pm 0.04$ with a $\chi^2/ndf = 0.85$. For (c) y - $\mu = 0.013 \pm 0.49$ mm and $\sigma = 22.6 \pm 0.4$ mm with a $\chi^2/ndf = 0.85$.For (d) y' - $\mu = 0.082 \pm 0.041$ and $\sigma = 2.1 \pm 0.03$ with a χ^2/ndf1.25. All four residuals are consistent with Gaussian distributions, centred upon $\delta^m = 0$. The resolutions in $x - x'$ are equivalent to those in $y - y'$, suggesting no bias, towards a given direction, is induced in the fitting method.

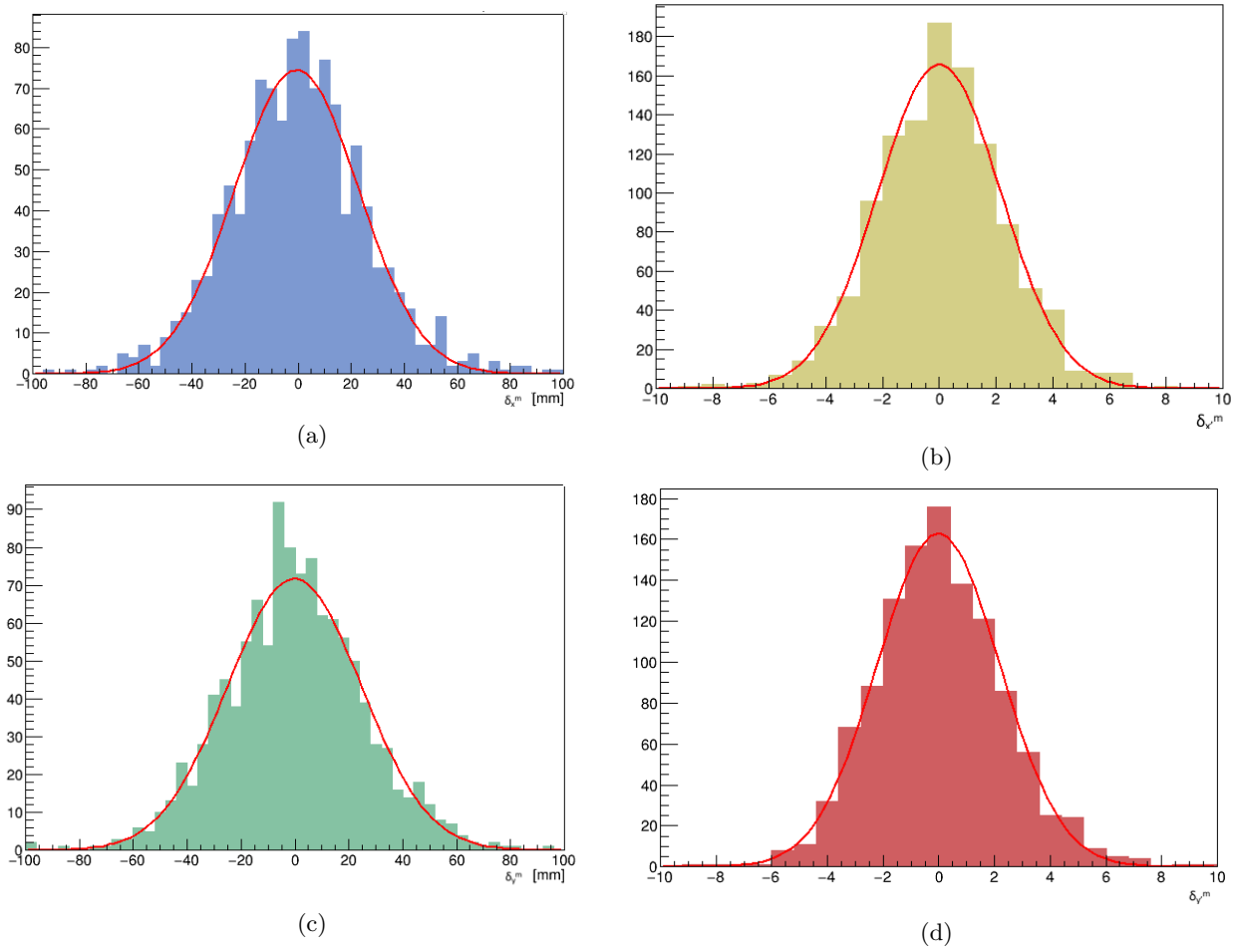

Figure 5.19: Distributions of particle "method residuals" for reconstructed Monte Carlo (ReconEvent) tracks traversing a cooling channel with a geometry comparable to data run 07417. This residual denotes the difference between the measured (x, x', y, y') and that extrapolated from the upstream data through exploiting the matrix elements calculated in this analysis. Each distribution is fitted with a Gaussian. For (a) x - $\mu = -0.2 \pm 0.5$ mm and $\sigma = 22.3 \pm 0.4$ mm with a $\chi^2/ndf = 1.22$.. For (b) x' - $\mu = 0.023 \pm 0.05$ and $\sigma = 2.1 \pm 0.04$ with a $\chi^2/ndf = 1.24$. For (c) y - $\mu = 0.013 \pm 0.49$ mm and $\sigma = 22.6 \pm 0.4$mm with a $\chi^2/ndf = 0.89$. For (d) y' - $\mu = 0.082 \pm 0.041$ and $\sigma = 2.1 \pm 0.03$ with a $\chi^2/ndf = 1.09$. The residuals in all four dimensions are consistent with Gaussian distributions, centred upon $\delta^m = 0$. No systematic bias is observed. The resolutions in $x - x'$ is equivalent to those in $y - y'$ suggesting no bias, towards a given direction, is induced by the fitting method.

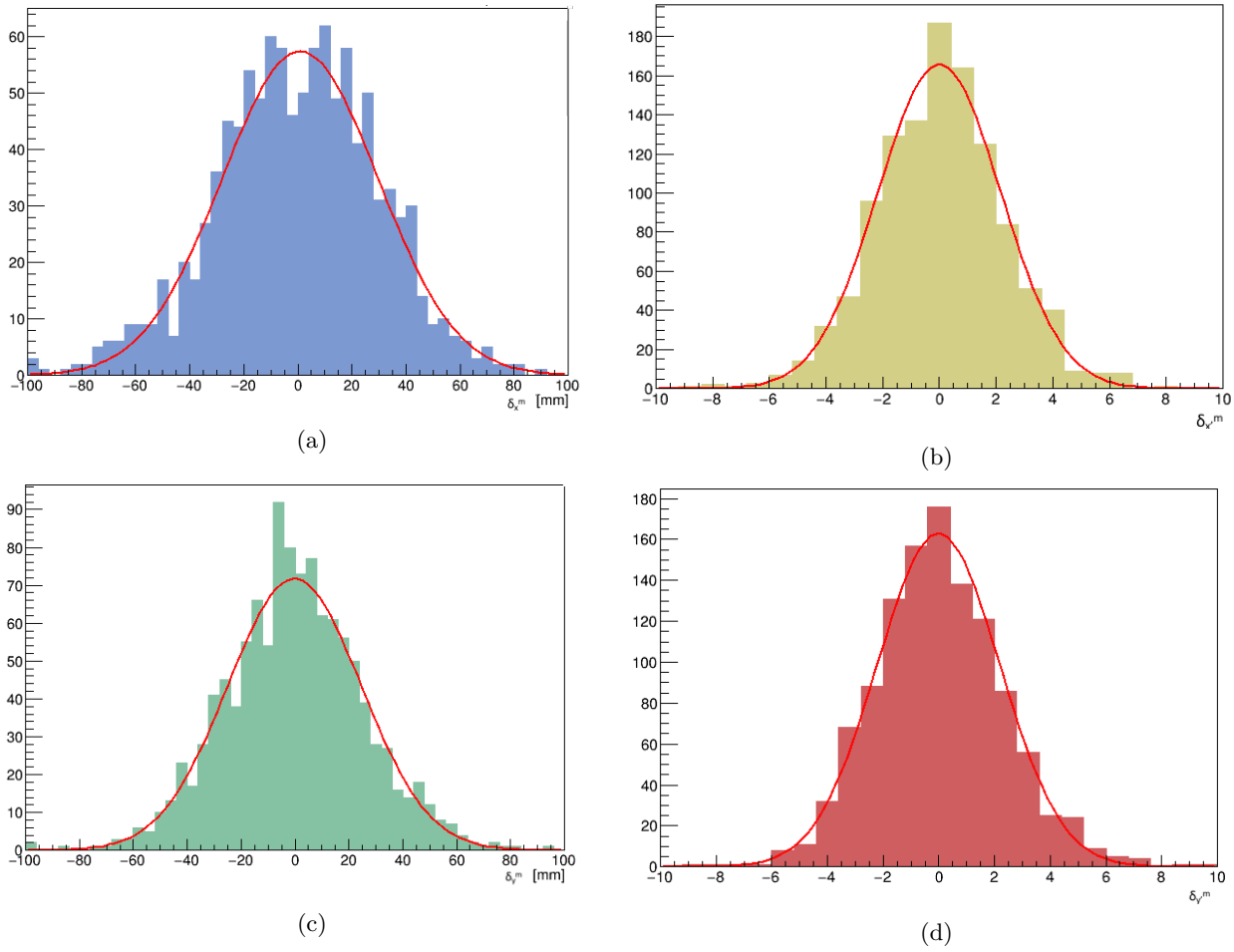

Figure 5.20: Distributions of "method residuals" for particles within the 07417 data sample. This residual denotes the difference between the measured (x, x', y, y') and that extrapolated from the upstream data through exploiting the matrix elements calculated in this analysis. Each distribution is fitted with a Gaussian curve. For (a) x- The fitted Gaussian has $\mu = 0.82 \pm 0.9$ mm and $\sigma = 28.9 \pm 0.75$ mm. The distribution is, therefore, consistent with a Gaussian centred on 0, with a χ^2/ndf of 0.95. For (b) x' - The fitted Gaussian has $\mu = -0.04 \pm 0.08$ and $\sigma = 2.56 \pm 0.06$. The distribution is, therefore, consistent with a Gaussian centred on 0, with a χ^2/ndf of 0.99. For (c) y -The fitted Gaussian has $\mu = 0.75 \pm 0.90$ mm and $\sigma = 28.4 \pm 0.7$ mm. The distribution is, therefore, consistent with a Gaussian centred on 0, with a χ^2/ndf of 1.18. For (d) - The fitted Gaussian has $\mu = 0.016 \pm 0.081$ mm and $\sigma = 2.7 \pm 0.06$. The distribution is, therefore, consistent with a Gaussian centred on 0, with a χ^2/ndf of 0.91.

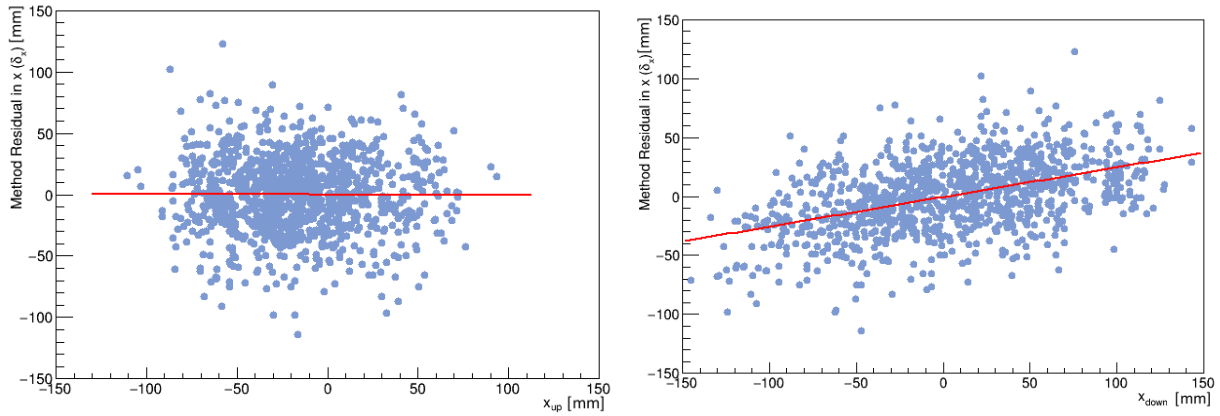

(a) (b)

Figure 5.21: Plots showing the distribution of track point method residual, δx, as function of position x co-ordinate for tracks obtained from data run 07417 at the upstream (a) and downstream (b). In the case of a perfect fit this residual would be 0. There is some variance which is expected given the Gaussian spread in measured residuals. (a) The resulting distribution forms an ellipse centred around $(0, 0)$. A correlation factor of 0.003 is derived. A straight line is fit to the distribution; a gradient = -0.0029 ± 0.012, consistent with a flat line, and offset = -0.02 ±0.04, is found. (b) A linear correlation is now observed compared to the analogous upstream distribution; this is to be expected. The distribution remains centred around (0,0). There are no odd outlying clusters or apparent curvature at the tails. This suggests no underlying systematic effect exists in the measured residuals which has not yet been accounted for. There is a small absence of events around the dead channel region at ≈ 90 mm. A correlation factor of 0.47 is found. A straight line is fit to the distribution; a gradient = 0.25± 0.01 and offset = -0.46 ±0.4, is found.

consideration. In the case of an exact fit to an aligned system the method residuals would all be "0." In reality, however, there exists some finite difference in the derived downstream co-ordinates and the actual downstream co-ordinate which is represented by the Gaussian nature of the measured residual distributions, discussed in Section 5.8.10.

No correlation is observed between the upstream x and x' co-ordinates and the corresponding residual, suggesting no geometric systematic bias in the residual calculation. The points form an ellipse centred around $(0, 0)$ with a finite width representing the resolution of the measurements. However, when considering the relationship between track point residuals and their corresponding downstream co-ordinate the elliptical distribution becomes centred around a diagonal line. This indicates some inherent correlation is present between the method residual and the resulting measured downstream co-ordinate. These are a consequence of the correlations discussed in Section 5.8.9 and there does not appear to be any non-linearities.

5.9 Limiting Sources of Systematic Errors

This section presents a review of several sources of systematic error inherent within both the Monte Carlo and data. These are both a consequence of fitting algorithms and material effects introduced by interactions with the detector subsystems within the cooling channel.

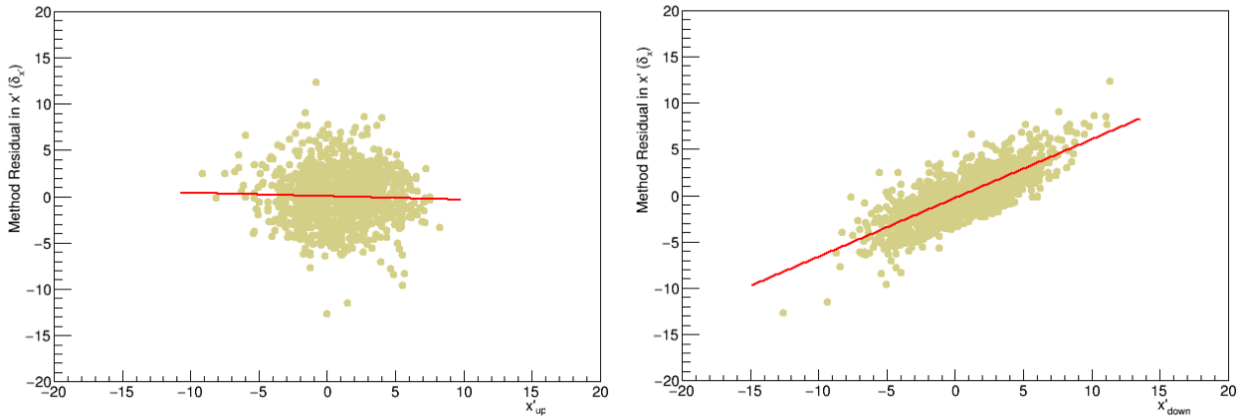

(a) (b)

Figure 5.22: Plot showing the distribution of track point method residual, $\delta x'$, as a function of the particle x' co-ordinate both upstream (a) and downstream (b) for tracks obtained from data run 07417. In the case of a perfect fit this residual would be 0. There is some variance which is expected given the Gaussian spread in measured residuals. (a) The resulting distribution forms an ellipse centred around $(0, 0)$. A correlation factor of 0.004 is derived. A straight line is fit to the distribution with a gradient = -0.038 $\pm$ 0.021, consistent with a flat line, and offset = -0.02 $\pm$0.04. (b) A linear correlation is now observed compared to the analogous upstream distribution. The distribution remains centred around (0,0). There are no odd outlying clusters or apparent curvature at the tails. This suggests no underlying systematic non-linear effect exists in the measured residuals which has not yet been accounted for. A correlation factor of 0.79 is derived. A straight line is fit to the distribution; a gradient = 0.633 $\pm$ 0.010 and offset = -0.23 $\pm$0.21, is found.

5.9.1 Errors due to Fitting Procedure:

1. Non-Linearities in the transfer matrix elements:

In order to obtain the matrix elements via linear least squares fitting, outlined in Section 5.4.1, a linear relationship is assumed between the upstream and downstream track point co-ordinates. In reality, however, some curvature could exist in the tails of the fitted co-ordinate plots. This is analogous to the effect of spherical aberrations in optical physics and results from the idea that the tracks which are on the very edges of the tracker in x and y are brought to a focus, by the Focus Coil, at points further back in z than those closer to the centre of the beam. Non-linearities would result in inaccurate fits and it would be necessary to consider higher order transfer maps if the deviations became too severe. These non-linearities are unavoidable but a rectangular cut could be imposed on both the horizontal and vertical axes of each of the mapping plots to limits their effects. Nevertheless, from Figures 5.16a to 5.17d, it can be concluded that the effects of non-linearities in this data sample were minimal. Consequently, no rectangular cut was applied in this analysis; it is assumed that evaluating only the first order transfer matrix is sufficient.

5.9.2 Errors due to Beam line Material Effects:

2. Scattering and Scraping in the Trackers or Focus coil windows:

Multiple scattering, as discussed in Chapter 2, occurs when a particle's trajectory is interrupted by the presence of atoms or molecules causing deviations from its original path. Scattering of the muons within the cooling channel can take place due to the presence of the various detector components and windows.

Muons pass through 15 planes of scintillating fibres within each tracker as well as aluminium windows in the Spectrometer Solenoids and Focus Coil. Scattering at either of the trackers or the Focus Coil windows could cause inaccuracies in the matrix calculation and, therefore, the measured misalignment.

The muon may be scattered to the extent that it travels outside of the aperture of the tracker and is effectively "scraped" from the beam. This is a statistical effect and mean Equation 5.74 is only approximate; the scraping introduces a bias if it is asymmetric. The effect becomes systematic if the beam is not on axis. Asymmetric scraping of the beam could result in the mean of the downstream position distributions, i.e. x_d and y_d, being shifted towards zero as the furthest tail is removed and effectively "scraped-off" the distribution causing asymmetric tails.

If we assume that the distribution of upstream particle co-ordinates follows a perfect Gaussian distribution of mean μ and width σ then the particle upstream x and x' can be expressed as

$$x_u \approx G(\mu_x, \sigma_x^2), \tag{5.97}$$

and

$$x'_u \approx G(\mu_{x'}, \sigma_{x'}^2). \tag{5.98}$$

and similarly for y and y'. The distribution of the particles' measured downstream co-ordinates, taken at distance $z = L$ from the upstream measurements, can be described by Gaussian distributions of the form

$$x_d \approx G(\mu_x + \mu_{x'}(L), \sigma_x^2 + \sigma_{x'}^2(L^2) + \sigma_{MCS}^2(L^2)), \tag{5.99}$$

and

$$x'_d \approx G(\mu_{x'}, \sigma_{x'}^2 + \sigma_{MCS}^2). \tag{5.100}$$

where a total scattering angle of σ_{MCS} is assumed. A non-zero mean $\sigma_{x'}$ results in a shift of $\mu_{x'}(L)$ in the mean of the downstream position distribution and, therefore, a spread in x' translates in a growing spread in position. Multiple scattering will result in a smearing effect on the downstream co-ordinates of the particle.

If the only uncertainty on the measured particle co-ordinates were this scattering then it could be removed by looking at the residuals between the true and reconstructed samples, however, a problem arises in the way in which the distribution is sampled within the trackers. Each tracker station fiducial surface is circular and ≈ 30 cm in diameter. It was shown in Section 5.8.5 that the width of the position distributions is ≈ 40 mm in the upstream tracker and ≈ 80 mm in the downstream tracker for both x and y. Both are well within the tracker volume. However, it is possible from looking at the downstream x and y distributions (Figures 5.10b and 5.9b) that the sample was not fully contained within the trackers and, therefore, the observed mean may not, in fact, be the true mean of the sample.

Consider a detector with limits $(-x_L, x_L)$, and again assuming a Gaussian spread of μ_x and width of σ_x the sample mean is defined as

$$= \int_{-x_L}^{x_L} xG(\mu_x, \sigma_x)dx \tag{5.101}$$

$$= \int_{-x_L}^{x_L} \frac{x}{\sqrt{2}\pi\sigma_x} e^{-\frac{(x-\mu_x)^2}{2\sigma_x^2}} dx. \tag{5.102}$$

Setting $v = \frac{x-\mu_x}{2\sigma_x}$ and substituting in gives

$$= \int_{\frac{-(x_L-\mu_x)}{\sqrt{\sigma}_x}}^{\frac{x_L-\mu_x}{\sqrt{\sigma}_x}} \frac{\sqrt{2}\sigma_x v + \mu_x}{\sqrt{\pi}} e^{-v^2} dv. \tag{5.103}$$

Evaluating gives

$$= \sqrt{\frac{2}{\pi}}\sigma_x \int_{\frac{-(x_L-\mu_x)}{z}}^{\frac{x_L-\mu_x}{\sqrt{\sigma}_x}} e^{-z^2} dz + \frac{\mu_x}{2}(erf(\frac{x_L-\mu_x}{\sqrt{2}\sigma_x}) - erf(\frac{-x_L-\mu_x}{\sqrt{2}\sigma_x})) \tag{5.104}$$

$$= \frac{\mu_x}{2}(erf(\frac{x_L-\mu_x}{\sqrt{2}\sigma_x}) - erf(-\frac{x_L-\mu_x}{\sqrt{2}\sigma_x})) - \sqrt{\frac{2}{\pi}} e^{-\frac{x_L^2+\mu_x^2}{2\sigma_x^2}} sinh(\frac{x_L\mu_x}{\sigma_x^2}). \tag{5.105}$$

If the distribution is contained within the detector, such that $\sigma_x/x_L << 1$, the sample mean reflects the true mean of the sample. However, if there is significant scattering and asymmetric scraping occurring, which results in the distribution going outside the detector window, i.e. $\sigma_x/x_L >> 1$, then the true mean cannot be measured.

If the samples mean significantly deviates from "0" at the downstream tracker the measured distribution will become asymmetrically sampled. If the distribution has a positive mean, a particle that scatters towards the positive x is more likely to scatter out of the detector volume. This will lead to a systematic bias in the measurements of position at the downstream tracker and, therefore, errors in the results of this study.

In order to limit the effects of scattering, a radial cut is applied to the projected downstream x_d, y_d co-ordinates given known upstream co-ordinates and the measured transfer matrix. The spread of these projected position co-ordinates $\sigma_{x,y}$ is used to ensure that the projected downstream track radius, r, lies within the tracker aperture:

$$r = \sqrt{(x_d + n\sigma_x)^2 + (y_d + n\sigma_y)^2} < 150mm, \tag{5.106}$$

where n can be varied to make the cut more or less strict. In the final analysis $n = 1$. Figure 5.23a and 5.23b show how the upstream and downstream trace space beam distribution in the $x - x'$ plane are changed by the scraping cut respectively. The cut removes the tracks which lie in the extremes of the momentum (x') tails. This reduces the total spread, in trace space, of the beam upstream. The result is that downstream the beam retains its elliptical shape with much fewer tracks at extremes in either position or momentum.

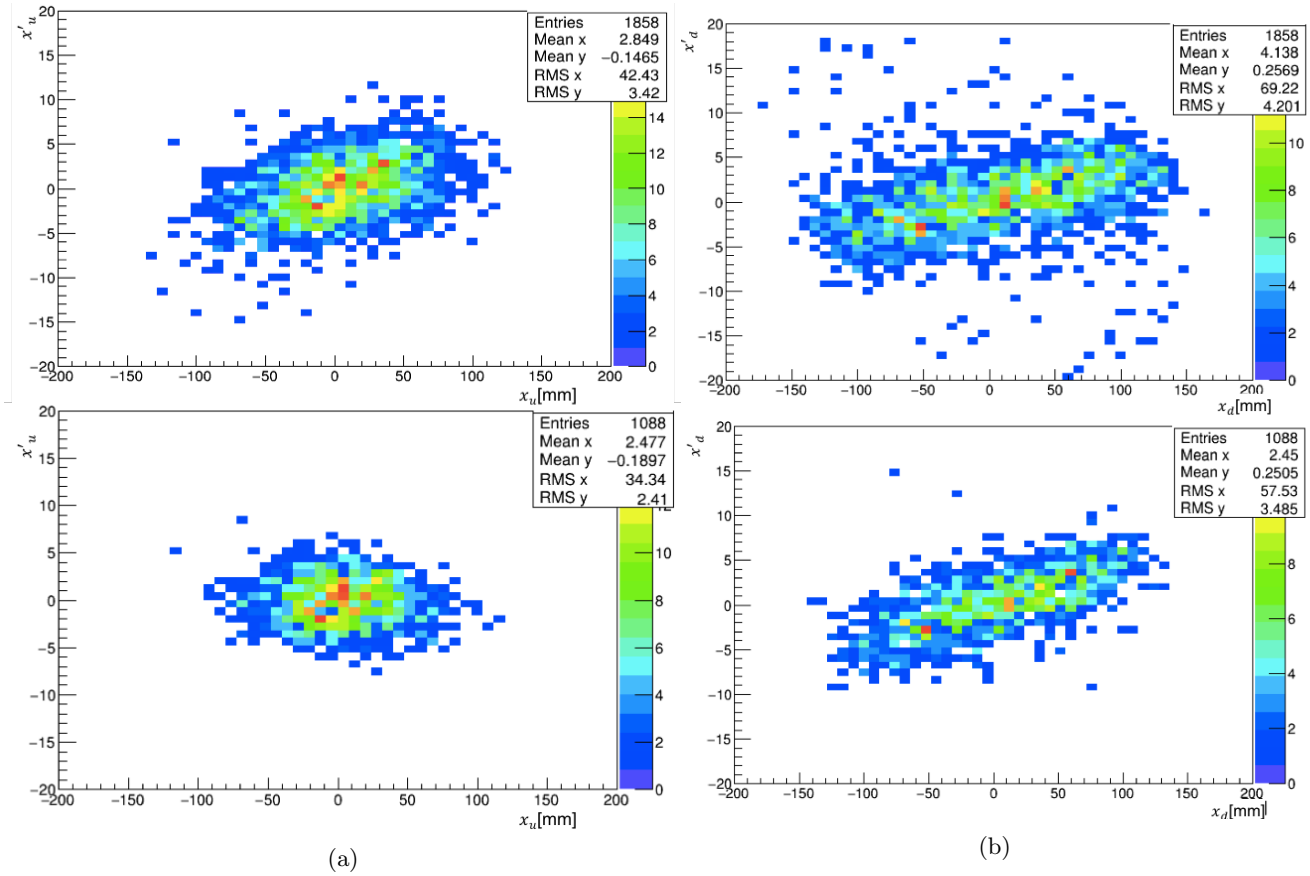

(a) (b)

Figure 5.23: Upper plots show trace space distribution in the $x - x'$ plane for upstream (a) and downstream (b) prior to application of scraping cut. Lower plots show the trace space after the cut is applied. The effect of the cut in the upstream trace space is to remove particles which are at extremes in either x direction. This reduces the beam spread (RMS) in both x and x'. This suggests the cut is removing the intended events from the sample and therefore reducing the likelihood that scraping will affect the measured misalignments. In the downstream trace space distribution the beam spread (RMS) in both x and x' is reduced and the many tracks which were originally at the momentum extremes have been removed from the sample. The distribution has much lower momentum spread as these events are the most likely to scatter from the beam

Figure 5.24 shows how the calculated matrix element M_{02} of the data sample changes as the value of n is increased. M_{02} is directly related to the drift space between the trackers and should = 18.94 mm. Figure 5.24 shows that for n < 1.5 the calculated M_{02} tends towards this expected value, however, always remaining below. Between $0 < n < 1$ the value of M_{02} converges just below the expected value at around 17 mm. Between $1.5 < n < 1.8$ the calculated M_{02} has large variations. This is due to statistical errors which become more significant now that the number of tracks is reduced. After $n = 1.8$ the number of tracks passing the cut is so small that no matrix can be calculated.

The fact that the closest the calculated M_{02} gets to the expected 18.94 mm, even at the chosen value of $n = 1$, is 17mm is a result of the limited data sample size. In reality a stricter cut is necessary and some of the tracks included in the end analysis may still scrape from the beam as a lower than necessary cut must be used. During the Summer 2016 running of "Step IV" larger quantities of data have been taken, increasing the amount of track-points allowing a stricter scraping cut to be applied helping lift the accuracy of the overall measured transfer matrix.

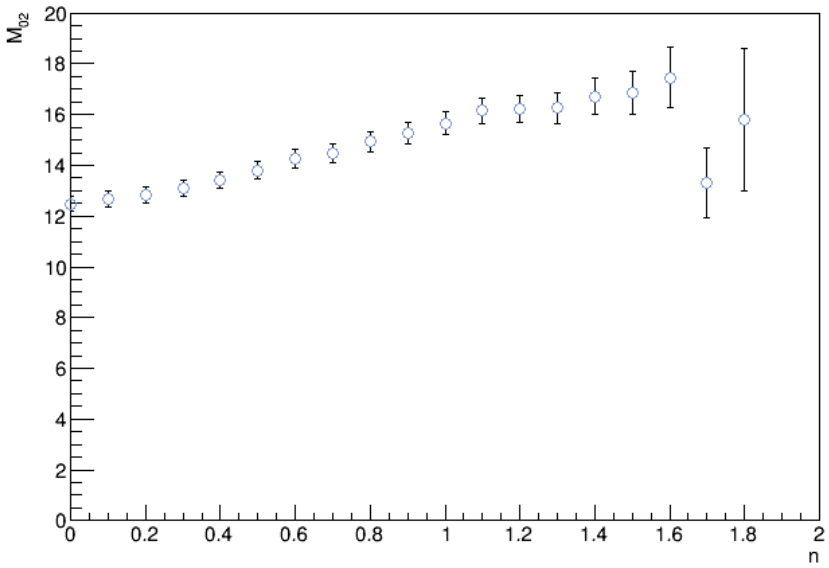

Figure 5.24: Plot showing how variations of the required number of $\sigma_{x,y}$ alters the calculated M_{02} value. This is directly related to the distance between the trackers and is expected to be around 18.94 mm. Any number $n > 1.8$ leads to the matrix calculation failing. Between $n = 0 - 1$ the value of M_{02} is shown to rise in the direction of the expected value but converges just under it at around 17 mm. After $n = 1.5$ the number of tracks is low and statistical variations cause large discrepancies. Therefore $n = 1$ is chosen for the final analysis. The calculated M_{02} here is an average over all muon tracks in the sample for each scraping cut setting.

Figures 5.25a to 5.25c show how the method residuals of the x co-ordinate vary when $n = 0, 0.5$, and 1.5. It is apparent for the case of $n = 0$, i.e. no scraping cut but all other cuts are applied, the distribution has a significantly larger σ when compared to Figure 5.20a. When the cut is then increased to $n = 0.5$ 206 events are removed. This is a relatively small percentage decrease of $\approx 11\%$, the fitted σ is reduced by ≈ 1 mm and the mean is moved closer to the unbiased case of 0. This is a result of track points in the long tails being eliminated. When n is further increased to 1.5, considerably more track points are eradicated from the sample.

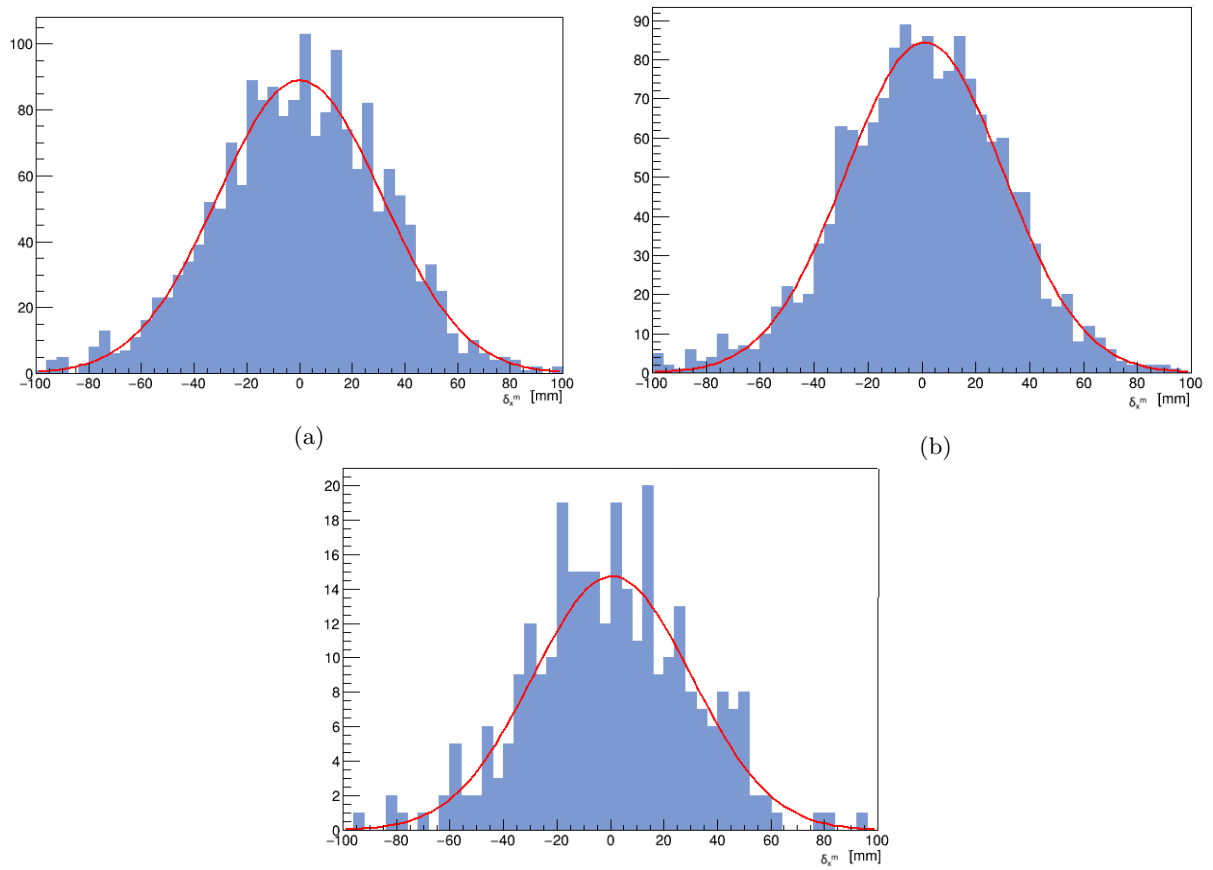

(a) (b) (c)

Figure 5.25: Method residuals, δx^m, for track points within data set 07417 when the scraping cut, Equation 5.106, is varied in (a) the cut is removed. A Gaussian fit gives a mean consistent with 0 and σ of 31.78 $\pm$ 0.73 mm, larger than in Figure 5.20a. The sample here has a total of 1858 tracks. The distribution remains consistent with the Gaussian fit with a χ^2/ndf of 0.99, suggesting no large bias was removed by the chosen cut of $n = 1$. In (b) $n = 0.5$, in comparison to the $n = 0$ case the mean is still consistent with 0 and the σ is found to be slightly smaller at 30.61 $\pm$ 0.8 mm. The overall decrease in events passing all cuts when moving from a cut of $n = 0$ to $n = 0.5$ is only around 200 events-with a total of 1602 events now remaining in the sample. The distribution remains consistent with the Gaussian fit with a χ^2/ndf of 1.15. In (c) $n = 1.5$. The distribution has a σ of 30.21 $\pm$ 0.9 mm however there are much fewer tracks in the sample than in the chosen $n = 1$ case with only 294 events passing all section criteria.

Nevertheless, statistical fluctuations are now more significant and the distribution is less consistent with the Gaussian fit. Only 294 events now remain in the sample. Consequently, it is decided that the optimum scraping cut for this data sample is to set $n = 1$. This is a compromise between scraping contributing significantly to the achievable resolution and having enough tracks to limit the impact of statistical errors.

The chosen scraping cut ($n = 1$) removes a total of 771 events from data set 07417. This is a relatively high percentage decrease of 41 %.

3 Energy loss:

As the particles move through the channel they may lose energy. This should not change the x' or y' of the particle, only the energy of the particle as, unlike scattering, energy loss does not change particle direction. The particle losses energy in the longitudinal plane, no transverse deflections should occur, therefore, no cuts were applied in this analysis to correct for energy losses.

5.9.3 Optimisation and Justification of P-Value Cut

Within the tracker reconstruction algorithm the "P-Value" provides a"goodness-of-fit" measurement for each SciFiTrack which has been reconstructed using the methods discussed in Section 5.5.1. For each fitted track a test statistic, χ^2 is computed, such that, for a track of length N,

$$\chi^2_{track} = \sum_{k=1}^{N} \chi^2_k. \tag{5.107}$$

This "goodness-of-fit" test can be made by calculating a probability $P(\chi^2, ndf)$, where ndf describes the number of degrees of freedom in the fit and is equal to the number of measurements (this is ideally 15, one per station, per plane) minus the number of parameters to estimate (5). This probability ($P(\chi^2, ndf)$) is the "P-Value" of the associated track. The "P-Value" describes the probability of observing a χ^2 as extreme, or more extreme, than the one measured if a uniform solenoidal field is assumed. Given this definition it is true that the higher the residuals of a track the lower the "P-value", and therefore, it is generally a good idea to exclude the tracks with the very lowest P-Values.

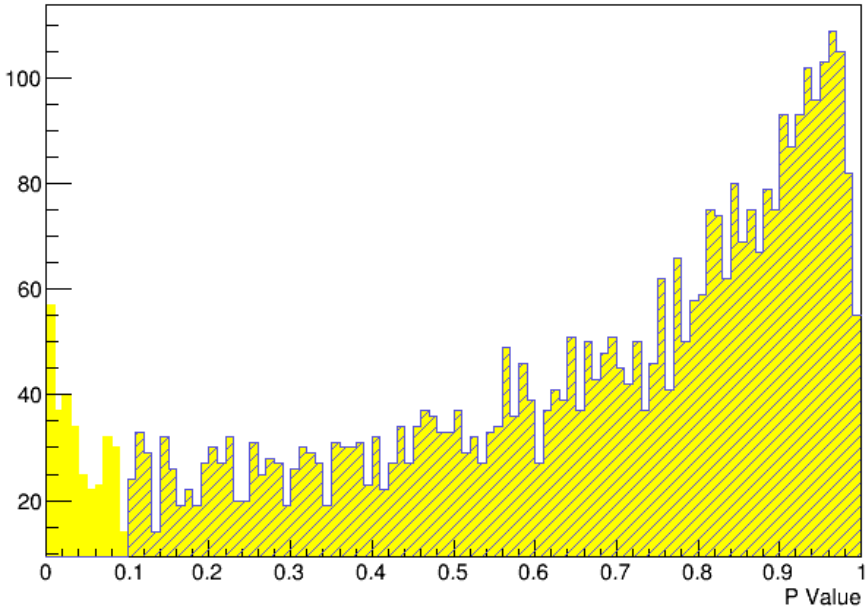

Figure 5.26: Distribution of track P-Values for data sample 07417 this plot was made following the TOF_{12} cut so tracks here are muons, given the cuts calculated efficiency. The distribution follows an exponential shape towards P-value = 1, with a slight dip just prior to that maximum. There is some excess of tracks at $0 \leq P \lessapprox 0.06$. This will be removed by the cut.

Figure 5.26 shows the distribution of track P-Values for the data sample. The distribution has a constant exponential shape. This is to be expected, the optimal, "flat," distribution is not possible due to the range of approximations and assumption made during development of the tracker reconstruction algorithms in MAUS. There is, however, a significant excess in the first bin compared to the neighbouring bin. This suggests that there may be some effect causing a small number of tracks to be poorly reconstructed. This could be explained by considering the non-Gaussian nature of Multiple Coulomb Scattering and energy straggling. The need for better understanding of Multiple Coulomb Scattering and Energy Loss was discussed in Section 2.5. In this

analysis these tracks will be removed by the P-value cut.

A P-Value cut was applied to the tracks such that only tracks with P-Value > 0.1 were selected. Figures 5.27a to 5.27c show how the method residual distribution for the derived downstream x co-ordinate is altered as the strictness of this P-Value cut is varied.

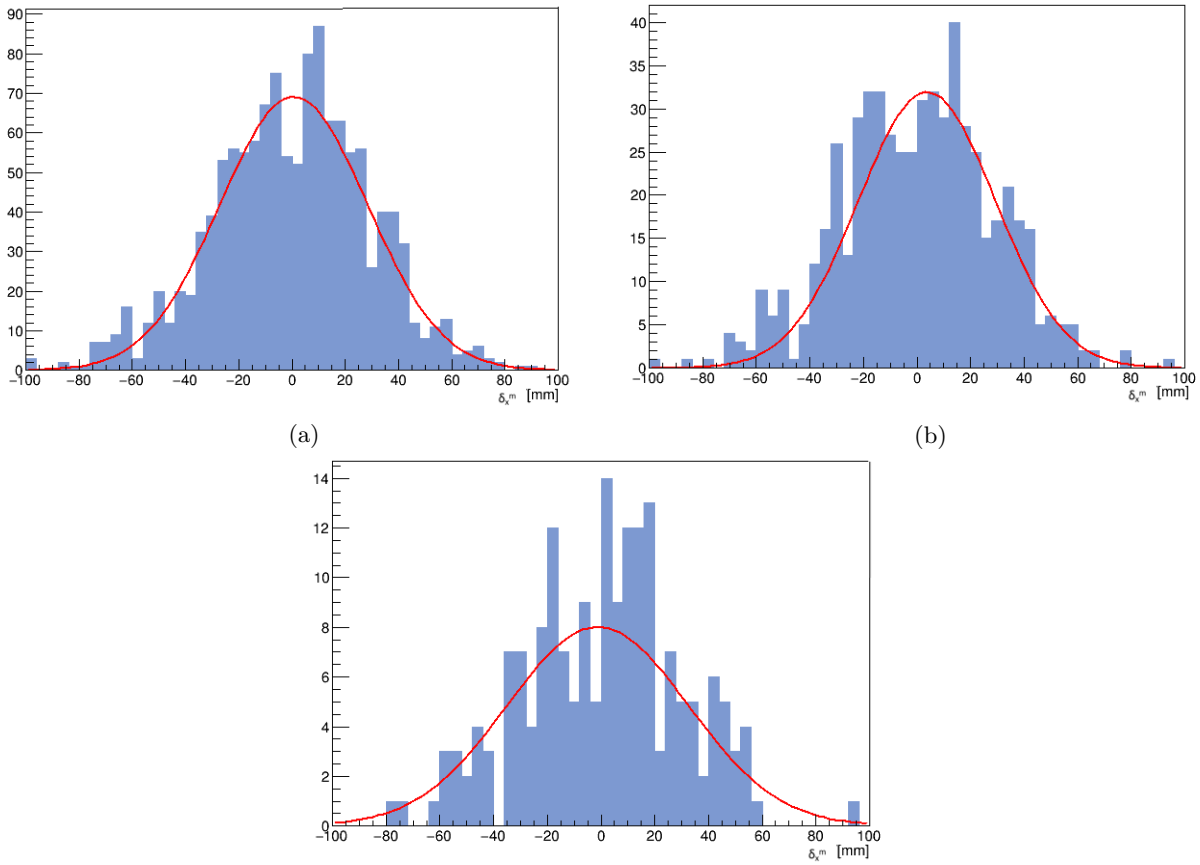

Figure 5.27: Distribution of method residuals, δx^m, for track points obtained from the data sample when (a) no P-value cut is applied but all other section criteria remain in place, including the scraping cut which has removed a large number of the events from this distribution. A Gaussian fit gives a mean consistent with 0 and a σ of 28.75 $\pm$ 1.2 mm. A total of 1289 events remain in this sample. The distribution is now less consistent with the Gaussian fit with a χ^2/ndf of 1.87. In (b) a much stricter P-Value > 0.5 is applied along with all other criteria. Clearly the number of events in the sample is reduced, with only 580 events passing all cuts. The distribution has lost its Gaussian shape and the cut is deemed too strict to be used as the statistical errors per bin have become too significant to make accurate conclusions. A fit to the distribution gives a mean shifted slightly from 0 to 0.61 ± 0.2 and a σ of 29.42 $\pm$ 0.75. The distribution remains fairly consistent with the Gaussian fit, a χ^2/ndf of 1.25 is shown. In (c) an even stricter P-Value > 0.8 is applied along with all other cuts. Clearly the number of events in the sample is very low now, with only 185 events passing all cuts. The distribution has lost some of its Gaussian shape and the cut is deemed to strict to be used as the statistical errors per bin will be too significant to make accurate conclusions.

In the case of no P-value cut the distribution remains Gaussian in shape with fit parameters and statistical errors similar to that in the chosen P-value > 0.1 case (see Figure 5.20a). It is clear from these three figures that even in the strictest case of P-Value > 0.8, although statistical deviations become more significant, the distributions do not lose their Gaussian shape and no obvious bias or excess of events is introduced or removed.

Despite these plots showing that little bias or overall obvious systematic feature is removed by this cut

the analysis still requires P-Value > 0.1. It is believed this is a good idea, as although not a strict cut, it will provide some insurance against any reconstruction errors or any extremely poorly fitted tracks which would disrupt and create inaccuracies in the final transfer matrix calculation. Tracks with low P-Values could be a result of random electronics noise, muon decays or pions, all of which will cause inaccuracies in the calculated transfer matrices if included in the fitted data. The same P-Value cut is used for both data and reconstructed Monte Carlo. A validation of the derivation of the P-Value for both Monte Carlo and data is presented in [224]. It is shown that the MC and data P-value distributions show close agreement, and both will possess the same excess at low P-Values.

5.9.4 Straight Tracks Conclusions

It may be concluded from the results presented throughout Section 5.8 and the plots shown in Figure 5.15 that the fitting method has been successful. It is shown to re-create the expected results for straight tracks passing through a "field-off" Focus Coil within the estimated errors, with an accuracy of $< 1\sigma_{stats}$ in the majority of cases, for both Monte Carlo samples and data. There is still, however, some discrepancy between the Monte Carlo samples and data. Further discussion of this systematic uncertainty is given in Section 5.12.

No viable statistic test has been produced to help quantify these variations. [225] and [226] give an overview of various statistical techniques used for multivariate analyses both in particle physics and beyond. Most of these techniques involve calculating a "goodness of fit" between some measured pdf i.e. $y(\vec{x})$ to some parent pdf i.e. $f(\vec{x})$. This describes testing "goodness of fit" for the mapping of many variables to one variable and not doing a simultaneous "goodness of fit" between a system of pdf's i.e. $y_1(\vec{x})), y_2(\vec{x})...y_n(\vec{x})$ to see if it is consistent with some parent system, i.e. $f_1(\vec{x}), f_2(\vec{x})....f_m(\vec{x})$, which is the situation in this analysis. Therefore, no goodness-of-fit value was derived here to quantify the total deviation between data and expectation.

The method residuals for all four co-ordinates for both Monte Carlo and data samples are consistent with Gaussian distributions centred on 0. The measured RMS values of the distributions of these residuals indicate that, within the limits of the detector, the transfer matrices can be accurately determined to a precision which will allow estimates of the misalignment of the Focus Coil to be carried out.

Various cuts have been applied to the data to achieve this level of accuracy and these are detailed in Section 5.6.1. These will stay in place throughout the following analysis, with the exception of the TOF_{12} range cut which will vary depending on the input momentum of the beam in order to best select the purest muon beam.

5.10 Analysis of "Field-on" Data

In the preceding section the fitting algorithm was verified for a zero-current Focus Coil run. It will now be applied to data in which the Focus Coil has a non-zero current. Once the transfer matrix is calculated it is

possible to establish whether any physical misalignment has occurred at the Focus Coil relative to the beam axis (z) using the method outlined in Section 5.3.1.

In the subsequent analysis the Focus Coil current was set to +100 Amps. Additional data was taken in the late Summer of 2016 and will contribute to the final publication of misalignment measurements, however, the analysis presented in this thesis will focus only on the +100 Amp data taken in December 2015.

5.10.1 Data Samples 07534-35: +100Amps

Two runs (07534-07535) obtained during the "Step IV" commissioning stage of MICE were utilised in the following analysis; muons with an initial momenta 200 MeV/c were selected prior to entering the cooling channel. The beam line settings for quadruples (Q1-9) and dipoles (D1-2) as well as the decay solenoid (DS) are summarised in Table 5.3. During this study the Focus Coil is operated in "Flip" mode. It follows, therefore, from the discussion presented in Section 2.3.7, that no net change angular momentum is produced in the Focus Coil module.

When MICE operates in "Flip" mode the two coils within the Focus Coil structure are set to have opposing polarities and, therefore, produce Larmor angle rotations in opposing directions. Thus, the rotation produced by the positive coil is cancelled by that of the negative coil, resulting in a net rotation of "0." Consequently, the x and y components are expected to be de-coupled.

Magnet	200 MeV/c : 07534-35 Current/[A]
D1	202.8
D2	100.4
DS	3.9 T
Q1	57.8
Q2	105.7
Q3	64.6
Q4	177
Q5	237.3
Q6	157.3
Q7	157.7
Q8	238.6
Q9	203.8
FC	+100
FC Mode	Flip
SSD	All 0
SSU	All 0

Table 5.3: Table listing the settings of the beam line magnets including the quadrupole magnets (Q1-Q9), the dipoles (D1-D2) and the Decay Solenoid (DS) for samples 07534 and 07535. Figure 3.2 gives a schematic of the position of these magnets relative to the MICE cooling channel. The Focus Coil (FC) is set at a current of +100A. The spectrometer solenoids, surrounding both trackers (SSU and SSD) were both off in this configuration.

Figure 5.28 shows the distribution of times take for every particle in the combined sample to traverse from TOF1 to TOF2. Three distinct regions are visible. The largest and most densely populated muon peak, centred $\approx$ 31 ns corresponds to the "muon" peak. Additionally, there is some apparent pion contamination

resulting in a peak centred $\approx$ 35 ns, and the significantly smaller decay electron peak, centred $\approx$ 27 ns. Particles with $31 < TOF_{12} < 31.7$ ns are selected for this analysis. All other tracker resolution and particle identification criteria, outlined in Section 5.6.1, will remain enforced in this study.

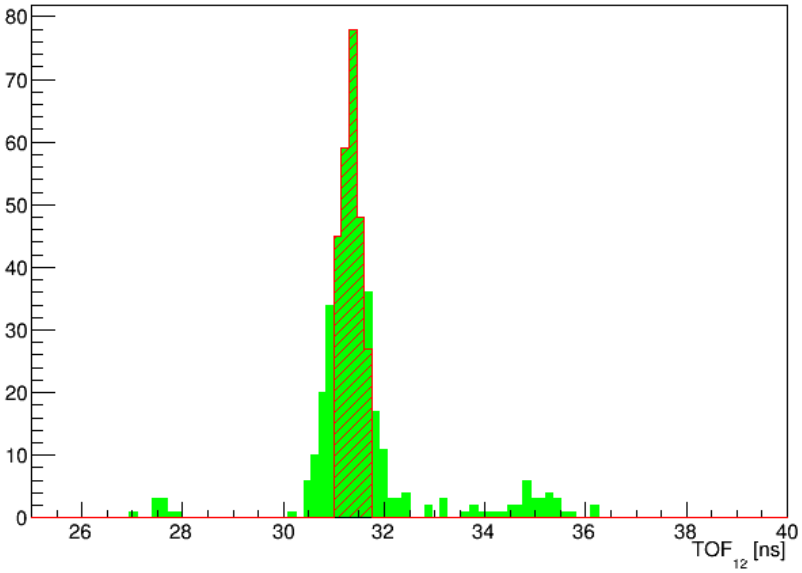

Figure 5.28: Distribution of the times taken for each particle to transit between the upstream TOF1 detector and downstream TOF2 detector for combined data set 07534-07535. In these runs incoming particles have a preselected p_z of 200 MeV/c. The Focus Coil has an operational current of +100 A throughout. This plot was produced after all tracker resolution cuts, with the exception of the scraping cut, were enforced. The shaded region represents the selected particles, corresponding to a window of $31 < TOF_{12} < 31.7$ ns .

5.10.2 Monte Carlo Simulation for Focus Coil - "Field-on"

Two Monte Carlo simulations, comparable to the data run, are produced: a true Monte Carlo, containing MCEvents and a "digitised", reconstructed, Monte Carlo. The geometry used to produce the Monte Carlo mimics that used for runs 07534-35 and includes knowledge of the current tracker calibration and modelling of noise and dead channels. Direct comparison can then be made between reconstructed-"digitised"- Monte Carlo and real data. Any mis-alignments at the Focus Coil will become apparent through comparing the calculated matrix elements. Figure 5.29 shows the TOF_{12} distribution for tracks in the reconstructed Monte Carlo sample. A TOF_{12} selection of $31 < TOF_{12} < 31.7$ ns is used.

5.10.3 Cut-flow For Data and Reconstructed Monte Carlo Tracks

Table 5.4 presents the cumulative effect of enforcing each selection criteria on the total number of tracks in the samples.

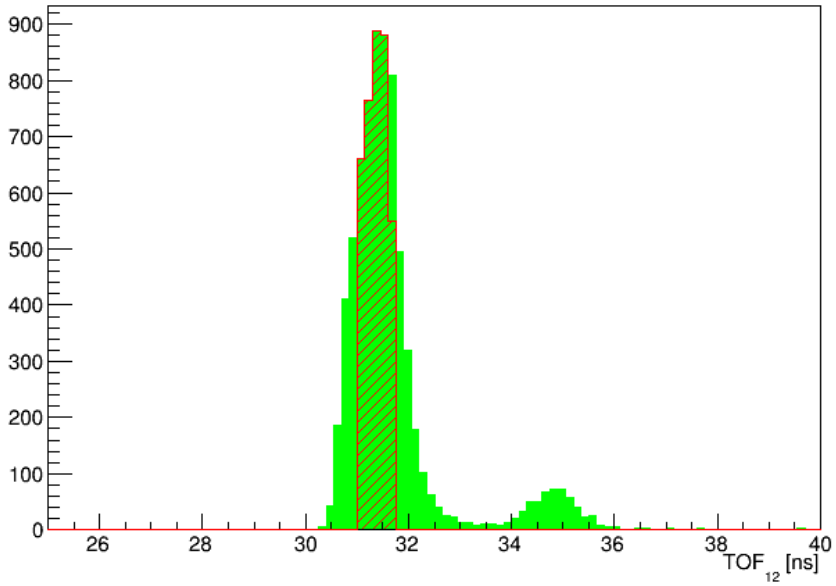

Figure 5.29: Distribution of the times taken for each particle to transit between the upstream TOF1 detector and downstream TOF2 detector for reconstructed Monte Carlo tracks travelling through a geometry comparable to that used in runs 07534/35. In this sample the incoming particles have a preset p_z of 200 MeV/c. The Focus Coil has an operational current of +100 A throughout. This plot was produced after all tracker resolution cuts, with the exception of the scraping cut, were enforced. The shaded region shows tracks selected for this analysis. These correspond to the bins with highest muon purity. A selection window of $31 < TOF_{12} < 31.7$ ns is chosen.

Criterion	Data	Recon. MC
Has Space Points in Tracker 0 and 1	2253	38898
Has hits in both TOF1 and TOF2	2250	38896
Has space points in all 5 stations of tracker 0	2151	38625
Has space points in all 5 stations of Tracker 1	2012	38702
Has 15 clusters in Tracker 0	1177	17441
Has 15 clusters in Tracker 1	811	17559
Is in assumed muon peak in TOF_{12} time	285	3745
Passes P Value Cut > 0.1	257	3702
Has- 10 track points in both trackers	235	3699
$\sqrt{(x+\sigma_x)^2+(y+\sigma_y)^2} < 150$	233	3557
After all Cuts applied	**233**	**3557**

Table 5.4: Table showing the cumulative effect of enforcing each cut on the number of tracks remaining, broken down cut-by-cut, for the data samples 07534 and 07535 data and corresponding reconstructed Monte Carlo. All criteria are outlined in Section 5.6.1. The data has very few tracks remaining, as a result relatively large statistical errors are anticipated on the derived matrix elements and as a result the misalignment calculation.

5.10.4 Beam Distribution for FC +100Amps

Figures 5.30a to 5.33b show the distributions of both upstream and downstream particle co-ordinates for the combined data set. The total number of data tracks, after all cuts are applied, is 233. It is therefore expected that statistical errors will be relatively large in this study.

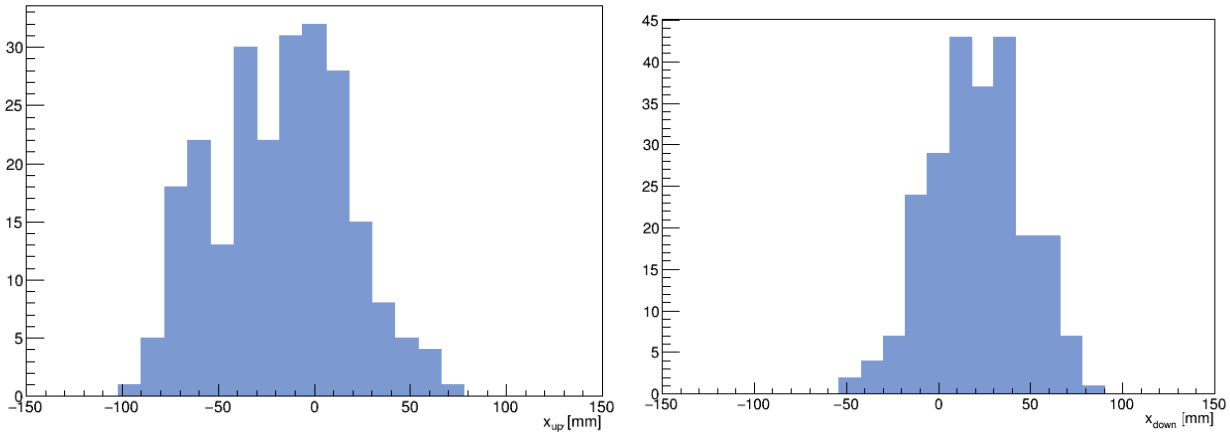

(a) (b)

Figure 5.30: Distributions of particle x co-ordinate after all selection criteria, including the scraping cut, are applied for data sets 07534 and 07535. Both samples have an operational Focus Coil current of +100A. (a) Upstream: The distribution has mean = -12.65 ± 1.39 mm and RMS = 34.2 ± 2.1 mm. (b) Downstream: The distribution has a mean of 17.72 ± 2.43 mm and RMS of 37.37 ± 4.32 mm. The quoted errors are purely statistical.

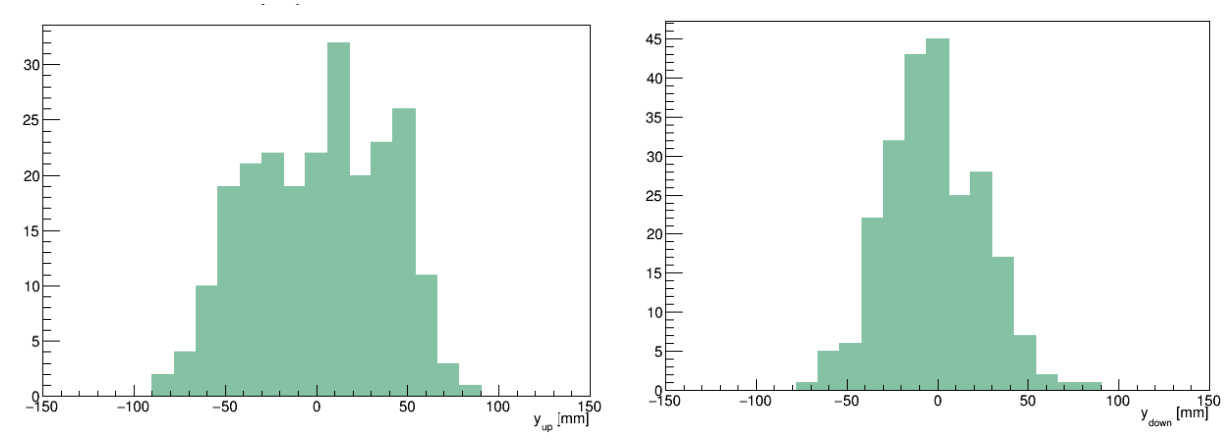

(a) (b)

Figure 5.31: Distribution of particle y co-ordinate after all selection criteria, including the scraping cut, are applied for data sets 07534 and 07535. Both runs have an operational Focus Coil current of +100A. (a) Upstream: The distribution has a mean of -14.85 ± 1.32 mm and RMS of 40.70 ± 2.89 mm (b) Downstream: The distribution has a mean of -12.65 ± 1.34 mm and RMS = 34.2 ± 4.27 mm. The quoted errors are purely statistical

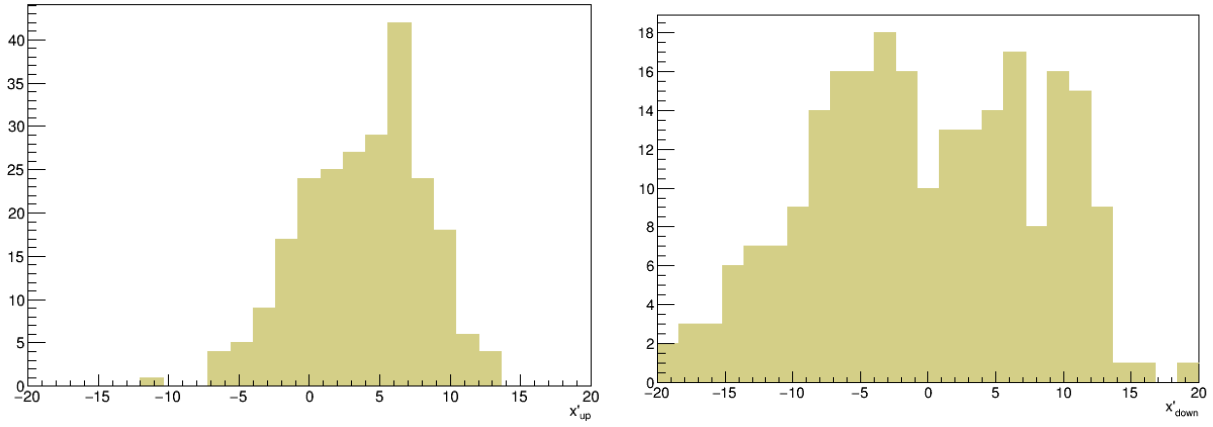

(a) (b)

Figure 5.32: Distribution of particle x' co-ordinate after all selection criteria, including the scraping cut, are applied for data sets 07534 and 07535. Both runs have an operational Focus Coil current of +100A. (a) Upstream: The distribution has a has mean = 3.78 ± 0.34 and RMS=4.29 ± 0.01(b) Downstream: The distribution has a mean of -1.04 ± 0.34 and RMS = 9.22 ± 0.23. The quoted errors are purely statistical

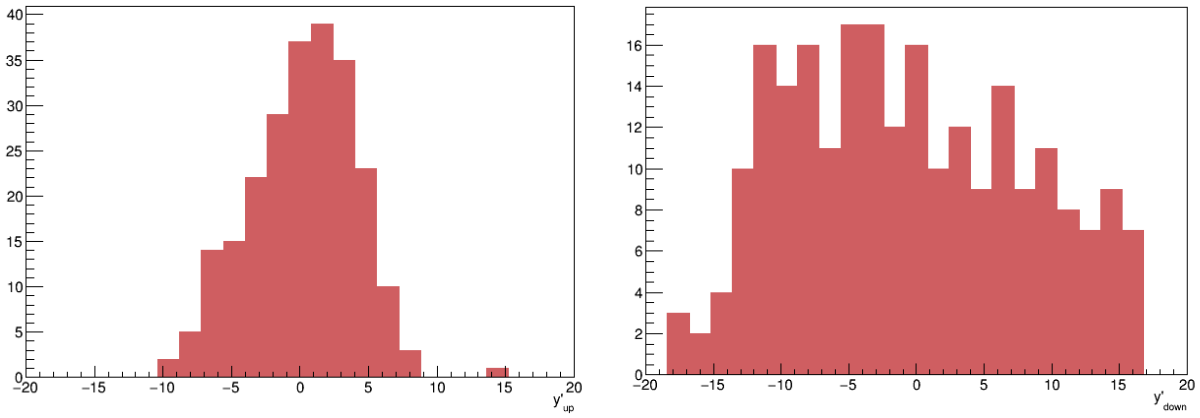

(a) (b)

Figure 5.33: Distribution of particle y' co-ordinate after all selection criteria, including the scraping cut, are applied for data sets 07534 and 07535. Both runs have an operational Focus Coil current of +100A. (a) Upstream: The distribution has a has a mean 0.92 ± 0.45 and RMS = 3.71 ± 0.98 b) Downstream: The distribution has mean 0.70 ± 0.67 and RMS = 10.93 ± 1.34. The quoted errors are purely statistical

5.11 Calculating Focus Coil Misalignment

5.11.1 Fitting Procedure

The next, and definitive step in this study, is to use the derived transfer matrix, $\underline{\underline{M}}^m$, calculated from data sets 07534-35, to place limits on the transverse misalignment, taking into account both position and angular misalignment, of the Focus Coil axes relative to the nominal beam axis.

This is accomplished by constructing a succession of Monte Carlo simulations, commencing with a 0-misaligned geometry, and calculating the analytical transfer matrix, $\underline{\underline{M}}^a$, for each geometry. MINUIT [227] is then employed to minimise the calculated total "score function" (S) :

$$S = \sum_i \sum_j \chi^2_{i,j}, \tag{5.108}$$

where

$$\chi^2_{i,j} = \frac{(M^a_{i,j} - M^m_{i,j})^2}{\sigma^2_{i,j}} \tag{5.109}$$

by moving the Focus Coil in the x, y directions as well as rotating by θ_x and θ_y on each iteration of the fitting procedure. $\underline{\underline{\sigma}}$ here represents a 4×5 matrix of statistical error on the derived transfer matrix elements. The aim is to minimise the total χ^2 or "score function" over iterative corrections to the Monte Carlo. Each iteration aims to make the Monte Carlo configuration more "data-like."

This permits a limit to be placed on the amount of misalignment between the Focus Coil's magnetic axis and the nominal central, beam, axis. The geometry which gives MINUIT's "best fit" can then be used to quote a measurement of the Focus Coil's transverse misalignment. This fit will be an overall fit and takes into account all 20 transfer matrix elements.

As discussed in Section 5.3.1, the fitting algorithm proceeds in a number of steps, fitting for three different quantities separately:

1. Attempt to fit the coil current, by looking at the upper quadrant of the focussing part of the transfer matrix terms, M_{01}, M_{02}, M_{11} and M_{12}.

2. Attempt to fit x and x' by looking at the transfer matrix elements corresponding to a horizontal kick i.e. M_{00} and M_{10}.

3. Attempt to fit y and y' looking at the transfer matrix elements which correspond to a vertical kick i.e. M_{02} and M_{03}.

For each iteration of the fitting routine, therefore, three "sub-fits" are carried out and the "best fit" of the overall transfer matrix is updated between each of these three "sub-fits." The end calculation of the optimum location of the magnetic axes and therefore the calculated misalignment of the Focus Coil takes into account both misalignment terms in x and y as well as rotational offsets in θ_x and θ_y and the effects this will have on the scale factor i.e. effective magnetic field acting on the particle with each change in Focus Coil position.

MINUIT works by calculating the score (χ^2) function for each parameter (P_i) (i.e. the focus coil current and transverse position). MINUIT calculates numerical derivatives of χ^2 with respect to each parameter. The fit is updated at each step dP_i and moves in the direction which minimises the score (χ^2) value. The more parameters in the fit the longer MINUIT will take to calculate the derivatives. As the numerical calculation of the transfer matrix is reasonably CPU intensive, this makes the algorithm run slowly. An estimate of the coil's position takes around 1.5 hours to compute.

Splitting the fitting into just three sub-routines helps save some CPU time. However, by carrying out the fitting in the three stages described it is assumed that only certain P_i's can affect certain transfer matrix

terms, for example, the fit to the focussing terms is optimised by varying current. In doing so it is assuming that the misalignment cannot affect the focussing terms. If the x and y misalignment did affect these terms then these misalignments would have to be included in this fit too causing the fitting algorithm to have further complexity. However, given the discussions throughout Section 5.1-5.3 it can be shown that the focussing transfer matrix elements are indeed only sensitive to variations in current parameter. Therefore, the current can be selected based on these terms alone; and the fitting routine can then go on to find the "kick" terms and misalignment parameters.

5.11.2 Fitting Outcome

Figure 5.34 shows an array of plots arranged according to the corresponding position in the transfer matrix. The blue points are the derived transfer matrix elements for the combined run 07534-07545 data sample. The TOF_{12} range has, once again, been sub-divided into 5 equally wide TOF_{12} bins. The error bars represent the statistical errors which are calculated as discussed in Section 5.8.8. **The red line represents the final output of the mis-alignment algorithm obtained through applying Equation 5.109 to the data sample in each TOF_{12} bin separately. The optimised χ^2 takes into account the horizontal, vertical and focusing terms and corresponds to the matrix of the Focus Coil with the mis-alignment displayed in Table 5.5. The "fitted line" is therefore not a fitted line to the data points shown in each plot but rather represents a projection of the single matrix element derived from the optimisation routine outlined in Section 5.11.1. This routine takes into account the full $4D \rightarrow 4D$ map in all TOF_{12} bins simultaneously.**

The plot positions in this array correspond to the elements they represent in the transfer matrix:

$$\underline{\underline{M}} = \begin{pmatrix} M_{00} & M_{01} & M_{02} & M_{03} & M_{04} \\ M_{10} & M_{11} & M_{12} & M_{13} & M_{14} \\ M_{20} & M_{21} & M_{22} & M_{23} & M_{24} \\ M_{30} & M_{31} & M_{32} & M_{33} & M_{34} \end{pmatrix}.$$

Appendices B and C give the measured transfer matrices for the data and optimised misalignment fit respectively. The gradient of these fit lines corresponds to the elements dependence upon TOF_{12} and therefore upon p_z and are presented in Appendix D (Table D.1). The first column (red) represents the constant offset terms for each fit. These give the largest contribution to the calculated mis-alignment values for each co-ordinate. Considering now the remaining 4×4 matrix it becomes apparent that the on-diagonal plots are equivalent, within errors. These terms represent the mapping of each downstream co-ordinate to the same co-ordinate upstream. The two focussing (i.e. the upper left and lower right (green)) quadrants are equivalent. The angular momentum terms (i.e. upper right and lower left (purple) quadrants) represent the

couplings between x_d, x'_d and y_u, y'_u and vice versa and are all ≈ 0, within errors, suggesting no correlation and therefore, by definition no net rotation in the beam for this run. This is to be expected given the Focus Coil was operational in Flip mode and both the spectrometer solenoids were off during runs 07534-35.

Table 5.5 shows the values for $dx, d\theta_x, dy, d\theta_y$ where $d\theta_x$ and $d\theta_y$ are angular offsets relative to the beam axis (z) and the current scale factor, I which were used in the geometry which produced the optimum fit from MINUIT. These are the measurements of misalignment at the Focus Coil for these data samples. I is expected to be +100 for a +100A FC setting which is confirmed by the fitting, within errors. The user guide for MINUIT, [227], gives detailed description of how the software parameterises fitting errors. The errors listed take into account the statistical errors of the data itself which were given to MINUIT in the form of the $\underline{\underline{\sigma}}$ matrix as well as combined relative errors between points in the sub-plots which were used in the fitting routines. Table 5.5 shows that, within statistical errors, the measured misalignment from data set 07534 and 07535 is consistent with the coil being correctly aligned.

dx/[mm]	θ_y /[rad]	dy /[mm]	θ_x /[rad]	I/[A]
-6.07 ± 9.79	0.017 ± 0.030	6.64 ± 11.00	0.020 ± 0.024	101.69 ±10.84

Table 5.5: Table shows the calculated values of translational and rotational offsets of the Focus Coil magnetic axes relative to the assumed aligned axis which would lie along the beam axis. The resulting values are consistent, within error, with there being no mis-alignment in the focus coil either horizontally or vertically. The calculated current is also consistent with the expected current of +100A within the errors provided by the fitting routine (MINUIT). These errors take into account the statistical error inherent in each data point as well as the relative error between points in the plots used for the MINUIT fitting procedure.

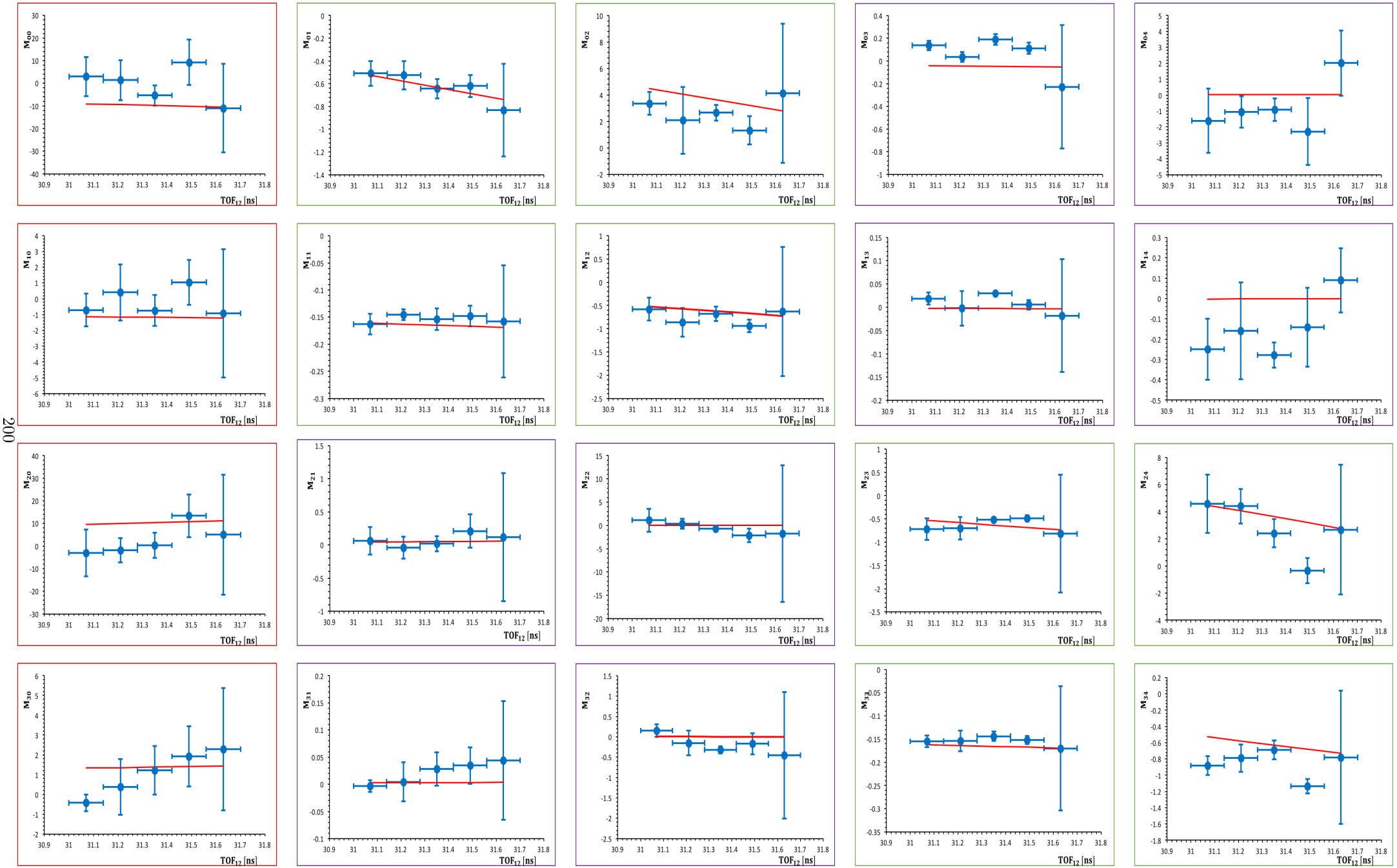
M00
M01
M02
M03
M04
M10
M11
M12
M13
M14
M20
M21
M22
M23
M24
M30
M31
M32
M33
M34
TOF12 [ns]

Figure 5.34: Plots showing the variation in calculated transfer matrix elements with TOF_{12} time. The elements position corresponds to its position in the transfer matrix definitions. Each plot is a projection of a single element. The region in TOF_{12} is selected to have the highest muon purity and is then sub-divided into 5 equally sized bins. The transfer matrix has been calculated independently for particles in each of these 5 bins. The red line shows the projection of the MINUIT fit to the entire data sample which gives the optimised Focus Coil position and therefore the measured misalignment. This fit takes into account all elements of the transfer matrix for each TOF_{12} bin. **The red line therefore represents MINUITs overall optimised fit to the total data sample projected onto each matrix element. These plots serve to help visualise how well the fitting routine presented in this thesis represents the data only and are not direct fits to these plots. The red line is not a fitted line to the data points shown in each plot but rather represents the outcome of the misalignment fitting routine which took into account the each TOF_{12} bin's transfer matrix as a whole and found a minimised χ^2 which incorporated knowledge of each of the full $4D \rightarrow$ 4D mappings.**

5.11.3 Monte Carlo of Misalignment

In order to cross-check the data with the derived misalignment values and quantify any further sources of systematic deviation in the method an "updated Monte Carlo" was generated. This used an "updated" geometry which included the values for dx, dy and $d\theta_x$, $d\theta_y$, presented in Table 5.5 to generate Monte Carlo MCEvents and ReconEvents. Figure 5.37 shows the resulting measured transfer matrix elements for these updated Monte Carlo samples along with the data, again as functions of TOF_{12}. The two Monte Carlo samples are consistent with one-another and in all cases the transfer elements show little variation with TOF_{12} which is to be expected given the narrow TOF_{12} window and the decoupling between transverse and longitudinal motion in the Focus Coil. It is apparent that the statistical errors dominate the data sample and as a result the data shows larger bin-to-bin variations. The statistical errors can only be reduced by increasing the size of the sample. Accounting for deviations between the data and these updated Monte Carlo samples will be the focus of the following section.

5.12 Further Error Analysis

Figure 5.37 shows that both the true and reconstructed Monte Carlo are consistent with each other, and, in most cases are identical. For most TOF_{12} bins the data agrees with the Monte Carlo within $1\sigma_{stats}$. However, in some cases there are discrepancies between the matrix elements calculated from Monte Carlos and data. There are a number of possible sources of these discrepancies:

1. **Variation in Coil Size and Shape** - The effective magnetic field is heavily dependent upon the size, shape and number of turns within the Focus Coil. If these were mis-calculated then the effective current in the Monte Carlo would differ from the true current and, as a result, the magnetic field acting in reality may not be consistent with that in the Monte Carlo.

   The importance of cross-checking the set current with the effective current acting upon the muons in the Focus Coil was discussed in Section 5.3.6. Consideration was given to the current dependent (focusing) terms within fitting procedure. The effective current determines the effective magnetic field acting on the particle at the Focus Coil and is dependent upon the the coil size, shape and the number of turns within it. The various engineering uncertainties related to Focus Coil geometry were outlined in Section 5.3.6. Precise knowledge of the length, thickness and inner radius of the coils is necessary to exclude systematic uncertainty which will result from these engineering concerns.

   The impact of a change in size and shape of the Focus Coil on the calculated transfer matrix calculations has been considered. In order to determine how sensitive the fitting algorithm is to the coil dimensions, a series of Monte Carlo simulations have been generated using the 07534-35 geometry but with variations in length, thickness and inner radius of the Focus Coils. Figure 5.35 gives a visual representation of what is meant by the length, thickness and inner radius of a given magnet within the Focus Coil.

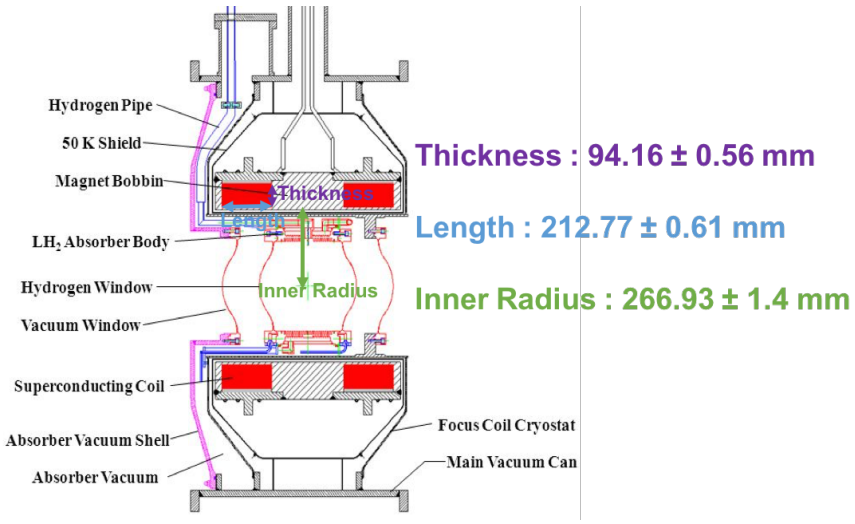

Figure 5.35: Schematic of the Focus Coil with the various dimensions labelled. The coils are shown in red here inside the cryostat of the AFC module. The coloured arrows indicate the corresponding dimension. The values and tolerances quoted on the right are taken from [180] and are obtained from a measured field map. The theoretical Focus Coil field is tweaked to get best agreement between measured field map and theoretical field map. In this study, each of the coil dimensions was changed by either +5% or −5% the aim being to estimate the impact of any miscalculation of these dimensions on the derived misalignment measurements.

Each of the coil dimensions is changed by either +5% or −5% and a Monte Carlo truth sample is generated. The rest of the geometry and beam settings remain the identical to run 07534 and 07535. The measured misalignments, documented in Section 5.11.1, have been placed into the geometry, consequently, the results of the alignment calculation should be comparable to those in Table 5.5. Table 5.6 displays the calculated misalignments for these altered coil geometries:

Δ	dx/[mm]	θ_y /[rad]	dy /[mm]	θ_x /[rad]	I/[A]
Δr **+5%**	-4.38± 0.476	-0.020 ± 0.031	0.760 ± 0.530	0.020 ± 0.007	84.29±0.26
Δr **-5%**	-4.90 ± 0.482	-0.020 ± 0.031	0.345± 0.339	0.020 ± 0.007	85.79±0.38
ΔT**+5%**	-7.00± 0.459	0.013 ± 0.026	10.59 ± 0.32	0.020 ± 0.026	98.18±0.52
ΔT **-5%**	-8.34 ± 0.52	0.007 ±0.025	10.67±0.57	0.020 ±0.028	97.89±0.36
ΔL **+5%**	-6.83±0.53	-0.012 ±0.031	10.23 ±0.30	0.020 ±0.028	98.53±0.28
ΔL **-5%**	-8.09± 0.29	0.020±0.031	9.79±0.40	-0.02 ± 0.035	98.36±0.32

Table 5.6: Table showing the effects of changing the inner radius (r), thickness (T) and length (L) of the coils within the Focus Coil by ± 5% on the calculated misalignments.

The statistical errors are much smaller compared to the data sample. This is to be anticipated given the relative sizes of the samples. The results, presented in Table 5.6, demonstrate that a mis-calculation of any of the 3 dimensions will have little effect on the calculated rotational offset. Nonetheless, a deviation in the inner radius results in a misalignment in y of ≈ 0 mm and a smaller, but still significant, offset in x. Additionally, variations in the thickness or length of the coils results in misalignments, much closer expectation, denoted by the outcome of the unaltered coils listed in the first row. The changes in

thickness and length of the coil have only small effects on the scale factor (effective current), however, changes in the inner radius has a much larger effect.

It can be concluded that engineering uncertainties, due to lack of precise knowledge of the coil dimensions, act as a systematic uncertainties in the fitting routine and have some influence on how accurate the misalignment calculations are. Further study may be necessary to ensure that the coil dimensions are accurately described within the MAUS geometry. The total systematic error on the derived matrix elements for each TOF_{12} bin resulting from these engineering uncertainties, dM_{ij}, can be calculated such that,

$$d(M_{ij}) = \frac{\Delta(M_{ij})}{\Delta C} \times dC, \tag{5.110}$$

where C denotes either T, L or r, dC denotes the corresponding engineering tolerances and ΔM_{ij} denotes the difference between the derived M_{ij} for the expected coil dimensions, derived from true Monte Carlo, and those from the altered true Monte Carlo. Each dC can be calculated from Table 1 in [180]: for ΔT the uncertainty is 0.56 mm, for ΔL the uncertainty is 0.61 mm and for Δr it is 1.4 mm.

The error bars in the plots in Figure 5.37 show how taking into account the systematic uncertainty which results from engineering errors affects the matrix elements calculated from data. It is evident that the total contribution from these systematic errors is small relative to the statistical errors on each bin.

2. **Particle Mis-Identification** - The TOF_{12} cut may not be 100% efficient. It is conceivable that some pions or decay electrons are present in the data. This should, however, be a small proportion of the overall particles in the sample given the narrow TOF_{12} selection window. The purity (ϵ_{TOFPID}) of the selected TOF_{12} region can be evaluated using the truth Monte Carlo (MCEvents) sample, such that

$$\epsilon_{TOFPID} = \Big(\frac{N_{\mu}^{true}}{N_{e+\mu+\pi}^{true}}\Big)_{31}^{31.7} \tag{5.111}$$

where N^{true} denotes the number of events of each particle type which remain after the TOF_{12} cut is applied. For the truth Monte Carlo the TOF_{12} time must be derived via matching the track to its corresponding reconstructed Monte Carlo track.

ϵ_{TOFPID} will be a direct measure of the cut's efficiency. For runs 07534-35 it is found that the electron contamination is found to be 0, however, there is a pion contamination of 1%. The total average error due to mis-identification of particle tracks is, therefore, 1%. This leads to an estimated 2 background events in the end data sample after all other cuts. Consequently, the TOF_{12} cut is a relatively efficient way of discriminating from decay electrons and has a 99% efficiency for pion rejection. Given the

small number of pions expected in the sample it is unlikely that this is the sole culprit of the observed deviations in the figures in 5.37.

3. **Momentum .v. Time-of-Flight** - The TOF_{12} times are quantised into just 5 discrete bins. It has been assumed that the TOF_{12} bins are directly related to the particle momentum bins. This may not be the case, if, for example, the path taken by the particle isn't exactly on the axis or the particle's mass is mis-identified (this should have only a small contribution, however, given the above cut efficiency).

   Figure 5.36 displays a distribution of track longitudinal momentum (p_z) against TOF_{12} time for tracks obtained from the Monte Carlo truth sample. Given that the sample is divided into 5 discrete time-of-flight bins between 31-31.7 ns, each of which will be 0.14 ns wide, it is assumed that within each of these bins all particles have the same momentum. From the plot shown in Figure 5.36 it is clear that there is a non-zero within-bin gradient and in fact there will be some spread in particle momentum for each bin. The plot is fitted and a gradient of $-31.61[MeV/c]/ns$ is found meaning there is a 4.43 MeV/c momentum spread per bin given the momentum varies linearly. The points in the plots in Figure 5.37 are placed in the centre of the bin so the error on each point due to difference in momentum should be $\pm$2.2 MeV/c. The most notable source of errors will, however, be due to momentum overlap between TOF_{12} bins which result from the continuous nature of the particle momentum spread.

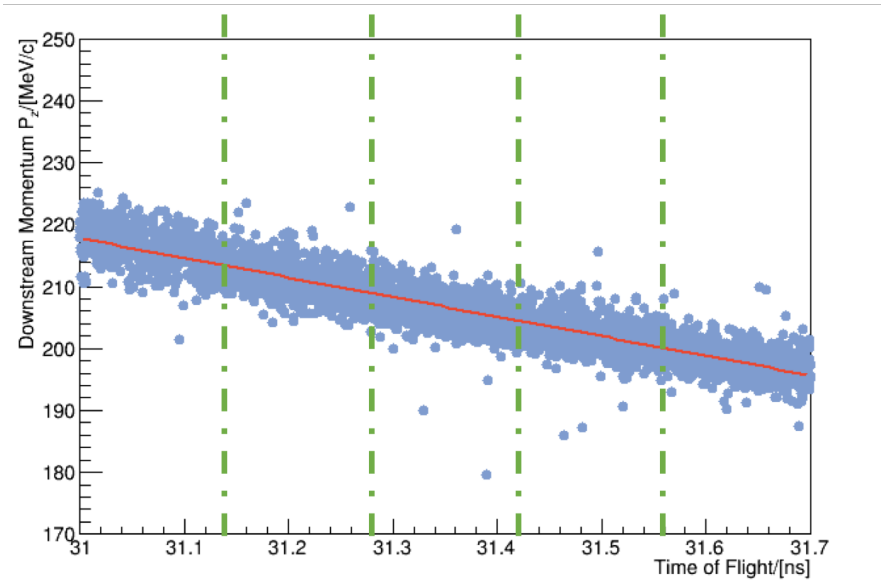

Figure 5.36: Plot showing particle momentum against the time it takes to travel between the TOF1 and TOF2 detectors. The tracks are obtained from the Monte Carlo truth sample after particle ID cuts have been applied. The plot is fitted with a straight line and a gradient of -31.61 $\pm$0.22 and intercept of 1198 $\pm$7 is derived. This results in an error on each point in each of the points in the plots in Figure 5.37 of $\pm$2.2 MeV/c. The green lines show how the corresponding 5 bins which were used in the transfer matrix plots. The points in the plots in Figure 5.37 are placed in the centre of each bin .

4. **Limited Data Sample** - It is apparent from the plots in Figure 5.37 that statistical errors are much larger than the known systematic errors. In order to develop this method of misalignment calculation it will be beneficial to have a larger data sample and, consequently, reduced statistical errors. This will

allow a better evaluation of the overall limitations of the method to be established and resolved. To continue this study and further verify the misalignment measurement more data is essential.

5.13 Conclusions and Future Analysis

Throughout Chapter 5 a unique method for measuring magnet misalignment using single particle transfer matrices for both Focus Coil "field-off" and "field-on" data samples has been presented. Transfer matrices, derived from a multi-dimensional mapping between particle upstream and downstream trace space co-ordinates, are used to put constraints on the misalignment of the Focus Coil's magnetic axis relative to the MICE beam axis. This is a novel use for measuring misalignment of component magnets within a beam line. The technique will benefit MICE as a consistency check against direct measurements and can be developed into a beam-based alignment technique for any multi-magnet accelerator in which a particle's co-ordinate can be measured on entrance and exit of a component magnet.

No transverse translational or rotational displacement is observed for the data, within the limits of the analysis. However, in order to develop this method it will be beneficial to have a larger sample and, therefore, limit the effects of statistical errors. This will allow a better evaluation of the overall limitations of the method. As this study goes towards publication further current settings will be needed for overall conclusions and the accuracy and reliability of these measurements to be calculated. Additional data has been taken in late Summer 2016, but did not form part of this thesis. The method outlined in this chapter has been shown to accurately predict, within understood errors, the matrix element for straight track data. It will, therefore, be used to establish misalignment in future data sets.

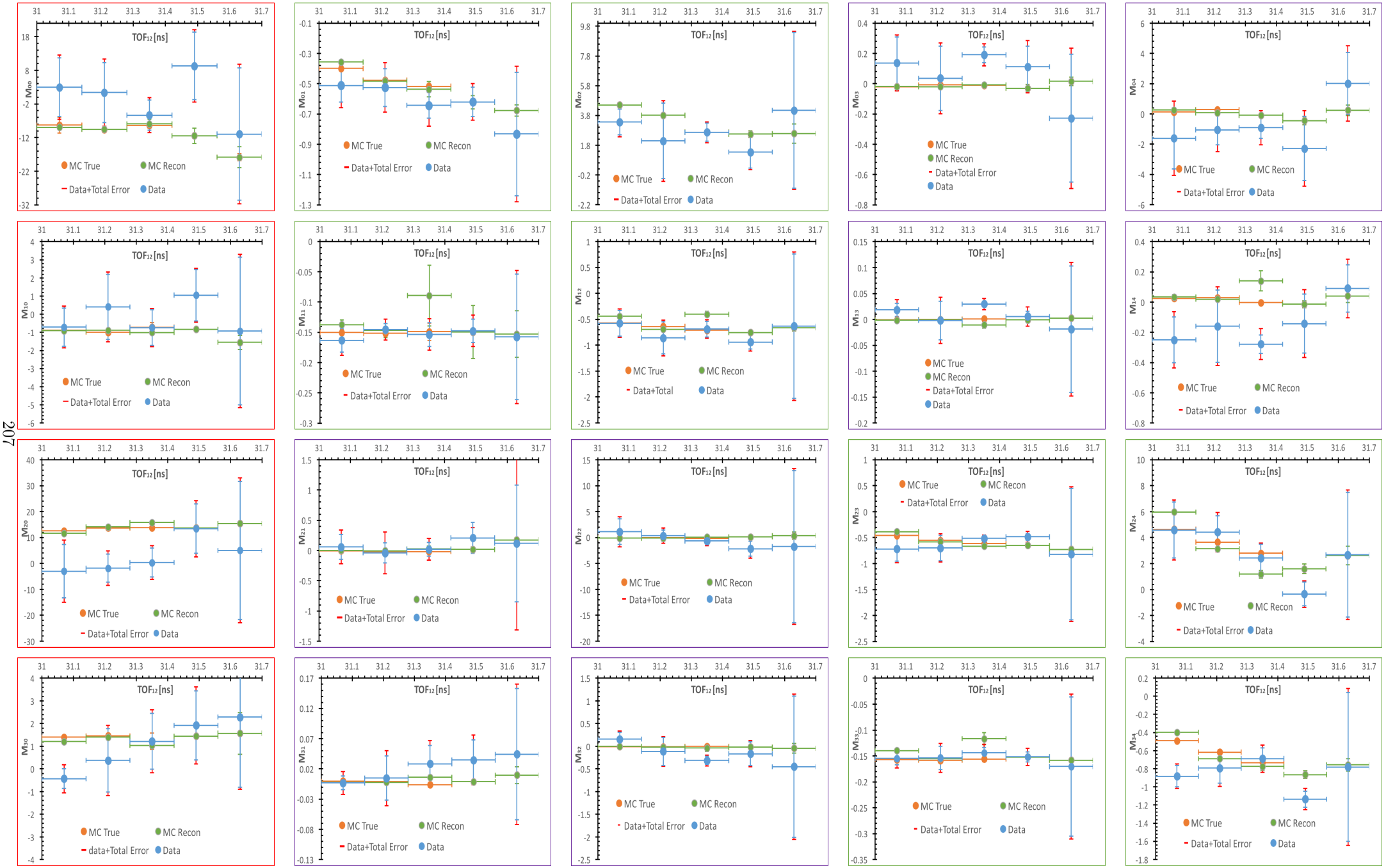
TOF12 [ns]
M00
M01
M02
M03
M04
M10
M11
M12
M13
M14
M20
M21
M22
M23
M24
M30
M31
M32
M33
M34
MC True
MC Recon
Data+Total Error
Data
data+Total Error
Data+Total

Figure 5.37: An array of plots showing how each transfer matrix element varies with TOF_{12} time. The position of the plot corresponds to its position in the matrix. The selected TOF_{12} region, which corresponds to the region of highest muon purity, has been split into 5, equally sized TOF_{12} bins. The transfer matrix has then been calculated separately for particles in each of these 5 bins. The plots here are projections of the resulting transfer matrices. The Monte Carlo simulations presented in the plots have been constructed with the measured mis-alignment as listed in Table 5.5 incorporated into the simulation geometry. The total error which includes statistical errors and systematic and engineering uncertainties, discussed in Section 5.12, are shown in red. The statistical errors give the largest contributions to total error and are included in fitting routine. These are the main source for inconsistencies between data and the MC.

Chapter 6

Summary

Throughout this thesis two independent studies, completed as part of the "Step IV" physics program of the Muon Ionisation Cooling Experiment, have been presented. The purpose of this chapter is to situate these two studies in a wider context both within MICE and the broader particle physics community. The various factors which necessitate MICE are reiterated and the experimental results outlined in Chapters 4 and 5 are summarised. The chapter culminates in a discussion of the future outlook for MICE and the experimental effort required as it reaches its denouement.

Chapter 1 presented a synopsis of contemporary understanding of the Standard Model of particle physics. It was noted that, despite being hugely successful in parameterising experimental data, the Standard Model still engenders some controversy. The following salient issues are considered:

- The Hierarchy Problem - There is still no complete scientific consensus for why the weak force is 10^{32} times stronger than gravity.
- Dark Matter candidates - Large fractions of the universe consist of non-Standard Model particles. Thus far no viable dark matter candidate has been observed.
- Matter: Antimatter Asymmetry - In the early universe most of the matter and antimatter annihilated. Only a small fraction of baryonic matter remained. There are several theories about the origins of this asymmetry, all outside of the Standard Model.
- Unifying Gravity with other fundamental forces - The Standard Model offers no approach to unify gravity with the three other fundamental forces. There have been numerous endeavours to add a "graviton" into the Standard Model; nevertheless, its existence is yet to be experimentally verified.
- Neutrino Mass/Mixing - The original Standard Model proposed massless neutrinos. It has now been conclusively proven that neutrinos "mix" flavours, the implication being that they must possess mass. Precise measurements of the oscillation parameters are needed to fully comprehend the neutrino mass

hierarchy, search for CP violation and ascertain whether they are Majorana or Dirac particles. The numerous current and anticipated neutrino experiments are considered in Section 1.4.8.

There have been many subsequent theories, and extensions, to the Standard Model, most notably those which hypothesise supersymmetric particles ([28] - [31]) or invoke extra dimensions [33]; nonetheless, there has been no conclusive proof of either. The Large Hadron Collider, situated at CERN, is currently the highest energy machine ever constructed, operating at a centre-of-mass energy of 13TeV. It is conceivable that the LHC may help resolve some of these issues but it is probable that further, even higher energy machines, will be required. A muon collider has the advantages, over conventional machines, that it would produce highly tuned, high centre-of-mass energy lepton collisions which would not suffer from radiative losses, unlike similar e^+e^- colliders. In addition, the interactions in muon colliders would not be convoluted by parton distribution functions as is the case for hadron machines.

Subsequent to the discovery of the Higgs particle it has become necessary to gain precise measurements of its properties. Muons have the benefit of possessing higher mass than electrons ($\approx 200m_e$) signifying an enhanced coupling to the Higgs boson. Muons are, consequently, a perfect candidate for a "Higgs Factory," [57] permitting additional and more precise measurements of:

- Higgs branching fractions and related coupling;
- Higgs coupling to the Top quark;
- Higgs mass and width;
- Higgs self-couplings; and,
- The total Higgs decay width.

Section 1.3 presented a design for a prospective muon collider. In order to construct muon colliders it is essential to accelerate large fluxes of muons to high energies. A muon beam produced via conventional pion decay has a sizeable spread in phase space; this must be significantly reduced for it to fit inside the accelerator facility. Due to the finite lifetime of the muon, the only viable approach to cooling a muon beam is via ionisation cooling. Chapter 2 gave a theoretical definition of this process; ionisation cooling is yet to be ascertained.

Furthermore, Chapter 1 outlined how the discovery of neutrino mass has necessitated further examination of the neutrino sector. A schematic for a proposed Neutrino Factory, in which neutrinos are produced via muon decay, is presented. In order to attain the desired neutrino fluxes at the Neutrino Factory these muons must be cooled.

The pursuit to prove the feasibility of ionisation cooling is galvanised by its importance to the successful construction of both a Muon Collider or Neutrino Factory. The Muon Ionisation Cooling Experiment [68] aims to demonstrate ionisation cooling. Ionisation cooling describes the reduction in phase-space volume occupied by a beam as it traverses an absorber material. Within the final stages of MICE the longitudinal

momentum is restored meaning only the transverse emittance is diminished. This is referred to as "sustainable ionisation cooling." Chapter 3 gave a comprehensive overview of the physical apparatus employed by MICE in order to attain its design goals.

MICE is presently operational in its "Step IV" commissioning stage. The analyses presented in Chapters 4 and 5 exist in the context of this "Step IV" stage of the MICE experiment. During this phase it is essential to characterise, and correct accordingly, any sources of systematic uncertainties on the cooling measurements. This thesis has exhibited two independent studies which form part of this undertaking:

- A Measurement of Muon Polarisation at the Downstream Calorimeter - Electrons or positrons can enter the cooling channel via decay processes or can be stripped from the walls of the RF cavities in the latter stages of MICE. Background positrons in MICE can occupy the same momentum space as the muons; however, the single particle emittance of the background positrons is larger than that of the signal muons. As a result, the presence of decay positrons in the channel will produce a systematic uncertainty upon the cooling measurement. In order to achieve the desired beam purity of $> 99.8\%$ MICE must be able to reject positron contaminants with an efficiency of $> 99.9\%$.

  Complications arise in calculating the positron flux from muon decay as the angular distribution of the decay positrons is dependent upon the muon's polarisation at decay. The kinematics of charged pion decay are well understood and the muon polarisation at production is, therefore, calculable. However, when traversing a magnetic beam line composed of multiple materials and magnetic elements it is expected that some depolarisation will occur. This will present a systematic uncertainty on the muon polarisation and, consequently, on the MICE emittance measurement.

  One way to characterise the level of depolarisation which occurs within MICE is to measure the muon polarisation upon decay at the downstream calorimeter, the Electron-Muon Ranger. Within Chapter 4 a method for deriving muon polarisation at the EMR is outlined. The angular distribution of the decay positrons produced by the decay of muons at the detector is derived. The distribution of angles at which the positrons are produced, relative to the initial muon direction, is utilised to ascertain a measurement of the average muon polarisation at the point of decay. This can be compared to the expected polarisation, i.e. that anticipated given knowledge of the kinematics of pion decay and the various beam line magnet settings.

  Initially a polarised Monte Carlo sample was set up, based on a realistic MICE geometry. Both a true Monte Carlo sample, independent of the detector response, and a digitised version of the same Monte Carlo sample were passed though the fitting algorithms, and the respective muon polarisations at the point of decay derived. Comparisons between the two Monte Carlo simulations allowed characterisation of systematic uncertainties and any biases to be identified. These could then be countervailed within the real data sample.

  For an initial muon beam polarisation of +1 a measured downstream polarisation of $+0.933 \pm 0.243$

(stat.) ± 0.194 (sys.) was obtained from the digitised Monte Carlo. This is both consistent with that derived from the true Monte Carlo sample (+1.131±0.171 (stat.) ± 0.128 (sys.)) and the expected value. Accordingly, the algorithm presented in this thesis was proven to have the ability to successfully identify the polarisation of a muon beam using positron tracks at the downstream calorimeter, within acknowledged errors.

The fitting algorithms were then applied to an unpolarised data set to allow verification of the method derived in Chapter 4. A polarisation of -0.02139± 0.21936 (stat.) ± 0.18543 (sys.) ± 0.00721 (depol.) ± 0.00120 (det.). was obtained. This is consistent with the expected value of "0" within $\pm 1\sigma_{TOTAL}$. σ_{stat} refers to the statistical fitting errors on this measurements, σ_{sys} to the error due to a systematic bias in the reconstruction and fitting algorithm and $\sigma_{depol.}$ is added to account for the maximum depolarisation effect caused when the muons come to a stop in the EMR. $\sigma_{det.}$ describes uncertainty due to the various detection resolutions inherent in both the hardware and software employed.

The polarisation of the muon at the point of decay, is, within known errors, equivalent to the expected polarisation. The depolarisation of the muon beam as it traverses the channel is minimal. This suggests the method outlined in this chapter can be used to accurately determine the polarisation of the muon beam at the point of decay. Thus, the algorithm can aid background rejection and help improved muon purity. It may therefore be used to measure and monitor beam polarisation in future MICE runs as well as having some impact on how future facilities may monitor their own beam depolarisation. This, not only acts to demonstrate the diversity of measurements the MICE detectors can make but the method presented here can be adapted to other machines in which the monitoring of the polarisation of a particle is necessary.

This study also has further implications as the neutrino fluxes in a future Neutrino Factory will also be dependent upon muon polarisation at the point of decay. It is necessary to comprehend and monitor the polarisation of the muons in the accelerator sub-systems, prior to their decay, in order to accurately characterise the neutrino flux. Consequently, this analysis is a significant result which can be taken into consideration when outlining the instrumentation techniques to be utilised at a future muon or neutrino facility.

- A Measurement of Coil Misalignment using Transfer Matrices - In Chapter 5 single particle transfer matrices were derived from data taken at the two scintillating fibre trackers, positioned either side of the central Focus Coil. These were then used to place limits on any misalignment between the Focus Coil's axis and the global, beam, axis. The Focus Coil, in the subsequent MICE configurations, will surround the absorber material. It is, therefore, within the Coil that the ionisation cooling will take place. It is essential that any misalignments of the magnetic axis relative to the global axis are calculated in order to gain accurate measurements of emittance reduction taking place in the absorber material. Characterising the misalignment in all magnets and between all detectors is, therefore, essential to

ensuring MICE reaches its design goals. This was a unique analysis, and the first time single particle transfer matrices have been exploited in this way.

No transverse translational or rotational misalignment was observed, within the limits of the method. As a result, the Focus Coil is assumed to be aligned with the trackers and the beam axis. However, statistical errors were large and to gain a more complete understanding further data is required.

The technique exhibited in this thesis can be adapted to any multi-component accelerator system in which a particle's position is monitored upon entrance and exit of a given component. Consequently, the analysis presented in Chapter 5 has significant implications for accelerator physics as a whole.

These results are a small part of the commissioning and calibration stage of the MICE experiment. Following the completion of this stage, in 2018, the experiment could enter its "demonstration of ionisation cooling" stage in which the experiment will obtain the first measurement of sustainable ionisation cooling. At the time of the original publication of this thesis it was not yet known whether this would, in fact, transpire.

MICE has now taken data with all its particle identification devices, including the SciFi trackers. The first direct emittance measurements taken using the SciFi trackers are currently under analysis, along with measurements of the change in normalised transverse amplitude observed in the "Step IV" configuration. Examination of this data will allow characterisation of the physical processes that underlie the ionisation-cooling effect.

It is noted in Chapter 2 that prior to obtaining any conclusive proof of ionisation cooling a more accurate, data-driven, combined, model of multiple scattering and energy loss in liquid hydrogen is needed. In Section 2.5 a number of simulations were presented and compared to existing data from the MuScat experiment. During 2017 considerable effort was directed towards measurement of scattering distributions in the channel for both Liquid Hydrogen and Lithium Hydride absorbers. Data was taken both with and without cooling allowing examination of energy loss to also take place. The aim being to gain better parameterising of muon scattering at large angles. It is anticipated that the results of these studies, along with those of "Step IV," will be published throughout 2018-19.

Bibliography

[1] David Grittiths, "Introduction to Elementary Particles," Wiler-Vch, 2nd Edition, *ISBN-10: 3527406018, ISBN-13: 978-3527406012* (2008)

[2] R. P. Feynman, "Mathematical Formulation of the Quantum Theory of Electromagnetic Interaction," *Phys. Rev., **80** (1950) 440 - 457*

[3] P.A.M. Dirac , "The Quantum Theory of the Emission and Absorption of Radiation," *Proceedings of the Royal Society of London A. **114** (767) 243 - 265 (1927)*

[4] E. Fermi, "Quantum Theory of Radiation," *Reviews of Modern Physics. **4** 87-132 (1932)*

[5] Gell-Mann Murray, "The Eight-Fold Way: A Theory of Strong Interactions," California Institute of Technology Laboratory, *CTSL-20 (1961)*

[6] S. L. Glashow, "Partial-symmetries of weak interactions," *Nucl.Phys. **22** (1961) 579-588*

[7] S. Weinberg, "A Model of Leptons," *Phys. Rev. Lett. **19** (1967) 1264 -1266*

[8] A. Salam, "Weak and Electromagnetic Interactions," *Conf. Proc. C680519 (1968) 367-377*

[9] J. Beringer et al., "Review of Particle Physics. Particle Data Group," *Phys. Rev., D **86** (2017) 010001*

[10] ATLAS and CMS Collaborations, "Combined Measurement of the Higgs Boson Mass in pp Collisions at $\sqrt{s}$ =7 and 8 TeV with the ATLAS and CMS Experiments," *Phys. Rev. Lett. **114** (2015) 191803*

[11] P. W. Anderson,"Plasmons, Gauge Invariance, and Mass," *Phys. Rev. Lett. **130** (1)(1963) 439*

[12] F. Englert and R. Brout,"Broken Symmetry and the Mass of Gauge Vector Mesons," *Phys. Rev. Lett. **13** (1964) 321*

[13] P. W. Higgs, "Broken symmetries, massless particles and gauge fields," *Phys. Rev. Lett. **12** (1964) 132*

[14] P. W. Higgs, "Broken Symmetries and the Masses of Gauge Bosons," *Phys. Rev. Lett. **13** (1964) 508*

[15] G. S. Guralnik; C. R. Hagen; T. W. B. Kibble, "Global Conservation Laws and Massless Particles," *Phys. Rev. Lett. **13** (1964) 585-587*

[16] P. W. Higgs, "Spontaneous symmetry breakdown without massless bosons," *Phys. Rev.* ***145*** *(1966) 1156*

[17] T. W. B. Kibble, "Symmetry breaking in non-Abelian gauge theories," *Phys. Rev.* ***155*** *(1967) 1554*

[18] ATLAS Collaboration,"Observation of a new particle in the search for the Standard Model Higgs boson with the ATLAS detector at the LHC," *Phys. Lett. B* ***716*** *(2012) 1-29*

[19] CMS Collaboration, "Observation of a new boson at a mass of 125 GeV with the CMS experiment at the LHC," *Phys. Lett. B* ***716*** *(2012) 30*

[20] ATLAS Collaboration, "Evidence for the spin-0 nature of the Higgs boson using ATLAS data," *Phys. Lett. B* ***726*** *(2013) 120*

[21] CMS Collaboration,"Study of the Mass and Spin-Parity of the Higgs Boson Candidate via Its Decays to Z Boson Pairs," *Phys. Rev. Lett.* ***110*** *(2013) 081803*

[22] Daniel V. Schroeder and Michael Peskin, "An Introduction to Quantum Field Theory," Westview Press Inc; Reprint edition, *ISBN-10: 0201503972*, *ISBN-13: 978-0201503975* (1995)

[23] E. Noether, "Invariant Variation Problems," *Gott. Nachr.* ***1918*** *(1918) 235-257*, *Transp. Theory Statist. Phys.* ***1****, 186 (1971)*

[24] Wu, C.-S., "Recent Investigation of the Shapes of β-Ray Spectra," *Reviews of Modern Physics.* ***22****(4) (1950) 386-398*

[25] Mathew Reece, "Physics at a Higgs Factory," *Int. J. Mod. Phys. A* ***31****, 1644003 (2016)*

[26] VI Tevnov, "Higgs Factories," *Proceedings of Science IHEP-LHC 2012, Institute for High Energy Physics, Protvino, Moscow region, Russia*, *arXiv:1307.3893* ***[physics.acc-ph]****, (2013)*

[27] D. Hanneke, S. Fogwell, and G. Gabrielse, "New Measurement of the Electron Magnetic Moment and the Fine Structure Constant," *Phys. Rev. Lett.* ***100*** *120801 (2008)*

[28] S. R. Coleman, J. Mandula, "All Possible Symmetries of the S Matrix," *Phys. Rev.* ***159*** *(1967) 1251-1256*

[29] Y. .A. Golfand, E. P. Likhtman, "Extension of the Algebra of Poincare Group Generators and Violation of P invariance," *JETP Lett.* ***13*** *(1971) 323-326*

[30] R. Haag, J. T. Lopuszanski, M. Sohnius, "All possible generators of supersymmetries of the S-matrix," *Nucl. Phys. B* ***88*** *(1975) 257*

[31] Pierre Fayet, "About the origins of the supersymmetric standard model," *Nucl. Phys. Proc. Suppl,* ***101*** *(2001) 81-98*

[32] Christian Autermann, "Experimental Status of Supersymmetry after the LHC Run-I," *arXiv:1609.01686v1* ***[hep-ex]****(2016)*

[33] N. Arkani-Hamed, S. Dimopoulos, G. R. Dvali, "The Hierarchy Problem and New Dimensions at a Millimeter," *Phys.Lett.B* ***429*** *(1998) 263-272*

[34] ATLAS Collaboration, "Search for TeV-scale gravity signatures in high-mass final states with leptons and jets with the ATLAS detector at $s = \sqrt{13}$ TeV," *Physics Letters B* ***760*** *(2016) 520 - 537*

[35] CMS Collaboration, "Search for dark matter, invisible Higgs boson decays, and large extra dimensions in the ll+E_T^{miss} final state using 2016 data," ***CMS-PAS-EXO-16-052*** *(2016)*

[36] Ade, P. A. R.,Aghanim, N., Armitage-Caplan, C., Planck Collaboration et al., "Planck 2013 results. I. Overview of products and scientific results," Table 9. Astronomy and Astrophysics 1303: 5062, *arXiv:1303.5062* ***[astro-ph.CO]*** *(2013)*

[37] Jarosik, N. et al., "Seven-Year Wilson Microwave Anisotropy Probe (WMAP) Observations: Sky Maps, Systematic Errors, and Basic Results," *Astrophysical Journal Supplement* ***192*** *(2011)*

[38] Rubin, Vera C., Ford, W. Kent, Jr., "Rotation of the Andromeda Nebula from a Spectroscopic Survey of Emission Regions," *Astrophysical Journal, vol.* ***159*** *(1970) 379*

[39] D.Walsh, R.F.Carswell, R.J.Weymann, " 0957 + 561 A, B: twin quasistellar objects or gravitational lens," *Nature* ***279****, (1979) 381-384*

[40] Penzias, A. A., Wilson, R. W, "A Measurement of Excess Antenna Temperature at 4080 Mc/s," *The Astrophysical Journal.* ***142*** *(1978) (1) 419-421*

[41] Copi, C. J.; Schramm, D. N.; Turner, M. S. "Big-Bang Nucleosynthesis and the Baryon Density of the Universe," *Science* ***267*** *(1997) 192-199*

[42] LHCb Collaboration,"First Observation of CP Violation in the Decays of B0s Mesons," *Phys. Rev. Lett.* ***110*** *(2013) 221601*

[43] BABAR and Belle Collaborations, "First Observation of CP Violation in $\bar{B} \to D_{cp}h^0$ Decays by a Combined Time-Dependent Analysis of BABAR and Belle Data," *Phys. Rev. Lett.* ***115*** *121604 (2015)*

[44] Gary Steigman, "Primordial Nucleosynthesis in the Precision Cosmology Era," *Annu. Rev. Nucl. Part. Sci.* ***57*** *(2007) 463-491*

[45] Rovelli, C. , "Notes for a Brief History of Quantum Gravity," Presented at the 9th Marcel Grossmann Meeting in Roma, *arXiv:gr-qc/0006061 (2001)*

[46] A. Einstein, "The Collected Papers of Albert Einstein, Volume 6: The Berlin Years: Writings, 1914?1917 -The Foundation of General Relativity," Princeton University Press, *ISBN 978-0-691-01734-1* (1997)

[47] Feynman, R. P.; Morinigo, F. B.; Wagner, W. G.; Hatfield, B, "Feynman Lectures on Gravitation", Addison-Wesley, *ISBN 0-201-62734-5* (1995)

[48] B. Pontecorvo, "Mesonium and anti-mesonium," *Sov. Phys. JETP* ***6*** *(1957) 429*

[49] R. Davies, Don S Harmor, K.C Homan "Search for Neutrinos from the Sun," *Phys. Rev.Lett.* ***20*** *(1968) 1205-1209*

[50] Fukuda Y et al 1998 (Super-Kamiokande Collaboration), "Evidence for Oscillation of Atmospheric Neutrinos," *Phys. Rev. Lett.* ***81*** *(1998) 1562*

[51] SNO collaboration, "Direct Evidence for Neutrino Flavor Transformation from Neutral-current Interactions in the Sudbury Neutrino Observatory," *Phys. Rev. Lett.* ***89*** *(2002) No. 1 011301*

[52] Bruning, Oliver Sim, Collier, Paul, Lebrun, P , Myers, Stephen , Ostojic, Ranko ,Poole, John, Proudlock, Paul,"LHC Design Report 1 the LHC Main Ring," ***CERN-2004-003-V-1****(2004)*

[53] Pippa Wells (ATLAS Collaboration),"Physics Program of the LHC Upgrades," Presented at Lepton Photon Conference -CERN *(2013)*

[54] The HiLumi, HL-LHC Project, `http://hilumilhc.web.cern.ch/`

[55] The International Linear Collider, "The ILC Technical DesignReport," `http://www.linearcollider.org/ILC/Publications/Technical-Design-Report` *(2013)*

[56] M. Aicheler, P. Burrows, M. Draper, T. Garvey, P. Lebrun, K. Peach, N. Phinney, H. Schmickler, D. Schulte and N. Toge, "A Multi-TeV linear collider based on CLIC technology: CLIC Conceptual Design Report," ***CERN-2012-007*** *(2012)*

[57] D. Neuffer, M.Palmer, Y. Alexahin, C. Ankenbrandt, J. P. Delahaye, "A Muon Collider As A Higgs Factory," *arXiv:1502.02042* ***[physics.acc-ph]*** *(2015)*

[58] M.S Berger, "Higgs Bosons at Muon Colliders," *arXiv:hep-ph/0110390 (2001)*

[59] Valery Telnov, INP, Novosibirsk "Higgs Factory" talk at "LHC on the March", Protvino, `https://indico.cern.ch/event/202467/contributions/388890/attachments/304878/425874/telnov-higgs-factories.pdf`*(2012)*

[60] Tao Han and Zhen Liu, "Potential precision of a direct measurement of the Higgs boson total width at a muon collider," *Phys. Rev. D* ***87*** *033007 (2013)*

[61] Alexander Conway, Hans Wenzel, Estia Eichten, Ronald Lipton "Measuring the Higgs Self-Coupling Constant at a Multi-TeV Muon Collider," ***FERMILAB-FN-0979-PPD*** *(2013)*

[62] Conveners: Sally Dawson (BNL), Andrei Gritsan (Johns Hopkins), Heather Logan (Carleton), Jianming Qian (Michigan), Chris Tully (Princeton), Rick Van Kooten (Indiana), "Higgs working group report," *arXiv:1310.8361v2* ***[hep-ex]*** *(2014)*

[63] Matthew J. Dolan, Christoph Englert and Michael Spannowsk, "Higgs self-coupling measurements at the LHC," *arXiv:1206.5001v2* ***[hep-ph]****, (2012)*

[64] M. Purohit, "Can we observe $h \to c\bar{c}$?", Presented at the Higgs Factory Muon Collider Workshop at UCLA, *2013* (unpublished)

[65] Daniel Kaplan, "Overview of Muon Cooling," Proceedings from COOL15 *(2015)*

[66] R. B. Palmer, J. S. Berg, R. C. Fernow, J. C. Gallardo, H. G. Kirk, Y. Alexahin, D. Neuffer, S. A. Kahn, and D. Summers, "A Complete Scheme of Ionization Cooling for a Muon Collider," *arXiv:0711.4275* ***[physics.acc-ph]****(2007)* .

[67] Vladimir Shiltsev, " On the Future High Energy Colliders," *arXiv:1509.08369* ***[physics.acc-ph]****, (2015)*

[68] Proposal to the Rutherford Appleton Laboratory, An International Muon Ionization Cooling Experiment, ***MICE-Note 21*** *(2003)*

[69] Particle Data Group, "Neutrino Mass, Mixing, And Oscillations," `http://pdg.lbl.gov/2015/reviews/rpp2015-rev-neutrino-mixing.pdf` *(2017)*

[70] Maki, Z. Nakagawa, M.Sakata, S."Remarks on the Unified Model of Elementary Particles," *Progress of Theoretical Physics.* ***28*** *(1962) 870*

[71] S.M. Bilenky, J. Hosek, and S.T. Petcov, "On the oscillations of neutrinos with Dirac and Majorana masses," *Phys. Lett. B* ***94*** *(1980) 495*

[72] J. Schechter and J.W.F. Valle, "Neutrino masses in SU(2) x U(1) theories," *Phys. Rev. D* ***22*** *(1980) 2227*

[73] A.G. Cohen, S.L. Glashow, and Z. Ligeti, "Disentangling Neutrino Oscillations," *Phys. Lett. B* ***678*** *(2009) 191*

[74] L. Wolfenstein, "Neutrino Oscillations in Matter," *Phys. Rev.* ***D17*** *(1978) 2369-2374*

[75] S. P. Mikheev and A. Yu. Smirnov, "Resonance Amplification of Oscillations in Matter and Spectroscopy of Solar Neutrinos," *Sov. J. Nucl. Phys.* ***42*** *(1985) 913-917*

[76] V. Barger et al.,"Matter effects on Three-Neutrino Oscillations," *Phys. Rev.* ***D22*** *(1980), 2718*

[77] Image Taken from `https://inspirehep.net/record/1114323/plots` *(2016)*

[78] Hyper-Kamiokande Collaboration, "Letter of Intent: The Hyper-Kamiokande Experiment: Detector Design and Physics Potential," *arXiv:1109.3262* ***[hep-ex]****, (2011)*

[79] Noνa Collaboration, "First measurement of muon-neutrino disappearance in NOvA," *Phys. Rev.* ***D93*** *(2016) 051104*

[80] Noνa Collaboration, "First measurement of electron neutrino appearance in NOvA," *Phys. Rev. Lett.* ***116*** *(2016), 151806*

[81] T2K Collaboration, "First combined analysis of neutrino and antineutrino oscillations at T2K," *arXiv:1701.00432v1* ***[hep-ex]*** *(2017)*

[82] A. M. Dirac, "The Quantum theory of electron," *Proc. Roy. So c. Lond. A* ***117****(1928) 610-624*

[83] E. Majorana, "Theory Of The Symmetry Of Electrons And Positrons," *Nuovo Cim.* ***14*** *(1937) 171-184*

[84] Palash B.V, "Dirac, Majorana and Weyl fermions," *arXiv:1006.1718* ***[hep-ph]*** *(2011)*

[85] Pascoli and S.T. Petcov, "The SNO Solar Neutrino Data, Neutrinoless Double Beta-Decay and Neutrino Mass Spectrum," *Phys. Lett.* ***B544*** *(2002) 239*

[86] S.M. Bilenky et al., "Short-baseline neutrino oscillations and neutrinoless double-beta decay in schemes with an inverted mass spectrum," *Phys. Rev.* ***D54*** *(1996), 4432*

[87] S.M. Bilenky et al., "Constraints from Neutrino Oscillation Experiments on the Effective Majorana Mass in Neutrinoless Double Beta-Decay," *Phys. Lett.* ***B465*** *(1999) 193*

[88] COBRA Collaboration,"The COBRA Double Beta Decay Experiment," *Nucl. Phys. Proc. Suppl. 229-232 (2012) 488*

[89] CUORE Collaboration,"CUORE: A Cryogenic Underground Observatory for Rare Events," *arXiv:hep-ex/0212053v1 (2002)*

[90] N Ishihara et al., "The DCBA Experiment for Studying Neutrinoless Double Beta-decay," *J.Phys.Conf.Ser.* ***203*** *(2010) 012071*,

[91] M. Danilovd et al., "Detection of Very Small Neutrino Masses in Double-Beta Decay using Laser Tagging," *Phys.Lett.* ***B480*** *(2000) 12-18*

[92] GERDA Collaboration, "Gerda: The GERmanium Detector Array for the search of neutrinoless double beta decays of 76-Ge at LNGS," *Nucl. Phys. Proc. Suppl.* ***143*** *(2005) 567-567*

[93] US KamLAND Collaboration, "Proposal for US Participation in KamLAND," `http://kamland.stanford.edu/Technical/KamLAND.US.Proposal.pdf` *(1999)*

[94] The Majorana Collaboration,"The Majorana Demonstrator: A Search for Neutrinoless Double-beta Decay of 76Ge," *Nucl. Phys. Proc. Suppl.* ***217*** *(2011) 44-46*

[95] XMASS Collaboration, "XMASS experiment," *Nucl. Phys. Proc. Suppl.* ***143*** *(2005) 506-506*

[96] Piquemal F. et al. (SuperNEMO Collaboration), "The SuperNEMO project," *Phys. At. Nucl.**69** (2006), 2096-2100*

[97] Agostini, M. et al. (GERDA Collaboration), "Results on Neutrinoless Double-beta Decay of 76-Ge from Phase I of the GERDA Experiment," *Phys. Rev. Lett. **111** (12) (2013) 122503.*

[98] EXO Collaboration, "Observation of Two-Neutrino Double-Beta Decay in Xe136 with the EXO-200 Detector," *Phys. Rev. Lett. **107** (2011) 212501*

[99] A. Palazzo,"Phenomenology of light sterile neutrinos: a brief review," *Mod. Phys. Lett. A **28** No. 7 (2013) 1330004*

[100] J.N. Abdurashitov et al, " Measurement of the solar neutrino capture rate with gallium metal. III: Results for the 2002-2007 data-taking period," *Phys. Rev. C**80**:015807 (2009)*

[101] G. Mention, M. Fechner, T. Lasserre, T.A. Mueller, D. Lhuillier, M. Cribier, and A. Letourneau, "The Reactor Antineutrino Anomaly," *Phys. Rev. D**83** (2011) 073006*

[102] C. Athanassopoulos et al.(LSND Collaboration), "Evidence for anti-muon-neutrino to anti-electron-neutrino oscillations from the LSND experiment at LAMPF," *Phys.Rev.Lett., **77** (1996) 3082-3085*

[103] A. A. Aguilar-Arevalo et al. (MiniBooNE Collaboration),"A Search for electron neutrino appearance at the $\Delta m^2 \approx$1eV 2 scale," *Phys. Rev. Lett. **103** (2009) 111801*

[104] A.A. Aguilar et al, "Improved Search for $\nu_\mu \to \nu_e$ Oscillations in the MiniBooNE Experiment," *Phys. Rev. Lett., **110**:161801 (2013)*

[105] P. Kyberd et al., "Neutrinos from Stored Muons Letter of Intent to the Fermilab Physics Advisory Committee," ***FERMILAB-LOI-2013-02** (2013)*

[106] KamLAND Collaboration, "Precision Measurement of Neutrino Oscillation Parameters with KamLAND," *Phys.Rev.Lett. **100** (2008) 221803*

[107] Hisakazu Minakata, Masashi Sonoyama (Tokyo Metropolitan U.), Hiroaki Sugiyama (KEK, Tsukuba), "Determination of theta(23) in Long-Baseline Neutrino Oscillation Experiments with Three-flavor Mixing Effects," *Phys.Rev. **D70** (2004) 113012*

[108] T2K Collaboration, K. Abe et al., "Observation of Electron Neutrino Appearance in a Muon Neutrino Beam," *Phys. Rev. Lett. **112** (2014) 061802*

[109] Daya Bay Collaboration, "Observation of Electron-Antineutrino Disappearance at Daya Bay," *Phys. Rev. Lett. **108** (2012), (17) 171803*

[110] F. Capozzi et al.,"Status of three-neutrino oscillation parameters", *Phys. Rev. **D89** (2014) 093018*

[111] M.C. Gonzalez-Garcia, M. Maltoni, and T. Schwetz, "Updated fit to three neutrino mixing: status of leptonic CP violation," *JHEP* ***11*** *052 (2014)*

[112] D.V. Forero, M. Tortola and J.W.F. Valle, "Neutrino oscillations refitted," *Phys. Rev.* ***D90*** *(2014) 093006*

[113] M. Apollonio et al. (Chooz Collaboration) "Limits on Neutrino Oscillations from the CHOOZ Experiment," *Phys. Lett. B* ***466*** *(1999), 415-430*

[114] Y. Abe et al. Double Chooz Collaboration, "Indication of Reactor electron anti-neutrino Disappearance in the Double Chooz Experiment, " *Phys. Rev. Lett.* ***108*** *(2012) 131801*

[115] J.K. Ahn et al. , RENO Collaboration, "Observation of Reactor Electron Antineutrino Disappearance in the RENO Experiment," In: *Phys. Rev. Lett.* ***108*** *(2012) 191802*

[116] P. Adamson et al., MINOS Collaboration, "Improved Search for Muon-Neutrino to Electron-Neutrino Oscillations in MINOS," *Phys. Rev. Lett.* ***107*** *(2011) 181802*

[117] LBNF/DUNE Collaboration, "Long-Baseline Neutrino Facility (LBNF) and Deep Underground Neutrino Experiment (DUNE) Conceptual Design Report Volume 1: The LBNF and DUNE Projects," *arXiv:1601.05471* ***[physics.ins-det]*** *(2016)*

[118] R. N. Cahn et al. LBNL, "White Paper: Measuring the Neutrino Mass Hierarchy," *arXiv 1307.5487v2* ***[hep-ex]*** *(2014)*

[119] R.B.Patterson, "Prospects for measurement of the neutrino mass hierarchy," *arXiv:1506.07917v3* ***[hep-ex]*** *(2016)*

[120] S. Goswami et al., "Probing the Neutrino Mass Hierarchy via Atmospheric Survival Rates in Megaton Water Cerenkov Detector," *Nucl. Phys. (Proc. Supp.) B* ***143*** *(2005) 121*

[121] J. Scott Berg et al., (The IDS-NF Collaboration), "International Design Study for the Neutrino Factory," IDSNF contribution to the 54th ICFA Beam Dynamics Newsletter *(2011)*

[122] Image taken from `http://map.fnal.gov/`

[123] Alex J. Dragt, "Numerical third-order transfer map for solenoid," *NIM A* ***298*** *441-459 (1990)*

[124] S. Y. Lee, "Accelerator Physics", World Scientific, *ISBN 981-02-3710-3 (1999)*

[125] H. Goldstein, "Classical Mechanics," 3rd ed., Addison-Wesley, Reading, *ISBN: 9781292026558 (2000)*

[126] Alex J. Dragt, "An Overview of Lie Methods For Accelerator Physics," Proceedings of PAC2013, Pasadena, USA, 2013, pp. 1134-1138.

[127] Chris Rogers, "Beam Dynamics in an Ionisation Cooling Channel," PhD Thesis, Imperial College London (2007)

[128] Yongjun Li, Xiaobiao Huang, "A Practical Approach to Extract Symplectic Transfer Maps Numerically for Arbitrary Magnetic elements, " *arXiv:1511.00710* ***[physics.acc-ph]*** *(2015)*

[129] A. Chao, "Lecture Notes on Topics in Accelerator Physics," ***SLAC-PUB-9574*** *(2002)*

[130] Mario Conte, William Mackay, "An Introduction to Physics of Particle Accelerators" World Scientific, 2nd Edition, *ISBN:13 978-981-277-961-8 (pbk) (2008)*

[131] J. Liouville, "Note sur la Theorie de la Variation des constantes arbitraires, " Translated from: *Journal de Mathematiques Pures et Appliquees, Ser. I, 3 pp. 342-349 (1838)*

[132] Ken Takayama, "Note on the Courant and Snyder Invariant," *IEEE Transactions on Nuclear Science, Vol. NS-30, (1983)*

[133] G. Penn and J. S. Wurtele, "Beam Envelope Equations for Cooling of Muons in Solenoid Fields" , In: *Phys. Rev. Lett., vol.* ***85*** *(2000) 764-767*

[134] Robinson, K," Radiation effects in circular electron accelerators," *Phys. Rev. Ill (1958) 373*

[135] D. Mohl, G. Petrucci, L. Thorndahl, and S. van der Meer, "Physics and technique of stochastic cooling," *Phys. Rept.* ***58*** *(1980)*

[136] Budker, G. I. "An effective method of damping particle oscillations in proton and antiproton storage rings," *Soviet Atomic Energy.* ***22*** *(5): 438-440. (1967)*

[137] A. N. Skrinskii and V. V. Parkhomchuk, "Method of cooling beams of charged particles," *Sov. J. Part. Nucl.* ***12*** *(3): 223247. (1981)*

[138] MICE Website: `http://mice.iit.edu`

[139] S. Holmes, "The Physics of Muon Cooling for a Neutrino Factory," DPhil Thesis, University of Oxford (2006)

[140] B. Rossi, "High-energy particles," Prentice-Hall, Inc., Englewood. Cliffs, NJ, (1952)

[141] E. Rutherford, "The Scattering of α and β Particles by Matter and the Structure of the Atom", *Philosophical Magazine. Series* ***6*** *vol.* ***21*** *(1911)*

[142] G. Moliere, "Theorie der Streuung schnellcr geladener Teilchen. II. Mehrfach- und Vielfach- streuung," (translated to English), Z. Naturforsch. 3a, 78 (1948)

[143] H.A. Bethe, "Molieres Theory of Multiple Scattering," *Phys. Rev.* ***89*** *(1953) 1256*

[144] H. Snyder, W. T. Scott, "Multiple Scattering of Fast Charged Particles," *Phys. Rev.* ***76*** *(1949) 220*

[145] W.T. Scott, "The Theory of Small-Angle Multiple Scattering of Fast Charged Particles," *Rev. Mod. Phys.* ***35*** *(1963) 231*

[146] S.A. Goudsmit and J. L. Saunderson, "Multiple Scattering of Electrons. I," *Phys. Rev.* ***57*** *(1940) 24* and "Multiple Scattering of Electrons. II," *Phys. Rev.* ***58*** *(1940) 36*

[147] H.W. Lewis, "Multiple Scattering in an Infinite Medium," *Phys. Rev* ***78*** *(1950) 526*

[148] A. Tollestrup, J. Monroe, "Multiple scattering calculations for hydrogen, helium, lithium and beryllium," *NFMCC technical note MC-176 (2000)*

[149] WWM Allison, "Calculations of energy loss and multiple scattering (ELMS) in molecular hydro- gen," *J. Phys. G: Nucl. Part. Phys.* ***29*** *(2003) 17011703*

[150] V.L. Highland, "Some practical remarks on multiple scattering," *Nucl. Instrum. Methods* ***129*** *497 (1975)*; with added input from *Nucl. Instrum. Methods* ***161*** *(1979) 171*

[151] G.R. Lynch and O.I Dahl, "Approximations to multiple Coulomb scattering," *Nucl. Instrum. Methods* ***B58*** *(1991) 6*

[152] G. Wentzel, "Zwei Bemerkungen uber die Zerstreuung korpuskularer Strahlen als Beugungserscheinung," *Z. Phys., 40:590, (1926)*

[153] GEANT4 Collaboration, S. Agostinelli et al., "GEANT4: A Simulation toolkit," *Nucl. Instrum. Meth.* ***A506*** *(2003) 250-303.*

[154] R.C Fernow, "ICOOL: A Simulation Code for Ionization Cooling of Muon Beams, "Proceedings of the 1999 Particle Accelerator Conference, New York *(1999)*

[155] L Urban, "Changes in Multiple Scattering between G4 8.1 and 9.0," *Presented at RMKI 13-19 September 2007*

[156] H. Bethe, "Molieres Theory of Multiple Scattering," *Phys. Rev.* ***89*** *(1953) 1256-1266*

[157] U. Fano, "Penetration of Protons, Alpha Particles, and Mesons," *Ann. Rev. Nucl. Sci.* ***13*** *1 (1963)*

[158] MuScat Collaboration, "The Scattering of Muons in Low Z Materials," *Nucl. Instrum. Meth.* ***B251*** *(2006) 41-55*

[159] M. Ellis on Behalf of MuScat, "Results from MuSCAT," Presented at HSS06, 7th September 2006

[160] Timothy Calisle, "Step IV of the Muon Ionization Cooling Experiment (MICE) and the Multiple Scattering of Muons," DPhil Thesis, University of Oxford (2013)

[161] Saurabh Kumar Vij, "Simulation of Muons Energy Loss in Lithium Hydride for the Neutrino Factory Design Study," Masters Thesis, Delhi University, India and ENSTA Paris Tech, France (2010)

[162] L.D. Landau, "On The Energy Loss of Fast Particles by Ionization," *J. Exp. Phys. (USSR)* ***8*** *(1944) 201*

[163] P.V. Vavilov, "Ionization Losses of High-energy Heavy Particles," *Sov. Phys. JETP **5** (1957) 749*

[164] Mark Rayner, "The Development of a Novel technique for Characterizing the MICE Muon Beam and Demonstrating its Suitability for a Muon Cooling Measurement," PhD Thesis, University of Oxford (2011)

[165] A. Dobbs, C. Hunt, K. Long, E. Santos and C. Heidt,"The Reconstruction Software for the MICE Scintillating Fibre Trackers," *20th International Conference on Computing in High Energy and Nuclear Physics (CHEP2013) IOP Publishing, Journal of Physics: Conference Series **513** (2014)*

[166] A. Aloisio et al., KLOE collaboration, "The KLOE Electromagnetic Calorimeter," *Nucl. Inst. and Meth. **A 494** (2002) 326*

[167] Ruslan Asfandiyarov, "Totally Active Scintillator Tracker-Calorimeter for the Muon Ionization Cooling Experiment," PhD Thesis, University of Geneva (2014)

[168] D. Li, A. DeMello, S. Virostek, M. Zisman, R. Rimmer, " A 201-MHz Normal Conductinf RF Caviitiy For The MICE Experiment," *Proceedings of EPAC08, Genoa, Italy (2008)*

[169] MICE Collaboration, "The MICE Muon Beam on ISIS and the beam-line instrumentation of the Muon Ionization Cooling Experiment," *Journal of Instrumentation, Vol. **7** No. **5** (2012)*

[170] MICE Collaboration, "Pion contamination in the MICE muon beam," *JINST **11** (2016) No. **3** P03001*

[171] MICE Collaboration, "Characterisation of the muon beams for the Muon Ionization Cooling Experiment," *European Journal of Physics C, Vol. **73** No. **10** (2013)*

[172] MICE Collaboration, "Electron-Muon Ranger: performance in the MICE Muon Beam," *JINST **10** P12012 (2015)*

[173] V. Blackmore, C. Hunt, J.B. Lagrange, J. Pasternak, C. Rogers, P. Snopok, H. Witte on the behalf of the MICE Collaboration, "The MICE Ionisation Cooling Demonstration: Technical Note," ***MICE Note 452** (2014)*

[174] T. Millington, "MICE Hall Re-survey," ***MICE Note 458** (2014)*

[175] T Millington, A Hooper, "ISIS Survey Report, MICE Hall TOF0 Date: 19/01/2016," ***MICE Note 483** (2016)*

[176] T Millington, A Hooper, "ISIS Survey Report, MICE Hall TOF1 Date: 03/03/2016," ***MICE Note 484** (2016)*

[177] T Millington, A Hooper, "ISIS Survey Report, MICE Hall EMR Date: 03/03/2016," ***MICE Note 486** (2016)*

[178] M. Apollonio, J. Cobb, M. Dawson, T. Handford, P. Lau, W. Lau, J. Tacon, M. Tacon, S. Yang, "The MICE Diffuser System," *Proceedings of EPAC08, Genoa, Italy (2008)*

[179] D. E. Baynham, T. W. Bradshaw, J. H. Cobb, M A Green, W. W. Lau, S. Q. Yang, "Progress on the Design and Fabrication of the MICE Focusing Magnets," ***MICE Note 275*** *(2009)*

[180] J.H Cobb, "Preliminary dimensions of Focus Coil coils," ***MICE Note 495*** *(2016)*

[181] H. Witte, J. Tarrent, A. Bross , "Partial Return Yoke Performance-General Concept and Performance," *Proceedings of PAC2013, Pasadena, CA USA (2013)*

[182] Edward Santos, "Progress at the Intensity Frontier on Neutrino-Nucleus Interaction Cross Sections and Muon Ionization Cooling," PhD Thesis, Imperial College London (2015)

[183] M. Bogmilov, "The MICE Particle Identification System," *Nucl. Phys.* ***B*** *(proc. Suppl.) 215 (2011) 316 -318*

[184] A. R. Sandstrom, "Background and Instrumentations in MICE," PhD Thesis, University of Geneva (2007)

[185] V. Verguilov, V. Palladino on behalf of MICE Collaboration,"Particle Identification Devices in MICE," *Proceedings at DIPAC '09, Basel Switzerland , C09-05-25.6, p.321-323 (2009)*

[186] MAUS User Guide: `http://micewww.pp.rl.ac.uk/maus`

[187] Chris Rogers, Chris Tunnell on behalf of the MICE Collaboration,"MAUS:MICE Analysis Users Software," *Proceedings of IPAC 2011 (2011)*

[188] ROOT User Guide: `https://root.cern.ch/guides/users-guide`

[189] D. Cline, B. Norum, R. Rossmanith, "Polarization in a Muon Collider," in *Physics Potential and Development of Muon Colliders, Proc., 3rd Int. Conf., San Francisco, Dec. 1995, Elsevier, in press (1996)*

[190] R. Bayes et al (Twist Collaboration),"TWIST: precision measurement of the muon decay parameters," *J. Phys. Conf. Ser.* ***312*** *102004 (2011)*

[191] Michel L,"Interaction between Four Half-Spin Particles and the Decay of the μ-Meson," *Proc. Phys. Soc.* ***A63*** *p. 514 (1950)*

[192] Bouchiat C and Michel L, "Theory of μ-Meson Decay with the Hypothesis of Nonconservation of Parity," *Phys. Rev.* ***106*** *170 (1957)*

[193] Sirlin A,"Polarization of Electrons in Muon Decay with General Parity- Nonconserving Interactions," *Phys. Rev.* ***108*** *844 (1957)*

[194] Glen Marshall, TRIUMF, "Muon Physics Student Lecture", 2013

[195] M. Apollonio et al, "Oscillation Physics With A Neutrino Factory," ***CERN-2004-002, pp.87-184*** *(2002)*

[196] A. Blondel, "Muon polarisation in the neutrino factory," *Nucl.Instrum.Meth.* ***A451*** *131-137 (2000)*

[197] Charles M. Ankenbrandt et al,"Status of muon collider research and development and future plans," *Phys. Rev Spec. Topics - Accelerators and Beams, Vol.* ***2****, 081001 (1999)*

[198] The Muon Collider Collaboration, "$\mu^+\mu^-$ Collider A Feasibility Study," *Fermi Lab Conf.-96/092, LBNL - 38946 (1996)*

[199] Rajendran Raja and Alvin Tollestrup, "Calibrating the energy of a 5050 GeV muon collider using spin precession," *Phys. Rev. D* ***58*** *013005 (1998)*

[200] D. Cline, "A Higgs-Factory $\mu - \mu$ Collider," ***eConf C960625 LTH094*** *(1996)*

[201] B.Norum, R. Rossmanith, "Precision Energy Measurements in a Muon Collider Using Polarization," *Prepared for Conference: C98-06-22, p.871-873 Proceedings (1998)*

[202] L. H. Thomas, "The kinematics of an electron with an axis," *Philos. Mag.* ***3****, 1-22 (1927)*

[203] Benntett et al., Muon g-2 collaboration, "Final Report of the Muon E821 Anomalous Magnetic Moment Measurement at BNL," *Phys. Rev. D* ***73*** *072003 (2006)*

[204] James Bueno, "A direct measurement of $P_\mu^\pi \zeta$ from muon decay," PhD Thesis, The University of British Columbia (2010)

[205] Bargmann V, Michel L and Telegdi V L, "Precession of Particles Moving in a Homogeneous Electromagnetic Field," *Phys. Rev. Lett.* ***2*** *435-436 (1959)*

[206] F. Drielsma, "Electron Muon Ranger (EMR) Hardware Characterisation," Masters Thesis, University of Geneva (2013)

[207] Tom Roberts, "G4beamline User's Guide 3.04," `www.muonsinternal.com/muons3/g4beamline/G4beamlineUsersGuide.pdf`

[208] R.D Klem,"Depolarisation of Negative Muons Stopping in Liquid Hydrogen", The Enrico Fermi Institute for Nuclear Studies, University of Chicago, *Nuovo Cim.* ***A48*** *(1967) 743-779*

[209] S.G Barov et al, "Depolarisation of muons in solid hydrogen," *Hyperfine Interactions* ***32*** *(1986) 557-559*

[210] A Buhler et al, "Measurements of muon depolarisation in several materials," *Nuovo Cim (1965)* ***39****: 824.(1965)*

[211] Bob Epstrein, "Depolarization of Muons in Solids," *Phys. Rev.* ***142*** *217 (1964)*

[212] John H. Cobb, "The Alignment of the MICE Magnet Modules, " ***MICE Note 445*** *(2014)*

[213] Martin Berz, "Modern Map Methods in Particle Beam Physics," Academic Press, San Diego *(1999)*

[214] Steven Lund, "Beam Stability and Control in Solenoid Transport Channels," Presentation at *Heavy Ion Fusion Symposium, Tokyo Institute of Technology, Japan (2008)*

[215] M. Rosetti Conti, A Bacci, "Beam Based Alignment Methods For Cavities And Solenoids In Photo-injectors," *Proceedings of IPAC2016, Busan, Korea (2016)*

[216] U. Bravar, J. Cobb, "Initial Study of MICE Magnet Alignment Requirements," ***MICE Note 064*** *(2003)*

[217] L Bottura, M Buzio, S Pauletta, N Smirnov, "Measurement of magnetic axis in accelerator magnets: critical comparison of methods and instruments," Presented at *IMTC 2006 Instrumentation and Measurement Technology Conference Sorrento, Italy (2006)*

[218] J. Cobb, V. Blackmore, "Magnetic Axes of the Focus Coils," ***MICE Note 496*** *(2016)*

[219] P. Hanlet, S.Griffiths, " Introductory Thoughts on Quench Detection and Quench Protection for Integrated MICE Superconducting Solenoids," ***MICE Note 435*** *(2014)*

[220] The MICE Magnetic Shielding Group, "Mitigation of stray magnetic fields in MICE," ***MICE Note 419*** *(2013)*

[221] Holger Witte, "MICE Step IV PRY Error Field," Presented at *MICE Analysis Meeting 30th April 2015*

[222] John Wolberg, "Data Analysis Using the Method of Least Squares," Springer, *ISBN: 978-3-540-25674-8 (2006)*

[223] MICE Collaboration, "The design, construction and performance of the MICE scintillating fibre trackers," *Nuclear Instruments and Methods in Physics Research Section A: Accelerators, Spectrometers, Detectors and Associated Equipment, vol.* ***659****, no.* ***1****, pp. 136 - 153 (2011)*

[224] Christopher Hunt, PhD Thesis, "High Precision Track Reconstruction and First Emittance Measurements in the MICE Step IV Cooling Channel," (2017)

[225] G. Palombo, "Multivariate Goodness of Fit Procedures for Unbinned Data: An Annotated Bibliography," *arXiv:1102.2407v1* ***[stat.AP]*** *(2011)*

[226] Konstantinos Fragiadakis, Simos G. Meintanis, "Goodness-of-fit tests for multivariate Laplace distributions," *Mathematicaland Computer Modelling* ***53*** *(2011) 769 -779*

[227] F. James, CERN Computing and Networks Division, "MINUIT- Function Minimization and Error Analysis: Reference Manual, " *CERN Program Library Long Writeup D506*

Appendix A

Straight Track Transfer Matrices (Data)

$31 < TOF_{12} < 31.3$

$$\begin{pmatrix} 1.667 \pm 1.218 & 0.9667 \pm 0.025 & 17.7 \pm 0.95 & -0.042 \pm 0.025 & -0.195 \pm 0.815 \\ -0.1659 \pm 0.115 & -0.0113 \pm 0.003 & 0.743 \pm 0.099 & -9.95 \times 10^{-5} \pm 1 \times 10^{-4} & 0.086 \pm 0.061 \\ 3.337 \pm 1.699 & 0.006 \pm 0.567 & -0.274 \pm 1.02 & 0.979 \pm 0.084 & 20.13 \pm 0.91 \\ 0.372 \pm 0.129 & -0.0007 \pm 0.005 & -0.046 \pm 0.108 & -0.0015 \pm 0.0050 & 1.045 \pm 0.043 \end{pmatrix}$$

$31.3 < TOF_{12} < 31.6$

$$\begin{pmatrix} -0.73 \pm 1.64 & 0.789 \pm 0.09 & 17.39 \pm 0.52 & -0.01 \pm 0.08 & -0.291 \pm 0.621 \\ -0.34 \pm 0.18 & -0.009 \pm 0.005 & 0.837 \pm 0.070 & -0.0049 \pm 0.0044 & 0.0146 \pm 0.0846 \\ 3.15 \pm 1.99 & -0.0375 \pm 0.0527 & 0.824 \pm 1.132 & 0.894 \pm 0.098 & 17.10 \pm 0.78 \\ 0.345 \pm 0.188 & -0.0008 \pm 0.006 & 0.104 \pm 0.076 & -0.0768 \pm 0.0065 & 0.792 \pm 0.066 \end{pmatrix}$$

$31.6 < TOF_{12} < 31.9$

$$\begin{pmatrix} 1.92 \pm 2.08 & 0.902 \pm 0.0334 & 17.97 \pm 1.01 & -0.105 \pm 0.095 & -0.472 \pm 0.851 \\ -0.28 \pm 0.27 & -0.0155 \pm 0.0072 & 0.784 \pm 0.119 & -0.0035 \pm 0.0069 & -0.025 \pm 0.079 \\ 3.98 \pm 4.13 & 0.0092 \pm 0.0584 & 1.142 \pm 0.547 & 1.073 \pm 0.114 & 21.06 \pm 1.23 \\ 0.478 \pm 0.273 & 0.0062 \pm 0.0034 & 0.057 \pm 0.0548 & 0.0080 \pm 0.0111 & 1.045 \pm 0.0377 \end{pmatrix}$$

$31.9 < TOF_{12} < 32.2$

$$\begin{pmatrix} 3.01 \pm 1.97 & 0.732 \pm 0.007 & 14.52 \pm 1.41 & 0.06 \pm 0.073 & 0.812 \pm 0.841 \\ -0.19 \pm 0.19 & -0.0287 \pm 0.0010 & 0.519 \pm 0.143 & 0.0074 \pm 0.0058 & 0.104 \pm 0.0603 \\ 5.04 \pm 0.88 & 0.0681 \pm 0.0378 & -1.028 \pm 0.42 & 0.754 \pm 0.080 & 17.63 \pm 1.07 \\ 0.522 \pm 0.146 & -0.0025 \pm 0.0077 & -0.076 \pm 0.0255 & -0.018 \pm 0.003 & 0.905 \pm 0.041 \end{pmatrix}$$

$32.2 < TOF_{12} < 32.5$				
-4.87 ± 3.59	0.631 ± 0.122	15.75 ± 1.68	-0.136 ± 0.160	0.848 ± 0.558
-0.97 ± 0.45	-0.031 ± 0.010	0.816 ± 0.254	-0.00696 ± 0.0140	0.101 ± 0.056
13.42 ± 7.66	0.0232 ± 0.0990	-2.138 ± 1.350	0.5697 ± 0.144	22.04 ± 1.23
0.457 ± 0.306	-0.018 ± 0.008	-0.105 ± 0.098	-0.03 ± 0.02	1.00 ± 0.20

Table A.1: Tables show the derived fitted transfer matrix and corresponding errors for each TOF_{12} bin for straight track data sample 07417. The first column denotes the offsets in each co-ordinate. Of the remaining $4\times$ 4 matrix the diagonal elements should = 1. M_{02} and M_{24} correspond to the drift length and should be 18.94. All the other terms should be 0.

Appendix B

Field On Data Transfer Matrices

$31 < TOF_{12} < 31.14$

$$\begin{pmatrix} 2.96 \pm 8.67 & -0.51 \pm 0.11 & 3.36 \pm 0.86 & 0.137 \pm 0.172 & -1.615 \pm 2.017 \\ -0.709 \pm 1.05 & -0.163 \pm 0.019 & -0.578 \pm 0.249 & 0.018 \pm 0.0129 & -0.249 \pm 0.151 \\ -2.97 \pm 10.28 & 0.059 \pm 0.207 & 1.12 \pm 2.476 & -0.721 \pm 0.234 & 4.58 \pm 2.16 \\ -0.432 \pm 043 & -0.0032 \pm 0.0115 & 0.157 \pm 0.154 & -0.154 \pm 0.125 & -0.882 \pm 0.117 \end{pmatrix}$$

$31.14 < TOF_{12} < 31.28$

$$\begin{pmatrix} 1.369 \pm 8.90 & -0.525 \pm 0.124 & 2.08 \pm 2.53 & 0.035 \pm 0.213 & -1.056 \pm 0.986 \\ 0.403 \pm 1.79 & -0.1456 \pm 0.0097 & -0.860 \pm 0.309 & -0.002 \pm 0.004 & -0.156 \pm 0.238 \\ -1.83 \pm 5.37 & -0.04 \pm 0.21 & 0.364 \pm 0.166 & 0.363 \pm 1.075 & 4.42 \pm 1.28 \\ 0.374 \pm 1.40 & 0.005 \pm 0.036 & -0.115 \pm 0.300 & -0.154 \pm 0.022 & -0.793 \pm 0.168 \end{pmatrix}$$

$31.28 < TOF_{12} < 31.42$

$$\begin{pmatrix} -5.34 \pm 4.45 & -0.644 \pm 0.08 & 2.66 \pm 0.60 & 0.1901 \pm 0.0526 & -0.91 \pm 0.71 \\ -0.74 \pm 0.98 & -0.153 \pm 0.019 & -0.689 \pm 0.151 & 0.0295 \pm 0.0029 & -0.278 \pm 0.061 \\ 0.351 \pm 5.55 & 0.0189 \pm 0.1121 & -0.67 \pm 0.47 & -0.516 \pm 0.035 & 2.42 \pm 1.05 \\ 1.213 \pm 1.227 & 0.0282 \pm 0.0301 & -0.315 \pm 0.088 & -0.144 \pm 0.010 & -0.688 \pm 0.119 \end{pmatrix}$$

$31.42 < TOF_{12} < 31.56$

$$\begin{pmatrix} 9.29 \pm 10.05 & -0.62 \pm 0.10 & 1.331 \pm 1.071 & 0.112 \pm 0.134 & -2.29 \pm 2.11 \\ 1.05 \pm 1.42 & -0.148 \pm 0.019 & -0.941 \pm 0.133 & 0.0055 \pm 0.0100 & -0.142 \pm 0.194 \\ 13.4 \pm 9.50 & 0.209 \pm 0.252 & -2.16 \pm 1.46 & -0.484 \pm 0.064 & -0.34 \pm 0.92 \\ 1.92 \pm 1.53 & 0.0346 \pm 0.0332 & 0.166 \pm 0.260 & -0.152 \pm 0.009 & -1.135 \pm 0.088 \end{pmatrix}$$

$31.56 < TOF_{12} < 31.70$				
-10.97 ± 19.62	-0.832 ± 0.406	4.14 ± 5.25	-0.228 ± 0.422	2.015 ± 2.046
-0.926 ± 4.07	-0.158 ± 0.103	-0.634 ± 1.392	-0.0187 ± 0.121	0.091 ± 0.158
5.028 ± 26.70	0.1187 ± 0.966	-1.737 ± 14.69	-0.820 ± 1.27	2.678 ± 4.791
2.286 ± 3.090	0.044 ± 0.108	-0.451 ± 1.556	-0.17 ± 0.13	-0.781 ± 0.821

Table B.1: Table presenting the derived transfer matrices calculated for 5 TOF_{12} regions. These were calculated independently and correspond to the data points in the plots presented in Figure 5.34

Appendix C

Matrices For Misalignment Limit "Fit to Data"

$31 < TOF_{12} < 31.14$	$31.14 < TOF_{12} < 31.28$
$\begin{pmatrix} -9.112 & -0.528 & 4.486 & -0.040 & 0.01599 \\ -1.127 & -0.162 & -0.525 & -0.0025 & -0.0029 \\ 9.63 & 0.042 & 0.014 & -0.529 & 4.48 \\ 1.33 & 0.0028 & 0.007 & -0.162 & -0.526 \end{pmatrix}$	$\begin{pmatrix} -9.46 & -0.580 & 4.081 & -0.044 & 0.0170 \\ -1.149 & -0.164 & -0.577 & -0.0027 & -0.0023 \\ 10.038 & 0.046 & 0.0141 & -0.581 & 4.07 \\ 1.356 & 0.003 & 0.0066 & -0.164 & -0.578 \end{pmatrix}$

$31.28 < TOF_{12} < 31.42$	$31.42 < TOF_{12} < 31.56$
$\begin{pmatrix} -9.804 & -0.631 & 3.66 & -0.0471 & 0.018 \\ -1.170 & -0.166 & -0.629 & -0.003 & -0.0018 \\ 10.44 & 0.0492 & 0.0146 & -0.632 & 3.649 \\ 1.381 & 0.0032 & 0.0061 & -0.166 & -0.630 \end{pmatrix}$	$\begin{pmatrix} -10.15 & -0.683 & 3.22 & -0.051 & 0.0191 \\ -1.19 & -0.168 & -0.680 & -0.0031 & -0.0011 \\ 10.85 & 0.053 & 0.015 & -0.683 & 3.211 \\ 1.41 & 0.0034 & 0.0056 & -0.168 & -0.681 \end{pmatrix}$

$31.56 < TOF_{12} < 31.70$
$\begin{pmatrix} -10.49 & -0.733 & 2.77 & -0.054 & 0.020 \\ -1.21 & -0.169 & -0.730 & -0.0033 & -0.00053 \\ 11.25 & 0.0565 & 0.0157 & -0.734 & 2.758 \\ 1.429 & 0.0036 & 0.0051 & -0.169 & -0.731 \end{pmatrix}$

Table C.1: Table displaying the derived "best-fit" matrix which gives the misalignment of the coil in run 07534-35. These were calculated independently and correspond to the data points in the plots presented in Figure 5.34

Appendix D

Transfer Matrix TOF_{12} dependence

		j			
i	0	1	2	3	4
0	-2.482	-0.3833	-3.059	-0.0256	0.0072
1	-0.148	-0.0143	-0.359	-0.0013	0.0042
2	2.8857	0.0025	0.0038	-0.3658	-3.0680
3	0.182	0.0014	-0.0033	-0.0134	-0.365

Table D.1: $\frac{\Delta M_{ij}}{\Delta TOF_{12}}$ showing variation in calculated matrix elements over the the fits to 5 separate TOF_{12} bins. These corresponds to the gradients of the plots in Figure 5.34. The gradients of the defocussing terms i.e. upper right and lower left quadrants are small with the variation in the focussing terms i.e. upper left and lower right being larger.